ENHANCEMENT OF REAL-TIME ABSOLUTE GNSS POSITIONING PERFORMANCE

GERÇEK-ZAMANLI MUTLAK GNSS KONUMLAMA PERFORMANSININ İYİLEŞTİRİLMESİ

BERKAY BAHADUR

ASSOC. PROF. DR. METİN NOHUTCU

Supervisor

Submitted to
Graduate School of Science and Engineering of Hacettepe University
as a Partial Fulfillment to the Requirements
for the Award of the Degree of Doctor of Philosophy
in Geomatics Engineering

2021

To my beloved wife and family.

ABSTRACT

ENHANCEMENT OF REAL-TIME ABSOLUTE GNSS POSITIONING PERFORMANCE

Berkay BAHADUR

Doctor of Philosophy, Department of Geomatics Engineering
Supervisor: Assoc. Prof. Dr. Metin NOHUTCU
June 2021, 152 pages

In recent years, the Global Navigation Satellite System (GNSS) community has experienced dramatic changes with the influence of global technological trends, such as digitalization, big data, artificial intelligence, unmanned aerial vehicles, autonomous cars, mobile and wearable technologies, etc. The requirement for instantaneous positioning solutions driven by mainly up-to-date technological trends has had considerable importance nowadays like never before. As a consequence, there has recently been growing attention to achieve higher positioning accuracy in real-time with more cost-effective GNSS solutions. In order to respond the increasing requirement, so many efforts have been made recently to enhance the existing positioning models. At this point, absolute positioning techniques have taken significant interest from the GNSS users for a long time since they eliminate the requirement of the simultaneous reference station and therefore provide cost-effectiveness and operational simplicity compared to the relative/differential GNSS positioning techniques. Furthermore, absolute positioning techniques are naturally compatible with the low-cost GNSS receivers, most of which are in mobile devices. Although the great majority of low-cost GNSS chipsets are able to provide only single-frequency observations, some chipset manufacturers have released new low-cost models which can record dual-frequency code and phase observations. To achieve higher positioning accuracy more cost-effectively, more complicated and enhanced approaches are required for real-time absolute GNSS positioning techniques. In this context, the main objective of this thesis is to provide enhanced positioning approaches for real-time absolute GNSS positioning techniques, taking single- and dual-frequency GNSS receivers

into consideration. For this purpose, two fundamental positioning approaches were proposed in this thesis to be employed with three absolute GNSS positioning techniques, namely single-frequency code pseudorange positioning, single-frequency code-phase combination, and dual-frequency Precise Point Positioning (PPP) solutions. While the first approach was designed to work with real-time service (RTS) products of the International GNSS Service (IGS), ultra-rapid products are the fundamental orbit and clock source for the second approach. Both positioning approaches are compatible with the multi-GNSS solution that contains GPS, GLONASS, Galileo, and BDS satellites. On the other side, this thesis proposed a novel filtering method that integrates the robust Kalman filter and variance component estimation methods for real-time absolute GNSS positioning techniques. Besides, to perform the proposed positioning approaches and algorithms, a GNSS analysis software, which is named PPPH-RT, was developed as a part of this thesis. Several experimental tests were conducted to evaluate the performance of enhanced positioning approaches. All positioning processes were performed in kinematic mode as being compatible with real-time conditions. The results showed that the positioning performance of real-time absolute positioning techniques employing ultra-rapid products can be improved with the proposed positioning approach. Employment of WHU (Wuhan University) ultra-rapid products which have an update interval of 1 hour in the multi-GNSS solution provided better positioning performance for all real-time positioning techniques. The results also indicated that ultra-rapid products with the enhanced positioning approaches are an important alternative for real-time positioning solutions, especially considering that they can be employed without any additional connection. On the other hand, the results demonstrated that the enhanced positioning approach with IGS-RTS products provides better positioning performance for all real-time absolute GNSS positioning techniques when compared with ultra-rapid products. In addition, unlike ultra-rapid products, there was not any time-dependent deterioration in the positioning performance obtained from the IGS-RTS products. However, one drawback of the IGS-RTS products is the requirement of an external connection. Moreover, when the performance of the proposed filtering method was analyzed, it is understood that the proposed filtering method is able to handle stochastic properties of multi-GNSS observations better than conventional approaches and improves the positioning performance of real-time absolute GNSS positioning solutions considerably. Compared with the traditional filtering approach which contains a standard Kalman filter with the weighting scheme depending on higher variance ratios, the proposed filtering method improves the 3D positioning accuracy of real-time single-frequency code pseudorange positioning, single-frequency code-phase combination, and dual-frequency PPP solutions by 52.5%, 24.8%, and 43.9%, respectively.

Keywords: Absolute GNSS positioning, Real-time, Multi-GNSS, Ultra-rapid products, IGS-RTS products, Robust Kalman filter, Variance component estimation

ÖZET

GERÇEK-ZAMANLI MUTLAK GNSS KONUMLAMA PERFORMANSININ İYİLEŞTİRİLMESİ

Berkay BAHADUR

Doktora, Geomatik Mühendisliği Bölümü
Tez Danışmanı: Doç. Dr. Metin NOHUTCU
Haziran 2021, 152 sayfa

Küresel Navigasyon Uydu Sistemi (GNSS) topluluğu, dijitalleşme, büyük veri, yapay zeka, insansız hava araçları, otonom arabalar, mobil ve giyilebilir teknolojiler gibi küresel teknolojik akımların etkisiyle son yıllarda önemli değişiklikler yaşamaktadır. Çoğunlukla bu güncel teknolojik akımlar tarafından yönlendirilen anlık konum belirleme çözümlerine olan ihtiyaç bugünlerde geçmişte hiç olmadığı kadar önem arz etmektedir. Bunun bir sonucu olarak son zamanlarda daha uygun maliyetli GNSS çözümleri ile gerçek-zamanlı olarak daha yüksek konum belirleme doğruluğuna erişebilmek için artan bir ilgi mevcuttur. Artan ilgiye cevaben mevcut konum belirleme modellerini iyileştirmek amacıyla son zamanlarda yoğun gayret sarf edilmiştir. Bu noktada, eşzamanlı referans istasyon ihtiyacını ortadan kaldırması ve bu sayede rölatif ve/veya diferansiyel GNSS konum belirleme tekniklerine kıyasla daha uygun maliyet ve uygulama kolaylığı sağlaması nedeniyle mutlak konum belirleme teknikleri uzun süredir GNSS kullanıcıları tarafından büyük ilgi görmektedir. Dahası, mutlak konum belirleme teknikleri çoğunluğu mobil cihazlarda bulunan düşük maliyetli GNSS alıcıları ile doğal olarak uyumludur. Düşük maliyetli GNSS alıcılarının büyük çoğunluğu yalnızca tek frekanslı gözlemleri sağlayabilse de bazı üreticiler çift frekanslı kod ve faz gözlemlerini kaydedebilen yeni düşük maliyetli alıcı modellerini yakın geçmişte piyasaya sürmüşlerdir. Daha uygun maliyetle daha yüksek konum belirleme doğruluğuna erişebilmek için gerçek-zamanlı mutlak GNSS konum belirleme tekniklerinde daha karmaşık ve gelişmiş yaklaşımlara ihtiyaç duyulmaktadır. Bu kapsamda, bu tezin temel amacı tek ve çift frekanslı GNSS alıcılarını düşünerek gerçek-zamanlı mutlak GNSS konum belirleme teknikleri için gelişmiş

konum belirleme yaklaşımları sağlamaktır. Bu amaçla, bu tezde tek frekanslı kod konumlama, tek frekanslı kod-faz kombinasyonu ve çift frekanslı hassas nokta konumlama (Precise Point Positioning, PPP) olmak üzere üç mutlak konum belirleme tekniğiyle birlikte kullanılmak için iki temel konum belirleme yaklaşımı önerilmiştir. İlk yaklaşım Uluslararası GNSS Servisi'nin (International GNSS Service, IGS) gerçek-zamanlı servis (Real-time Service, RTS) ürünleriyle çalışmak üzere tasarlanırken, ikinci yaklaşım için ultra-hızlı ürünler temel uydu yörünge ve saat kaynağı olarak kullanılmıştır. Her iki yaklaşım da GPS, GLONASS, Galileo ve BDS uydularını içeren çoklu-GNSS çözümüyle uyumludur. Diğer taraftan, bu tez gerçek-zamanlı mutlak GNSS konum belirleme teknikleri için robust Kalman filtresi ve varyans bileşen tahmini yöntemlerini birleştiren yeni bir filtreleme metodu önermektedir. Ek olarak, önerilen konum belirleme yaklaşımlarını ve algoritmalarını uygulayabilmek için PPPH-RT adlı bir GNSS analiz yazılımı da bu tez kapsamında geliştirilmiştir. Gelişmiş konum belirleme yaklaşımlarının performansını değerlendirmek amacıyla çeşitli deneysel testler gerçekleştirilmiştir. Tüm konum belirleme çözümleri, gerçek-zaman koşullarına uygun olacak şekilde kinematik işleme modunda gerçekleştirilmiştir. Sonuçlar, ultra-hızlı ürünleri kullanan gerçek-zamanlı mutlak konum belirleme tekniklerinin performansının önerilen yaklaşımla iyileştirilebileceğini göstermektedir. Çoklu-GNSS çözümünde, 1 saatlik yineleme periyoduna sahip WHU (Wuhan University) ultra-hızlı ürünlerinin kullanılması tüm gerçek-zamanlı konum belirleme teknikleri için daha iyi konum belirleme performansı sağlamıştır. Ayrıca sonuçlar, özellikle herhangi bir ilave bağlantı gerektirmeden çalışabildikleri göz önüne alındığında gelişmiş konum belirleme yaklaşımları ile ultra-hızlı ürünlerin gerçek-zamanlı konum belirleme çözümleri için önemli bir alternatif olduğunu ortaya koymuştur. Öte yandan, sonuçlar gelişmiş konum belirleme yaklaşımları ile IGS-RTS ürünlerinin, ultra-hızlı ürünlere kıyasla tüm gerçek-zamanlı mutlak GNSS konum belirleme teknikleri için daha bir iyi konum belirleme performansı sergilediğini göstermektedir. Ayrıca, ultra-hızlı ürünlerin aksine IGS-RTS ürünlerden elde edilen konum belirleme performansında herhangi bir zamana bağlı kötüleşme olmamıştır. Yine de ek bir bağlantıya duyulan ihtiyaç IGS-RTS ürünler için bir dezavantaj olarak görülebilir. Diğer taraftan, önerilen filtreleme metodun performansı incelendiğinde sonuçlar bu metodun çoklu-GNSS gözlemlerinin stokastik özelliklerini geleneksel yaklaşımlara göre daha iyi bir şekilde belirleyebildiğini ve bu sayede gerçek-zamanlı mutlak GNSS konum belirleme çözümlerinin performansını önemli ölçüde iyileştirdiğini göstermektedir. Standart Kalman filtresi ve daha yüksek öncül varyans oranı yöntemini içeren geleneksel filtreleme yaklaşımı ile kıyaslandığında önerilen yöntem, gerçek-zamanlı tek frekanslı kod konumlama, tek frekanslı kod-faz kombinasyonu ve çift frekanslı PPP çözümlerinin üç boyutlu konum belirleme doğruluğunu sırasıyla %52,5, %24,8 ve %43,9 oranında iyileştirmiştir.

Keywords: Mutlak GNSS konum belirleme, Gerçek zamanlı, Çoklu-GNSS, Ultra-hızlı ürünler, IGS-RTS ürünler, Robust Kalman filtresi, Varyans bileşen tahmini

ACKNOWLEDGMENTS

First of all, I would like to express my sincere gratitude to my supervisor, Assoc. Prof. Dr. Metin Nohutcu, for his guidance, support, and encouragement throughout my thesis studies. At every stage of this thesis, he supported me with his knowledge, experience, and motivation.

I would like to thank my thesis committee members, Prof. Dr. Doğan Uğur Şanlı, Prof. Dr. Bahadır Aktuğ, Prof. Dr. Aydın Üstün, and Assist. Prof. Dr. Kamil Teke, for their valuable suggestions, comments, and contributions.

I wish to extend my thanks to all colleagues at the Department of Geomatics Engineering for their support and collaborations.

This study was supported by the Scientific and Technological Research Council of Turkey (TUBITAK) under grant number 118Y410. This support is also gratefully acknowledged.

Finally, a special thank goes to my wife, Özge, for her endless support, tolerance, and love throughout this thesis. I would not complete this thesis without her support and encouragement. I also would like to thank my family for their unconditional love and support.

Berkay BAHADUR
June 2021, Ankara

CONTENTS

Page

LIST OF TABLES

LIST OF FIGURES

1. INTRODUCTION

1.1. Background

Over the last few decades, the relative and/or differential techniques, which can provide highly accurate positioning solutions, have been extensively utilized in GNSS (Global Navigation Satellite System) applications. In these techniques, most of the GNSS error sources can be eliminated through reference stations whose precise coordinates are known priorly. Also, more precise reference coordinates result in better positioning accuracy in relative and/or differential techniques. Typically, at least two or more GNSS receivers are employed in relative and differential positioning techniques to reach high positioning accuracy, which can raise the operational cost and system complexity. Besides, the distance from the reference station(s) influences the positioning accuracy obtained from the differential and relative techniques substantially (Hofmann-Wellenhof, Lichtenegger and Wasle, 2007). On the other side, being an absolute GNSS positioning technique, PPP (Precise Point Positioning) has been a promising alternative to conventional GNSS techniques (Zumberge et al., 1997). On a global scale, PPP can provide a millimeter- to centimeter-level positioning accuracy with only a stand-alone GNSS receiver. In this context, PPP employs precise satellite products produced depending on a global network, i.e. the IGS (International GNSS Service) network (Kouba and Héroux, 2001). Additionally, zero-differenced dual-frequency ionosphere-free combination of code and phase measurements are applied for the elimination of the ionospheric effect in the PPP technique.

PPP has come along with unprecedented benefits to the GNSS community, including the possibility of working with single-receiver only and therefore elimination of the necessity for reference stations. Owing to its increasing popularity among the GNSS users, PPP has been utilized as a fundamental positioning method in numerous GNSS applications, e.g. measuring seismic wave motions (Kouba, 2003; Xu et al., 2013, 2019), dynamic displacement detection (Yigit and Gurlek, 2017; Paziewski, Sieradzki and Baryla, 2018), atmospheric monitoring (Lu et al., 2016; Zhang et al., 2018a), offshore positioning (Alkan and Ocalan, 2013), etc. Despite providing highly accurate positioning solutions, PPP still needs a relatively long initialization time, which is called convergence time, for the convergence of non-integer phase ambiguity parameters. In general, approximately one-hour observation period is needed for achieving a positioning accuracy of 5 cm or better horizontally using the traditional PPP technique (Choy, Bisnath and Rizos, 2017). In recent years, several studies have indicated that the ambiguity resolution (AR) methods can be applied for lessening the

average convergence period of the traditional PPP technique (Ge et al., 2008; Laurichesse et al., 2009; Geng et al., 2010; Collins et al., 2010). Since the integer nature of phase ambiguities are recovered with PPP-AR methods, they are able to reduce the convergence period of PPP considerably. However, PPP-AR methods require external data, e.g. phase bias corrections, which are typically disseminated by a service provider.

New global and regional navigation satellite systems have emerged over the past decade, i.e. the European Global Navigation Satellite System (Galileo), Chinese BeiDou Navigation Satellite System (BDS), Indian Regional Navigation Satellite System (IRNSS), and Japanese Quasi-Zenith Satellite System (QZSS). Along with the completed Russian Global Navigation Satellite System (GLONASS) constellation, the emergence of new satellite systems has given rise to dramatic changes in the GNSS community. The integration of multiple GNSS constellations, i.e. multi-GNSS, has offered substantial prospects for obtaining more enhanced positioning performance from the GNSS techniques owing to additional navigation signals and satellite resources. In recent studies, it has been demonstrated that the positioning performance of PPP is augmented with the multi-GNSS integrations substantially (Li et al., 2015; Cai et al., 2015; Pan, Chai and Kong, 2017; Bahadur and Nohutcu, 2018). However, to assure interoperability of multi-constellation, it is necessary to recognize the fundamental distinctions amid the navigation systems, e.g. signal structures, time-scales, reference frames, etc. Therefore, to achieve optimum positioning solutions, more enhanced models are required in the integration of multi-constellation. In PPP processing, precise products which are produced in a common time-scale and reference frame can be utilized to make the integration of multi-GNSS easier. In this regard, IGS initiated the Multi-GNSS Experiment (MGEX) project which aims to produce precise products for multi-constellation, including Galileo, GLONASS, BDS, QZSS besides GPS (Global Positioning System) (Montenbruck et al., 2017). Although IGS MGEX products mostly resolve the interoperability problem of multi-GNSS in terms of the reference frame and time scale, there still exist some specific inconsistencies that need to be dealt with in the integration of multi-GNSS, which are mainly dependent on the positioning model and source of orbit and clock corrections.

Over the last decade, real-time highly accurate GNSS positioning solutions have been received growing interest. Nowadays, many GNSS applications also require to access positioning solutions in real-time together with high positioning accuracy. In parallel to increasing attention, in 2013, IGS started its real-time service (IGS-RTS) to disseminate satellite orbits and clocks instantaneously. Thanks to IGS-RTS products, it has been possible to perform real-time PPP solutions (RT-PPP) with standalone receivers on a global scale (Hadas and Bosy, 2015). Since IGS-RTS products are provided as corrections to satellite orbit and clocks that are acquired from the broadcast ephemeris, they promise better positioning performance in comparison with standard point positioning applications with broadcast data.

Though IGS-RTS products included only GPS satellites initially, nowadays several IGS analysis centers also provide orbit and clock corrections for multi-constellation within the IGS-RTS stream. In the literature, there are numerous studies indicating that IGS-RTS can be employed effectively in many GNSS applications, such as earthquake monitoring (Jin and Su, 2019), atmospheric sensing (Li et al., 2014), precipitation forecasting (Zhao, Yao and Yao, 2018), aerial triangulation (Shi et al., 2017), etc. Nonetheless, IGS-RTS corrections are broadcast through an online stream and therefore can be only accessed via an external connection. On the other hand, for real-time GNSS applications, another alternative is to employ ultra-rapid products that contain predicted satellite orbits and clock offsets. Ultra-rapid products can be applied without any simultaneous connection on the contrary to IGS-RTS products. However, in comparison to the final products, their accuracy is considerably lower since they are dependent on the prediction.

Nowadays, the vast majority of GNSS mass-market is composed of single-frequency low-cost receivers taking account of the sensors in smartphones and other mobile devices (GSA, 2019). Therefore, single-receiver single-frequency positioning solutions which are compatible with relatively low-cost GNSS receivers have been attracting a lot of interest within the GNSS community. Conventionally, Single (or Standard) Point Positioning (SPP) has been used as the fundamental GNSS positioning method with broadcast ephemeris. However, its orbits and clock corrections have the accuracy of meter-level, which is not sufficient for precise positioning. Also, global ionosphere models that are broadcast with navigation messages, such as Klobuchar (Klobuchar, 1987), NeQuick-G (EC, 2016), and BDGIM (Yuan et al., 2019) cannot mitigate a considerable amount of the total ionospheric delay, i.e. $25 - 50\%$. In this manner, positioning accuracy acquired from SPP is not better than 8-10 m, even if a geodetic GNSS receiver is utilized (Pan et al., 2019; Li and Geng, 2019). Thus, numerous studies, including regional clock and ionosphere corrections (Li et al., 2019; Zheng et al., 2020), improved stochastic models (Fan et al., 2019), integration of multi-constellation (Ning, Han and Zhang, 2018), etc., have been done to augment the performance of single-frequency absolute positioning techniques recently. Additionally,the single-frequency ionosphere-free (IF) combination can be constituted once carrier phase observations are also usable (Yunck, 1993). Single-frequency IF combination can eliminate a substantial part of total ionospheric delay without any external correction. Some researches have shown that the single-frequency IF combination could provide relatively high positioning accuracy in comparison with the other single-frequency ionosphere mitigation approaches (Schüler, Diessongo and Poku-Gyamfi, 2011; Sterle, Stopar and Prešeren, 2015). However, a relatively long initial time is required for achieving a sufficient accuracy in this combination because of non-integer phase ambiguities similar to the traditional PPP approach.

Finally, some manufacturers have recently introduced relatively low-cost dual-frequency GNSS receivers. Moreover, the number of smartphone models containing dual-frequency GNSS receivers is increasing each day. By this means, it has been possible to use dual-frequency positioning solutions with more cost-effective receivers. For instance, the PPP technique which relies on dual-frequency ionosphere-free combination can be employed with mobile devices. However, there are still some critical issues about low-cost dual-frequency GNSS receivers that should be addressed. Shortly before, it has been reported that most low-cost dual-frequency receivers can currently record only civilian GNSS signals, which decreases the number of available satellites for GPS constellation as some block type of GPS satellites transmits only one civilian signal (Nie, Liu and Gao, 2020). Furthermore, measurements recorded by low-cost dual-frequency receivers are quite noisier than standard high-end GNSS receivers and this causes a longer convergence time as well as the deterioration in positioning accuracy. Therefore, it is essential to handle GNSS error sources very carefully for dual-frequency positioning with cost-efficient GNSS receivers.

1.2. Research Objectives

In recent years, global technological developments have given rise to dramatic changes in trends of the GNSS community. Higher positioning accuracy with more cost-effective GNSS solutions has great importance for up-to-date technologies, such as digitalization, big data, artificial intelligence, autonomous cars, unmanned aerial vehicles, wearable technologies, etc. Moreover, there is an increasing demand for accessing real-time positioning solutions in most of the new-generation GNSS applications. As a consequence, recent GNSS studies have mainly focussed on developing more rigorous positioning models with relatively low-cost receivers in real-time. Although differential and relative positioning techniques, as fundamental GNSS approaches, provide high positioning accuracy, it can be said that their real-time applications are not cost-effective in most cases. Therefore, for a long time, there has been a trend in the GNSS community towards absolute positioning techniques, which remove the dependency on reference stations or networks. On the other side, single-frequency GNSS receivers still dominate the low-cost market as previously mentioned. At the same time, relatively low-cost GNSS chipsets that enable code and phase observations in dual-frequencies have been released recently by some manufacturers. Considering that the overwhelming majority of single-frequency devices in the mass market and also dual-frequency devices are going to be commonly accessible soon due to the decreasing prices, this thesis primarily aims to enhance the positioning performance of real-time absolute positioning techniques with single- and dual-frequency receivers.

The fundamental part of conducting real-time positioning solutions is to access satellite or-

bits and clock products in real-time. At this point, there are two essential options for real-time orbits and clock corrections. The first is to use IGS-RTS products, which are generated as corrections to satellite orbit and clocks obtained from the broadcast ephemeris. The second is to apply the predicted orbit and clock corrections, namely ultra-rapid products, that are distributed by some IGS MGEX centers for real-time GNSS solutions. Both options can be used in real-time applications, however, their characteristics and implementation strategies differ greatly from each other, which is required to be considered in GNSS processing. In this regard, this thesis also aims at the evaluation of orbit and clock sources that are employed in real-time GNSS solutions and at determining the optimal option for absolute point positioning.

In the single-frequency code-based positioning, it is essential to cope with the ionospheric effect where dual-frequency combinations are not available to eliminate it. The broadcast ephemeris provides the parameters of global ionosphere models to eliminate the ionospheric effect for the GNSS measurements. However, as previously mentioned, they are not proper for precise positioning due to their relatively lower accuracy. Alternatively, the predicted version of GIMs (Global Ionosphere Maps) disseminated by several analysis centers can be exploited for real-time single-frequency solutions. Their spatial and temporal resolutions can alter depending on the production strategies employed by the corresponding analysis center. On the other side, some IGS-RTS providers present real-time ionospheric products that can be adopted for the mitigation of the ionospheric effect in real-time single-frequency positioning applications. This thesis also aims at providing a more suitable solution for the elimination of the ionospheric effect in the single-frequency absolute GNSS positioning.

As described previously, the advent of new regional and global navigation systems presents significant opportunities to achieve enhanced positioning performance from absolute GNSS positioning techniques. Still, owing to essential differences between the satellite systems, it is required to more complex models in the integration of multi-GNSS. To benefit from multi-GNSS better, this thesis also aims to provide optimal positioning approaches, that ensure the interoperability of different navigation systems, for real-time absolute GNSS positioning techniques.

Conventionally, the Kalman filter is employed as the optimal estimator in most of the real-time GNSS applications (Gelb, 1974; Teunissen and Montenbruck, 2017). In Kalman filter estimation, the proper definition of functional and stochastic models has crucial importance in achieving the most optimum positioning results. The inappropriate stochastic definition of observations and process dynamics, which reflect temporal variations of estimated parameters, can bring about the divergence or decline in filtering performance. Besides, unexpected dynamic model errors and observation outliers affect the performance of the Kalman filter

adversely. When it comes to absolute GNSS positioning, it is very challenging to specify stochastic characteristics appropriately for multi-GNSS observations. In this regard, the robust Kalman filter which combines robust statistics methods with traditional Kalman filter can be utilized to improve the effectiveness and optimality of the filtering process (Yang, Song and Xu, 2002). Additionally, another problem of stochastic modeling in the multi-GNSS integration is to specify a proper weighting scheme for different types of observations coming from distinct navigation systems. Considering all of them, this thesis additionally aims to propose a novel filtering method that enables a more rigorous weighting approach for multi-GNSS observations and so achieve more enhanced positioning performance for real-time absolute GNSS positioning techniques.

Finally, it is apparent that the realization of extensive researches which are planned as a part of this thesis is not possible with current GNSS analysis software. Therefore, it is aimed to develop a GNSS analysis software that is able to perform real-time absolute GNSS positioning solutions compatible with enhanced positioning models and algorithms proposed in the study. Thereby, it is also projected that this thesis contributes to future studies that will be carried out in this field by providing an important infrastructure in terms of software and algorithms.

1.3. Thesis Outline

A total of seven chapters are included in this thesis. The conceptual background, main motivation, principal objectives, and general outline of the thesis is provided in the first chapter.

Chapter 2 presents a brief overview of current global navigation satellite systems, containing GPS, GLONASS, Galileo, and BDS. Moreover, second chapter provides the fundamental observation equations for code and phase measurements. Also, at the end of this chapter, the introduction of functional models for absolute GNSS positioning techniques is given.

Chapter 3 describes GNSS error sources in regards to absolute positioning techniques as well as their mitigation strategies. This chapter discusses GNSS error sources comprehensively considering the different sources for real-time orbits and clock corrections along with the receiver specifications.

Chapter 4 starts with the mathematical definition of Kalman filter estimation. Afterward, the chapter describes the detail of robust Kalman filter methods that are used to achieve optimal filtering solution in the thesis. Finally, the introduction of the Helmert variance component

estimation that is employed in constructing a rigorous weighting scheme for multi-GNSS observations is given in this chapter.

Chapter 5 gives details of the proposed filtering method integrating Helmert variance component estimation method with the robust Kalman filter to achieve a more realistic stochastic model for multi-GNSS observations. Also, the chapter provides the enhanced positioning approaches developed for real-time absolute GNSS positioning techniques considering different orbit and clock sources comprehensively. The chapter ends with the presentation of the software solutions which are developed in this thesis.

Chapter 6 provides the experiments evaluating the performance of enhanced positioning approaches as well as the proposed filtering approach. Firstly, the description of observation data that are employed in the experimental tests is presented together with the satellite visibility analysis. The chapter analyzes the results acquired from the experimental tests depicting the positioning performance of enhanced positioning approaches in several aspects. Finally, at the end of the chapter, the proposed filtering method is assessed in terms of positioning performance for real-time absolute positioning techniques.

The conclusions which are drawn from this thesis as well as recommendations for future studies are presented in Chapter 7.

2. ABSOLUTE GNSS POSITIONING TECHNIQUES

This chapter is devoted to describe functional models of absolute GNSS positioning techniques considering single- and dual-frequency receivers. Before the functional models, a general overview which presents the current status of GNSS constellations is given to provide a basis for the subsequent sections and chapters. Also, the chapter includes the fundamental definition of code pseudorange and carrier phase observations for multi-constellation.

2.1. GNSS Overview

This section exhibits up-to-date situation of GNSS, that are GPS, GLONASS, Galileo, and BDS, including key characteristics of the systems as well as the current status of their constellation and navigation signals.

2.1.1. GPS

The US-developed GPS was the first navigation system to become fully operational. Its nominal constellation contains twenty-four MEO (medium-altitude Earth orbit) satellites aligned equally in six orbital planes having a 55° inclination with respect to the equator. The altitude of satellites from the Earth's surface is nearly 20200 km, which means their temporal resolution is one-half a sidereal day. The GPS constellation is designed to provide at least four visible satellites anywhere on the Earth, which ensures the global coverage of the system for positioning and navigation purposes. As of May 2021, the GPS constellation comprises thirty-one operational satellites, which are eight Block IIR, seven Block IIR-M, twelve Block IIF as well as four GPS III satellites (GPS, 2020).

GPS signals are closely dependent on satellite type and therefore have evolved with the modernization of GPS satellites. Traditionally, in Block IIR satellites, coarse acquisition (C/A) and precise P(Y) codes are provided on the L1 frequency, while the L2 frequency includes only the P(Y) code, similar to the first versions of GPS satellites, the last of which was decommissioned in 2019, i.e. the Block I, II, and IIA satellites. Block IIR-M satellites whose first was launched in 2005 provided a new civilian signal on L2 frequency (L2C) together with the new military code (M code) on both L1 and L2 frequencies. In addition, a third civilian signal on a new carrier frequency (L5) was introduced with the advent of Block IIF satellites in 2010. Finally, as a part of the ongoing modernization project, new generation

GPS satellites, that is GPS III satellites, have started to be launched since 2018. GPS III satellites have introduced with a lot of improvements as well as an additional civilian signal on L1 frequency (L1C) (Teunissen and Montenbruck, 2017). Table 2.1 presents a summary for the current situation of the GPS constellation containing block types, satellite numbers, and navigation signals.

Table 2.1: Current status of GPS constellation and navigation signals.

Block Type	**Satellite Numbers**	**Frequencies (MHz)**		
		L1 (1575.42)	**L2** (1227.60)	**L5** (1176.45)
IIR	8	+	+	-
IIR-M	7	+	+	-
IIF	12	+	+	+
GPS III	4	+	+	+

2.1.2. GLONASS

GLONASS which was developed by the Russian Federation has been operational since 2011 as the second global navigation system. Its constellation nominally consists of twenty-four MEO satellites equally aligned in three orbital planes having an $65°$ inclination. Their altitude is approximately 19130 km, which means that their orbital period is nearly $11^h\ 16^m$. GLONASS adopts a special geodetic reference system, namely PZ-90 (Parametri Zemli 1990), in its broadcast orbits. Therefore, it is required to perform a transformation to other Earth-centered Earth-fixed systems, e.g. Geodetic Reference System 1980 (GRS80), World Geodetic System 1984 (WGS84), etc., when coordinates of GLONASS satellites are calculated from broadcast ephemeris (GLONASS-ICD, 2016). As of May 2021, the GLONASS constellation is composed of twenty-eight satellites which are twenty-two operational, three in maintenance, two in test-phase, and one spare.

Each GLONASS satellite includes authorized and open signals on its L1 and L2 frequencies. However, GLONASS typically transmits navigation signals using FDMA (frequency division multiple access) modulation, unlike the other navigation systems which employ CDMA (code division multiple access) modulation. So, each GLONASS satellite broadcast navigation signals employing the same ranging code in different frequencies. The related FDMA signal frequency for a specific GLONASS satellite is defined depending on its channel number (c) as follows (Teunissen and Montenbruck, 2017):

$$f_{L1}(c) = (1602.0 + c \cdot 0.5625)\ \text{MHz} \tag{2.1}$$

$$f_{L2}(c) = (1246.0 + c \cdot 0.4375)\ \text{MHz} \tag{2.2}$$

In comparison with CDMA signals, better protection against narrowband interferences can be provided with the use of FDMA signals because once a time, only one or a few satellites is influenced by such interference. However, it increases system complexity as well as unexpected variations in code and phase hardware biases. Therefore, as a part of the ongoing GLONASS modernization project, GLONASS-K satellites, which introduce an additional signal with CDMA (L3) in 1202.025 MHz, have been launched since 2011 to enhance interoperability with other navigation systems. Table 2.2 provides the up-to-date status of operational GLONASS satellites with their signal capabilities.

Table 2.2: Up-to-date status of GLONASS constellation and navigation signals.

Block Type	**Satellite Number**	**Frequencies (MHz)**		
		FDMA		**CDMA**
		L1 $(1602.0+k.0.5625)$	**L2** $(1246.0+k.0.4375)$	**L3** (1202.025)
M	23	+	+	-
M+	2	+	+	+
K1	3	+	+	+

2.1.3. Galileo

ESA (European Space Agency) has been developing Galileo being the only civilian navigation system with the financial support of the EU (European Union). In 2005, the launch of the first Galileo satellite initiated the in-orbit validation element (GIOVE) phase, and the second GIOVE satellite was launched in 2008. Afterward, in 2011 and 2012, two pairs of Galileo IOV (in-orbit validation) satellites were consecutively launched for the initial system validation. The full operational capability (FOC) phase has continued and it is planned to be finalized in the following years with the launch of the remaining satellites. The nominal Galileo constellation comprises 30 MEO satellites, twenty-four operational as well as six spares, which are distributed evenly in three orbital planes having a inclination of $55°$. As of May 2021, there exist twenty-four usable satellite in the Galileo constellation. As the first pair of FOC satellites, two Galileo satellites, namely E14 and E18, were launched in 2014, however, they are unexpectedly sent into erroneous orbits which have higher eccentricity than planned. According to official constellation information of Galileo, they are currently in usable status (Galileo, 2020).

Galileo satellites transmit ten different navigation signals in five carrier frequencies, namely E1, E5, E6, E5a, E5b. Indeed, there are three Galileo carrier frequencies, E5a and E5b are additional sidebands that are obtained from the original E5 carrier frequency. Moreover, three fundamental positioning services are provided by each Galileo satellite, which are the

commercial service (CS), open service (OS), and public regulated service (PRS). Galileo OS is provided through E1, E5a, and E5b carrier frequencies (E1-B/C, E5a-I/Q, E5b-I/Q), while E1 and E6 carrier frequencies support PRS (E1-A, E6-A). CS is only provided through E6 carrier frequency (E6-B/C). On the other side, the Galileo E5 carrier is generated using the AltBOC (alternate binary offset carrier) modulation, that is more resistant to the multipath effect. The modulation techniques, which are the binary phase-shift keying (BPSK) and composite binary offset carrier (CBOC), are also employed to generate other Galileo navigation signals. Figure 2.1 demonstrates the spectral characteristics of Galileo navigation signals, including supported positioning services and modulation techniques (Subirana, Zornoza and Hernández-Pajares, 2013).

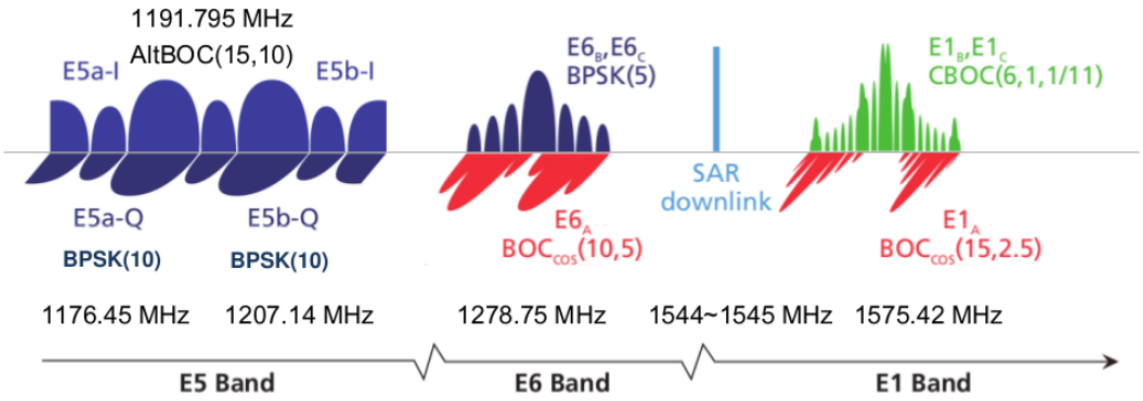

Figure 2.1: Spectral characteristics of Galileo signals. Courtesy of Stefan Wallner (Subirana, Zornoza and Hernández-Pajares, 2013).

2.1.4. BDS

China initiated BDS in 1994 as an independent satellite navigation system. Fundamentally, the construction of BDS includes three main phases. As the first phase of the BDS demonstration system, namely BDS-1, two experimental BDS satellites were launched in 2000. In 2003, the BDS-1 phase was completed following that the third experimental BDS satellite was sent to orbit successfully. Afterward, BDS regional system was activated when the first satellite was launched in 2007 as a part of the BDS-2 phase. In 2012, BDS provided regional coverage in the Asia-pacific thanks to fourteen operational satellites, which are four MEO satellites, five IGSO (inclined geosynchronous orbit) satellites, and five GEO (geostationary Earth orbit) satellites. GEO satellites cover a region between $55°$S - $55°$N latitudes and $70°$E - $150°$E longitudes. Also, the orbital period of IGSO satellites is one sidereal day, like GEO satellites. However, their orbits have a considerable inclination concerning the Equator plane, which results in a ground-tracks similar to figure-of-eight shape in the related region. Moreover, the orbits of MEO satellites have an altitude of 21530 km, which means that their

orbital period is $12^h\ 53^m$ (Teunissen and Montenbruck, 2017). As of May 2021, the BDS-2 constellation is composed of three MEO, seven IGSO, and five GEO satellites. As the final phase, the BDS global system, BDS-3 is currently about to be completed and it is anticipated that BDS will gain global coverage shortly. As of May 2021, the BDS-3 constellation includes twenty-four MEO, three IGSO, and two GEO satellites (BDS, 2020).

BDS-2 navigation signals are transmitted in three carrier frequencies, namely B1 (1561.098 MHz), B2 (1207.14 MHz), and B3 (1268.52 MHz). There are two navigation signals modulated in each of BDS-2 carrier frequencies, six navigation signals in total. B1 and B2 frequencies support BDS-2 open service, whereas the other navigation signals are provided by the authorized service. Besides, BDS-2 provides an open navigation service which is akin to SBAS (satellite-based augmentation systems) to enhance real-time positioning applications. On the other side, BDS-3 comes along with additional three navigation signals including B1C (1575.42 MHz), B2A (1176.45 MHz), and B2A+B (1191.795 MHz) in addition to the overlapping frequencies B1, B2, and B3. Table 2.3 presents the current status of the BDS constellation providing satellite types, numbers and their navigation signals (BDS, 2020).

Table 2.3: Current status of BDS constellation and navigation signals.

			Frequencies (MHz)					
	Satellite		**B1C**	**B1**	**B3**	**B2**	**B2A+B**	**B2A**
	Type	**No**	(1575.42)	(1561.098)	(1268.52)	(1207.14)	(1176.45)	(1191.795)
BDS-2	GEO	5	-	+	+	+	-	-
	IGSO	7	-	+	+	+	-	-
	MEO	3	-	+	+	+	-	-
BDS-3	GEO	2	+	+	+	+	+	+
	IGSO	3	+	+	+	+	+	+
	MEO	24	+	+	+	+	+	+

2.2. GNSS Observations

Code pseudorange, carrier phase, and Doppler observations are the three fundamental measurements in GNSS. As the essential part of GNSS positioning, the code and phase observations are explained in this section.

2.2.1. Code Psuodarange Observation

Apparent signal travel time from navigation satellite to GNSS receiver is measured to derive code pseudorange observations. To obtain the apparent signal travel time, the signal's code

broadcast by navigation satellite is compared and aligned with its replica generated by the GNSS receiver. It provides unambiguous signal travel time from the satellite antenna phase center at signal emission time to the receiver antenna phase center at signal reception time. These observations are mentioned as code pseudoranges since they deviate from the actual signal travel time substantially because of the synchronization errors in satellite and receiver clocks regarding the related GNSS system time in addition to the other influences on the signal transmission. Typically, code pseudorange observation (P) in meters is given by:

$$P_{i,r}^{s,j} = \rho + c\,(dt_r^s - dT^{s,j}) + T_r^{s,j} + I_i^{s,j} + c\,(b_{i,r}^s - b_i^{s,j}) + \varepsilon(P_{i,r}^{s,j}) \tag{2.3}$$

where c is the velocity of light in vacuum. Subscripts r and i indicate the receiver and frequency index of the related system ($i = 1, 2, ..$), while superscripts s and j demonstrate satellite system, such as GPS (G), GLONASS (R), Galileo (E), and BDS (C), and satellite number, respectively. Other terms are given below:

ρ : Geometric distance in meters.

dt_r^s : Receiver clock offset in seconds.

$dT^{s,j}$: Satellite clock offset in seconds.

$T_r^{s,j}$: Tropospheric delay in meters.

$I_i^{s,j}$: First-order ionospheric delay on the frequency (i) in meters.

$b_{i,r}^s$: Receiver code hardware bias on the frequency (i) in seconds.

$b_i^{s,j}$: Satellite code hardware bias on the frequency (i) in seconds.

$\varepsilon(P_{i,r}^{s,j})$: Observation noise and multipath.

2.2.2. Carrier Phase Observation

The phase difference between the carrier signal transmitted by the satellite and its receiver-generated replica is utilized to derive the carrier phase observations. In this way, only the fractional phase shifts can be determined by GNSS receivers, therefore the full cycles of the carrier phase are ambiguous. Although carrier phase observations are substantially more precise than code psudorange observations, they also include ambiguity parameters due to the unknown integer part of cycles. A millimeter level ranging accuracy can be obtained with carrier phase observations after the successful resolution of their ambiguity parameters. Similar to code pseudoranges, the receiver and satellite clock offsets as well as the other error sources influence carrier phase observations. Phase carrier observation (L) in meters

can be given as follows:

$$L_{i,r}^{s,j} = \rho + c\,(dt_r^s - dT^{s,j}) + T_r^{s,j} - I_i^{s,j} + c\,(B_{i,r}^s - B_i^{s,j}) + \lambda_i^s\, N_i^{s,j} + \varepsilon(L_{i,r}^{s,j}) \qquad (2.4)$$

where $B_{i,r}^s$ and $B_i^{s,j}$ indicate the receiver and satellite phase hardware biases on the frequency (i) in seconds, respectively. Furthermore, λ_i^s represents the wavelength of corresponding frequency (i) in meters, while $N_i^{s,j}$ demonstrate the integer number of cycles, namely phase ambiguity. The other terms presented in Equation 2.4 are equivalent to those described in the code observation. Still, as shown in Equation 2.4, the sign of ionospheric delay is opposite for the phase observation. This results from the that the ionosphere impacts code and phase measurements reversely because of the differences in group and phase velocities in dispersive mediums.

2.3. Absolute GNSS Positioning Techniques

By definition, absolute GNSS positioning refers to the techniques which employ a standalone GNSS receiver without any simultaneous reference station to acquire the 3D coordinates of the desired point. This section introduces the functional models of three fundamental absolute GNSS positioning techniques that are utilized in the thesis, namely the single-frequency code pseudorange positioning, single-frequency code-phase combination, and dual-frequency Precise Point Positioning (PPP).

2.3.1. Single-frequency Code Pseudorange Positioning

For a GPS satellite (j), the code pseudorange observation on the first frequency is reorganized using Equation 2.3 as:

$$P_{1,r}^{G,j} = \rho + c\,\widetilde{dt}_r^{\,G} - c\,\widetilde{dT}^{G,j} + T_r^{G,j} + I_1^{G,j} + \varepsilon(P_{1,r}^{G,j}) \qquad (2.5)$$

where $\widetilde{dt}_r^{\,G}$ and $\widetilde{dt}^{G,j}$ are the reformed receiver and satellite clock offsets and are written by:

$$\widetilde{dt}_r^{\,G} = dt_r^G + b_{1,r}^G \quad \text{and} \quad \widetilde{dT}^{G,j} = dT^{G,j} + b_1^{G,j} \qquad (2.6)$$

The reformed receiver clock offset ($\widetilde{dt}_r^{\,G}$) includes receiver code hardware bias along with actual receiver clock error and they are estimated together because of their high correlation. Furthermore, the reformed satellite clock offset, which also contains satellite code hardware bias, is corrected using external clock resources, such as broadcast ephemeris or precise

satellite products. However, satellite clock corrections provided in IGS precise products and broadcast ephemeris are generated based on a particular signal or a signal combination. For GPS satellites, the dual-frequency ionosphere-free combination of code observations on first and second frequencies is used as the reference signal combination in the generation of satellite clock corrections (Steigenberger et al., 2015). Therefore, GPS clock corrections embrace additional satellite code hardware biases and they cannot be applied directly for correcting the satellite clock errors in single-frequency observations. The satellite clock correction generated depending on the dual-frequency ionosphere-free combination is formulated by:

$$dT_{IF}^{G,j} = dT^{G,j} + \frac{f_1^2}{f_1^2 - f_2^2}\, b_1^{G,j} - \frac{f_2^2}{f_1^2 - f_2^2}\, b_2^{G,j} \tag{2.7}$$

For single-frequency observations, the correction is rearranged by:

$$\widetilde{dT}^{G,j} = dT^{G,j} + b_1^{G,j} \tag{2.8}$$

$$= dT_{IF}^{G,j} - \frac{f_2^2}{f_1^2 - f_2^2}\,(b_1^{G,j} - b_2^{G,j}) \tag{2.9}$$

$$= dT_{IF}^{G,j} - T_{GD} \tag{2.10}$$

where T_{GD} indicates the timing (or total) group delay (TGD) and it is represented as proportional to $(b_1^{G,j} - b_2^{G,j})$ which is named the Differential Code Biases (DCBs) between the corresponding frequencies. For single-frequency users, GPS satellites transmit the TGD parameter in the broadcast ephemeris. Additionally, for single-frequency observations, DCBs generated and disseminated by some IGS agencies can be utilized to align satellite clock corrections. Finally, after correcting the reformed satellite clock offset using the clock correction which relies on ionosphere-free clock reference, Equation 2.5 is rewritten by:

$$P_{1,r}^{G,j} = \rho + c\,\widetilde{dt}_r^{\,G} + T_{GD}^{G} + T_r^{G,j} + I_1^{G,j} + \varepsilon(P_{1,r}^{G,j}) \tag{2.11}$$

Herein, together with the tropospheric delay and TGD, the ionospheric delay needs to be corrected because it is not possible in single-frequency code pseudorange positioning to mitigate its effect using ionosphere-free combinations. The mitigation strategies which can be applied for these error sources will be explained comprehensively in the next chapters.

Equation 2.11 contains a specific parameter for the receiver clock offset which is defined in GPS time system. As previously mentioned, every navigation system has a different receiver clock offset parameter due to their distinct time scales. As a common practice in the integration of multi-constellation, the Inter-system bias (ISB) parameters are introduced regarding a reference GNSS time scale, instead of allocating separate receiver clock parameters for

each navigation system (Cai and Gao, 2013; Li et al., 2015). Typically, GPS time-scale is chosen as the reference for introducing ISB parameters to other navigation systems since IGS precise products as well as most the GNSS receivers are dependent on the GPS time system (Li et al., 2015; Abd-Rabbou, El-Shazly and Ahmed, 2018). Accordingly, for multi-constellation, single-frequency code psuedorange observation is written as follows:

$$P_{1,r}^{G,j} = \rho + c\,\widetilde{dt}_r^{\,G} + T_{GD}^{G} + T_r^{G,j} + I_1^{G,j} + \varepsilon(P_{1,r}^{G,j}) \tag{2.12}$$

$$P_{1,r}^{R,j} = \rho + c\,\widetilde{dt}_r^{\,G} + ISB^{G,R} + T_{GD}^{R} + T_r^{R,j} + I_1^{R,j} + \varepsilon(P_{1,r}^{R,j}) \tag{2.13}$$

$$P_{1,r}^{E,j} = \rho + c\,\widetilde{dt}_r^{\,G} + ISB^{G,E} + T_{GD}^{E} + T_r^{E,j} + I_1^{E,j} + \varepsilon(P_{1,r}^{E,j}) \tag{2.14}$$

$$P_{1,r}^{C,j} = \rho + c\,\widetilde{dt}_r^{\,G} + ISB^{G,C} + T_{GD}^{C} + T_r^{C,j} + I_1^{C,j} + \varepsilon(P_{1,r}^{C,j}) \tag{2.15}$$

Equations 2.12 to 2.15 constitute the functional model of single-frequency multi-GNSS code pseudorange positioning, which consists of three position components, one tropospheric delay, one receiver clock offset defined in the GPS time, and three ISB parameters ($ISB^{G,R}$, $ISB^{G,E}$, $ISB^{G,C}$) for GLONASS, Galileo and BDS, respectively.

2.3.2. Single-frequency Code-Phase Combination

Once carrier phase observations are available together with code pseudoranges, the single-frequency code-phase combination, in other words, single-frequency ionosphere-free combination on the GPS first frequency can be formed as follows (Yunck, 1993):

$$\Phi_{1,r}^{G,j} = 0.5 \cdot (P_{1,r}^{G,j} + L_{1,r}^{G,j}) \tag{2.16}$$

From Equation 2.3 and Equation 2.4, the single-frequency code-phase combination is written by:

$$\begin{aligned}\Phi_{1,r}^{G,j} =& \rho + c\,(dt_r^G - dT^{G,j}) + T_r^{G,j} + 0.5\,c\,(b_{1,r}^G - b_1^{G,j} + B_{1,r}^G - B_1^{G,j}) + \\ & 0.5\,\lambda_1^G\,N_1^{G,j} + \varepsilon(\Phi_{1,r}^{G,j})\end{aligned} \tag{2.17}$$

To employ the satellite clock corrections which are generated depending on the ionosphere-free clock reference, like the code pseudorange positioning model, Equation 2.17 is rewritten as:

$$\Phi_{1,r}^{G,j} = \rho + c\,\widetilde{dt}_r^{\,G} - c\,\widetilde{dT}^{G,j} + T_r^{G,j} + \widetilde{N}_1^{G,j} + \varepsilon(\Phi_{1,r}^{G,j}) \tag{2.18}$$

where $\widetilde{dt}_r^{\,G}$ and $\widetilde{dT}^{G,j}$ are the reformed receiver and satellite clock offsets described previously. $\widetilde{N}_1^{G,j}$ indicates the reformed ambiguity parameter which contains code and phase hardware biases together with the integer ambiguity parameter, and it is given as:

$$\widetilde{N}_1^{G,j} = 0.5\ \lambda_1^G\ N_1^{G,j} + 0.5\ c\ (B_{1,r}^G - B_1^{G,j}) - 0.5\ c\ (b_{1,r}^G - b_1^{G,j}) \tag{2.19}$$

When the satellite clock offset is corrected with the use of ($dT_{IF}^{G,j}$), the single-frequency code-phase combination is given by:

$$\Phi_{1,r}^{G,j} = \rho + c\ \widetilde{dt}_r^{\,G} + T_{GD}^G + T_r^{G,j} + \widetilde{N}_1^{G,j} + \varepsilon(\Phi_{1,r}^{G,j}) \tag{2.20}$$

Similar to the previous section, the single-frequency code-phase combinations of multi-GNSS observations are written as follows:

$$\Phi_{1,r}^{G,j} = \rho + \widetilde{dt}_r^{\,G} + T_{GD}^G + T_r^{G,j} + \widetilde{N}_1^{G,j} + \varepsilon(\Phi_{1,r}^{G,j}) \tag{2.21}$$

$$\Phi_{1,r}^{R,j} = \rho + \widetilde{dt}_r^{\,G} + ISB^{G,R} + T_{GD}^R + T_r^{R,j} + \widetilde{N}_1^{R,j} + \varepsilon(\Phi_{1,r}^{R,j}) \tag{2.22}$$

$$\Phi_{1,r}^{E,j} = \rho + \widetilde{dt}_r^{\,G} + ISB^{G,E} + T_{GD}^E + T_r^{E,j} + \widetilde{N}_1^{E,j} + \varepsilon(\Phi_{1,r}^{E,j}) \tag{2.23}$$

$$\Phi_{1,r}^{C,j} = \rho + \widetilde{dt}_r^{\,G} + ISB^{G,C} + T_{GD}^C + T_r^{C,j} + \widetilde{N}_1^{C,j} + \varepsilon(\Phi_{1,r}^{C,j}) \tag{2.24}$$

Equations 2.21 to 2.24 form the functional model of single-frequency multi-GNSS code-phase combination, including three position components, one tropospheric delay, one receiver clock offset defined in the GPS time, three ISB parameters for other navigation systems, and a float ambiguity parameter for each observed satellite. As the ionospheric delays in code and carrier observations have equal magnitudes but in adverse directions, the first-order ionospheric delay is assumed to be mitigated in the single-frequency code-phase combination. Moreover, the combination reduces the noise of code pseudorange observations considerably due to carrier phase observations. However, the integer nature of phase ambiguities disappears with this combination because of the hardware biases accumulated in the ambiguity parameters. Therefore, this combination entails a relatively long initial time for the convergence of the phase ambiguities, which is necessitated to achieve higher positioning accuracy.

2.3.3. Dual-frequency PPP

In the traditional PPP technique, undifferenced ionosphere-free combinations of dual-frequency code and phase measurements are employed. For a GPS satellite, dual-frequency (*i*=1, 2)

ionosphere-free combination is formed as follows (Kouba and Héroux, 2001):

$$a = \frac{f_1^2}{f_1^2 - f_2^2}, \quad b = -\frac{f_2^2}{f_1^2 - f_2^2} \tag{2.25}$$

$$P_{IF,r}^{G,j} = a\ P_{1,r}^{G,j} + b\ P_{2,r}^{G,j} \quad \text{and} \quad L_{IF,r}^{G,j} = a\ L_{1,r}^{G,j} + b\ L_{2,r}^{G,j} \tag{2.26}$$

In this regard, using Equation 2.3 and Equation 2.4, the observation equations of dual-frequency ionosphere-free combinations are written as:

$$P_{IF,r}^{G,j} = \rho + c\widetilde{dt}_{IF,r}^{G} - c\widetilde{dT}_{IF}^{G,j} + T_r^{G,j} + \varepsilon(P_{IF,r}^{G,j}) \tag{2.27}$$

$$L_{IF,r}^{G,j} = \rho + c\widetilde{dt}_{IF,r}^{G} - c\widetilde{dT}_{IF}^{G,j} + T_r^{G,j} + \tilde{N}_{IF}^{G,j} + \varepsilon(L_{IF,r}^{G,j}) \tag{2.28}$$

where $\widetilde{dt}_{IF,r}^{G}$ and $\widetilde{dT}_{IF}^{G,j}$ are the reformed receiver and clock offsets for the ionosphere-free combination, respectively, while $\tilde{N}_{IF}^{G,j}$ represents the noninteger phase ambiguity parameter for the ionosphere-free combination. They can be indicated as follows:

$$\widetilde{dt}_{IF,r}^{G} = dt_r^G + b_{IF,r}^G \quad \text{and} \quad \widetilde{dT}_{IF}^{G,j} = dT^{G,j} + b_{IF}^{G,j} \tag{2.29}$$

$$\tilde{N}_{IF}^{G,j} = \lambda_{IF}^G\ N_{IF}^{G,j} + (B_{IF,r}^G - B_{IF}^{G,j}) - (b_{IF,r}^G - b_{IF}^{G,j}) \tag{2.30}$$

where also

$$\lambda_{IF}^G\ N_{IF}^{G,j} = a\ \lambda_1^G\ N_1^{G,j} + b\ \lambda_2^G\ N_2^{G,j} \tag{2.31}$$

$$b_{IF,r}^G = a\ b_{1,r}^G + b\ b_{2,r}^G \quad \text{and} \quad b_{IF}^{G,j} = a\ b_1^{G,j} + b\ b_2^{G,j} \tag{2.32}$$

$$B_{IF,r}^G = a\ B_{1,r}^G + b\ B_{2,r}^G \quad \text{and} \quad B_{IF}^{G,j} = a\ B_1^{G,j} + b\ B_2^{G,j} \tag{2.33}$$

The reformed receiver clock offset ($\widetilde{dt}_{IF,r}^{G}$) can be estimated in the filtering process, while the reformed satellite clock offset ($\widetilde{dT}_{IF}^{G,j}$) needs to be corrected. The satellite clock corrections provided by both broadcast ephemeris and IGS precise products can be employed to eliminate the reformed satellite clock offset without the TGD parameter because it already contains code hardware bias which relies on the ionosphere-free clock reference. After correcting the satellite clock offsets and introducing ISB parameters similar to the previous sections, the dual-frequency ionosphere-free combinations are written for multi-constellation

by:

$$P_{IF,r}^{G,j} = \rho + c\widetilde{dt}_{IF,r}^{G} + T_r^{G,j} + \varepsilon(P_{IF,r}^{G,j}) \tag{2.34}$$

$$L_{IF,r}^{G,j} = \rho + c\widetilde{dt}_{IF,r}^{G} + T_r^{G,j} + \tilde{N}_{IF}^{G,j} + \varepsilon(L_{IF,r}^{G,j}) \tag{2.35}$$

$$P_{IF,r}^{R,j} = \rho + c\widetilde{dt}_{IF,r}^{G} + ISB^{G,R} + T_r^{R,j} + \varepsilon(P_{IF,r}^{R,j}) \tag{2.36}$$

$$L_{IF,r}^{R,j} = \rho + c\widetilde{dt}_{IF,r}^{R} + ISB^{G,R} + T_r^{R,j} + \tilde{N}_{IF}^{R,j} + \varepsilon(L_{IF,r}^{R,j}) \tag{2.37}$$

$$P_{IF,r}^{E,j} = \rho + c\widetilde{dt}_{IF,r}^{E} + ISB^{G,E} + T_r^{E,j} + \varepsilon(P_{IF,r}^{E,j}) \tag{2.38}$$

$$L_{IF,r}^{E,j} = \rho + c\widetilde{dt}_{IF,r}^{E} + ISB^{G,E} + T_r^{E,j} + \tilde{N}_{IF}^{E,j} + \varepsilon(L_{IF,r}^{E,j}) \tag{2.39}$$

$$P_{IF,r}^{C,j} = \rho + c\widetilde{dt}_{IF,r}^{C} + ISB^{G,C} + T_r^{C,j} + \varepsilon(P_{IF,r}^{C,j}) \tag{2.40}$$

$$L_{IF,r}^{C,j} = \rho + c\widetilde{dt}_{IF,r}^{C} + ISB^{G,C} + T_r^{C,j} + \tilde{N}_{IF}^{C,j} + \varepsilon(L_{IF,r}^{C,j}) \tag{2.41}$$

Equations 2.34 to 2.4 constitute the functional model of traditional multi-GNSS PPP, which contains three position components, one receiver clock offset defined in the GPS time, one tropospheric delay, three ISB parameters for other navigation systems, and a noninteger ambiguity parameter for each observed satellite as the estimated parameters. Conventionally, this model requires a relatively long initial time, namely convergence time, for the successful convergence of float ambiguity parameters.

Consequently, this chapter presents the functional models of three absolute GNSS positioning techniques adopted in this thesis, together with the description of fundamental GNSS observations. Different positioning techniques can suffer from distinct error sources as can be observed from the positioning models provided in this chapter. Up to now, the observation equations have been provided as including only the most common GNSS error sources. The other special error sources whose influences are relatively lower have been not mentioned in the observation equations. For absolute GNSS positioning techniques, the error sources and their mitigation strategies will be handled comprehensively in the next chapter.

3. GNSS ERROR SOURCES IN REAL-TIME ABSOLUTE POSITIONING

Many error sources influence GNSS signals, and the handling of these error sources appropriately paves the way for the achievement of high positioning accuracy. GNSS error sources show variations depending on the applied orbit and clock sources, such as broadcast ephemeris or IGS precise products, and also on the functional model of positioning techniques. This chapter describes GNSS error sources in real-time absolute positioning techniques and their mitigation strategies considering the differences of the applied orbit and clock sources as well as the positioning models.

3.1. Satellite Orbits and Clock Corrections

To conduct GNSS positioning applications instantaneously, it is very essential to access satellite orbits and clock corrections in real-time. In general, there exist two options for simultaneous satellite products besides navigation data. The first is to use the ultra-rapid products which are generated by some IGS agencies including the predicted orbits and clock corrections. The second option is to apply IGS real-time corrections that are disseminated to update the satellite orbit and clocks calculated from the navigation message. This section describes real-time satellite orbits and clock corrections considering these two options as well as their application strategies.

In these days, some IGS agencies generate ultra-rapid products, which can be employed for GNSS positioning, navigation and timing applications in real-time. As a significant advantage, ultra-rapid products can be applied without any simultaneous connection, which enables their employment in offline GNSS applications. For a long time, ultra-rapid products of GPS satellites have been provided by IGS, and they have 5-cm orbit and 3-ns clock accuracies currently (https://www.igs.org/products/). In recent years, some IGS analysis centers have initiated to produce ultra-rapid products for the satellite systems that are emerged newly. With the IGS MGEX project, Wuhan University (WHU) has been generating ultra-rapid products, with a 5-minutes sampling rate and 1-hour updating period, for GPS, Galileo, GLONASS, and BDS satellites (ftp://igs.ign.fr/pub/igs/products/mgex). Additionally, the CODE (Centre for Orbit Determination in Europe) has added Galileo satellites to its ultra-rapid products very recently which already contain GPS and GLONASS satellites (Prange et al., 2020). These products offer considerable opportunities to make use of the potential benefits of multi-frequency multi-constellation in real-time GNSS positioning. Table 3.1

presents the current ultra-rapid products as providing the constellation they include, sampling, and update intervals. For a relevant epoch, the three-dimensional satellite position and clock correction are usually calculated by a polynomial interpolation, e.g. the Lagrange interpolation method, using the ultra-rapid products. Herein, it should also be mentioned that satellite positions provided by ultra-rapid products relate to the satellite's center of mass (CoM).

Table 3.1: A general overview of ultra-rapid products.

Product	Navigation System	Sampling rate (sec)	Update Interval (hour)
IGS	GPS	900	6
CODE	GPS, GLONASS, Galileo	900	24
WHU	GPS, GLONASS, Galileo, BDS	300	1

On the other side, IGS-RTS has been providing satellite orbits and clock corrections since 2013 via its real-time streams (Hadas and Bosy, 2015). IGS-RTS products are disseminated as the State Space Representation (SSR) corrections based on Radio Technical Commission for Maritime Services (RTCM) format over the internet using the Networked Transport of RTCM via Internet Protocol (NTRIP). Fundamentally, SSR corrections include satellite orbits and clock errors in addition to satellite signal biases. Furthermore, some IGS agencies additionally provide atmospheric corrections, e.g. ionospheric and tropospheric delays (IGS-SSR, 2020). As satellite orbits and clocks are broadcast as corrections to the broadcast ephemeris, before applying the IGS-RTS corrections, it is necessary to compute satellite orbit and clock corrections from the related navigation message. For the multi-GNSS integration, an important point is to consider the essential differences between the navigation systems, i.e. time-scale and reference frame. For GPS, Galileo, and BDS, satellite coordinates can be computed with their navigation messages using Keplerian ephemeris models as described in their interface control documents (GPS-ICD, 2020; Galileo-ICD, 2018; BeiDou-ICD, 2020). However, GLONASS broadcast ephemeris provides satellite coordinates as a Cartesian state vector representation. Position (x, y, z) and velocity vector (V_x, V_y, V_z) components of GLONASS satellites can be determined at a given epoch (t_i) through numerical integration of the differential equations given as follows(GLONASS-ICD, 2016):

$$\frac{dx}{dt} = V_x \tag{3.1}$$

$$\frac{dy}{dt} = V_y \tag{3.2}$$

$$\frac{dz}{dt} = V_z \tag{3.3}$$

$$\frac{V_x}{dt} = -\frac{GM}{r^3}\, x - \frac{3}{2} J_2^0\, \frac{GM \cdot a_e^2}{r^5}\, x(1 - 5\frac{z^2}{r^2}) + w_E^2 x + 2 w_E V_y + \ddot{x} \tag{3.4}$$

$$\frac{V_y}{dt} = -\frac{GM}{r^3}\, y - \frac{3}{2} J_2^0\, \frac{GM \cdot a_e^2}{r^5}\, y(1 - 5\frac{z^2}{r^2}) + w_E^2 y - 2 w_E V_x + \ddot{y} \tag{3.5}$$

$$\frac{V_z}{dt} = -\frac{GM}{r^3}\, z - \frac{3}{2} J_2^0\, \frac{GM \cdot a_e^2}{r^5}\, z(3 - 5\frac{z^2}{r^2}) + \ddot{z} \tag{3.6}$$

where $r = \sqrt{x^2 + y^2 + z^2}$, and also
$a_e = 6378136$ m – semi-major (equatorial) axis of the PZ-90 Earth's ellipsoid,
$GM = (398600441.80.8) \cdot 10^6$ m^3/s^2 – gravitational constant (mass of the Earth's atmosphere included),
$J_2^0 = 1082625.75 \cdot 10^{-9}$ – second degree zonal coefficient of normal potential,
$w_E = 7.2921151467 \cdot 10^{-5}$ rad/s – mean angular velocity of the Earth.

The forth-order Runge-Kutta method can be utilized to solve the numerical integration with the initial conditions; $x = x(t_r)$, $y = y(t_r)$, $z = z(t_r)$, $V_x = \dot{x}(t_r)$, $V_y = \dot{y}(t_r)$ and $V_z = \dot{z}(t_r)$. Where t_r indicates the reference epoch. Additionally, perturbing accelerations $(\ddot{x}, \ddot{y}, \ddot{z})$ are transmitted within the GLONASS broadcast ephemeris. On the other hand, the reference frame of satellite position obtained from the GLONASS broadcast ephemeris is PZ-90, and therefore it is required to conduct a coordinate transformation to GRS80 or WGS84 reference frames for integration with GPS observations.

On the other hand, when navigation messages are utilized, the satellite clock correction (Δt_r) can be computed as follows:

$$\Delta t_r = a_0 + a_1 \cdot (t_i - t_r) + a_2 \cdot (t_i - t_r)^2 \tag{3.7}$$

where t_i and t_r are the given and reference epochs in seconds, a_0, a_1 and a_2 demonstrate the satellite clock bias, clock drift and drift rate corrections provided in the broadcast ephemeris.

The SSR orbit correction parameters are broadcasted as radial, along-track, and cross-track directions (Figure 3.1), that are utilized to compute the final satellite position as correction to the satellite coordinates obtained from the navigation message. With the SSR orbit corrections, the final satellite position is calculated as follows:

$$\mathbf{X}_{fin} = \mathbf{X}_{broad} - \delta\mathbf{X} \tag{3.8}$$

where

$\mathbf{X}_{fin}$: corrected satellite position

$\mathbf{X}_{broad}$: satellite position obtained from the broadcast ephemeris

$\delta\mathbf{X}$: SSR satellite position correction

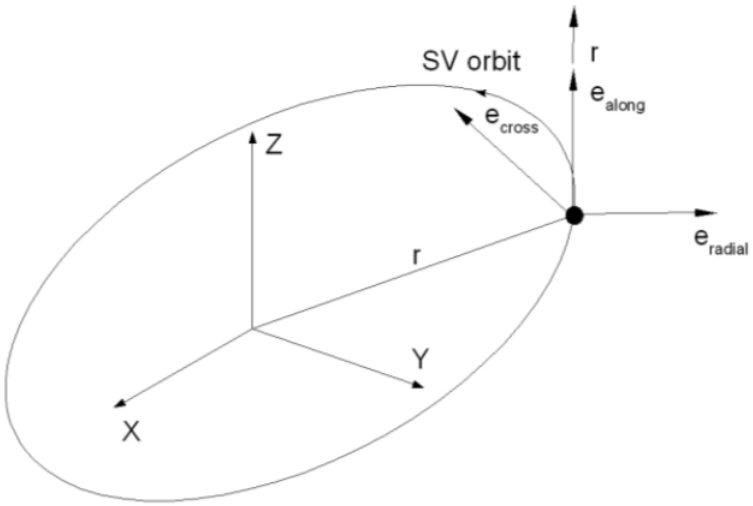

Figure 3.1: Orbit components in radial, along-track and cross-track directions (IGS-SSR, 2020).

The correction is acquired as follows:

$$\mathbf{e}_{along} = \frac{\mathbf{r}}{|\mathbf{r}|} \tag{3.9}$$

$$\mathbf{e}_{cross} = \frac{\mathbf{r} \times \dot{\mathbf{r}}}{|\mathbf{r} \times \dot{\mathbf{r}}|} \tag{3.10}$$

$$\mathbf{e}_{radial} = \mathbf{e}_{along} \times \mathbf{e}_{cross} \tag{3.11}$$

$$\delta\mathbf{X} = [\mathbf{e}_{radial}\ \mathbf{e}_{along}\ \mathbf{e}_{cross}]\ \delta\mathbf{O} \tag{3.12}$$

where

$\mathbf{r} = \mathbf{X}_{broad}$	:	position vector that include Earth Centered Earth Fixed (ECEF) coordinates of satellite computed from the broadcast ephemeris
$\dot{\mathbf{r}}$	:	velocity vector in ECEF computed from the broadcast ephemeris
$\mathbf{e}_i$	:	unit vector in the related direction
$\delta\mathbf{O}$	:	orbit correction vector

The individual correction terms and their velocities of orbit correction vector is given by:

$$\delta\mathbf{O} = \begin{bmatrix} \delta O_{radial} \\ \delta O_{along} \\ \delta O_{cross} \end{bmatrix} + \begin{bmatrix} \delta \dot{O}_{radial} \\ \delta \dot{O}_{along} \\ \delta \dot{O}_{cross} \end{bmatrix} (t_i - t_r) \tag{3.13}$$

where $\delta O_{radial},\ \delta O_{along},\ \delta O_{cross}$ and $\delta \dot{O}_{radial}\ \delta \dot{O}_{along}\ \delta \dot{O}_{cross}$ indicate the orbit correction

terms acquired from the SSR orbit message and $(t_i - t_r)$ represents the time difference from the reference epoch. Herein, it should also be mentioned that the reference of satellite position computed by navigation messages and the SSR corrections is to the satellite antenna phase center unless otherwise specified.

Similarly, the satellite clocks obtained from the broadcast ephemeris are corrected using the SSR clock corrections as follows:

$$\Delta t_{sat} = \Delta t_{broad} - \frac{\delta C}{c} \tag{3.14}$$

where

Δt_{sat} : final satellite clock correction.

Δt_{broad} : satellite clock correction computed with the broadcast ephemeris.

δC : clock correction from the SSR message.

c : velocity of light.

The SSR clock corrections are similarly generated depending on the satellite clock reference, that is a signal or signal combination identical to that of the navigation message, with the polynomial coefficients as:

$$\delta C = C_0 + C_1 \, (t_i - t_r) + C_2 \, (t_i - t_r)^2 \tag{3.15}$$

where $C_0,\ C_1,\ C_2$ are the polynomial coefficients transmitted in the SSR clock correction message, and $(t_i - t_r)$ is the time difference from the reference epoch.

3.2. Timing (or Total) Group Delay (TGD)

As previously stated, a signal or signal combination, e.g. ionosphere-free combination is typically utilized to generate the satellite clock corrections in IGS precise products and broadcast ephemeris. For GPS and GLONASS, the ionosphere-free combination of dual-frequency code observations (P(Y)-codes) on conventional L1 and L2 signals are employed as the clock reference in both precise ephemeris and navigation message. Similarly, for Galileo satellites, clock corrections are generated with respect to the ionosphere-free combination of code observations on E1 and E5a signals (Steigenberger et al., 2015). As regards BDS satellites, the clock corrections in IGS precise products are determined depending on the dual-frequency ionosphere-free combination of code observations on B1 and B2 signals, while the legacy B3 signal has been selected as the clock reference in the BDS broadcast ephemeris (BeiDou-ICD, 2020). Therefore, it is a necessitate aligning with the satellite

clock corrections in the GNSS applications where different signal or combination is adopted as described in the previous sections.

For the single-frequency users, navigation messages include the timing (or total) group delay, namely TGD, parameters to align with the satellite clock corrections. While GPS and GLONASS navigation messages contain a TGD parameter that aligns the satellite clock corrections for the single-frequency positioning on L1 signals, Galileo and BDS navigation messages provide two TGD parameters to correct the satellite clock corrections for the related navigation signals. More details about TGD parameters can be reached in the user control documents of related navigation systems (GPS-ICD, 2020; GLONASS-ICD, 2016; Galileo-ICD, 2018; BeiDou-ICD, 2020). On the other hand, TGD parameters can be derived from the differential code biases (DCB) as described in Equation 2.8. In this regard, DCBs generated and distributed by some IGS analysis centers can be used to acquire the TGD parameters. Also, daily DCBs for multi-GNSS satellites have been provided by some MGEX agencies regularly for a while (Wang et al., 2016). Several DCBs between different GNSS signals are provided in the multi-GNSS DCB files, which enables a broader spectrum in multi-GNSS positioning applications. Finally, positioning techniques where the dual-frequency ionosphere-free combination is adopted as the functional models, such as traditional PPP, do not require any TGD correction.

3.3. Relativistic Effects

Conventionally, the design of GNSS satellites, in the idealized circular orbits, includes the compensation of general and special relativistic effects. Still, the distance between a GNSS satellite and the Earth deviates from nominal because of its slightly elliptical orbit in practice, which causes variations in the speed of the satellite. So, the satellite clocks are influenced by this speed deviation. The compensation procedure applied for the circular orbit is not enough to mitigate the effects of general and special relativity on GNSS satellites, so a additional relativistic correction is required to be applied (Teunissen and Montenbruck, 2017):

$$\Delta p = c\, e\, F\, \sqrt{a}\, \sin E_k \tag{3.16}$$

where c is the velocity of light, e and a are the eccentricity and semi-major axis of satellite orbit, E_k is the eccentric anomaly, and

$$F = -\frac{2\mu}{c^2} \tag{3.17}$$

with the Earth's gravitational constant μ. Alternatively, the relativistic clock correction can be computed as follows:

$$\Delta p = -2 \, \frac{\mathbf{r}^{sat} \cdot \mathbf{v}^{sat}}{c^2} \tag{3.18}$$

where $\mathbf{r}^{sat}$ and $\mathbf{v}^{sat}$ are the position and velocity vector of the satellite.

On the other side, there is a secondary relativistic effect on the GNSS signals, which is resulted from the space-time curvature owing to the gravitational field. This effect, which is called relativistic path correction or the Shapiro effect, is employed to correct the Euclidean distance between the receiver and satellite. The relativistic path correction is computed by the following equation:

$$\Delta_{rel} = \frac{2\mu}{c^2} \, \ln \frac{\rho^{sat} + \rho^{rec} + \rho^{sat}_{rec}}{\rho^{sat} + \rho^{rec} - \rho^{sat}_{rec}} \tag{3.19}$$

where ρ^{sat} is the geocentric distance of the satellite, ρ^{rec} is the geocentric distance of the receiver and ρ^{sat}_{rec} is the geometric distance between the receiver and satellite. Since the amount of relativistic path correction does not exceed 2 cm, it should be applied only in the GNSS applications which requires high positioning accuracy.

3.4. Troposphere

Including the troposphere and stratosphere, the neutral portion of the atmosphere affects the GNSS signals considerably. The impact of the neutral atmosphere is the same for the GNSS signals regardless of the observation type (code pseudorange or carrier phase) and frequency since it is not a dispersive medium for the GNSS signals (1-2 GHz). As the lower part of the atmosphere, the troposphere contains most of the moist gases and water vapor and in the atmosphere. Also, the stratosphere, lying from just above the troposphere to a height of nearly 50 km, is composed of mainly dry gases. The influence of the neutral atmosphere on the GNSS signals is frequently mentioned as the tropospheric delay in the GNSS literature. Because of the nondispersive nature, its influence on the GNSS signals cannot be removed by signal combinations, therefore it is required to correct the tropospheric delay in GNSS positioning techniques using an appropriate model (Hofmann-Wellenhof, Lichtenegger and Wasle, 2007).

The tropospheric delay (T_r) is associated with the signal propagation path (l) and the refrac-

tive index (n) as follows:

$$T_r = \int_s^r (n-1)\, dl = 10^{-6} \int_s^r N_{trop}\, dl \tag{3.20}$$

where N_{trop} is the tropospheric refractivity, which strictly depends on the atmospheric parameters, such as temperature and partial pressures of atmospheric constituents.

As a standard in the space geodesy techniques, the tropospheric delay is usually split up into the hydrostatic (dry) and non-hydrostatic (wet) components (Davis et al., 1985). The vast majority of tropospheric delay, approximately 90%, results from the hydrostatic component, which is mainly deu to dry gases. On the other side, the non-hydrostatic component, which includes most of the water vapor, is responsible for a significantly small portion of the total tropospheric effect. The hydrostatic component can be modeled empirically depending on the station's position as well as the atmospheric parameters, however, it is considerably rough to model the non-hydrostatic component of tropospheric delay because of the rapid variations in water vapor content.

Typically, the tropospheric delay is formulated as a function of zenith direction with a mapping function which is used to project the total delay along the satellite elevation angle:

$$T_r = ZTD_{dry}\, m_{dry}(E) + ZTD_{wet}\, m_{wet}(E) \tag{3.21}$$

where ZTD_{dry} and ZTD_{wet} represent the dry and wet components of zenith total tropospheric delay; $m_{dry}(E)$ and $m_{wet}(E)$ indicate the corresponding mapping functions for dry and wet components and E is the satellite's elevation angle.

The Saastamoinen model, which is one of the frequently used models in the GNSS applications, can be employed to acquire the dry part of total tropospheric delay as follows (Saastamoinen, 1972):

$$ZTD_{dry} = \frac{0.0022768 \cdot p}{1 - 0.00266 \cdot \cos(2\varphi) - 0.28 \cdot 10^{-6}\, h_{ell}} \tag{3.22}$$

where p denotes the pressure in millibar (mb), while φ and h_{ell} demonstrate the geographical latitude and ellipsoidal height of the station, respectively. As previously mentioned, it is quite difficult to model the wet part of tropospheric delay due to the irregularities in the water vapor content. As a common practice in the GNSS positioning applications, the wet troposphere component in zenith direction is predicted together with the other estimated parameters in the filtering process. Still, its impact can be mitigated with a priori model as

given in the following equation:

$$ZTD_{wet} = 10^{-6} \cdot (k_2^{'} + \frac{k_3}{T_m}) \cdot \frac{R_d \cdot e}{g_m \cdot (\lambda + 1)} \tag{3.23}$$

where e, T_m and λ indicate the atmospheric parameters, which are water vapor pressure, mean temperature weighted with water vapor pressure and water vapor decrease factor, respectively. Also, $k_2^{'}$ and k_3 demonstrate the refractivity constants which are determined empirically. The values provided in Nilsson et al., 2013 can be utilized for these coefficients. Furthermore, R_d represents the specific gas constant for dry constituents, which is $287.0464\ \mathrm{JK^{-1}kg^{-1}}$, and g_m is the mean gravity which equals $9.80665\ \mathrm{ms^{-2}}$.

On the other hand, the dry and wet parts of total tropospheric delay are derived from the modified Hopfield model as follows (Hopfield, 1969):

$$ZTD_i = 10^{-6}\ N_i \sum_{k=1}^{9} \frac{f_{k,i}}{k}\ r_i^k \tag{3.24}$$

where i represents the tropospheric part, dry (d) or wet (w). Also, N is the tropospheric refractivity and it is computed for the dry and wet parts as:

$$N_d = \frac{77.64 \cdot p}{T} \tag{3.25}$$

$$N_w = -\frac{12.95 \cdot e}{T} + \frac{371800 \cdot e}{T^2} \tag{3.26}$$

where p, e and T are the pressure (in mb), water vapor pressure (in mb) and temperature (in Kelvin), respectively. Herein, the coefficients $f_{k,i}$ can be calculated by:

$$f_{1,i} = 1,\ f_{4,i} = 4a_i(a_i^2 + 3b_i),\ f_{7,i} = b_i^2(6a_i^2 + 4b_i) \tag{3.27}$$

$$f_{2,i} = 4a_i,\ f_{5,i} = a_i^4 + 12a_i^2 b_i + 6b_i^2,\ f_{8,i} = 4a_i b_i^3 \tag{3.28}$$

$$f_{3,i} = 6a_i^2 + 4b_i,\ f_{6,i} = 4a_i b_i(a_i^2 + 3b_i),\ f_{9,i} = b_i^4 \tag{3.29}$$

with

$$a_i = -\frac{\cos z}{h_i}, \quad b_i = -\frac{\sin^2 z}{2h_i\ R_E} \tag{3.30}$$

$$r_i = \sqrt{(R_e + h_i)^2 - R_e^2 \sin^2 z} - R_e \cos z \tag{3.31}$$

$$h_d = 40136 + 148.72\ (T - 273.15)\ \mathrm{m} \tag{3.32}$$

$$h_w = 11000\ \mathrm{m} \tag{3.33}$$

where z indicates the zenith angle of the related satellite, R_e is the Earth's radius (6378137 m).

Tropospheric delay on GNSS signals can be determined using the Saastamoinen and Hopfield models as defined above. Still, these models require several meteorological parameters, i.e. the pressure, water vapor pressure, temperature, etc., in the computations. In practice, it is troublesome to obtain in-situ measurements of these meteorological parameters for every GNSS station. Instead, the empirical models which depend on the long-standing measurements are employed to acquire the meteorological quantities in the tropospheric delay estimation. The Global Pressure and Temperature 2 (GPT2) and its new version Global Pressure and Temperature 3 (GPT3) models provide substantial opportunity to get the meteorological parameters required in the tropospheric models on a global scale. Moreover, their coherent mapping functions, Vienna Mapping Functions 1 (VMF1), and its successor Vienna Mapping Functions 3 (VMF3) can be utilized to project the zenith tropospheric delay to the satellite elevation (Lagler et al., 2013; Landskron and Böhm, 2018). Additionally, Global Mapping Function can also be applied to project the zenith tropospheric delays to the related satellite elevation (Boehm et al., 2006).

3.5. Ionosphere

The ionosphere is a atmosphere layer extending from 60 to more than 2000 km. As the name suggests, it consists of electrically charged particles that are ionized as a result of solar ultraviolet radiations. The ionosphere influences the electromagnetic signals used in GNSS depending on the total electron density along the propagation path. Geomagnetic disturbances which are mainly arisen from solar radiations have a considerable impact on the electronic density and its distribution in the atmosphere during the day. On the other side, for the GNSS signals, the ionosphere is a dispersive medium, therefore, its impact alters depending on the observation type and frequency of the navigation signal (Hofmann-Wellenhof, Lichtenegger and Wasle, 2007). For carrier phase observations, the phase refractivity index of the first-order ionospheric effect can be expressed by the following approximation:

$$n_L = 1 - \frac{40.3\ N_e}{f^2} \tag{3.34}$$

where N_e is the total electron density ($\mathrm{el/m^3}$) and f is the signal frequency (Hz). Similarly, for code pseudorange observation, the group refractivity index of the first-order ionospheric effect is approximated as:

$$n_P = 1 + \frac{40.3\ N_e}{f^2} \tag{3.35}$$

The ionospheric signal delay on phase and code observations are written by the integration

of the entire propagation path as follows:

$$\Delta\tau_L = \int (n_L - 1)\, dl = -\frac{40.3}{f^2} \int N_e\, dl \tag{3.36}$$

$$\Delta\tau_P = \int (n_P - 1)\, dl = \frac{40.3}{f^2} \int N_e\, dl \tag{3.37}$$

The electron density in a tube with a cross-section of 1 m^2 is called the total electron content (TEC) and it is given as follows:

$$TEC = \int_r^S N_e\, dl \tag{3.38}$$

Integrating with Equation 3.36 and Equation 3.37, the ionospheric delay on phase and code observations can be written depending on TEC as follows:

$$\Delta\tau_L = -\frac{40.3}{f^2}\mathrm{TEC} \quad \text{and} \quad \Delta\tau_P = \frac{40.3}{f^2}\mathrm{TEC} \tag{3.39}$$

which indicates that the ionospheric delay has the same magnitude on both carrier phase and code pseudorange observations, but opposite signs. Therefore, the ionosphere advances carrier phase observations, while it causes a delay in code pseudorange observations. Additionally, for the mitigation of the first-order ionospheric delay, the dual-frequency ionosphere-free combinations can be utilized as its effect depends on the GNSS signal frequency owing to its dispersive nature. However, in single-frequency GNSS positioning, it is required to handle the ionospheric delay since it is not possible to use the dual-frequency ionosphere-free combinations.

For single-frequency users, global ionosphere models disseminated in the broadcast data, such as Klobuchar (Klobuchar, 1987), NeQuick-G (EC, 2016), BDGIM (Yuan et al., 2019), etc., can be used to mitigate the ionospheric effect on the GNSS signals. However, it is very tough to achieve precise positioning with these models due to their relatively low accuracy. Alternatively, GIMs produced by some IGS agencies can be used for the elimination of ionospheric delay. For instance, CODE, for a long time, has been providing 1-day predicted GIMs which can be employed in real-time GNSS positioning (http://ftp.aiub.unibe.ch/CODE/). The predicted GIMs of CODE include the gridded VTEC (vertical total electron content) values which are produced depending on a single layer spherical model with a sample rate of 1 hour. Using the predicted GIMs, the VTEC value of a specific location can be computed with a proper interpolation function considering the spatial and temporal resolutions.

On the other side, some IGS agencies contain ionospheric parameters in their correction streams within IGS-RTS. In this regard, ionospheric corrections are provided using spherical

harmonic expansions of a continuous global ionosphere model. The VTEC value of a specific point is computed in TECU ($1\mathrm{TECU} = 10^{16}\ \mathrm{el/m^2}$) as follows (IGS-SSR, 2020):

$$\mathrm{VTEC}(\varphi_{PP}, \lambda_{PP}) = \sum_{n=0}^{N} \sum_{m=0}^{min(n,M)} (C_{nm} \cos m\lambda_S + S_{nm} \sin m\lambda_S)\ P_{n,m}(\sin \varphi_{PP}) \quad (3.40)$$

where

N, M	degree and order of spherical expansion
n, m	indices for degree and order, respectively
$\mathrm{C_{nm}}$	cosine coefficients provided in the ionospheric corrections (TECU)
$\mathrm{S_{nm}}$	sine coefficients provided in the ionospheric corrections (TECU)
λ_{S}	mean sun fixed and phase shifted longitude of ionospheric pierce point (IPP) modulo 2π (radian)
λ_{PP}	longitude of the IPP (radian)
φ_{PP}	geocentric the latitude of IPP (radian)
$\mathrm{P_{n,m}}$	fully normalized associated Legendre function

with

$$\lambda_S = \left(\lambda_{PP} + (t - 50400)\frac{\pi}{43200}\right)\ \mathrm{modulo}2\pi \quad (3.41)$$

where t indicates the SSR epoch. Also, the IPP position in the spherical Earth model is computed as follows:

$$\varphi_{PP} = \arcsin(\sin \varphi_R \cos \psi_{PP} + \cos \varphi_R \sin \psi_{PP} \cos A) \quad (3.42)$$

where

φ_{R}	geocentric latitude of the station (radian)
λ_{R}	geocentric longitude of the station (radian)
ψ_{PP}	central angle of the IPP (radian)
A	the satellite azimuth (radian)

The central angle (ψ_{PP}) is computed as:

$$\psi_{PP} = \frac{\pi}{2} - E - \arcsin\left(\frac{R_E + h_R}{R_E + h_I}\cos E\right) \tag{3.43}$$

where

E	elevation angle of the satellite (radian)
$\mathrm{R_E}$	spherical Earth's radius (6370 km)
$\mathrm{h_I}$	height of ionospheric layer above the spherical Earth model (km)
$\mathrm{h_R}$	height of the station above the spherical Earth model (km)

The longitude of ionospheric pierce point is computed by:

$$\lambda_{PP} = \lambda_R + \arcsin\left(\frac{\sin\psi_{PP}\sin A}{\cos\varphi_{PP}}\right) \tag{3.44}$$

Finally, the slant total electron content (STEC) value at the related station is obtained by:

$$\mathrm{STEC} = \frac{\mathrm{VTEC}}{\sin(E + \psi_{PP})} \tag{3.45}$$

and the ionospheric delay on the corresponding frequency (f) along the propagation path is computed in meters as:

$$\Delta\tau_P = \frac{40.3}{f^2}\,\mathrm{STEC}\cdot 10^{16} \tag{3.46}$$

3.6. Antenna Phase Center Offset and Variation

Conventionally, the distance between the receiver and satellite antenna phase centers is the essential measurement of GNSS observations. However, the receiving and transmitting antennas have inconstant electrical phase centers, which alter depending on the direction of incoming signals in addition to the signal frequency. Moreover, though the broadcast ephemeris provides coordinates of the satellite antenna phase center, the reference of satellite coordinates acquired from the precise ephemeris is to the satellite's CoM. While it is not required to correct the satellite coordinates obtained from the broadcast ephemeris, an additional antenna phase center offset (PCO) needs to be applied when the precise ephemeris is utilized. For a long time, IGS and individual analysis centers have provided satellite PCOs and their variations (PCVs) using the Antenna Exchange (ANTEX) format which depends on a satellite-fixed coordinate system. This satellite-fixed coordinate system, namely the

yaw-steering altitude mode, refers to the satellite's CoM, and it is also defined with the three fundamental axes. While its Z-axis is oriented towards the Earth, the Y-axis of the system is perpendicular to the Sun and nadir directions. Finally, the right-hand coordinate system is completed with the X-axis (Figure 3.2). The unit vectors ($\hat{\mathbf{e}}_x,\ \hat{\mathbf{e}}_y,\ \hat{\mathbf{e}}_z$) which defines the system orientation is expressed as follows (Montenbruck et al., 2015):

$$\hat{\mathbf{e}}_x = \hat{\mathbf{e}}_y \times \hat{\mathbf{e}}_z, \qquad \hat{\mathbf{e}}_y = \frac{\hat{\mathbf{e}}_\odot \times \mathbf{r}}{|\hat{\mathbf{e}}_\odot \times \mathbf{r}|}, \qquad \hat{\mathbf{e}}_z = -\frac{\mathbf{r}}{|\mathbf{r}|} \tag{3.47}$$

where $\hat{\mathbf{e}}_\odot$ is the unit vector between the satellite and the Sun, $\mathbf{r}$ indicate the ECEF position vector of the satellite.

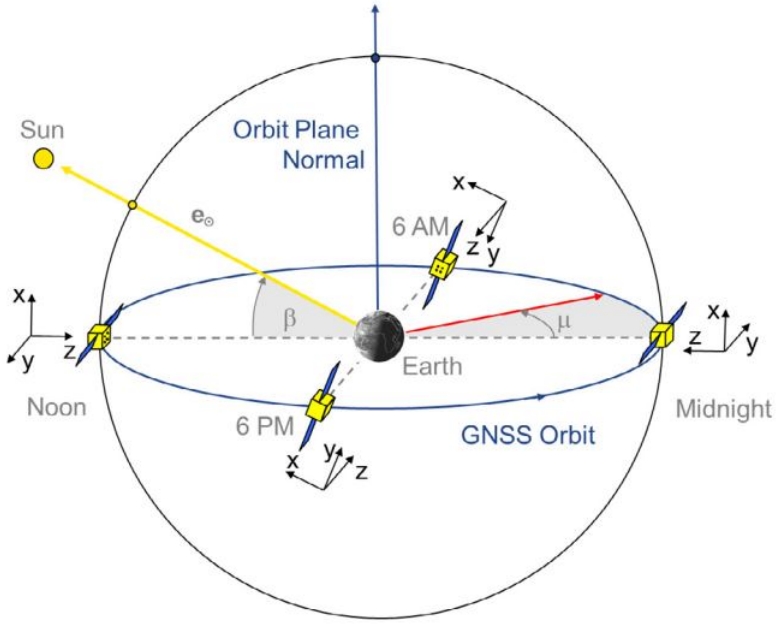

Figure 3.2: Nominal yaw-steering mode and GNSS satellite orientation (Montenbruck et al., 2015).

The satellite PCOs and PCVs are provided in the nominal yaw-steering attitude mode. When the precise ephemeris is utilized, it is required to correct the satellite coordinates using the PCO values as follows:

$$\mathbf{X}_{phase} = \mathbf{X}_{mass} + \begin{bmatrix} \hat{\mathbf{e}}_x & \hat{\mathbf{e}}_y & \hat{\mathbf{e}}_z \end{bmatrix}^{-1} \cdot \Delta\mathbf{x} \tag{3.48}$$

where $\Delta\mathbf{x}$ is the correction vector which includes the satellite PCOs, $\mathbf{X}_{mass}$ and $\mathbf{X}_{phase}$ are the position vectors referring to the CoM and antenna phase center of the satellite. Additionally, the PCV corrections can be applied to the GNSS observations as follows:

$$\rho_{cor} = \rho_{obs} + \mathrm{PCV}(elevation, azimuth) \tag{3.49}$$

where ρ_{obs} and ρ_{cor} indicate the observed and corrected observations, respectively.

As regards the receiver's antenna, the antenna reference point (ARP), which indicates a constant geometrical point, is defined on the base of the antenna because of the variations of the antenna phase center with the incoming signal. Antenna phase center position and its variations are typically provided as a correction to the ARP in the receiver-based local coordinate system (North, East, Up). Accordingly, PCO and PCV values of the receiver's antenna can be applied to the related observation as follows:

$$\mathbf{X}_{phase} = \mathbf{X}_{ARP} + \Delta\mathbf{x}_{pco} \tag{3.50}$$

$$\rho_{cor} = \rho_{obs} + \mathrm{PCV}(elevation, azimuth) \tag{3.51}$$

where $\mathbf{X}_{phase}$ and $\mathbf{X}_{ARP}$ indicate the position vector of receiver's APC and ARP, $\Delta\mathbf{x}_{pco}$ demonstrate the correction vector of PCO given in the local coordinate system, ρ_{obs} and ρ_{cor} are the observed and corrected observations, respectively.

For a long while, IGS has been generating and distributing the antenna PCOs and PCVs for GNSS satellites and receivers using the absolute antenna model. The latest version of the IGS absolute antenna model (igs14.atx) can be used to obtain the PCO and PCV corrections for multi-constellation satellites (Rebischung and Schmid, 2016).

3.7. Phase Wind-up Effect

Right-hand circularly polarized signals are transmitted by GNSS satellites for position, navigation, and timing purposes. They are emitted in two crossed dipoles (**x** and **y**) that are perpendicular to each other, and generate an electrical field rotating in the **xy**-plane. The relative orientation of receiving and transmitting antennas influences the electrical field of the electromagnetic signal and therefore the phase angle measured in the internal oscillators. This influence, which is named phase wind-up, results in a measurement error on the carrier phase observations, which can reach one cycle at most, in other words, 19 and 25 cm for the first and second frequencies of GPS (Wu et al., 1993). Though its impact may be neglected in most of the relative and differential positioning techniques, the phase wind-up effect should be considered in the absolute positioning techniques which use phase measurements.

Maneuvers in the antennas of receiver and satellite cause the phase wind-up effect, but it is mainly because of the satellite orbital motions. Since GNSS satellites are continuously trying to keep their solar panels pointed out towards the Sun, they typically rotate around their z-axis. As a consequence, the relative orientation of the receiver and satellite antennas

alters frequently, and the variations in the orientation bring the phase wind-up effect on the carrier phase observations. The phase wind-up effect can be modeled as follows (Wu et al., 1993):

$$\Delta\phi = \text{sign}(\hat{\mathbf{p}} \cdot (\mathbf{d}' \times \mathbf{d}))\ \cos^{-1}\left(\frac{\mathbf{d}' \cdot \mathbf{d}}{|\mathbf{d}'| \cdot |\mathbf{d}|}\right) \tag{3.52}$$

where $\hat{\mathbf{p}}$ indicate the unit vector pointing from the satellite to receiver, $\mathbf{d}'$ and $\mathbf{d}$ are the effective dipole vectors of the receiver and satellite antennas that are determined by the satellite-fixed coordinate unit vectors ($\hat{\mathbf{e}}_x, \hat{\mathbf{e}}_y, \hat{\mathbf{e}}_z$) and the receiver local coordinate unit vectors ($\hat{\mathbf{n}}, \hat{\mathbf{e}}, \hat{\mathbf{u}}$), respectively. The effective dipole vectors can be defined as:

$$\mathbf{d}' = \hat{\mathbf{e}}_x - \hat{\mathbf{p}}\,(\hat{\mathbf{p}} \cdot \hat{\mathbf{e}}_x) - \hat{\mathbf{p}} \times \hat{\mathbf{e}}_y \tag{3.53}$$

$$\mathbf{d} = \hat{\mathbf{n}} - \hat{\mathbf{p}}\,(\hat{\mathbf{p}} \cdot \hat{\mathbf{n}}) - \hat{\mathbf{p}} \times \hat{\mathbf{e}}. \tag{3.54}$$

Finally, it is required to guarantee the continuity of the phase observations between the consecutive epochs adding a full cycle to the phase wind-up correction provided in Equation 3.52, if it is necessary (Kouba and Héroux, 2001).

3.8. Site Displacement Effects

GNSS positioning provides the receiver's 3D coordinates in a global scale, e.g. in the international terrestrial reference frame (ITRF) or the IGS reference frames, depending on the employed satellite ephemeris. It is well-known that there are several forces acting on the Earth, such as solar and lunar gravity forces, loading caused by the oceans, ice, and atmosphere, which causes periodic deformations on the Earth crust and therefore influences the realization of the corresponding reference frames. Due to their high correlation over wide areas, they can be ignored in the differential and relative positioning techniques. However, to assure the compatibility of positioning solutions with the related reference frames which typically removes the periodic deformations, it is required to consider these site displacement effects in the absolute positioning techniques, when high positioning accuracy is demanded.

The solid Earth tide, polar tide, and ocean loading are the main site displacement effects, which can cause deformations up to a few dm. Other environmental effects, such as atmospheric loading, ground-water or snow loading, etc., are not considered in most of the absolute GNSS positioning techniques as their impacts are not greater than 1 cm. Additionally, the diurnal and semidiurnal atmospheric tides are not taken into account herein because of their considerably lower vertical amplitudes, approximately 2mm. Three main site dis-

placement effects are presented below in detail.

3.8.1. Solid Earth Tides

Gravitational forces of the Moon, Sun, and other celestial bodies cause deformations on the Earth's crust. Generally, these deformations, that are named the solid Earth tides, can reach up to 30 cm vertically and 5 cm horizontally. As previously mentioned, the displacements caused by the solid Earth tides need to be corrected in the absolute GNSS positioning techniques to obtain the coherent station coordinates (Kouba, 2015). According to the International Earth Rotation and Reference Systems Service (IERS) convention (Petit and Luzum, 2010), the displacement resulted from the solid Earth tides are modeled using a spherical harmonic expansion whose degree and order (n, m) are characterized by Love and Shida numbers. The Love and Shida numbers are specified based on the station's geographical location as well as the tidal frequency. The solid Earth tides are typically characterized by permanent and periodic components. The effect of the periodic component can be mitigated by averaging out over a period of 24 hours, unlike the permanent component whose effect can reach up to 12 cm in middle latitudes. In order to provide a station position completely consistent with the related coordinate frame, it is necessary to consider both components of the solid Earth tides in the positioning process (Kouba, 2015). Consequently, the site displacement induced by the solid Earth tides including the permanent and periodic components is modeled as follows:

$$\begin{aligned}\Delta\overrightarrow{r} = \sum_{j=2}^{3} \frac{GM_j R_e^4}{GMR_j^3}\left\{h_2\,\hat{\mathbf{r}}\left(\frac{3(\hat{\mathbf{R}}_j\cdot\hat{\mathbf{r}})^2-1}{2}\right)+3\,l_2\,(\hat{\mathbf{R}}_j\cdot\hat{\mathbf{r}})\left[\hat{\mathbf{R}}_j-(\hat{\mathbf{R}}_j\cdot\hat{\mathbf{r}})\,\hat{\mathbf{r}}\right]\right\} \\ +\left[-0.025\,m\,\sin(\varphi)\,\cos(\varphi)\,\sin(\Theta_{Gr}+\lambda)\right]\cdot\hat{\mathbf{r}}\end{aligned} \tag{3.55}$$

where:

φ, λ	the latitude and longitude of the station,
$\mathrm{GM_j}$	gravitational parameter for the Moon (j=2) or the Sun (j=3),
GM	gravitational parameter for the Earth,
$\hat{\mathbf{R}}_\mathrm{j}, \mathrm{R_j}$	unit vector from the geocenter to Moon (j=2) or Sun (j=3) and its magnitude,
$\mathrm{R_e}$	Earth's equatorial radius,
$\hat{\mathbf{r}}$, r	unit vector from the geocenter to the station and its magnitude,
$\mathrm{h_2}, \mathrm{l_2}$	nominal degree 2 Love and Shida numbers,
Θ_Gr	Greenwich Mean Sidereal Time.

Depending on the station's latitude, h_2 and l_2 are computed by:

$$h_2 = 0.6078 - 0.0006\,[(3\,\sin^2(\varphi) - 1)/2] \tag{3.56}$$

$$l_2 = 0.0847 + 0.0002\,[(3\,\sin^2(\varphi) - 1)/2] \tag{3.57}$$

3.8.2. Ocean Loading

Similar to the solid Earth tides, the gravitational forces of celestial bodies, particularly the Moon and Sun, give rise to variations of mass distribution in the oceans, which induces temporal deformations on the Earth's crust. When compared to the solid Earth tides, it can be said that displacements induced by the ocean loading are considerably smaller and more localized. Over a period of 24 hours, its effect can be neglected in static positioning. Also, the impact of ocean loading is very negligible for the stations which are far from the oceans. Still, for precise positioning applications, especially in the kinematic mode, the site displacement effect caused by the ocean loading should be taken into consideration (Kouba, 2015). With respect to the IERS convention (Petit and Luzum, 2010), its effect can be computed as follows:

$$\Delta c = \sum_j f_j\, A_{cj}\, \cos(w_j\, t + \chi_j + u_j - \phi_j) \tag{3.58}$$

where j indicates the eleven tidal waves ($\mathrm{M_2}$, $\mathrm{S_2}$, $\mathrm{N_2}$, $\mathrm{K_2}$, $\mathrm{K_1}$, $\mathrm{O_1}$, $\mathrm{P_1}$, $\mathrm{Q_1}$, $\mathrm{M_f}$, $\mathrm{M_m}$, $\mathrm{S_{sa}}$). f_j and u_j are dependent on the longitude of the lunar node, w and χ demonstrate the angular velocity and the astronomical arguments for the tidal wave component j at time t = 0^h. Finally, A_{cj} and ϕ_j indicate the station-specific amplitude and phase coefficients for the tidal wave component j.

3.8.3. Polar Tides

The deviations in the Earth's instantaneous rotation axis induce periodical deformations on the Earth's crust. The site displacement caused by these deformations, which are named polar tides, can reach up to 2.5 cm vertically and 0.7 cm horizontally. Contrary to the ocean loading and solid Earth tides, it is not possible to average out the effect of the polar tide over a 24-hour period. Therefore, it is required to model and correct its displacement effect for the GNSS applications where sub-centimeter positioning accuracy is desired (Kouba, 2015). Based on the IERS convention (Petit and Luzum, 2010), the impact of the polar tide can be

corrected in the latitude, longitude, and height components as follows:

$$\Delta\varphi = -9\ \cos(2\varphi)\,[(X_p - \overline{X}_p)\ \cos\lambda - (Y_p - \overline{Y}_p)\ \sin\lambda] \tag{3.59}$$

$$\Delta\lambda = 9\ \sin\varphi\,[(X_p - \overline{X}_p)\ \sin\lambda + (Y_p - \overline{Y}_p)\ \cos\lambda] \tag{3.60}$$

$$\Delta r = -33\ \sin 2\varphi\,[(X_p - \overline{X}_p)\ \cos\lambda - (Y_p - \overline{Y}_p)\ \sin\lambda] \tag{3.61}$$

where φ and λ represent the station latitude and longitude, $(X_p - \overline{X}_p)$ and $(Y_p - \overline{Y}_p)$ indicate the pole coordinate deviations from the mean poles ($\overline{X}_p$, $\overline{Y}_p$).

3.9. Cycle Slips

As previously described, carrier phase observations is considerably precise than code pseudorange observations. Therefore, it is common practice to employ phase observations for the GNSS applications to reach high positioning accuracy. For instance, the traditional PPP model relies on the ionosphere-free combinations of dual-frequency code and phase observations (Kouba and Héroux, 2001). Similarly, more precise positioning results can be acquired with the employment of phase observations in the single-frequency GNSS applications. Nonetheless, carrier phase observations suffer from the abrupt jumps that are typically called the cycle slips. To reach highly precise positioning results, it is very crucial to detect and compensate for the impact of cycle slips in the phase measurements.

Cycle slip is typically an instantaneous jump that is observed in the carrier phase observations because of the lock failure of the GNSS receiver in the signal tracking. Characteristically, a cycle slip arises in the phase measurement of one satellite at a specific epoch and influences the subsequent observations (Hofmann-Wellenhof, Lichtenegger and Wasle, 2007). Due to the discontinuity in the observations, cycle slips can deteriorate the positioning performance when they are not detected and repaired. In the literature, there exist various cycle slip detection methods that can be effectively utilized in GNSS applications. Herein, two cycle slip detection methods used in this study are provided for real-time absolute GNSS positioning considering the single- and dual-frequency receivers. It should also be clarified that as it is not possible to obtain the observations in the subsequent epochs, cycle slips are only detected but not repaired in real-time positioning. Instead, the epoch where the cycle slip is detected is treated as the beginning of a new arc.

In order to determine cycle slips for real-time dual-frequency positioning, the geometry-free

(GF) combination of phase observations is formed from Equation 2.4 by:

$$\begin{aligned} L^{s,j}_{GF,r} &= L^{s,j}_{1,r} - L^{s,j}_{2,r} \\ &= (I^{s,j}_2 - I^{s,j}_1) + c\,(B^{s}_{GF,r} - B^{s,j}_{GF}) + N^{s,j}_{GF} + \varepsilon(L^{s,j}_{GF,r}) \end{aligned} \tag{3.62}$$

with

$$B^{s}_{GF,r} = B^{s}_{1,r} - B^{s}_{2,r}, \quad B^{s,j}_{GF} = B^{s,j}_{1} - B^{s,j}_{2}, \quad N^{s,j}_{GF} = \lambda^{s}_{1}\, N^{s,j}_{1} - \lambda^{s}_{2}\, N^{s,j}_{2} \tag{3.63}$$

The GF combination removes the geometry-dependent terms, but it still contains the ionospheric delay and hardware biases in addition to phase ambiguities. Considering that the hardware biases do not change rapidly within a shorter period of time, such as with a sampling rate of 30 sec, they can be assumed as constant between two consecutive epochs. However, the ionospheric activity should be considered in the cycle slip detection as they cause substantial variations in the GF combinations, especially at low elevation angles. In this context, an elevation-dependent threshold value can be utilized to avoid the false cycle slip detection with the GF combination. Consequently, the cycle slip detection method that depends on the GF combination is provided as follows (El-Mowafy and Deo, 2015):

$$\mathrm{abs}(L^{s,j}_{GF,r}(t) - L^{s,j}_{GF,r}(t-1)) > k\,\sigma + \Delta l_{max} \tag{3.64}$$

where t indicates the corresponding epoch, k is a coefficient depending on the confidence level, usually 3 or 4, σ demonstrates the standard deviation of the GF combination, $\Delta \mathrm{l}_{\max}$ represents an empirical value that is utilized to bound possible ionosphere changes between consecutive epochs, $0.4\ \mathrm{m}$ can be selected. Additionally, the standard deviation of the GF combination (σ) can be defined according to the satellite's elevation angle as:

$$\sigma = \sqrt{2\,\sigma^2_{L_1} + \sigma^2_{L_2}} \cdot M(E), \quad M(E) = 1 + 10e^{-E/10} \tag{3.65}$$

where $\sigma^2_{\mathrm{L}_1}$ and $\sigma^2_{\mathrm{L}_2}$ are the standard deviations of phase observations on the first and second frequency. E also indicates the satellite's elevation angle.

The cycle slip detection method described above can't be utilized with single-frequency observations. In this regard, an alternative cycle slip detection method is proposed which can be applied for real-time single-frequency positioning as part of this thesis. In the proposed method, a single-frequency geometry-free (GF) combination can be formed using Equa-

tion 2.3 and Equation 2.4 as follows:

$$\begin{aligned}\Phi_{t,r}^{s,j} &= L_{1,r}^{s,j} - P_{1,r}^{s,j} \\ &= -2\, I_1^{s,j} + c\,(B_{1,r}^{s} - B_1^{s,j} + b_{1,r}^{s} - b_1^{s,j}) + \lambda_1^{s}\, N_1^{s,j} + \varepsilon(\Phi_{1,r}^{s,j})\end{aligned} \tag{3.66}$$

Similarly, this observable eliminates the satellite-dependent terms, but it still includes the hardware biases together with the doubled ionospheric delay as well as the phase ambiguity. Again, the hardware biases can be assumed to be constant between two consecutive epochs since they do not change rapidly in a short period, i.e. 30 seconds. In a similar manner, considering the ionospheric variation, a cycle slip detection method can be proposed for real-time single-frequency observations by the following equation:

$$\mathrm{abs}(\Phi_{1,r}^{s,j}(t) - \Phi_{1,r}^{s,j}(t-1)) > k\,\sigma + \Delta l_{max} \tag{3.67}$$

where the standard deviation of the single-frequency GF combination can be obtained as follows:

$$\sigma = \sqrt{\sigma_{L_1}^2 + \sigma_{P_1}^2} \tag{3.68}$$

where $\sigma_{\mathrm{L}_1}^2$ and $\sigma_{\mathrm{P}_1}^2$ indicate the standard deviations of phase and code measurements on the first frequency, respectively.

3.10. General Overview

In this section, GNSS error sources with regards to the real-time absolute positioning and their mitigation techniques have been provided. As previously mentioned, these error sources can alter depending on the applied orbit and clock source along with the functional model of the related positioning technique. In this regard, this section aims at providing a general overview of GNSS error sources for real-time absolute positioning techniques that are adopted as a part of this study. For this purpose, a summary of the real-time absolute positioning techniques with their error mitigation strategies are provided in Table 3.2. Herein, SF Code, SF Code-Phase and DF PPP represent the single-frequency code pseudorange positioning, single-frequency code-phase combination and dual-frequency PPP, respectively. The table also provides details of standard point positioning (SPP) technique as the fundamental GNSS positioning approach for the sake of comparison.

Table 3.2: Summary of GNSS error sources in the real-time absolute positioning techniques.

Error Source	SPP	IGS-RTS Correction			Ultra-rapid Products		
		SF Code	SF Code-Phase	DF PPP	SF Code	SF Code-Phase	DF PPP
Satellite orbit and clock source							
Broadcast ephemeris	+	+	+	+	-	-	-
IGS-RTS corrections	-	+	+	+	-	-	-
Ultra-rapid precise ephemeris	-	-	-	-	+	+	+
Instrumental delay							
Timing group delay	+	+	+	-	+	+	-
Relativistic effects							
Relativistic clock correction	+	+	+	+	+	+	+
Relativistic path correction	-	+	+	+	+	+	+
Atmospheric effects							
Ionosperic delay	+	+	-	-	+	-	-
Dry part of tropospheric delay	+	+	+	+	+	+	+
Wet part of tropospheric delay	-	E	E	E	E	E	E
Antenna phase center							
Satellite PCO and PCV	-	-	-	-	+	+	+
Receiver PCO and PCV	-	+	+	+	+	+	+
Others							
Carrier wind-up	-	-	+	+	-	+	+
Cycle slip detection	-	-	+	+	-	+	+
Site displacement effects	-	-	+	+	-	+	+

where + means the error is corrected, while - is not corrected. E refers to "estimated".

4. STOCHASTIC MODELING FOR ABSOLUTE GNSS POSITIONING

Real-time absolute positioning techniques have received considerable interest from the GNSS community in recent years. The primary reason behind increasing interest is the desire to achieve more precise positioning results with more cost-effective GNSS receivers. Especially, the arrival of new global satellite systems, such as BDS and Galileo, together with GLONASS whose orbital constellation was completed has recently begun a new era for the GNSS community and has also brought along significant possibilities to augment the performance of GNSS positioning applications. As regards the absolute GNSS techniques, more accurate and cost-effective positioning solutions can be acquired from the multi-GNSS integrations considering single- and dual-frequency receivers. Nonetheless, there are substantial differences between these systems, i.e. signal structure, time scale, reference frame, etc., which complicates the integration of multi-constellation. When also considering their typical difficulties, more complex functional and stochastic models are required to achieve the optimal positioning performance with the real-time absolute GNSS techniques. In this context, the functional models of the absolute GNSS techniques that are adopted in the thesis have been introduced in the previous chapters. Additionally, this chapter provides the advanced stochastic approaches for the real-time absolute multi-GNSS positioning.

In this thesis, the Kalman filter which is usually used in real-time GNSS solutions is adopted as the optimal estimator (Gelb, 1974; Teunissen and Montenbruck, 2017). The Kalman filter can provide detailed information about the time-dependent change of the state-space and also update the state-vector even if the number of measurements is fewer than that of estimated parameters, which makes it a very powerful alternative for optimal filtering. Still, the Kalman filter requires the proper definition of stochastic properties of estimated parameters and observations to achieve optimal positioning results. Inappropriate definition of the stochastic parameters gives rise to a decline in the filtering performance including unreliable estimation results and even divergence of the filtering process. Additionally, the performance of the Kalman filter is affected negatively by the existence of the dynamic model errors and gross errors. To reach more reliable positioning solutions, the robust Kalman filter methods, that includes an equivalent covariance matrix based on the robust statistic methods, can be employed for the real-time absolute GNSS positioning techniques (Yang, Song and Xu, 2002). On the other hand, another important problem with stochastic modeling is to identify the weights of different observation types when integrating multi-constellation due to the quality differences in both observations and satellite orbit and clock products. Conventionally, a priori variance coefficients are applied to define the weights of various observation types in

the multi-GNSS integrations (Zhou et al., 2018; Ning, Han and Zhang, 2018; Zheng et al., 2020). Nevertheless, this kind of approach which includes the constant variance ratios is far from reflecting the exact characteristics of different observation types coming from various navigation systems, which can cause substantial degradation in the filtering performance.

This chapter starts with the introduction of the Kalman filter, which is one of the most frequently employed estimation methods in real-time GNSS applications and also adopted as the optimal filter in this thesis. Afterward, the description of stochastic models is provided for the real-time absolute GNSS positioning techniques. Then, the advanced stochastic modeling approaches including the robust Kalman filter methods in addition to variance component estimation are described in this chapter.

4.1. Kalman Filtering

As an optimal recursive algorithm, the Kalman filter utilizes all available measurements as well as a priori information of the dynamic system and measurements to estimate a set of variables with the statistically minimized error. The Kalman filter is referred as a recursive procedure because of carrying previous information forwardly rather than registering all previous data in the filtering process. Besides, the Kalman filter is an optimal estimator since it satisfies the general optimality condition that can be written by (Gelb, 1974):

$$\lim_{n\to\infty} \mathrm{P}(|\hat{\mathbf{x}} - \mathbf{x}| < \varepsilon) \tag{4.1}$$

$$\mathrm{E}(\hat{\mathbf{x}}) = x \tag{4.2}$$

$$\mathrm{E}((\hat{\mathbf{x}} - \mathrm{E}(\hat{\mathbf{x}}))^T(\hat{\mathbf{x}} - \mathrm{E}(\hat{\mathbf{x}}))) = min \tag{4.3}$$

where n demonstrates the sample size, $\mathbf{x}$ and $\hat{\mathbf{x}}$ indicate the state-space and estimated state-space vectors, respectively. ε is a very small value, while P and E represent the statistical probability and expectation operators, respectively.

In the Kalman filter, the estimation process is controlled by a linear discrete-time system. For a nonlinear system, the optimal filtering process is driven by the extended Kalman filter where the nonlinear dynamic and measurement models are written as follows (Welch and Bishop, 1995):

$$\mathbf{x}_k = f(\mathbf{x}_{k-1}, \mathbf{w}_{k-1}) \tag{4.4}$$

$$\mathbf{z}_k = h(\mathbf{x}_k, \mathbf{v}_k) \tag{4.5}$$

where $\mathbf{x}_{\mathrm{k}}$ and $\mathbf{x}_{\mathrm{k}-1}$ are the state-space vectors which include the estimated parameters at

the epochs k and $\mathrm{k}-1$, respectively. $\mathbf{z}_{\mathrm{k}}$ is the measurement vector, f is the state transition function which defines the dynamic system model, h indicates the measurement model which relates the measurements and estimated parameters, and finally $\mathbf{w}_k$ and $\mathbf{v}_k$ are the system and measurement noise vectors with the Gaussian zero-mean, respectively.

Since the actual values of the noise vectors are not known at each distinct epoch, the state-space and measurement vectors is approximated as follows:

$$\tilde{\mathbf{x}}_k = f(\tilde{\mathbf{x}}_{k-1}, 0) \tag{4.6}$$

$$\tilde{\mathbf{z}}_k = h(\tilde{\mathbf{x}}_k, 0) \tag{4.7}$$

where $\tilde{\mathbf{x}}_k$ and $\tilde{\mathbf{z}}_k$ are the approximated state-space and measurement vectors. Since the random variables that are driven by a nonlinear dynamic process are not subject to the normal probability distribution, it is required to linearize the approximated state-space and measurement vectors by:

$$\mathbf{x}_k \approx \tilde{\mathbf{x}}_k + \mathbf{A}(\mathbf{x}_{k-1} - \hat{\mathbf{x}}_{k-1}) + \mathbf{W}_{w_{k-1}} \tag{4.8}$$

$$\mathbf{z}_k \approx \tilde{\mathbf{z}}_k + \mathbf{H}(\mathbf{x}_k - \hat{\mathbf{x}}_k) + \mathbf{V}_{v_{k-1}} \tag{4.9}$$

where $\hat{\mathbf{x}}_{\mathrm{k}}$ represent the posteriori estimate of the state-space. Also, $\mathbf{A}$ indicates the Jacobian matrix that includes the partial derivatives of f with respect to $\mathbf{x}$ and it is given by:

$$\mathbf{A}_{i,j} = \frac{\delta f_i}{\delta \mathbf{x}_j}\,(\hat{\mathbf{x}}_{k-1}, 0) \tag{4.10}$$

$\mathbf{W}$ indicates the Jacobian matrix that contains the partial derivatives of f with respect to $\mathbf{w}$:

$$\mathbf{W}_{i,j} = \frac{\delta f_i}{\delta \mathbf{w}_j}\,(\hat{\mathbf{x}}_{k-1}, 0) \tag{4.11}$$

$\mathbf{H}$ indicates the Jacobian matrix that embraces the partial derivatives of h with respect to $\mathbf{x}$:

$$\mathbf{H}_{i,j} = \frac{\delta h_i}{\delta \mathbf{x}_j}\,(\tilde{\mathbf{x}}_k, 0) \tag{4.12}$$

$\mathbf{V}$ indicates the Jacobian matrix that includes the partial derivatives of h with respect to $\mathbf{v}$:

$$\mathbf{V}_{i,j} = \frac{\delta h_i}{\delta \mathbf{v}_j}\,(\tilde{\mathbf{x}}_k, 0) \tag{4.13}$$

Besides, the prediction error ($\tilde{\mathrm{e}}_{\mathrm{x_k}}$) and measurement residual ($\tilde{\mathrm{z}}_{\mathrm{x_k}}$) can be expressed as fol-

lows:

$$\tilde{e}_{x_k} \approx \mathbf{A}\,(\mathbf{x}_{k-1} - \hat{\mathbf{x}}_{k-1}) + \epsilon_k \tag{4.14}$$

$$\tilde{e}_{z_k} \approx \mathbf{H}\,\mathbf{z}_k + \eta_k \tag{4.15}$$

where ϵ_k and η_k are the independent random variables which are assumed as Gaussian noise with zero-mean, and their covariance matrices are $\mathbf{WQW}^T$ and $\mathbf{VRV}^T$, respectively. Finally, these random variables are subject to the normal distribution theory by the following equations:

$$\mathrm{P}(\tilde{e}_{x_k}) \sim \mathrm{N}(0, [\tilde{e}_{x_k}, \tilde{e}_{x_k}^T]) \tag{4.16}$$

$$\mathrm{P}(\epsilon_k) \sim \mathrm{N}(0, \mathbf{WQ}_k\mathbf{W}^T) \tag{4.17}$$

$$\mathrm{P}(\eta_k) \sim \mathrm{N}(0, \mathbf{VR}_k\mathbf{V}^T) \tag{4.18}$$

Consequently, the extended Kalman filtering can be expressed by two processing steps, which are the prediction step (time-update) and correction step (measurement update). The first step consists of the estimation of the state vector that includes the estimated parameters and their covariance matrix. The measurements are utilized to correct the predicted state vector and therefore the final state estimation at the related epoch is acquired in the second step. The two-step procedure of the extended Kalman filter, which is summarized with regards to the GNSS positioning, is provided below.

Time-update:

$$\bar{\mathbf{x}}_k = \mathbf{A}_{k,k-1}\,\hat{\mathbf{x}}_{k-1} \tag{4.19}$$

$$\mathbf{P}_{\bar{\mathbf{x}}_k} = \mathbf{A}_{k,k-1}\,\mathbf{P}_{\hat{\mathbf{x}}_{k-1}}\,\mathbf{A}_{k,k-1}^T + \mathbf{Q}_{k,k-1} \tag{4.20}$$

Measurement-update:

$$\mathbf{K}_k = \mathbf{P}_{\bar{\mathbf{x}}_k}\mathbf{H}_k^T\left(\mathbf{H}_k\mathbf{P}_{\bar{\mathbf{x}}_k}\mathbf{H}_k^T + \mathbf{R}_k\right)^{-1} \tag{4.21}$$

$$\hat{\mathbf{x}}_k = \bar{\mathbf{x}}_k + \mathbf{K}_k\left(\mathbf{z}_k - h(\bar{\mathbf{x}}_k)\right) \tag{4.22}$$

$$\mathbf{P}_{\hat{\mathbf{x}}_k} = (\mathbf{I} - \mathbf{K}_k\mathbf{H}_k)\,\mathbf{P}_{\bar{\mathbf{x}}_k} \tag{4.23}$$

where $\bar{\mathbf{x}}_k$ and $\hat{\mathbf{x}}_k$ represent the predicted and updated state vectors with their covariance matrices $\mathbf{P}_{\bar{\mathbf{x}}_k}$ and $\mathbf{P}_{\hat{\mathbf{x}}_k}$, respectively. $\mathbf{A}_{k,k-1}$ and $\mathbf{Q}_{k,k-1}$ indicate the state transition and process noise matrices from $k-1$ to k. $\mathbf{K}_k$ is the Kalman gain matrix, $\mathbf{H}_k$ is the design matrix that contains the partial derivatives of the estimated parameters, $\mathbf{R}_k$ is the covariance matrix of the measurements, and finally $\mathbf{I}$ demonstrate the identity matrix with the proper dimension.

4.2. Stochastic Models for Absolute GNSS Positioning Techniques

In the Kalman filter, it is a requirement to define stochastic characteristics of measurements and the system noise which reflects the time-dependent variations of estimated parameters. The proper definition of the stochastic properties improves the effectiveness of the filtering process and therefore the positioning performance. While the process noise ($\mathbf{Q}_{k,k-1}$) is defined with the time-dependent kinematic behavior of the estimated parameters, the observation covariance matrix ($\mathbf{R}_k$) is constructed to define the statistical characteristics of the measurements. This section provides the stochastic models, including both stochastic characteristics of measurements and estimated parameters, for the absolute GNSS positioning techniques which are adopted in the thesis.

As explained in Section 2.3, the single-frequency code pseudorange positioning utilizes code pseudorange observations only. For the absolute positioning techniques as in this case, it can be assumed that the individual code observations are uncorrelated. Therefore, the observation covariance matrix includes diagonal elements only, which are actually the variances of code observations, as follows:

$$\mathbf{R}_k = \begin{bmatrix} \sigma^2_{P_1^{G,1}} & 0 & 0 & 0 & 0 & 0 & 0 & 0 & 0 & 0 \\ 0 & \sigma^2_{P_1^{G,2}} & 0 & 0 & 0 & 0 & 0 & 0 & 0 & 0 \\ 0 & 0 & \ddots & 0 & 0 & 0 & 0 & 0 & 0 & 0 \\ 0 & 0 & 0 & \sigma^2_{P_1^{R,1}} & 0 & 0 & 0 & 0 & 0 & 0 \\ 0 & 0 & 0 & 0 & \ddots & 0 & 0 & 0 & 0 & 0 \\ 0 & 0 & 0 & 0 & 0 & \sigma^2_{P_1^{E,1}} & 0 & 0 & 0 & 0 \\ 0 & 0 & 0 & 0 & 0 & 0 & \ddots & 0 & 0 & 0 \\ 0 & 0 & 0 & 0 & 0 & 0 & 0 & \sigma^2_{P_1^{C,1}} & 0 & 0 \\ 0 & 0 & 0 & 0 & 0 & 0 & 0 & 0 & \ddots & 0 \\ 0 & 0 & 0 & 0 & 0 & 0 & 0 & 0 & 0 & \sigma^2_{P_1^{C,n}} \end{bmatrix} \tag{4.24}$$

where $\sigma^2_{P_1^G}$, $\sigma^2_{P_1^R}$, $\sigma^2_{P_1^E}$ and $\sigma^2_{P_1^C}$ indicate the variances of pseudorange observations on the first frequency for GPS, GLONASS, Galileo and BDS satellites. The standard deviation of code pseudorange (σ_{P_1}) observation can be selected as a value between 0.3 and 3 m (Teunissen and Montenbruck, 2017).

Additionally, the noise level of GNSS observations, for both code and phase measurements,

are typically affected by the satellite's elevation angle. This is mainly because the effects of ionospheric and tropospheric delays on GNSS signals are significantly higher at low elevation angles. Also, the observations that are coming from the satellite at the low elevations suffer from the multipath effect much more compared with those at the greater elevation angles (Hofmann-Wellenhof, Lichtenegger and Wasle, 2007). Therefore, in order to relate the observation variance with the satellite elevation angle, an elevation-dependent weighting scheme can be utilized for the GNSS observations as follows:

$$\sigma_P^2 = \sigma_{P_0}^2 + \sigma_{P_0}^2 \cdot (\cos E)^2 \tag{4.25}$$

where $\sigma_{P_0}^2$ is the initial variance of code measurement, and E represents the satellite's elevation.

On the other side, the single-frequency code-phase combination model includes the single-frequency ionosphere-free combination of code and phase measurements as previously described. Similarly, the observation covariance matrix of the single-frequency code-phase combination consists of the uncorrelated observation variances as follows:

$$\mathbf{R}_k = \begin{bmatrix} \sigma^2_{\Phi_1^{G,1}} & 0 & 0 & 0 & 0 & 0 & 0 & 0 \\ 0 & \ddots & 0 & 0 & 0 & 0 & 0 & 0 \\ 0 & 0 & \sigma^2_{\Phi_1^{R,1}} & 0 & 0 & 0 & 0 & 0 \\ 0 & 0 & 0 & \ddots & 0 & 0 & 0 & 0 \\ 0 & 0 & 0 & 0 & \sigma^2_{\Phi_1^{E,1}} & 0 & 0 & 0 \\ 0 & 0 & 0 & 0 & 0 & \ddots & 0 & 0 \\ 0 & 0 & 0 & 0 & 0 & 0 & \sigma^2_{\Phi_1^{C,1}} & 0 \\ 0 & 0 & 0 & 0 & 0 & 0 & 0 & \ddots \end{bmatrix} \tag{4.26}$$

where $\sigma^2_{\Phi_1^G}$, $\sigma^2_{\Phi_1^R}$, $\sigma^2_{\Phi_1^E}$ and $\sigma^2_{\Phi_1^C}$ demonstrate the variances of single-frequency ionosphere-free combinations for GPS, GLONASS, Galileo and BDS satellites. The variance of the single-frequency ionosphere-free combination can be computed using the error propagation law as follows:

$$\sigma^2_{\Phi_1} = 0.25 \cdot \sigma^2_{P_1} + 0.25 \cdot \sigma^2_{L_1} \tag{4.27}$$

where $\sigma^2_{P_1}$ and $\sigma^2_{L_1}$ demonstrate the variances of code and phase measurements on the first frequency of the related satellite, respectively. The variance can be chosen as a value between 1 and 3 mm for the phase observations (Teunissen and Montenbruck, 2017). In Equa-

tion 4.27, it is apparent that the single-frequency ionosphere-free combination decreases the noise level of code pseudorange observations considerably because of the significantly lower noise level of carrier phase observations. Similarly, the elevation-dependent scheme defined in Equation 4.25 is employed to specify the weights of single-frequency ionosphere-free observations.

Finally, the dual-frequency PPP model consists of the dual-frequency ionosphere-free combination of code and phase measurements. The observation covariance matrix is constructed as including the uncorrelated ionosphere-free combinations as follows:

$$\mathbf{R}_k = \begin{bmatrix} \sigma^2_{P_{IF}^{G,1}} & 0 & 0 & 0 & 0 & 0 & 0 & 0 & 0 \\ 0 & \sigma^2_{L_{IF}^{G,1}} & 0 & 0 & 0 & 0 & 0 & 0 & 0 \\ 0 & 0 & \sigma^2_{P_{IF}^{R,1}} & 0 & 0 & 0 & 0 & 0 & 0 \\ 0 & 0 & 0 & \sigma^2_{L_{IF}^{R,1}} & 0 & 0 & 0 & 0 & 0 \\ 0 & 0 & 0 & 0 & \sigma^2_{P_{IF}^{E,1}} & 0 & 0 & 0 & 0 \\ 0 & 0 & 0 & 0 & 0 & \sigma^2_{L_{IF}^{E,1}} & 0 & 0 & 0 \\ 0 & 0 & 0 & 0 & 0 & 0 & \sigma^2_{P_{IF}^{C,1}} & 0 & 0 \\ 0 & 0 & 0 & 0 & 0 & 0 & 0 & \sigma^2_{L_{IF}^{C,1}} & 0 \\ 0 & 0 & 0 & 0 & 0 & 0 & 0 & 0 & \ddots \end{bmatrix} \tag{4.28}$$

where $\sigma^2_{P_{IF}}$ and $\sigma^2_{L_{IF}}$ represent the variances of dual-frequency ionosphere-free combination of code and phase measurements for the related satellite, respectively. Considering the error propagation law, the variances of dual-frequency ionosphere-free combinations are computed for GPS satellites as:

$$\sigma^2_{P_{IF}} = \frac{f_1^2}{f_1^2 - f_2^2}\,\sigma^2_{P_1} + \frac{f_2^2}{f_1^2 - f_2^2}\,\sigma^2_{P_2} = 6.481 \cdot \sigma^2_{P_1} + 2.389 \cdot \sigma^2_{P_2} \tag{4.29}$$

$$\sigma^2_{L_{IF}} = \frac{f_1^2}{f_1^2 - f_2^2}\,\sigma^2_{L_1} + \frac{f_2^2}{f_1^2 - f_2^2}\,\sigma^2_{L_2} = 6.481 \cdot \sigma^2_{L_1} + 2.389 \cdot \sigma^2_{L_2} \tag{4.30}$$

where $\sigma^2_{P_1}$ and $\sigma^2_{P_2}$ are the variances of code observations on the frequency L1 and L2, while $\sigma^2_{L_1}$ and $\sigma^2_{L_2}$ indicates the variances of phase observations on the frequency L1 and L2, respectively.

As previously mentioned, the noise levels of observations that are acquired from the distinct navigation systems are not similar due to the different techniques applied in the signal modulation together with the altered quality of their orbit and clock products. Therefore, there

exist different sort of observations coming from the various navigation systems, even if their observation type is identical. For the multi-GNSS, it is required to consider the different observation types to get the potential benefits of multi-GNSS positioning. Otherwise, the positioning performance can be deteriorated with the inappropriate definition of the stochastic characteristics of different observation types. Conventionally, a priori variance ratios are assigned to identify the weights of different observation types in the multi-GNSS process. In the literature, one of the commonly used procedure is to specify equal initial variance ratios for the multi-GNSS observations (Ning, Han and Zhang, 2018; Zhou et al., 2018; Zheng et al., 2020). Alternatively, in comparison with the GPS observations, higher variance ratios can be assigned to the observations coming from other navigation systems due to the general assumption that their orbit and clock products, and the measurements, have relatively lower precision levels (Pan et al., 2017; Bahadur and Nohutcu, 2018; Wang et al., 2019a). Consequently, two common weighting approaches that utilize constant variance ratios can be expressed as follows:

$$\text{Equal variance ratios} \qquad \begin{cases} \sigma^2_{P_1^G} : \sigma^2_{P_1^R} : \sigma^2_{P_1^E} : \sigma^2_{P_1^C} = 1 : 1 : 1 : 1 \\ \sigma^2_{L_1^G} : \sigma^2_{L_1^R} : \sigma^2_{L_1^E} : \sigma^2_{L_1^C} = 1 : 1 : 1 : 1 \end{cases} \tag{4.31}$$

$$\text{Higher variance ratios} \qquad \begin{cases} \sigma^2_{P_1^G} : \sigma^2_{P_1^R} : \sigma^2_{P_1^E} : \sigma^2_{P_1^C} = 1 : 2 : 2 : 2 \\ \sigma^2_{L_1^G} : \sigma^2_{L_1^R} : \sigma^2_{L_1^E} : \sigma^2_{L_1^C} = 1 : 2 : 2 : 2 \end{cases} \tag{4.32}$$

On the other hand, the Kalman filter also entails the appropriate definition of the process noise, which reflects the time-dependent variations of the estimated parameters. For the absolute GNSS positioning techniques that are adopted in this thesis, the estimated parameters are described together with the functional models in Section 2.3. Stochastic variations of estimated parameters with time, namely process noise, are modeled statistically with the proper spectral density in the Kalman filtering process. In this context, the conventional models that are employed to characterize the temporal variations of the estimated parameters are provided in Table 4.1 with their spectral density values considering all absolute GNSS positioning techniques used in this thesis.

4.3. Advanced Stochastic Modeling

As stated in the previous sections, the newly-emerged satellite systems not only offer considerable opportunities to enhance the performance of GNSS-based positioning applications but also bring along substantial difficulties in functional and stochastic modeling due to typ-

Table 4.1: Stochastic characteristics of the estimated parameters for the absolute GNSS positioning techniques.

Estimated Parameters	**Model**	**Spectral Density** $(\mathrm{m}^2/\mathrm{s})$
Position components	Random walk	0 (static mode) 10^1 (kinematic mode)
Receiver clock error	Random walk or white noise	10^5
Tropospheric wet delay	Random walk	10^{-9}
Inter-system bias	Random walk or white noise	10^{-7}
Phase ambiguity parameter	Random constant	0

ical differences between the navigation systems. To make use of the potential benefits of multi-constellation multi-frequency GNSS, it is very crucial to ensure the interoperability of multi-constellation with the enhanced or improved functional and stochastic modeling approaches. Although there is almost a consensus about the functional models of the absolute GNSS positioning techniques, which are also provided in Section 2.3, it is very tough to say that a standard stochastic approach has existed for the multi-GNSS positioning. Standard stochastic approaches have been provided comprehensively in the previous sections of this chapter. Still, these stochastic models are far from reflecting the actual stochastic characteristics of multi-constellation positioning, therefore more complex stochastic approaches are required in the filtering process. This section provides the mathematical background of advanced stochastic methods that can be utilized to improve the effectiveness and optimality of the estimation process with the Kalman filter as well as promising more realistic stochastic models for multi-GNSS observations.

4.3.1. Adaptive Robust Kalman Filtering

The Kalman filter requires the appropriate definition of stochastic properties of both estimated parameters and measurements to achieve optimal filtering estimation. However, it is very difficult to acquire and model their actual stochastic characteristics for the absolute multi-GNSS positioning techniques in most cases. Additionally, the gross errors in measurement and dynamic system errors deteriorate the performance of Kalman filtering and therefore the accuracy of estimated parameters. To overcome these deficiencies, the robust Kalman filter or maybe adaptive robust Kalman filter methods, which introduce an equivalent covariance matrix as well as the adaptive factor, can be utilized in the filtering process (Yang, He and Xu, 2001; Yang, Song and Xu, 2002; Guo and Zhang, 2014; Liu et al., 2019). In this way, the negative influence of unexpected errors and outliers on the filtering performance can

be eliminated, which therefore offers an increase in the filter optimality and effectiveness.

Fundamentally, the robust or adaptive robust Kalman filter methods differ from the traditional Kalman filter in computing the Kalman gain matrix. In the general perspective, the Kalman gain ($\overline{\mathbf{K}}_k$) is computed in the adaptive robust Kalman filter methods as follows:

$$\overline{\mathbf{K}}_k = \frac{1}{a_k}\mathbf{P}_{\bar{\mathbf{x}}_k}\mathbf{H}_k^T\left(\frac{1}{a_k}\mathbf{H}_k\mathbf{P}_{\bar{\mathbf{x}}_k}\mathbf{H}_k^T + \overline{\mathbf{R}}_k\right)^{-1} \tag{4.33}$$

where $\mathrm{a_k}$ is the adaptive factor which is computed depending on a robust function and takes values between 0 and 1. Also, $\overline{\mathbf{R}}_\mathrm{k}$ represents the equivalent covariance matrix of observations which is similarly obtained from a continuous robust function. Herein, the adaptive factor aims at removing the impact of dynamic system errors on the filtering process by compensating for the contribution of measurement update and time update. Moreover, the equivalent covariance matrix eliminates the negative influence of observation outliers and also reduces the contribution of observations in which greater weights are assigned unnecessarily (Yang, He and Xu, 2001). If the adaptive factor is removed from Equation 4.33, the rest of the equation indicates the computation of the Kalman gain matrix for the robust Kalman filtering as follows:

$$\overline{\mathbf{K}}_k = \mathbf{P}_{\bar{\mathbf{x}}_k}\mathbf{H}_k^T\left(\mathbf{H}_k\mathbf{P}_{\bar{\mathbf{x}}_k}\mathbf{H}_k^T + \overline{\mathbf{R}}_k\right)^{-1} \tag{4.34}$$

The Institute of Geodesy and Geophysics (IGG) III function, which is one of the most frequently employed functions for geodetic applications, can be utilized to calculate the equivalent covariance matrix as the following equations (Yang, Song and Xu, 2002; Guo and Zhang, 2014):

$$\overline{\mathbf{R}}_i = \mathbf{R}_i/\gamma_i \tag{4.35}$$

where γ_i is the variance inflation factor and it can be computed by:

$$\gamma_i = \begin{cases} 1 & |\tilde{v}_i| \le k_0 \\ \frac{k_0}{|\tilde{v}_i|}\left(\frac{k_1-|\tilde{v}_i|}{k_1-k_0}\right)^2 & k_0 < |\tilde{v}_i| \le k_1 \\ 0 & |\tilde{v}_i| > k_1 \end{cases} \tag{4.36}$$

where $\tilde{\mathrm{v}}_\mathrm{i}$ represents the standardized residual. k_0 and k_1 indicate the threshold values that can be chosen as $1.0 - 2.5$ and $3.0 - 8.0$ usually. Also, the standardized residual can be

calculated as follows:

$$\tilde{v}_i = \frac{v_i}{\sqrt{\hat{\sigma}_0^2 \mathbf{Q}_{v_i}}} \tag{4.37}$$

where $\mathrm{v_i}$ and $\mathbf{Q}_{\mathrm{v_i}}$ are the residual of the corresponding observation and its variance, respectively. Also, $\hat{\sigma}_0^2$ is the estimate of unit weight variance, which can be computed by the following equation:

$$\hat{\sigma}_0^2 = \frac{\boldsymbol{\varepsilon}^T \mathbf{Q}_{\boldsymbol{\varepsilon}}^{-1} \boldsymbol{\varepsilon}}{n} \tag{4.38}$$

where n denotes the observation number. Herein, $\boldsymbol{\varepsilon}$ shows the predicted residual (innovations) vector with its covariance matrix $\mathbf{Q}_{\boldsymbol{\varepsilon}}$. In the Kalman filter approach, the predicted residual vector and its covariance matrix is obtained from:

$$\boldsymbol{\varepsilon} = \mathbf{z}_k - h(\bar{\mathbf{x}}_k) \tag{4.39}$$

$$\mathbf{Q}_{\varepsilon} = \mathbf{H}_k \mathbf{P}_{\bar{\mathbf{x}}_k} \mathbf{H}_k^T + \mathbf{R}_k \tag{4.40}$$

The IGG III function can also be applied with respect to the posterior residual vector. However, in this case, the filter may not recognize the impact of unexpected errors properly because the observations and system dynamics have been distorted by the outliers already. Therefore, it can give rise to divergence from the desired filtering results. On the other hand, the conventional procedure of the IGG III function is to calculate the variance inflation factor for each observation and then to construct the equivalent covariance matrix depending on these variance inflation factors. Nonetheless, the employment of this standard procedure may pave the way to reduce the contribution of the normal equation matrix to the filter estimation. Alternatively, an improved iterative procedure that applies the IGG III function only for the observation possessing the largest standardized residual in each iteration can be employed to preserve the actual characteristics of the normal equation matrix. Thus, the original distributional properties of the observations and their actual correlations are conserved considerably (Guo and Zhang, 2014).

On the other side, an alternative robust function that depends on t-test statistics could be employed to define the equivalent covariance matrix in the robust Kalman filter. For the method, the threshold values applied in the robust equivalent function are determined depending on the t-test statistics in each epoch separately on the contrary to the IGG III function that utilizes constant threshold values (Zhang et al., 2018b). Based on Equation 4.37, the t-test

criterion-based classification method can be expressed by:

$$\gamma_i = \begin{cases} 1 & T_i \leq t_0(a_0, \tau) \\ \frac{t_0}{T_i}\left(\frac{t_1 - T_i}{t_1 - t_0}\right) & t_0(a_0, \tau) < T_i \leq t_1(a_1, \tau) \\ 0 & T_i > t_1(a_1, \tau) \end{cases} \tag{4.41}$$

where γ_i is the variance inflation factor as previously stated, t_0 and t_1 are t-test coefficients that are calculated at significance levels a_0 and a_1 which are usually selected as 0.1 and 0.01. Also, $\tau = \mathrm{n} - 1$ indicates the degree of freedom. $\mathrm{T_i}$ is the t-test statistic which is used in the classification and it is computed by the following equation:

$$T_i = \frac{\left| \tilde{v_i} - \frac{1}{n-1} \sum_{\substack{k=1 \\ k \neq i}}^{n} \tilde{v_k} \right|}{\left| \frac{1}{n-2} \sum_{\substack{k=1 \\ k \neq i}}^{n} \left(\tilde{v_i} - \frac{1}{n-1} \sum_{\substack{k=1 \\ k \neq i}}^{n} \tilde{v_k} \right) \right|} \tag{4.42}$$

where $\tilde{\mathrm{v}}_\mathrm{i}$ is the standardized residual for ith observation and n is the number of observations.

As previously stated, the adaptive Kalman filter additionally includes an adaptive factor to balance the contribution of time and measurement updates. In this regards, the adaptive factor which is computed based on the predicted residual vector is one of the most popular methods employed for the GNSS applications and it can be obtained as follows (Yang, He and Xu, 2001; Guo and Zhang, 2014):

$$a_k = \begin{cases} 1 & |\tilde{v}_k| \leq k_0 \\ \frac{k_0}{|\tilde{v}_k|}\left(\frac{k_1 - |\tilde{v}_k|}{k_1 - k_0}\right)^2 & k_0 < |\tilde{v}_k| \leq k_1 \\ 0 & |\tilde{v}_k| > k_1 \end{cases} \tag{4.43}$$

where k_0 and k_1 are the constant threshold values, which are typically selected as $1.5 - 3.0$ and $3.0 - 8.0$, respectively. Also, $\tilde{v}_k$ represents the test statistic that is calculated based on the predicted residuals as follows:

$$\tilde{v}_k = \frac{\boldsymbol{\varepsilon}^T \boldsymbol{\varepsilon}}{\sqrt{tr(\mathbf{Q}_{\boldsymbol{\varepsilon}})}} \tag{4.44}$$

where $\boldsymbol{\varepsilon}$ and $\mathbf{Q}_{\boldsymbol{\varepsilon}}$ are identical to those given in Equation 4.39 and Equation 4.40.

4.3.2. Variance Component Estimation

Traditional stochastic approaches for different types of observations coming from the various navigation systems have been provided in the previous sections. In these traditional approaches, constant initial variance ratios are utilized to identify the weights of different observation types. Typically, with respect to GPS observations, higher variance ratios are assigned for the observations of other navigation systems owing to the assumption that their observations and orbit and clock products have lower precision levels. However, traditional approaches cannot reflect the actual stochastic properties of different observation types for two fundamental reasons. Firstly, they are based on an assumption in determining the initial variance ratios for the observations. Secondly, the variance ratios are assumed to be constant during the whole process despite the actual stochastic characteristics of different observation types alters depending on time. Therefore, there exists a requirement for a more realistic weighting scheme that can be adapted to the stochastic variations of multi-constellation observations.

To obtain a more rigorous weighting scheme, VCE (variance component estimation) methods can be employed in the absolute multi-GNSS positioning. Up to now, several VCE methods have been applied successfully for geodetic applications, such as Helmert variance component estimation (HVCE) (Cai, Pan and Gao, 2014), minimum norm quadratic unbiased estimator (MINQUE) (Rao, 1971), best invariant quadratic unbiased estimator (BIQUE) (Koch, 1999), least-squares variance component estimator (LS-VCE) (Teunissen and Amiri-Simkooei, 2008), etc. Still, HVCE is the most popular and most frequently employed method for real-time GNSS applications as it can be integrated with the robust Kalman filter methods in a simple way. Additionally, HVCE is a very effective method for determining the weights of different types of observations having the same number of estimated parameters, which is similar to the situation in the absolute GNSS positioning which includes multi-constellation observations. Consequently, the HVCE method is typically employed together with the robust Kalman filter effectively.

The HVCE method entails a redundant number of observations which have the normal Gaussian distribution. It can be assumed that the predicted residual vector is a white noise sequence with the normal distribution after removing or mitigating the impact of dynamic system errors and observation outliers. For two different types of observations, the predicted residual vector and its covariance matrix can be given by (Zhang et al., 2018b):

$$\boldsymbol{\varepsilon} = \begin{bmatrix} \boldsymbol{\varepsilon}_1 \\ \boldsymbol{\varepsilon}_2 \end{bmatrix} \sim N \left(0, \begin{matrix} \mathbf{H}_{k1}\mathbf{P}_{\bar{\mathbf{x}}_k}\mathbf{H}_{k1}^T + \mathbf{R}_{k1} & \mathbf{H}_{k1}\mathbf{P}_{\bar{\mathbf{x}}_k}\mathbf{H}_{k2}^T \\ \mathbf{H}_{k2}\mathbf{P}_{\bar{\mathbf{x}}_k}\mathbf{H}_{k1}^T & \mathbf{H}_{k2}\mathbf{P}_{\bar{\mathbf{x}}_k}\mathbf{H}_{k2}^T + \mathbf{R}_{k2} \end{matrix} \right) \tag{4.45}$$

with

$$\boldsymbol{\varepsilon}_1 \sim N\left(0,\ \mathbf{H}_{k1}\mathbf{P}_{\bar{\mathbf{x}}_k}\mathbf{H}_{k1}^T + \mathbf{R}_{k1}\right) \tag{4.46}$$

$$\boldsymbol{\varepsilon}_2 \sim N\left(0,\ \mathbf{H}_{k2}\mathbf{P}_{\bar{\mathbf{x}}_k}\mathbf{H}_{k2}^T + \mathbf{R}_{k2}\right) \tag{4.47}$$

where $\mathbf{R}_{\mathrm{k1}}$ and $\mathbf{R}_{\mathrm{k2}}$ indicate the observation covariance matrices for two different observation types, while $\mathbf{H}_{\mathrm{k1}}$ and $\mathbf{H}_{\mathrm{k2}}$ represent their design matrices, respectively. For two residual vectors $(\boldsymbol{\varepsilon}_1, \boldsymbol{\varepsilon}_2)$, the unit weight variances can be computed as follows:

$$\hat{\sigma}_1^2 = \frac{\boldsymbol{\varepsilon_1}^T \mathbf{Q}_{\boldsymbol{\varepsilon_1}}^{-1} \boldsymbol{\varepsilon_1}}{n_1} \quad \text{and} \quad \hat{\sigma}_2^2 = \frac{\boldsymbol{\varepsilon_2}^T \mathbf{Q}_{\boldsymbol{\varepsilon_2}}^{-1} \boldsymbol{\varepsilon_2}}{n_2} \tag{4.48}$$

where n_1 and n_2 are the numbers of observations for two different observation types. $\mathbf{Q}_{\boldsymbol{\varepsilon_1}}$ and $\mathbf{Q}_{\boldsymbol{\varepsilon_2}}$ indicate the corresponding observation covariance matrices as previously described. The unit weight variances, $\hat{\sigma}_1^2$ and $\hat{\sigma}_2^2$ also refer to the variance component estimates for two different observation types. It is assumed that they are equal when the initial variances of two different observation types are specified properly. For the ith type of observation, the scale factor is specified by:

$$\hat{\lambda}_i = \frac{\hat{\sigma}_i^2}{c}\,\lambda_i \tag{4.49}$$

where c is a constant variance which can be selected as the reference variance of a specific observation. $\hat{\lambda}_{\mathrm{i}}$ and λ_{i} indicate the scale factors that are computed for the corresponding observation type in the current and previous iterations, respectively. In the HVCE method, the updated observation covariance matrices are obtained from the multiplication of the original ones with the related scale factors. This iterative procedure continues till the variance component estimates of two different observations are to be equal. Herein, though the HVCE method is described basically for two different observation types, it is also possible to apply this procedure to more than two observation types. While the HVCE method can be utilized to specify the variance ratio between code and phase measurements coming from the same navigation system, it could also be applied for identifying actual weights of a similar type of observations from different navigation systems.

5. ENHANCED POSITIONING APPROACHES AND SOFTWARE DEVELOPMENT

Over the past few years, there has been significant attention to reach high positioning accuracy with more cost-effective GNSS solutions as previously mentioned. Therefore, current GNSS researches mainly focus on the improvement of absolute positioning techniques which decrease operational costs significantly eliminating the dependence on simultaneous reference stations (Ning, Han and Zhang, 2018; Fan et al., 2019; Li et al., 2019; Nie, Liu and Gao, 2020). In addition to traditional dual-frequency PPP, which is the most common absolute positioning technique, single-receiver single-frequency positioning techniques have recently gained increasing popularity within the GNSS community because they can also be employed with the relatively low-cost GNSS receivers. Considering single-frequency receivers, which mostly are in smartphones and other mobile devices, dominate the GNSS mass-market, single-receiver single-frequency positioning interests an enormous number of users currently. On the other side, relatively low-cost dual-frequency GNSS receivers have been introduced by some receiver manufacturers shortly before. As a consequence, dual-frequency absolute positioning should be considered as a part of cost-effective GNSS solutions henceforward.

Nowadays, another critical issue for many GNSS applications is to reach highly accurate positioning solutions in real-time. To perform real-time positioning solutions, it is required to acquire satellite orbits and clock corrections, which are essential positioning components, simultaneously. As previously described, the employment of broadcast ephemeris that is provided by the related navigation signals cannot provide sufficient accuracy for precise positioning solutions. In this regard, there exist two fundamental options to access satellite orbits and clock corrections in real-time. Firstly, IGS-RTS products which are disseminated as corrections to the broadcast message can be employed for real-time positioning solutions (Hadas and Bosy, 2015). Currently, some analysis centers provide satellite orbits and clock products for multi-constellation satellites as part of IGS-RTS, which makes the real-time multi-GNSS solutions possible. Still, IGS-RTS products are broadcast via an online stream, and therefore an external connection is required to access their orbit and clock corrections. On the other side, there have been cases where the data connection of IGS-RTS can be interrupted or not be reached due to a temporary system failure or a network outage (El-Mowafy, Deo and Kubo, 2017). It can be assumed as a drawback because the positioning performance is influenced negatively in such situations. The second option is to employ the ultra-rapid products, which includes the predicted parts of satellite orbits and clock corrections, for real-time positioning solutions. Very recently, some IGS agencies have

extended their ultra-rapid products to contain multi-GNSS satellites, that offers substantial opportunities for multi-GNSS positioning solutions (ftp://igs.ign.fr/pub/igs/products/mgex). Ultra-rapid products, unlike IGS-RTS products, can be used without any simultaneous connection, which is a great advantage for GNSS users that do not have access to external online streams. Both two options can be employed for real-time positioning solutions, but their characteristics and requirements are considerably different. In this thesis, two different positioning approaches that are compatible with ultra-rapid and IGS-RTS products are proposed for real-time absolute GNSS positioning techniques considering their fundamental differences and supplementary components.

On the other side, the combination of multi-constellation, i.e. multi-GNSS, has provided substantial probabilities to augment the performance of absolute positioning techniques. However, due to the essential differences between navigation systems, enhanced functional and stochastic models are required to make use of the potential benefits of multi-GNSS better. Especially, the appropriate definition of stochastic properties for both estimated parameters and observations play a crucial role in achieving the optimal performance in the filtering process as well as the desired positioning accuracy from the related solution. Furthermore, another important issue about stochastic modeling is to define the weights of multi-GNSS observations as reflecting their actual stochastic characteristics. However, as previously described, existing stochastic models are far from representing the stochastic properties of different observation types that are coming from distinct navigation systems. In this regard, this thesis proposes a novel filtering method that integrates the variance component estimation and robust Kalman filtering for real-time absolute GNSS positioning. In this enhanced method, the robust Kalman filter is utilized to compensate the dynamic system errors and observation outliers, while the weights of different observation types are specified adaptively using the variance component estimation method. By this means, this thesis aims at providing a more realistic and rigorous filtering approach and therefore at augmenting the performance of real-time absolute GNSS positioning techniques.

Finally, it is clear that the available GNSS software packages cannot respond to the extensive researches that are proposed as part of this study. Therefore, a GNSS analysis software that is capable of conducting real-time absolute GNSS positioning solutions with the proposed positioning models and algorithms is developed in the study. The software, which is named PPPH-RT, is able to process multi-constellation observations, including GPS, GLONASS, Galileo, and BDS, also being compatible with three different absolute GNSS positioning modes which are adopted in this study. Moreover, it can employ both ultra-rapid and IGS-RTS products to acquire satellite orbits and clock corrections in real-time considering the positioning approaches provided in this study. Consequently, this chapter first provides a detailed explanation for the proposed filtering method for absolute GNSS positioning tech-

niques. Afterward, this chapter presents the enhanced positioning approaches that are offered as part of this thesis considering the IGS-RTS and ultra-rapid products. The chapter ends with the introduction of the GNSS analysis software that is developed in this thesis.

5.1. Proposed Filtering Method

As described previously, for real-time absolute GNSS positioning techniques, the Kalman filter suffers from dynamic system errors and observation outliers considerably. Besides, as regards muti-GNSS integrations, it is very problematic to determine the observation weights which are acquired from different navigation systems properly. Conventional weighting approaches that include constant variance ratios cannot represent the actual stochastic properties of multi-constellation observations. In order to overcome these troubles, the thesis proposes a novel filtering method that integrates the variance component estimation method and robust Kalman filtering. Thanks to the robust Kalman filter, the improved method gain resistance to dynamic system errors as well as the unexpected observation outliers which can be frequently observed in real-time applications. Moreover, observation variances are specified adaptively epoch by epoch using the variance component estimation.

The mathematical background of robust Kalman filtering and Helmert variance component estimation (HVCE) methods are provided in Section 4.3. Herein, the procedure of the proposed filtering method is explained conceptually. Firstly, as previously described, the observations should be a white noise sequence that is subjected to the normal distribution in the HVCE method. Therefore, before employing the HVCE method, it is very crucial to eliminate the impact of dynamic system errors and outlier observations in the filtering process. For this purpose, an equivalent covariance matrix is constructed by the robust Kalman filter to compensate for the undesirable influence of dynamic system errors and observation outliers. The robust function is employed depending on the predicted residuals to avoid the spread of unexpected errors in the filtering process. After, the HVCE method is applied to identify the weights of different observation types similarly depending on the predicted residuals. When applying the HVCE method, GPS observations are selected as the reference, and the observations obtained from the other navigation systems are realigned according to the reference using the iterative procedure described in Section 4.3. Herein, it should be mentioned that the HVCE procedure is applied for a specific type of multi-GNSS observations. For example, the HVCE is applied for multi-GNSS code pseudorange observations in the single-frequency code pseudorange positioning, while the weights of multi-GNSS code and phase observations are determined separately in the dual-frequency PPP. The detailed procedure of the proposed filtering method including the processing steps is provided as follows:

1. The robust Kalman filter is initiated with a priori parameters of the state vector ($\bar{\mathbf{x}}_0$) and its covariance matrix ($\mathbf{P}_{\bar{\mathbf{x}}_0}$) that are computed from Least-squares estimation for the first epoch.

2. The predicted residual vector ($\mathbf{V}_k$) and its covariance matrix ($\mathbf{S}_k$) are calculated by

$$\mathbf{V}_k = \mathbf{z}_k - h(\bar{\mathbf{x}}_k) \quad \text{and} \quad \mathbf{S}_k = \mathbf{H}_k \mathbf{P}_{\bar{\mathbf{x}}_k} \mathbf{H}_k^T + \mathbf{R}_k$$

3. The standardized residuals ($\tilde{v}_i$) are calculated separately for each observation as:

$$\tilde{v}_i = \frac{v_i}{\sqrt{\hat{\sigma}_0^2 \mathbf{Q}_{v_i}}}$$

4. The observation with the largest standardized residual is determined.

5. The robust function is employed only for the observation having the largest standardized residual and so the equivalent covariance matrix ($\overline{\mathbf{R}}_k$) is acquired. The procedure continues until the equivalent covariance matrices that are obtained from two consecutive iterations are to be equal.

6. Using the equivalent covariance matrix ($\overline{\mathbf{R}}_k$), the variance component estimates ($\hat{\sigma}_i^2$) for distinct navigation systems are computed by:

$$\hat{\sigma}_i^2 = \frac{\boldsymbol{\varepsilon_i}^T \mathbf{Q}_{\boldsymbol{\varepsilon_i}}^{-1} \boldsymbol{\varepsilon_1}}{n_i}$$

7. The variance component estimate of GPS observations is selected as the reference. Then, the scale factors ($\hat{\lambda}_i$) for the observations of other navigation systems, assigning the initial scale factors as 1, are calculated by:

$$\hat{\lambda}_i = \frac{\hat{\sigma}_i^2}{c} \lambda_i$$

8. The equivalent covariance matrix is updated by the multiplication with the corresponding scale factors for each navigation system. The procedure is iterated till the variance component estimates are equal.

9. With the final equivalent covariance matrix, the Kalman gain matrix ($\overline{\mathbf{K}}_k$), updated state vector ($\hat{\mathbf{x}}_k$), and its covariance matrix ($\mathbf{P}_{\hat{\mathbf{x}}_k}$) are computed.

10. Continue to the next epoch.

Additionally, the flowchart for the algorithm of the proposed filtering method is provided in Figure 5.1.

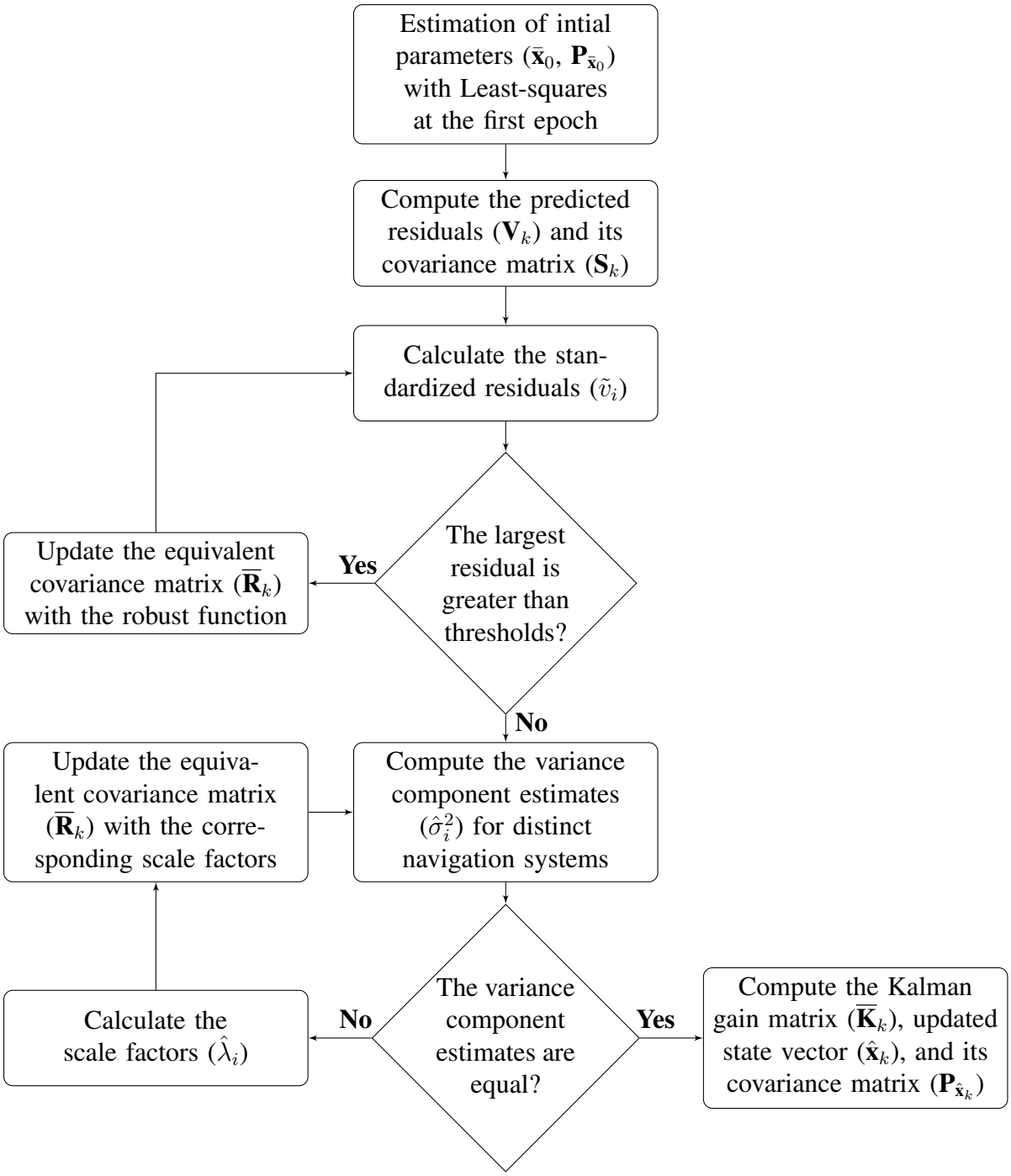

Figure 5.1: The flowchart for the algorithm of the proposed filtering method.

5.2. Enhanced Positioning Approaches

In this thesis, two positioning approaches are proposed for real-time GNSS positioning techniques. The first approach is designed to work with IGS-RTS products, while ultra-rapid products are utilized as fundamental orbit and clock source for the second approach. Both positioning approaches are compatible with the absolute GNSS positioning techniques that are adopted in this thesis. The first positioning approach can be named *online positioning*

mode as the IGS-RTS products are broadcast through an online stream. Ultra-rapid products, unlike the IGS-RTS products, can be utilized without any external connection, therefore the second positioning approach can be called *offline positioning mode*. As previously mentioned, positioning approaches considerably alter depending on the applied orbit and clock source due to their characteristics and production strategies. In this regard, this section describes these positioning approaches considering all complimentary components.

In the first step, it is required to define and import the related navigation sources, which include the required information to perform the real-time absolute GNSS positioning solution. This step is called data handling which is quite different for two positioning approaches. For the online positioning mode, the process starts with defining the real-time observations. The observations can be imported using any online stream, such as NTRIP, FTP, USB port, etc. Also, the broadcast ephemeris and SSR corrections are disseminated by the IGS-RTS stream. As previously stated, the IGS-RTS products are provided in the RTCM format via an internal connection using the NTRIP protocol. Therefore, it is necessary to access the IGS-RTS products with a compatible NTRIP client. To reach IGS-RTS products simultaneously, there exist some NTRIP client packages that are developed by some institutes or individual developers as part of the IGS real-time project. For instance, Bundesamt für Kartographie und Geodäsie (BKG) NTRIP client program (BNC), which is one of the most popular software among GNSS users, can be employed for the access of IGS-RTS products. The other NTRIP clients which are compatible with IGS-RTS products can be reached in https://igs.bkg.bund.de/ntrip/download. Since the SSR corrections are generated as corrections to the navigation message, it is required to import both broadcast ephemeris and SSR correction file. Most the IGS analysis centers generate real-time satellite orbit and clock products for multi-constellation. Furthermore, the SSR message disseminated by some analysis centers includes the ionosphere corrections, which could be applied for eliminating the ionospheric delay for single-frequency code pseudorange positioning. Furthermore, as previously described, it is required to correct TGDs for the single-frequency positioning. So, the DCB file that can be used to derive TGDs should be defined in the data handling step. In this context, the DCB files generated within the IGS MGEX project can be utilized. Finally, the IGS ANTEX file should be specified in this step to correct satellite and receiver PCOs and PCVs.

As regards offline positioning mode which contains the ultra-rapid products, the data handling step similarly starts with the description of real-time observations via an online data stream. In the offline positioning mode, there is no need for any simultaneous connection because of the employment of ultra-rapid products. The latest version of ultra-rapid products can be downloaded via the related FTP addresses, which are described previously, and they should be imported in the data handling step. With the IGS MGEX project, some analysis

centers, e.g. WHU and CODE, disseminate the ultra-rapid products which contain the predicted orbit and clock corrections for multi-GNSS satellites. The ultra-rapid products, unlike the IGS-RTS products, do not contain any correction parameter for the ionospheric delays. Therefore, it is required to define an ionospheric source that could be utilized for real-time GNSS solutions. In this regard, the predicted GIMs provided by some analysis centers can be utilized for the elimination of the ionospheric delay in the single-frequency code pseudorange positioning. In this thesis, the 1-day predicted GIMs generated by CODE are employed since it shows considerably better performance in comparison with the other predicted products provided by different analysis centers (Li et al., 2018). Besides, the MGEX DCB file and IGS ANTEX file should similarly be defined in this step to perform real-time absolute GNSS positioning solutions.

After the data handling, the following steps are quite similar for the two positioning approaches. In the second processing step, namely preprocessing, first the position of satellites at signal transmission time is computed using the corresponding algorithm explained in Section 3.1. Afterward, the observations are determined depending on the selected positioning model. For instance, the C/A code observation on GPS L1 frequency is selected for the single-frequency code pseudorange positioning, dual-frequency ionosphere-free combinations of code and phase observations on GPS L1 and L2 frequencies are adopted for the dual-frequency PPP model. The next operation is the basic quality check step which detects and eliminates the gross errors in observations along with the satellite orbits and clock corrections. Then, the elevation angles of the satellites are computed and the satellites with a smaller elevation angle than the cut-off angle are eliminated. The cycle slips are detected for the positioning models which include the carrier phase observations, such as the single-frequency code-phase combination, and dual-frequency PPP.

The next processing step is to model the GNSS error sources depending on the selected positioning models. The GNSS error sources with their mitigation strategies are described in Chapter 3 comprehensively. In this step, the impacts of GNSS error sources are computed according to the corresponding model and they are added to or subtracted from the observations. Although the GNSS error sources are similar for both positioning approaches, it should be mentioned that the satellite APC offset is not applied in the online positioning mode since the IGS-RTS products are generated based on the satellite APC, unlike the ultra-rapid products which refer to the CoM of the satellites. Additionally, regardless of the orbit and clock source, the other error sources can still differ depending on the selected positioning model, which are described in Table 3.2.

In the final processing step, the estimation process is conducted depending on the enhanced filtering method proposed in this thesis. The details of the proposed filtering method that

combines the variance component estimation and robust Kalman filtering are provided in Section 5.1. Herein, it should be mentioned that the estimated parameters can vary depending on the applied positioning models which are described Section 2.3. A general overview of the proposed positioning approaches is provided in Figure 5.2, including all processing steps.

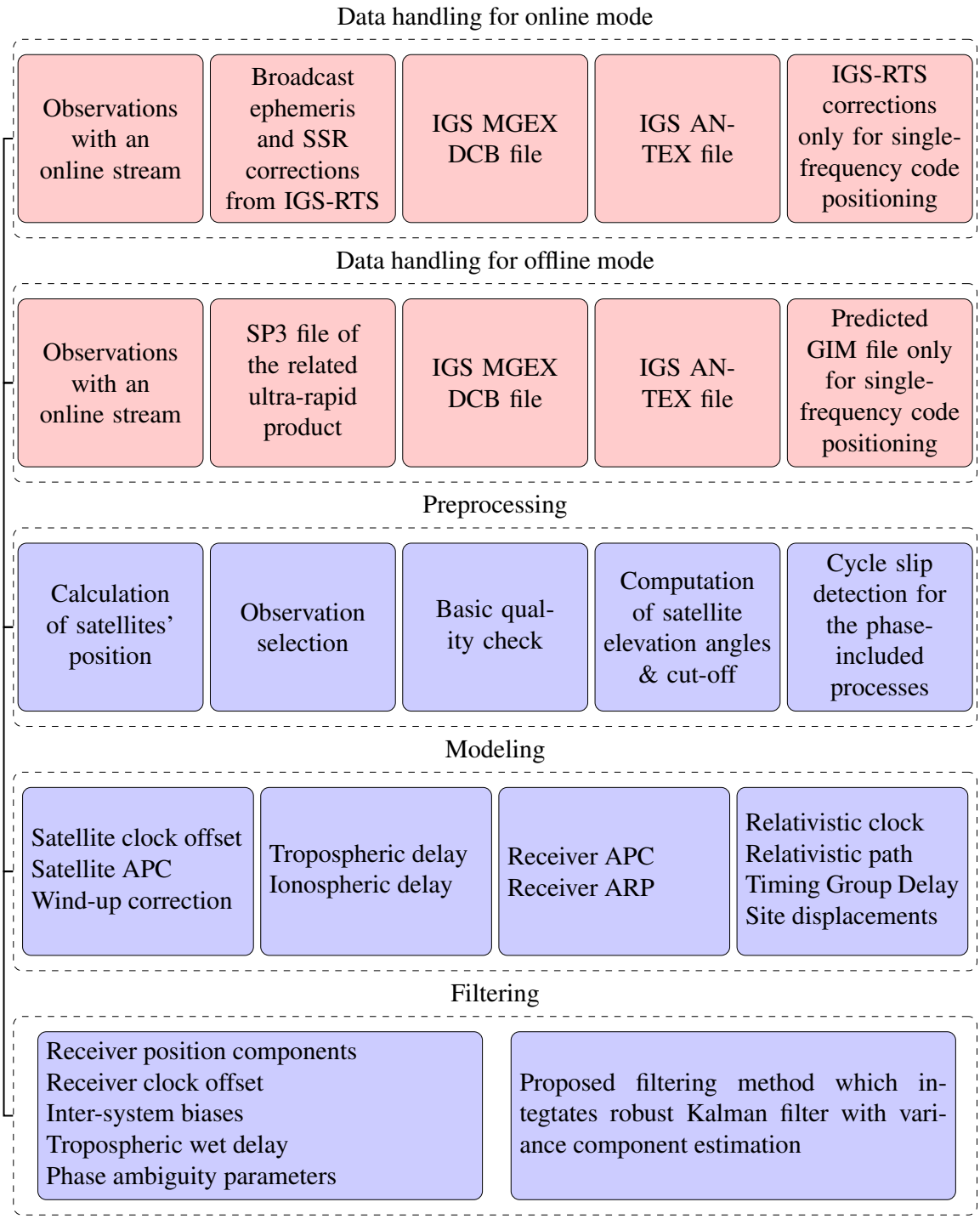

Figure 5.2: General overview of processing steps for the enhanced positioning approaches.

5.3. Software Development

To perform the real-time GNSS absolute positioning solutions based on the proposed positioning approaches, a GNSS analysis software has been developed as part of this thesis. The software, namely PPPH-RT, is an extensive version of PPPH software which is developed by the author as part of his master studies (Bahadur and Nohutcu, 2018). PPPH-RT is able to conduct real-time absolute GNSS positioning using multi-GNSS satellites. The software is developed as being completely compatible with the enhanced positioning approaches which are described in Section 5.2. Thus, both ultra-rapid and IGS-RTS products can be employed separately for real-time absolute positioning techniques, that are the single-frequency code pseudorange positioning, single-frequency code-phase combination, and dual-frequency PPP. This section introduces the PPPH-RT software package taking its comprehensive functionalities into consideration.

PPPH-RT follows the fundamental processing steps provided in Section 5.2, and it consists of five main processing tabs, which are data importing, preprocess&modeling, atmosphere, filtering options, and analysis. In the first processing tab (Figure 5.3), primarily the orbit and clock source is to be selected. As well as the IGS-RTS and ultra-rapid products, broadcast ephemeris is also provided as an option to be able to perform the basic navigation process, that is SPP solution. Secondly, the processing mode, which provides three options for the absolute GNSS positioning models adopted in this thesis, needs to be chosen in this tab. The remaining options from the navigation files to be defined to processing parameters will be specified based on the selections for orbit and clock source, and processing mode. As regards the navigation files, i.e. observation, DCB, and antenna files should be defined regardless of the options selected for the orbit and clock source, and the processing mode. Navigation file requires to be identified for the broadcast ephemeris and real-time corrections options, while SSR file which contains the IGS-RTS SSR corrections should be defined only when real-time corrections option is chosen. Furthermore, it is required to specify the ionosphere source if single-frequency code observation is selected for the process. At this point, there are two options. First, the ionosphere parameters provided within the SSR corrections can be applied for the mitigation of the ionospheric delay. As an alternative, the predicted GIMs can be employed for the single-frequency code pseudorange positioning. However, it is necessary to specify the related IONEX file to apply the second option. Finally, the data importing tab provides a system selection option to specify which navigation systems will be included in the positioning process. In this option, the four systems can be selected separately, while their combinations can be defined for the processes. Consequently, the data importing step is fundamentally utilized for the definition of navigation files and processing strategies to be applied for the positioning process.

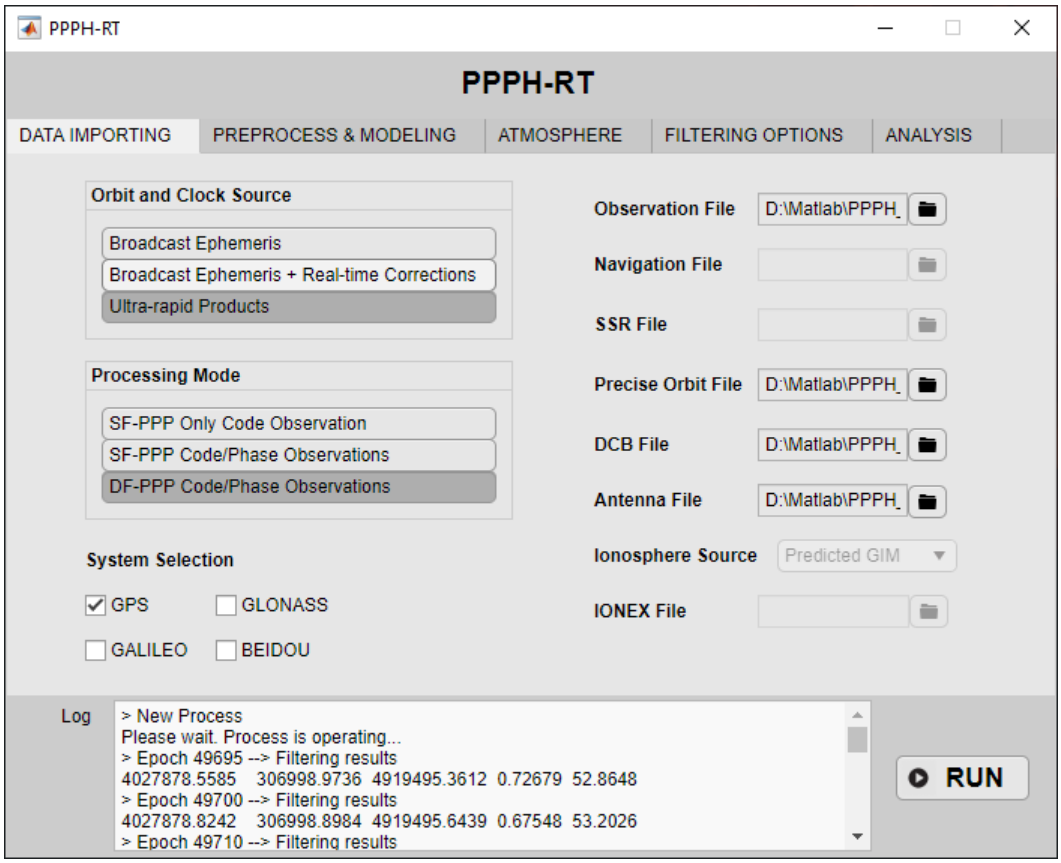

Figure 5.3: General overview and data importing tab of PPPH-RT software.

The preprocess&modelling tab that is illustrated in Figure 5.4 allows the user to select preprocessing options and modeling corrections to be applied in the processes. Elevation cut-off angle can be defined in this tab as well as the option of whether to apply the cycle slip detection for phase observations. The cycle slip detection process is able to be employed only for the positioning techniques which contain carrier phase observations, i.e. single-frequency code-phase combination and dual-frequency PPP. In this tab, numerous options are provided for the selection of modeling corrections. The available corrections are completely related to the selected positioning model described comprehensively in Table 3.2. Finally, the processing mode can be selected as static or kinematic in this stage, which defines how the filtering process to be performed.

The atmosphere tab (Figure 5.5) provides various options for the atmospheric corrections, including tropospheric and ionospheric delays. While the tropospheric corrections are commonly employed for the whole positioning techniques, the ionosphere is required to be corrected for only the single-frequency code pseudorange positioning. PPPH-RT is able to correct the tropospheric delay on the GNSS signals using both Saastamoinen and Modified Hopfield models as explained in Section 3.4. For these troposphere models, the required atmospheric parameters can be acquired from GPT2 and GPT3 models as well as the in-situ measurements. If the in-situ measurements are selected, it is necessary to define the cor-

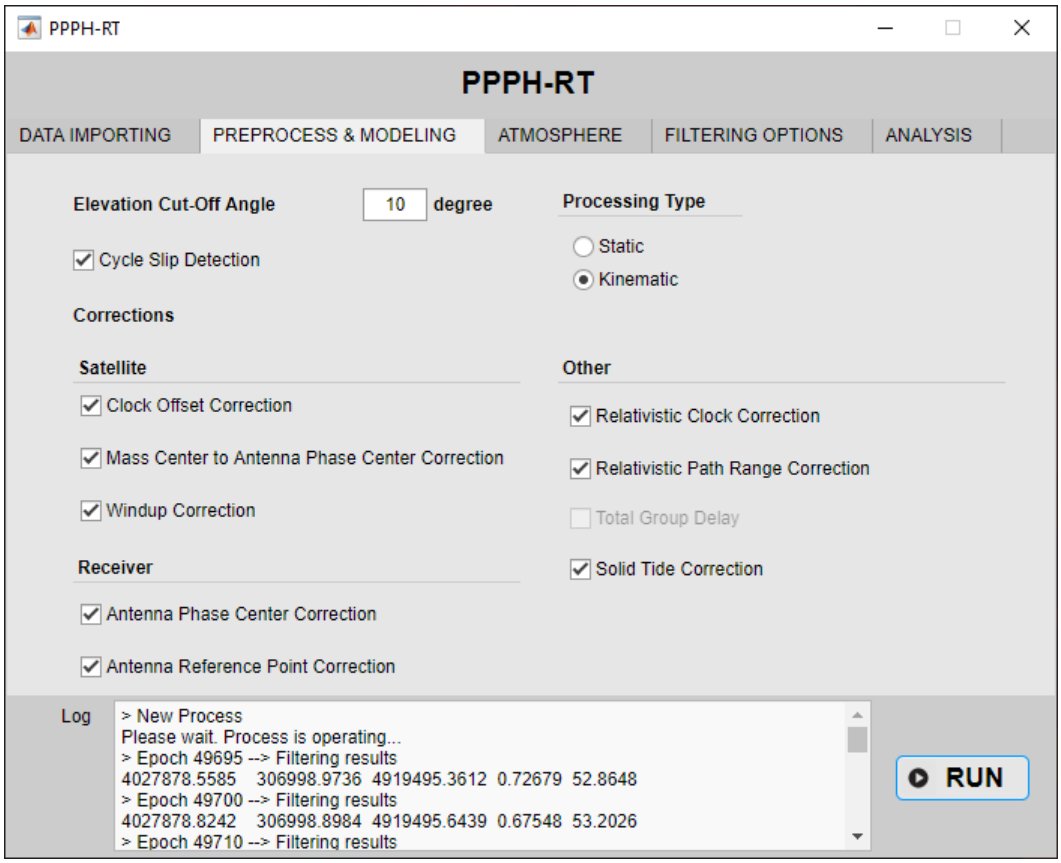

Figure 5.4: Preprocess&modelling tab of PPPH-RT software.

responding meteorological file collected at the GNSS station. Moreover, there exist three options for the tropospheric mapping function, which are VMF1, VMF, and GMF (Section 3.4). Besides, the gridded tropospheric products of VMF1 and VMF3 can be selected for the correction of the tropospheric delay on GNSS signals.

The filtering options tab, which is provided in Figure 5.6, is composed of several processing options for the filtering estimation. PPPH-RT adopts the enhanced filtering method which combines the variance component estimation and robust Kalman filtering as described in Section 5.1. In this regard, PPPH-RT allows users to define the parameters of the filtering process via the filtering options tab. For estimated parameters that can alter depending on the selected processing model, the initial and process uncertainties can be specified in the filtering options tab. Moreover, a priori position can be defined from the RINEX file, while a user-defined position can be employed as the initial position. In order to specify the measurement noises, there exist two numerical fields for code and phase observations in this tab. Finally, as compatible with the proposed filtering approach, there is an option to employ the variance component estimation for multi-GNSS measurements. Alternatively, the constant initial variance ratio method can be adopted for the multi-GNSS process by defining the user-specified variance ratios.

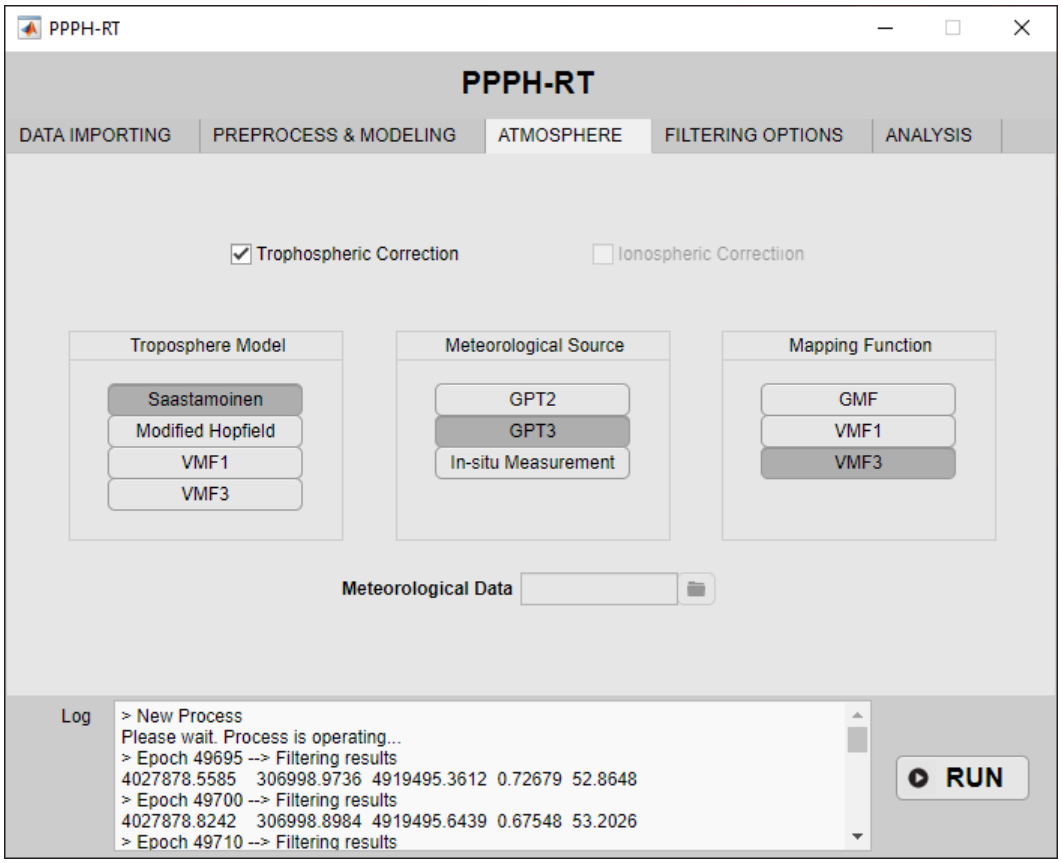

Figure 5.5: Atmosphere tab of PPPH-RT software.

In the final tab of PPPH-RT, namely the analysis tab (Figure 5.7), there are several analysis options to evaluate the positioning performance. According to a ground truth which is defined by the user, positioning error and RMS (root means square) error is computed in the local coordinate system, whose axes are defined to direct the north, east, and up directions, for the related positioning solution. Moreover, a convergence time, which is defined as the epoch when three-dimension positioning error decreases below a user-specified threshold and does not rise above the defined threshold in the following ten epochs, can also be computed for the positioning solution. Herein, the users are able to specify the convergence threshold using the convergence criteria field. Finally, numerous figures about the positioning performance can be plotted using the analysis functionalities provided in this tab, such as positioning errors, receiver clock estimation, satellite numbers, and tropospheric zenith total delay plots (Figure 5.8).

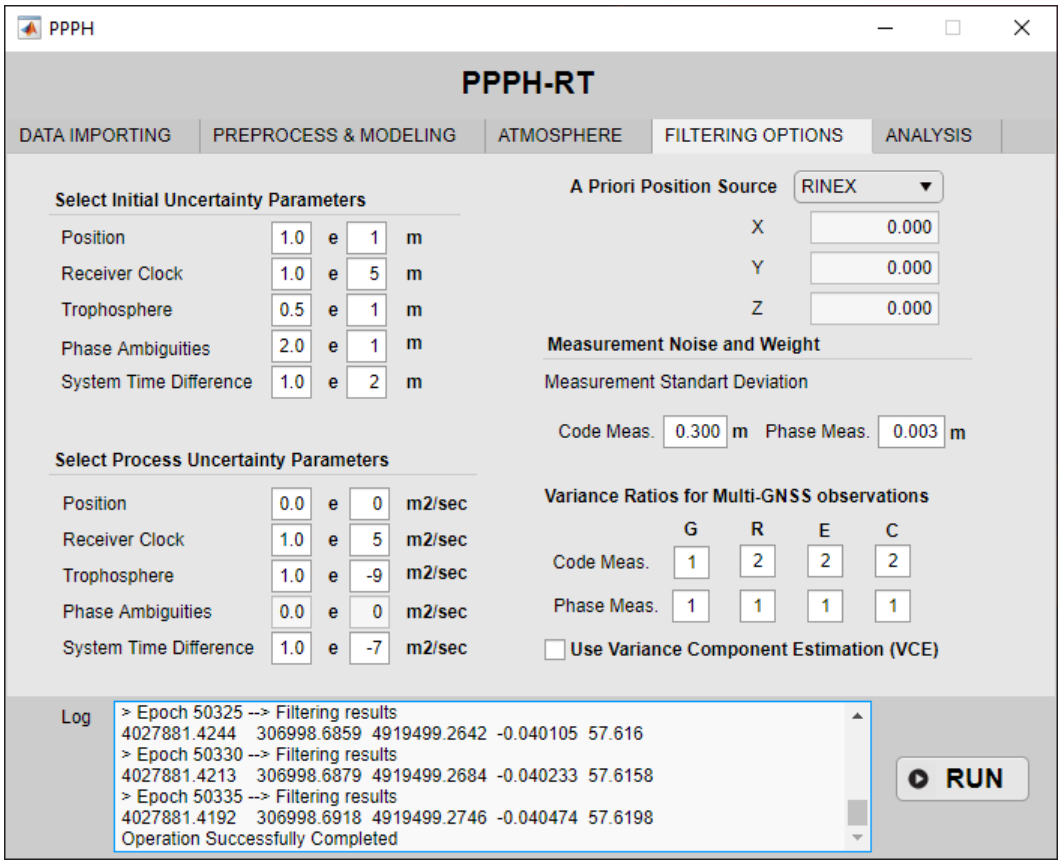

Figure 5.6: Filtering options tab of PPPH-RT software.

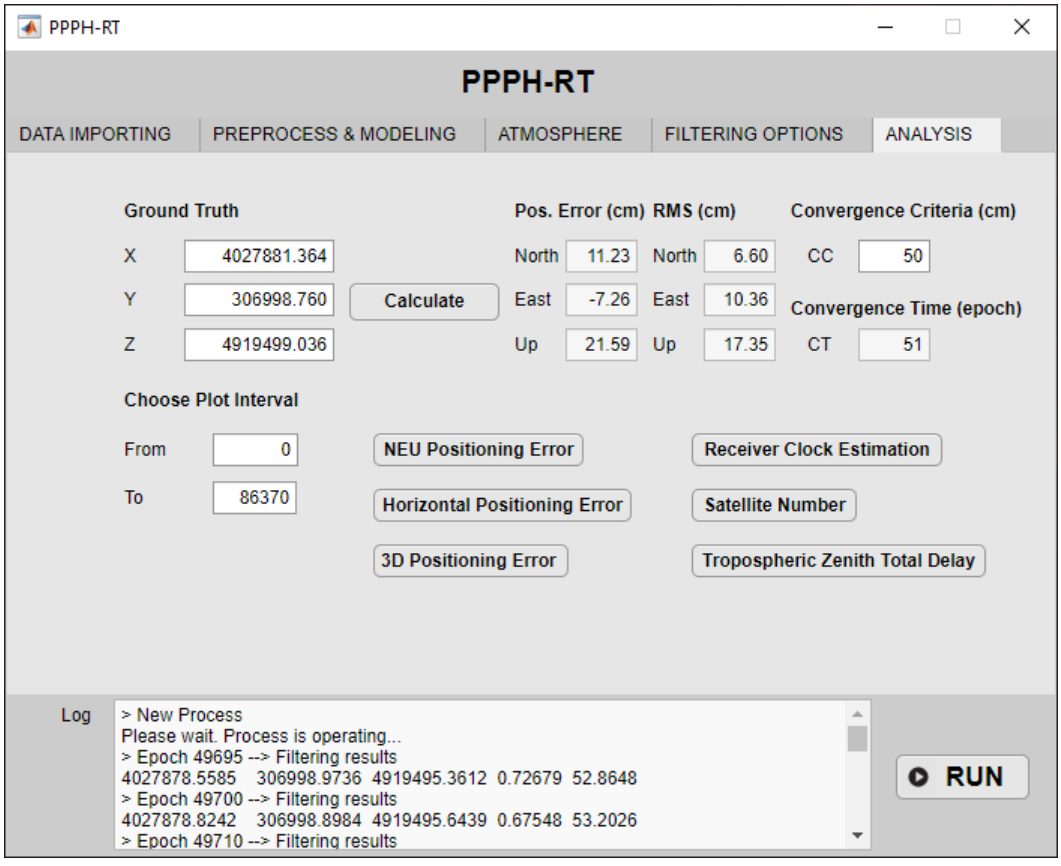

Figure 5.7: Analysis tab of PPPH-RT software.

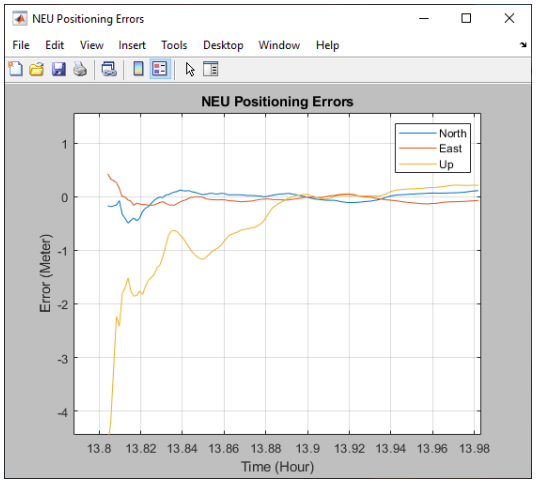

(a) Positioning errors in the north, east and up directions.

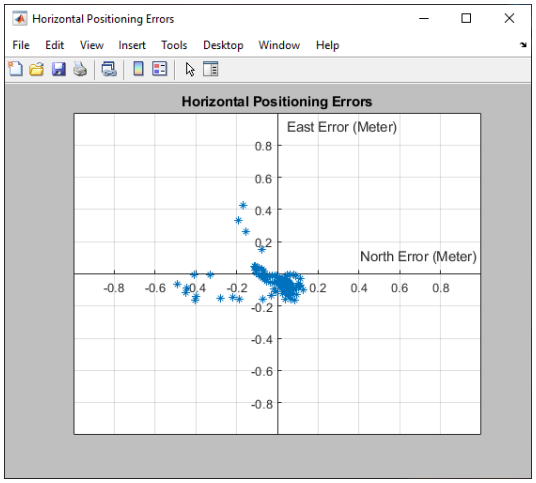

(b) Positioning errors in the horizontal directions.

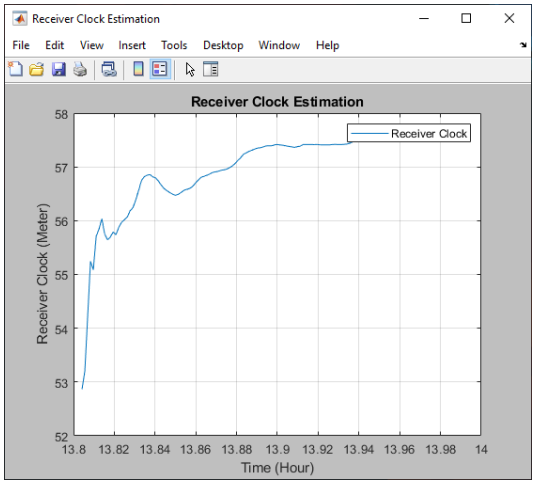

(c) Receiver clock estimation.

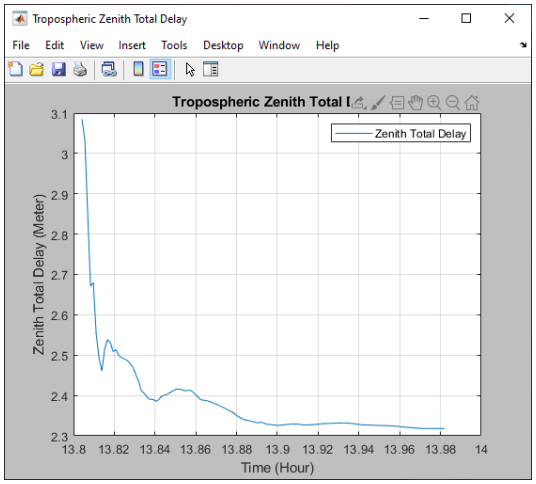

(d) Troposheric zenith total delay.

Figure 5.8: Examples of analysis plots of PPPH-RT.

6. EXPERIMENTAL TESTS, RESULTS AND ANALYSIS

Enhanced positioning approaches for real-time absolute GNSS positioning, together with the proposed filtering method, have been described in the previous chapters comprehensively. The aim of this chapter is to analyze the performance of enhanced positioning approaches in several aspects. In this regard, various experimental tests were performed to evaluate the positioning performance of real-time absolute GNSS positioning techniques that are proposed in this thesis. This chapter provides a detailed description of applied procedures in the experimental tests, results acquired from these experiments, and their performance analysis.

The chapter starts with the description of observation data that are utilized in the experimental tests. Together with the data description, an additional analysis investigating satellite visibility in the observation stations is presented for multi-constellation. Afterward, the positioning performance of SPP, which is the fundamental GNSS positioning approach, is evaluated to demonstrate its current capability and provide the basis for a reasonable comparison with the enhanced positioning approaches. The multi-GNSS solution that contains GPS, GLONASS, Galileo, and BDS constellations is also assessed for the SPP positioning performance in addition to the standard GPS-only SPP solution. On the other hand, the chapter exhibits the results of experimental tests performed to analyze the performance of enhanced positioning approaches proposed in this thesis. Firstly, a comprehensive analysis is performed for real-time absolute GNSS positioning with ultra-rapid products. Herein, three ultra-rapid products generated by different analysis centers are adopted for the performance evaluation test. Secondly, the performance of real-time absolute GNSS positioning techniques which employ IGS-RTS products is also assessed in the chapter. For both analyses, the results of GPS-only and multi-GNSS solutions are provided separately to assess the contribution of multi-constellation to the positioning performance. Finally, this chapter ends with the results of experimental tests conducted for the performance evaluation of the different robust Kalman filter methods and proposed filtering method.

6.1. Data Description and Satellite Visibility

To be used in the experimental tests, the daily observation dataset collected at fifteen IGS stations for a period of two weeks between April 26 and May 9, 2020, was obtained via IGS FTP servers. Global distribution was the main concern for the selection of the stations. The main reason why IGS stations were utilized in the experiments is that their highly precise reference coordinates are provided routinely and therefore the positioning performance can

be measured accurately in these stations. Also, the procedure applied in establishing IGS stations ensures the high quality of GNSS observations, which is mostly independent of the environmental and hardware-induced effects. So, these stations are very apropriate to evaluate the proposed positioning approaches and filtering method. Figure 6.1 illustrates geographical locations of the selected stations. All of the stations are parts of the IGS MGEX network and therefore they are equipped with GNSS receivers that can record the multi-GNSS observations. The receiver and antenna types of the selected stations are provided in Table 6.1. Additionally, the sampling interval of the observation dataset is 30 seconds. At this point, it should be mentioned that the observation data was acquired in post-processed mode, however, all positioning processes were performed in a totally real-time environment where the navigation data, i.e. observations, orbits and clock corrections, ionospheric data, etc., were processed epoch by epoch compatible with real-time positioning. Also, the kinematic mode, with a spectral density of $10^1\ m^2 s^{-1}$, was adopted in the processing of all positioning solutions since single-frequency receivers mostly require kinematic or dynamic positioning conditions.

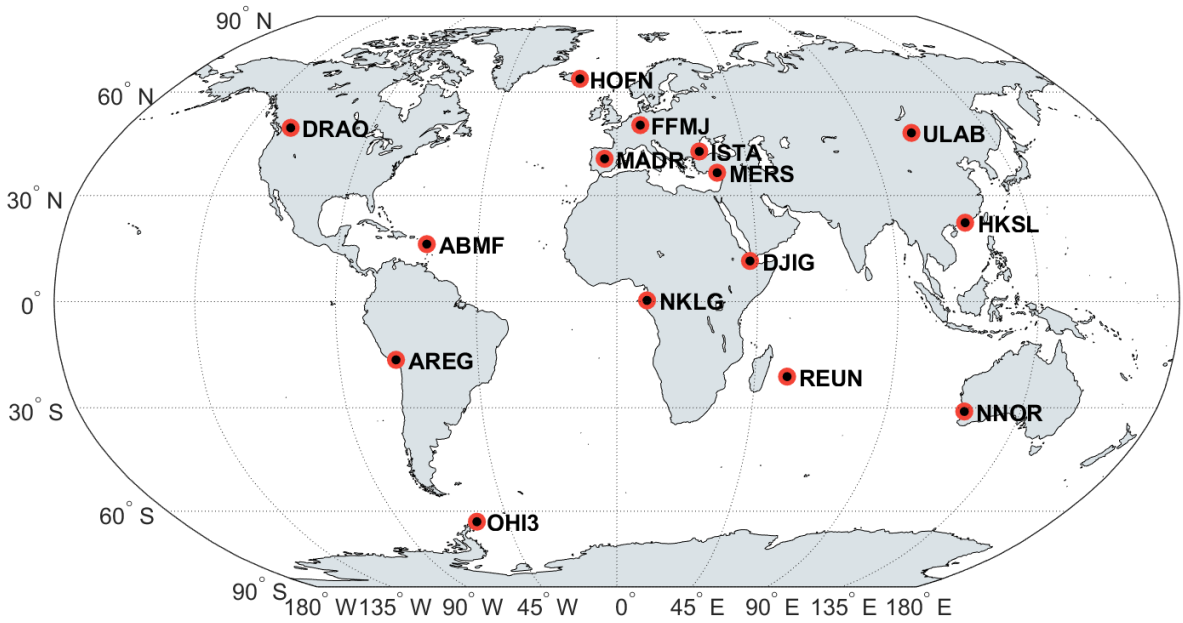

Figure 6.1: Geographical locations of the selected IGS MGEX stations.

On the other hand, satellite visibility is one of the critical factors for absolute GNSS positioning techniques because the number and geometry of available satellites considerably affects the positioning performance that could be acquired from these techniques. Therefore, the visibility of four-constellation, i.e. GPS, GLONASS, Galileo, BDS, at the selected stations is firstly investigated in this section before providing the positioning results. Figure 6.2 indicates the minimum, maximum and average visible satellite numbers per epoch for GPS, GLONASS, Galileo, and BDS constellations at the related stations during the ob-

Table 6.1: GNSS receiver and antenna types of the utilized stations.

Station	Receiver Type	Antenna Type
ABMF	SEPT POLARX5	TRM57971.00 NONE
AREG	SEPT POLARX5	TRM59800.00 NONE
DJIG	SEPT POLARX5	TRM59800.00 NONE
DRAO	SEPT POLARX5	TRM59800.00 SCIS
FFMJ	JAVAD TRE_3 DELTA	LEIAR25.R3 LEIT
HKSL	LEICA GR50	LEIAR25.R4 LEIT
HOFN	LEICA GR50	LEIAR25.R4 LEIT
ISTA	LEICA GR25	LEIAR25.R4 LEIT
MADR	JAVAD TRE_G3TH	AOAD/M_T NONE
MERS	LEICA GR50	LEIAR10 NONE
NKLG	SEPT POLARX5	TRM59800.00 SCIS
NNOR	SEPT POLARX5TR	SEPCHOKE_B3E6 NONE
OHI3	LEICA GR50	LEIAR25.R4 LEIT
REUN	SEPT POLARX5	TRM55971.00 NONE
ULAB	JAVAD TRE_3	JAVRINGANT_G5T NONE

servation period. The numbers were obtained by taking each observation epoch into account over the two-week period, that is 40320 individual epochs. Minimum and maximum numbers represent the fewest and greatest satellite numbers that appear during the observation period, while the average number is computed as the mean of satellite numbers considering all epochs. In the figure, satellite visibility is analyzed for every station separately because it is closely related to the geographical location of the observation site.

From Figure 6.2, it can be observed that the minimum satellite numbers are not under 5 for the GPS constellation considering all stations, while maximum satellite numbers can reach 13 at DJIG, HOFN, and NKLG stations. For GPS satellites, the average number per epoch ranges from 8.1 to 10.2 for the selected stations. Average satellite number exceeds 10 at DJIG and NKLG stations, which is not surprising because the design of GPS constellation offers a greater satellite number near the equatorial region. For the GLONASS constellation, the figure shows that minimum satellite number can drop 2 at the specific epochs taking all stations into account, while maximum number can reach 10 satellites for most of the utilized stations. Their average number per epoch is between 4.2 and 7.3 for the related stations. It can be said that there is no considerable difference between the stations in terms of average GLONASS satellites except for MERS station. When it comes to the satellite visibility of Galileo constellation, it can be observed that the minimum number is between 1 and 3, whereas the maximum number ranges from 7 to 11 considering all stations. For the Galileo constellation, the average number per epoch varies from 4.1 to 7.7 for the utilized stations. As regards the BDS constellation, excluding DRAO station, the minimum number of visible satellites can drop to 2 for three stations, while the maximum number can reach 19 at NNOR station. Their average number per epoch ranges from 5.7 to 14.5 excluding DRAO station.

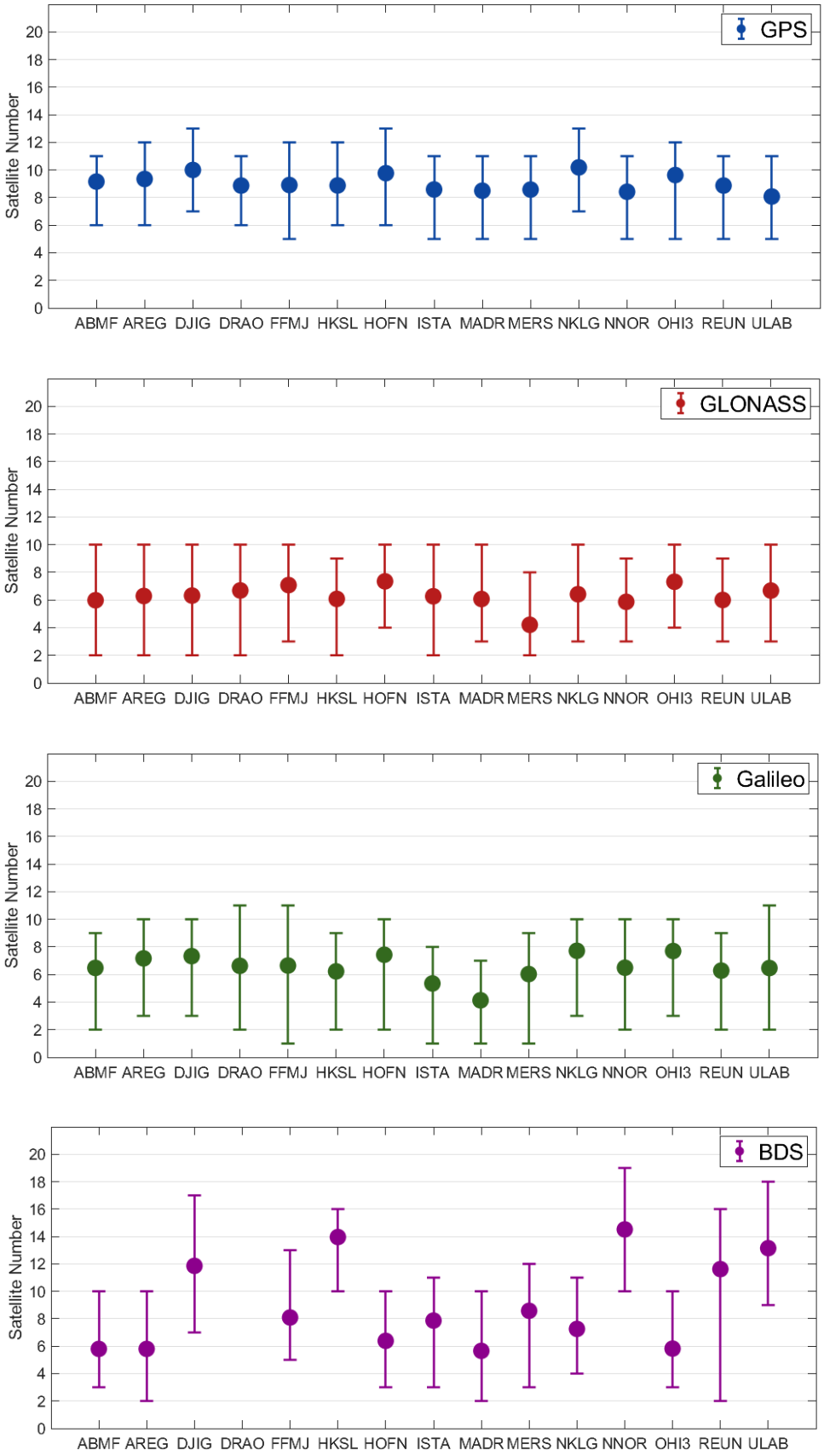

Figure 6.2: Minimum, average and maximum numbers of visible GPS, GLONASS, Galileo and BDS satellites per epoch in the selected stations.

Herein, it should be mentioned that observation files of DRAO station do not contain any observations of BDS satellites because of the receiver type. On the other hand, the station is located in North America which is one of the weakest regions in terms of satellite availability for the BDS constellation (Wang et al., 2019b). The average number of visible BDS satellites exceeds 14 at HKSL and NNOR stations which are located in the Asia-pacific region. This is mainly because the BDS constellation is designed to provide maximum satellite visibility in the Asia-pacific region owing to the geostationary BDS satellites.

Furthermore, Figure 6.3 demonstrates probability distributions of visible satellites per epoch for the GPS, GLONASS, Galileo, and BDS constellations, separately. In Figure 6.3, probability distributions are calculated considering the visible satellite numbers at all epochs of the two-week period for all utilized stations, which equals 604800 epochs in total. The figure also shows the means of visible satellite numbers for each constellation. These numbers were calculated as 9.1, 6.2, 6.5, and 9.0 for GPS, GLONASS, Galileo, and BDS. The results show that GPS is still the dominant navigation constellation on the global scale in terms of satellite visibility, while the other systems offer considerable satellite resources for positioning, navigation, and timing purposes. Especially, BDS has recently expanded its constellation with advances in the BDS-3 program. Consequently, the integration of multi-constellation, that is multi-GNSS, opens up substantial probabilities to augment the performance of GNSS applications.

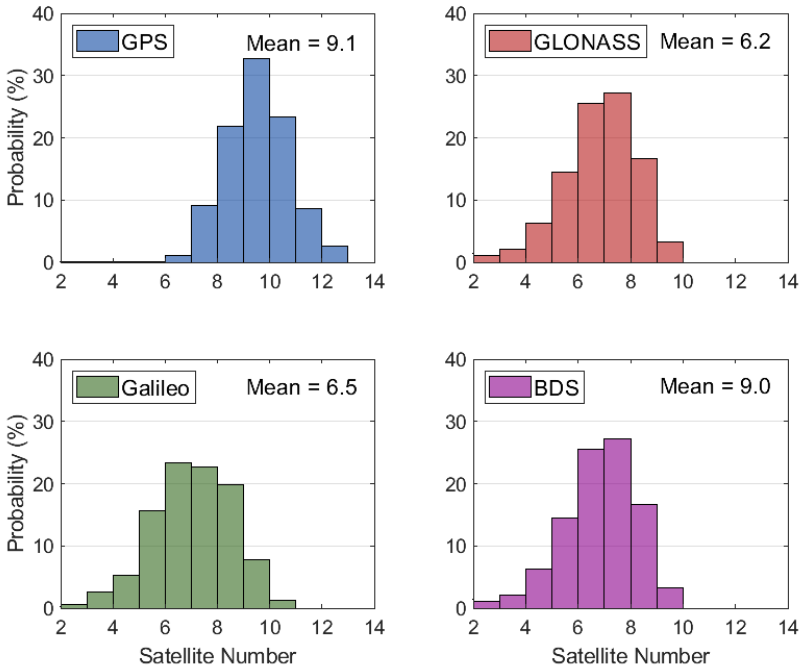

Figure 6.3: Distributions of the visible satellite numbers for GPS, GLONASS, Galileo and BDS constellations.

6.2. Performance Analysis of Standard Point Positioning (SPP)

As the fundamental GNSS positioning concept, SPP employs single-frequency code pseudorange observations together with broadcast ephemeris. Basically, SPP can be assumed as an absolute positioning technique. As previously described, the positioning performance of SPP is first evaluated to understand its current capability and provide a solid base for a reasonable comparison with enhanced positioning approaches proposed in this thesis. Firstly, the observation dataset introduced in the previous section was processed under the SPP scenario including only GPS satellites. To assess the contribution of multi-constellation, the same dataset was also processed as containing GPS, GLONASS, Galileo, and BDS satellites in the multi-GNSS SPP scenario. Herein, it should be mentioned that own broadcast ephemeris for each navigation system was utilized to acquire satellite orbits and clock corrections in addition to the broadcast-based ionospheric parameters, i.e. Klobuchar model (Klobuchar, 1987). Additionally, the differences between navigation systems, i.e. time-scale, reference frame, signal structure, etc., were taken into consideration for the multi-GNSS processes. Applied processing strategy is presented in Table 6.2 comprehensively.

Table 6.2: Processing strategies for the SPP solution.

Item	**Processing strategy**
Observations	Code pseudorange observations on L1 for GPS and GLONASS, E1 for Galileo, B1 for BDS
Satellite orbit and clock source	Broadcast ephemeris
Dry part of troposphere	Corrected using Saastamoinen (Saastamoinen, 1972) model with the GPT3 and VMF3 (Landskron and Böhm, 2018)
Wet part of troposphere	Not corrected or estimated
Ionosphere	Broadcast-based ionosphere model
TGD	Corrected with the broadcast ephemeris (Section 3.2)
Relativistic clock error	Corrected (Section 3.3)
Relativistic path error	Not corrected
Satellite antenna PCOs and PCVs	Not corrected
Receiver antenna PCOs and PCVs	Not corrected
Receiver antenna reference point	Corrected (Section 3.6)
Carrier wind-up	Not corrected
Cycle slip detection	Not implemented
Site displacement effects	Not corrected
Standard deviations of observations	0.3 m for code pseudoranges
Initial ratios of multi-GNSS observations	$\sigma^2_{P_1^G} : \sigma^2_{P_1^R} : \sigma^2_{P_1^E} : \sigma^2_{P_1^C} = 1 : 2 : 2 : 2$
Observation weights	Elevation dependent
Adjustment method	Robust Kalman filter with improved IGG III function (Section 4.3.1)

The results which are obtained from the SPP processes were evaluated in terms of positioning

performance. In this regard, the positioning error computed as the coordinate difference between that obtained from the related positioning process (X_P, Y_P, Z_P) and ground truth (X_G, Y_G, Z_G) was employed to indicate the positioning accuracy. Precise station coordinates disseminated by IGS in its weekly solution (SINEX format) were assumed to be ground truth and for each epoch, the positioning errors ($\Delta\mathbf{X}$) were calculated in the local coordinate system whose axes point towards the north, east, and up directions $(\Delta_n, \Delta_e, \Delta_u)$ as follows:

$$\Delta\mathbf{X}_{local} = \begin{bmatrix} \Delta_n & \Delta_e & \Delta_u \end{bmatrix}^T = \mathbf{A}^{-1} \cdot \Delta\mathbf{X} \tag{6.1}$$

with

$$\Delta\mathbf{X} = \begin{bmatrix} X_P - X_G \\ Y_P - Y_G \\ Z_P - Z_G \end{bmatrix}, \quad \text{and} \quad \mathbf{A} = \begin{bmatrix} -\sin\varphi\cos\lambda & -\sin\lambda & \cos\varphi\cos\lambda \\ -\sin\varphi\sin\lambda & \cos\lambda & \cos\varphi\sin\lambda \\ \cos\varphi & 0 & \sin\varphi \end{bmatrix} \tag{6.2}$$

where φ and λ indicate the ellipsoidal latitude and longitude of the observation station, respectively. On the other hand, the north and east directions constitute the horizontal component of the total positioning error, while the only up direction is the vertical component of the total error. Additionally, three-dimensional (3D) positioning error is utilized to represent the total amount of positioning error. These positioning errors are expressed as follows:

$$\Delta_{horizontal} = \sqrt{\Delta_n^2 + \Delta_e^2}, \quad \Delta_{vertical} = \Delta_u \tag{6.3}$$

$$\Delta_{3D} = \sqrt{\Delta_n^2 + \Delta_e^2 + \Delta_u^2} \tag{6.4}$$

To evaluate the positioning accuracy statistically, the root mean square (RMS) error is also employed in this thesis. For any component of the positioning error, the RMS error is calculated as:

$$RMS = \sqrt{\frac{\sum_{i=1}^{n} \Delta_i^2}{n}} \tag{6.5}$$

where Δ_i is the related positioning error for *i*th observation, n is the observation number.

Considering epoch-wise SPP solutions in 15 stations over a two-week period, Figure 6.4 depicts probability distributions of positioning errors computed for the GPS-only and multi-GNSS SPP solutions in the local coordinate system. The figure shows probability percentages which are calculated as the ratio of error frequencies to the total number of epochs rather than actual error frequencies. That is, the positioning solutions in a total of 604800 epochs were considered when a probability distribution was prepared (daily 2880 individual

epochs for 30-s sampling interval). The figure also indicates RMS and mean values for each positioning component, respectively. The mean values were computed as the absolute mean error. Since RMS values are statistically more sensitive to dispersion, they are mostly greater than mean values as expected. As shown in the figure, the mean and RMS errors in the up direction are considerably greater than those calculated for horizontal positioning components. RMS values are calculated as 3.487, 3.588, and 6.876 m in the north, east and up directions for the GPS-only solution. These numbers are 2.566, 3.045, and 5.184 m for the multi-GNSS solution, which means it provides a better position accuracy than the GPS-only solution by 26.4%, 15.1%, and 24.6% in the north, east, and up directions.

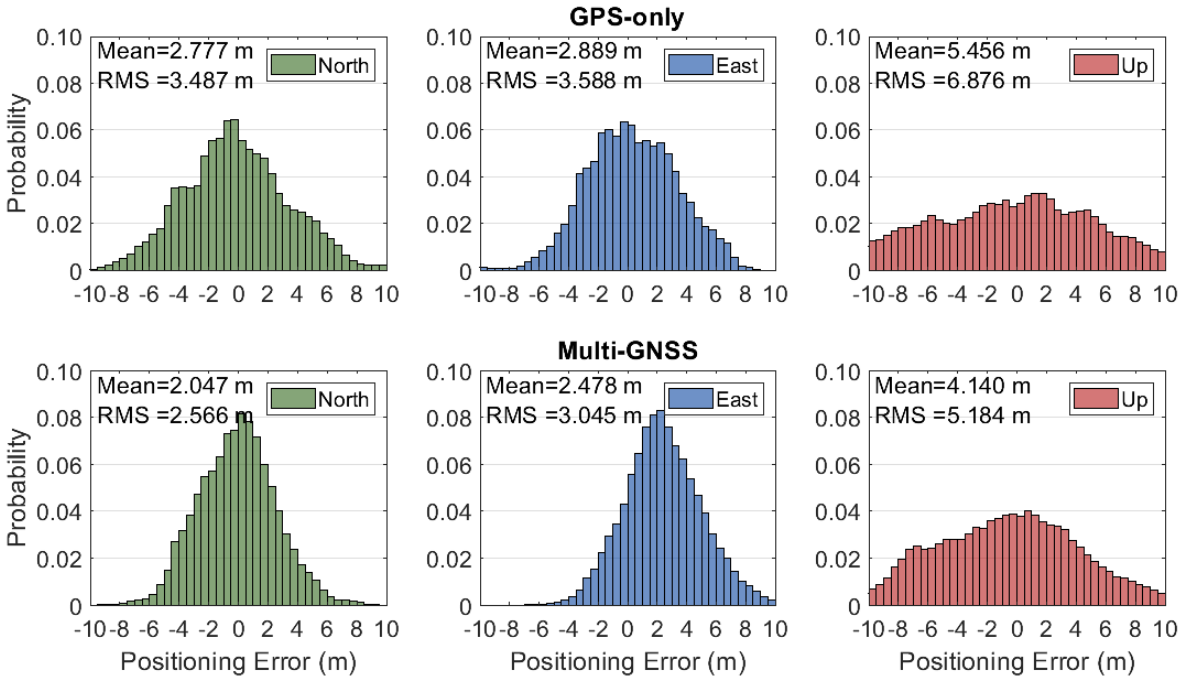

Figure 6.4: Probability distributions of positioning errors for the GPS-only and multi-GNSS SPP solutions.

In addition, Figure 6.5 presents temporal variation of 3D RMS values for the GPS-only and multi-GNSS SPP solutions. For any epoch in the figure, the RMS error was calculated considering the whole individual positioning solutions. In other words, 210 different daily positioning solutions of 15 stations over a two-week period were employed to compute the RMS error at any specific epoch. It can be observed from the figure that 3D RMS values alter between 4.782 and 9.793 m for the GPS-only solution. Similarly, 3D RMS values range from 4.872 to 7.511 m for the multi-GNSS solution. As shown in the figure, there is not any important time-dependent correlation for the SPP solutions. It is also apparent from the figure that except for a few epochs in the first minutes, the positioning performance of the multi-GNSS solution is substantially better than that of the GPS-only solution. Therefore, it can be said that the positioning performance of SPP is considerably augmented with the integration of multi-GNSS.

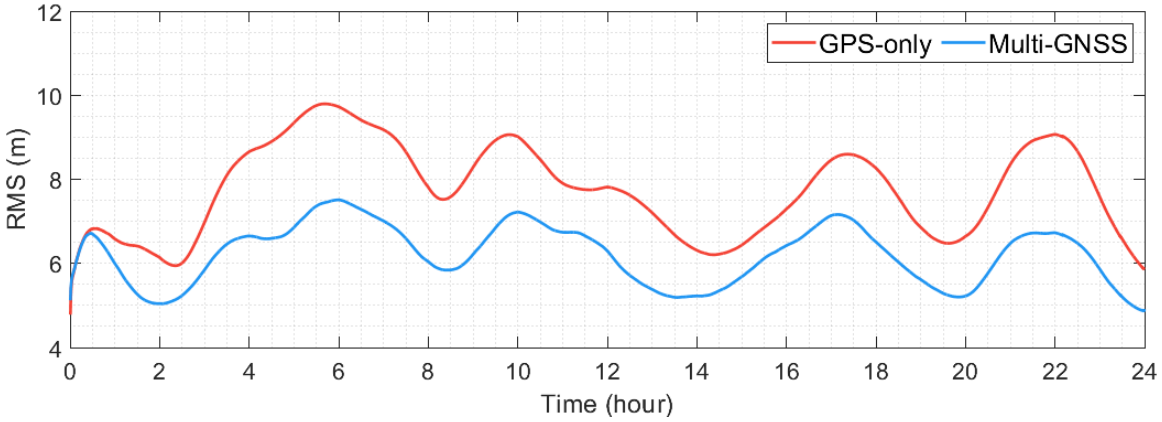

Figure 6.5: Temporal variation of 3D RMS errors for the GPS-only and multi-GNSS SPP solutions.

Table 6.3 demonstrates the station-based RMS values of horizontal, vertical, and 3D positioning errors computed for the GPS-only and multi-GNSS SPP solutions. Also, the average RMS values of horizontal, vertical, and 3D positioning errors computed for taking all stations into consideration are provided in the table. For the GPS-only solution, horizontal RMS errors change between 3.250 and 5.924 m for the stations, while vertical RMS errors range from 4.084 and to 11.945 m. Also, 3D RMS errors are between 5.449 and 12.402 m considering all stations. The average RMS values are 4.658, 6.876, and 7.821 m for horizontal, vertical, and 3D positioning errors, which reflect the positioning accuracy acquired from the GPS-only SPP solution.

Table 6.3: Station-based RMS values of horizontal, vertical, and 3D positioning errors for the GPS-only and multi-GNSS SPP solutions (in:m).

Station	**GPS-only**			**Multi-GNSS**		
	Horizontal	**Vertical**	**3D**	**Horizontal**	**Vertical**	**3D**
ABMF	4.480	7.335	8.164	3.394	5.499	6.133
AREG	4.635	6.484	7.469	3.837	4.479	5.430
DJIG	4.171	11.945	12.402	3.688	6.294	6.951
DRAO	4.872	5.555	6.786	5.732	4.451	6.390
FFMJ	3.981	6.772	7.484	3.921	4.956	5.865
HKSL	4.707	9.937	10.627	4.481	8.023	8.787
HOFN	3.250	8.093	8.501	2.495	5.793	6.127
ISTA	4.650	4.870	6.128	5.269	4.929	6.486
MADR	4.119	7.606	8.289	4.031	6.035	6.843
MERS	4.723	4.725	6.050	4.099	4.428	5.510
NKLG	4.836	4.917	6.256	3.363	4.513	5.254
NNOR	5.303	6.180	7.496	4.438	4.872	6.029
OHI3	3.639	4.606	5.449	3.206	3.138	4.052
REUN	5.779	4.084	6.169	6.815	4.132	6.841
ULAB	5.924	5.026	6.908	4.897	4.374	5.872
ALL	4.658	6.876	7.821	4.376	5.184	6.255

On the other hand, horizontal RMS errors are between 2.495 and 6.815 m, whereas vertical RMS errors vary between 3.138 and 8.023 m for the multi-GNSS SPP solution. Furthermore, 3D RMS errors range from 4.052 to 8.787 m when all stations are considered. For the multi-GNSS solution, the average RMS values of horizontal, vertical, and 3D positioning errors are calculated as 4.376, 5.184, 6.255 m, respectively. Excluding ISTA and REUN stations where the GPS-only solution presents slightly better positioning performance, the multi-GNSS solution significantly enhances the positioning performance of SPP for all stations. Taking all stations into consideration, the improvement ratios of the multi-GNSS solution are 6.1%, 24.6%, and 20.0% on average for horizontal, vertical, and 3D positioning errors, respectively. It can be stated that the improvement ratio of the multi-GNSS solution in the vertical component is remarkable, while the horizontal positioning performance is quite similar for both solutions.

6.3. Performance Analysis of Real-time Absolute GNSS Positioning with Ultra-rapid Products

This section presents the performance evaluation of real-time absolute GNSS positioning using ultra-rapid precise products. The performance analysis involves three absolute GNSS positioning techniques adopted in this thesis, i.e. the single-frequency code pseudorange positioning, single-frequency code-phase combination, and dual-frequency PPP. As previously described, there are different ultra-rapid products generated by several analysis centers. As a part of this thesis, three ultra-rapid products provided in Table 3.1, namely CODE, IGS, and WHU products, are employed for real-time absolute GNSS positioning. By this way, it is also aimed to evaluate the impact of these products, which have distinct characteristics, on the performance of real-time absolute GNSS positioning. Furthermore, two of these products, CODE and WHU, provide orbit and clock corrections for multi-GNSS satellites additionally. To analyze the contribution of multi-constellation, real-time absolute GNSS positioning processes were conducted under the multi-GNSS scenario as well as the GPS-only. GPS, GLONASS, and Galileo satellites were included in the multi-GNSS solution when the CODE product was applied, while BDS satellites were also employed besides these three navigation systems when the WHU product was utilized. This is because the CODE ultra-rapid product does not include precise products for BDS satellites.

6.3.1. Single-frequency Code Pseudorange Positioning with Ultra-rapid Products

For the single-frequency code pseudorange positioning, the two-week observation dataset was processed with three ultra-rapid products separately. In the rest of the thesis, these so-

lutions will be named regarding the name of the applied ultra-rapid product. Functional and stochastic models adopted for the single-frequency code pseudorange positioning were described in the previous chapters comprehensively. Besides, the processing strategies applied for the positioning solutions with ultra-rapid products are summarized in Table 6.4. For the performance assesment, the positioning errors specified in the previous section were employed similarly.

Table 6.4: Processing strategies applied for the single-frequency code pseudorange positioning solutions with ultra-rapid products.

Item	**Processing strategy**
Observations	Code pseudorange observations on L1 for GPS and GLONASS, E1 for Galileo, B1 for BDS
Satellite orbit and clock source	Ultra-rapid ephemeris
Dry part of troposphere	Corrected using Saastamoinen (Saastamoinen, 1972) model with the GPT3 and VMF3 (Landskron and Böhm, 2018)
Wet part of troposphere	Estimated
Ionosphere	1-day predicted GIM generated by CODE
TGD	Corrected with IGS MGEX products (Section 3.2)
Relativistic clock error	Corrected (Section 3.3)
Relativistic path error	Corrected (Section 3.3)
Satellite antenna PCOs and PCVs	Corrected with IGS antenna model (Section 3.6)
Receiver antenna PCOs and PCVs	Corrected with IGS antenna model (Section 3.6)
Receiver antenna reference point	Corrected (Section 3.6)
Carrier wind-up	Not corrected
Cycle slip detection	Not implemented
Site displacement effects	Not corrected
Standard deviations of observations	0.3 m for code pseudoranges
Initial ratios of multi-GNSS observations	$\sigma^2_{P_1^G} : \sigma^2_{P_1^R} : \sigma^2_{P_1^E} : \sigma^2_{P_1^C} = 1 : 2 : 2 : 2$
Observation weights	Elevation dependent
Adjustment method	Robust Kalman filter with improved IGG III function (Section 4.3.1)

Considering all epoch-wise positioning solutions at 15 stations over the two-week period, Figure 6.6 depicts probability distributions of positioning errors acquired from the GPS-only positioning processes with CODE, IGS, and WHU ultra-rapid products, respectively. As shown in the figure, positioning errors in the up directions are substantially greater than those in the horizontal directions as expected. From the figure, it can be also observed that, for the GPS-only solution which employs CODE ultra-rapid products, RMS values are 1.167, 0.937, and 2.995 m in the north, east, and up directions, while these numbers are 1.019, 0.796, and 2.564 m for the corresponding solution implementing WHU ultra-rapid products. As regards the GPS-only solution with IGS ultra-rapid products, corresponding RMS errors are 0.906, 0.643, and 2.475 m. Herein, it can be said that average horizontal and vertical positioning errors are not under 1 and 2 m respectively for the real-time single-frequency code pseudorange positioning regardless of the applied ultra-rapid products. Still, the position-

ing accuracy which can be acquired from the GPS-only code pseudorange positioning with ultra-rapid products is considerably better than that of SPP. The results also indicate that the accuracy of real-time GPS-only code pseudorange positioning which utilizes IGS ultra-rapid products are better than the other GPS-only solutions employing CODE and WHU products.

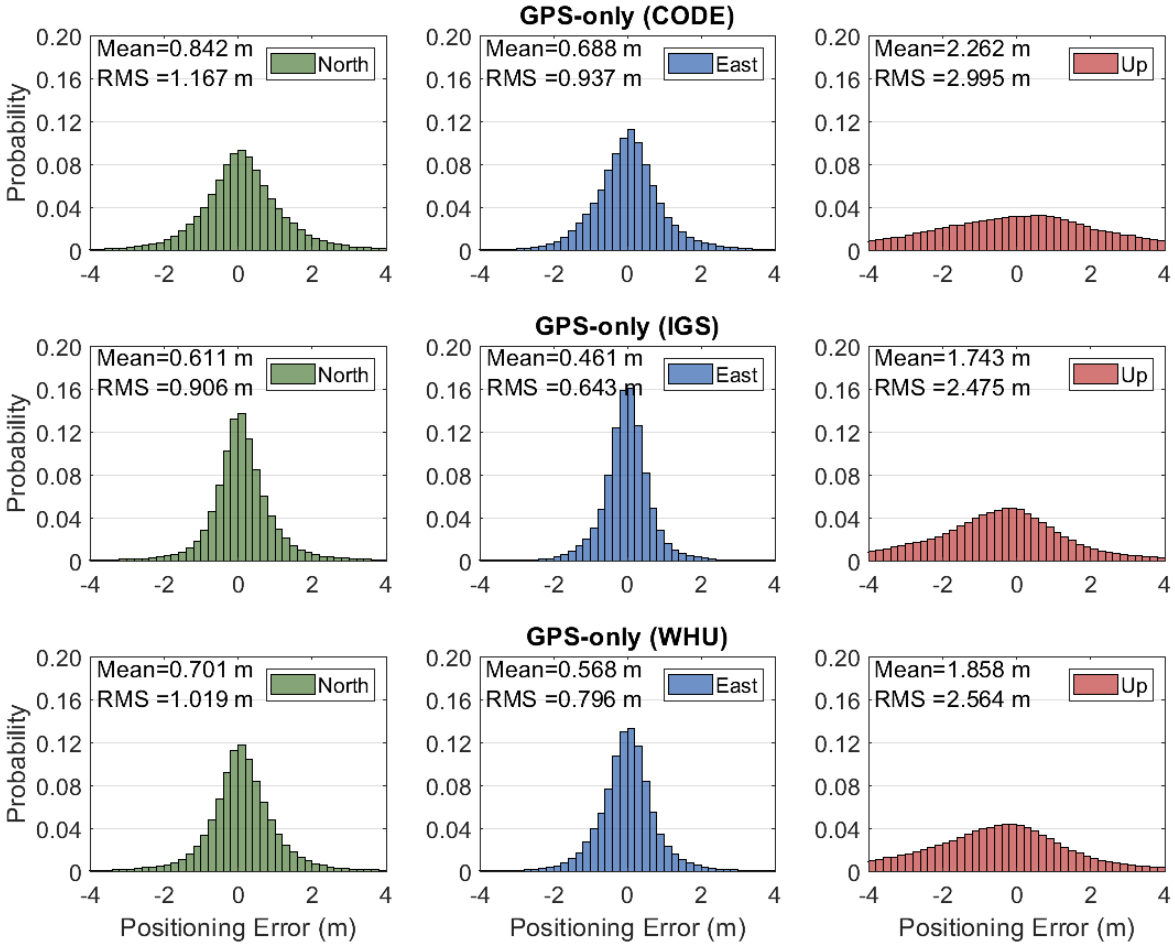

Figure 6.6: Probability distributions of positioning errors for the GPS-only single-frequency code pseudorange positioning solutions with CODE, IGS and WHU ultra-rapid products.

Figure 6.7 presents temporal variation of RMS values computed for 3D positioning errors obtained from the GPS-only solutions with CODE, IGS, and WHU ultra-rapid products. As shown in the figure, the performance of the GPS-only solution with CODE ultra-rapid products is worse than other solutions for very most of the epochs. In the first ten hours, the positioning performance obtained from IGS and WHU ultra-rapid products are quite similar, however, the performance of WHU products gets relatively worse in the following epochs, especially in the last six hours. In the figure, a significant point is that the positioning accuracy of single-frequency code pseudorange positioning deteriorates over time. For example, the average 3D RMS value computed for the GPS-only solution employing CODE products in the first six-hour period is 2.455 m, whereas the corresponding average 3D RMS value is computed as 3.642 m for the last six-hour period, which is worse by 32% approximately.

Similarly, 3D RMS values of the GPS-only solutions with IGS and WHU products are 1.904 and 1.990 m for the first six-hour period, while these numbers are 2.667 and 3.217 m for the last six-hour period respectively. The deterioration of positioning accuracy mostly stems from the potential decrease in the accuracy of ultra-rapid products moving away from the prediction epoch. The growth in the positioning error is more apparent after the sixteenth hour especially for the CODE and WHU solutions, where the IGS solution is more stable for temporal changes. Considering the time-dependent accuracy of the ultra-rapid products, it can be said that the update interval is critical for single-frequency code pseudorange positioning. Consequently, the figure confirms that the positioning solutions where IGS products were applied have the positioning performance better than the other products when 24-hour performances are considered.

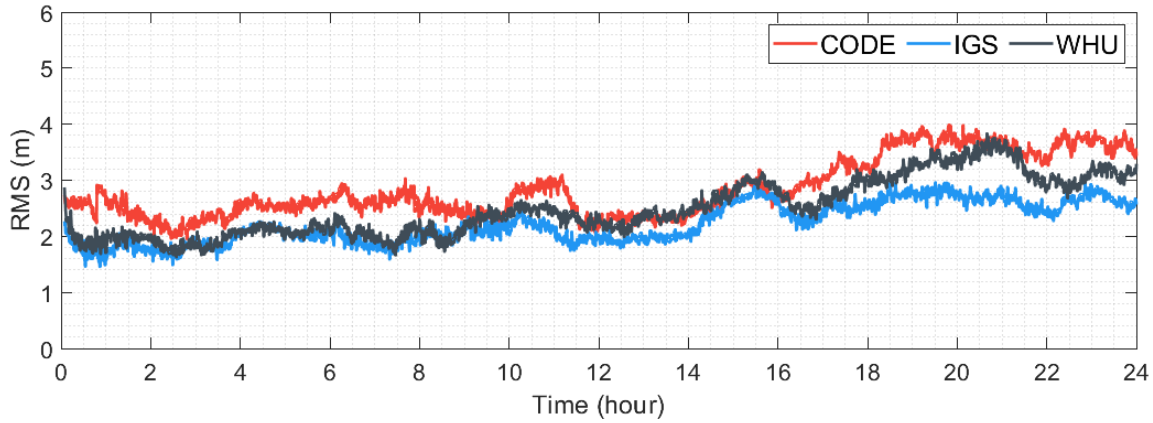

Figure 6.7: Temporal variation of 3D RMS errors for the GPS-only single-frequency code pseudorange positioning solutions with CODE, IGS, and WHU ultra-rapid products.

Figure 6.8 shows probability distributions of positioning errors obtained from the multi-GNSS positioning processes with CODE and WHU ultra-rapid products. Herein, it should be reminded that CODE ultra-rapid products contain orbits and clock corrections for GPS, GLONASS, and Galileo satellites, whereas WHU products include BDS satellites additionally. IGS ultra-rapid products were not included in multi-GNSS processes as they include only GPS satellites. As shown in the figure, the RMS values are computed as 0.937, 0.814 and 2.210 m in the north, east and up directions for the multi-GNSS solution employing CODE ultra-rapid products. When compared with its own GPS-only solution, the multi-GNSS solution with CODE ultra-rapid products augments the positioning performance by 19.7%, 13.1%, and 26.2% in the north, east, and up directions. Also, in comparison to the IGS product which provides the best performance for the GPS-only solution, the multi-GNSS solution with CODE ultra-rapid products enhances the vertical positioning accuracy by 10.7% but does not provide any improvement in the horizontal positioning performance. The multi-GNSS solution utilizing WHU ultra-rapid products has a considerably better performance than all GPS-only solutions. In the comparison with the GPS-only solution with

IGS ultra-rapid products, the multi-GNSS solution which employs WHU products augments the positioning accuracy by 19.4%, 3.6%, and 29.8%, respectively. Besides, from the figure, it is apparent that the multi-GNSS solution with WHU ultra-rapid product presents substantially better positioning performance in comparison to the multi-GNSS solution employing CODE product.

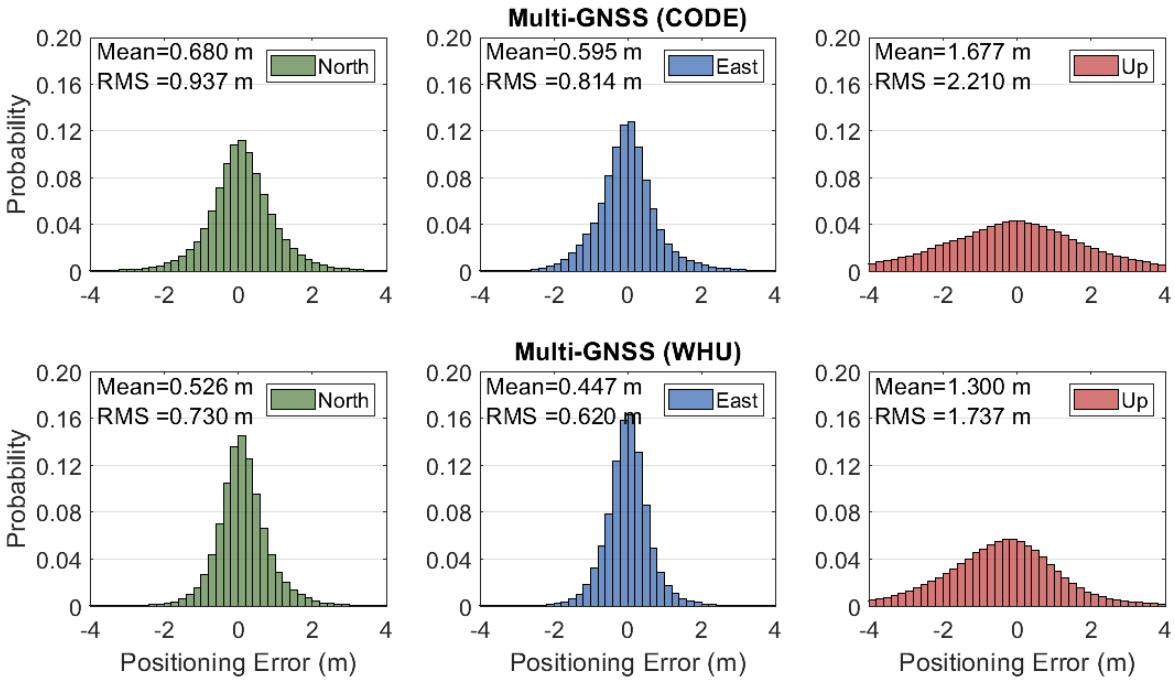

Figure 6.8: Probability distributions of positioning errors for the multi-GNSS single-frequency code pseudorange positioning solutions with CODE and WHU ultra-rapid products.

Figure 6.9 depicts temporal variation of RMS values computed for 3D positioning errors acquired from the multi-GNSS code pseudorange positioning solutions with CODE and WHU ultra-rapid products. It is apparent in the figure that the positioning performance of the multi-GNSS solution with WHU ultra-rapid products is considerably better than that acquired for CODE ultra-rapid products throughout 24-h processing period. For WHU ultra-rapid products, the presence of BDS satellites is a substantial advantage for achieving a better positioning solution in the multi-GNSS integration. On the other side, it can be observed from the figure that the positioning accuracy degrades over time for both multi-GNSS solutions which was the case for GPS-only solutions also. The average RMS values are calculated as 1.954 and 1.440 m for the first six-hour period, while the numbers are 3.221 and 2.395 m for the last six-hour period. Although the positioning performance gets worse with time, the results show that the temporal variation of positioning accuracy calculated for the multi-GNSS solutions is relatively lower than the GPS-only solutions. Consequently, it can be stated that the combination of multi-constellation enhances the performance of single-frequency code pseudorange positioning throughout the 24 hours considerably.

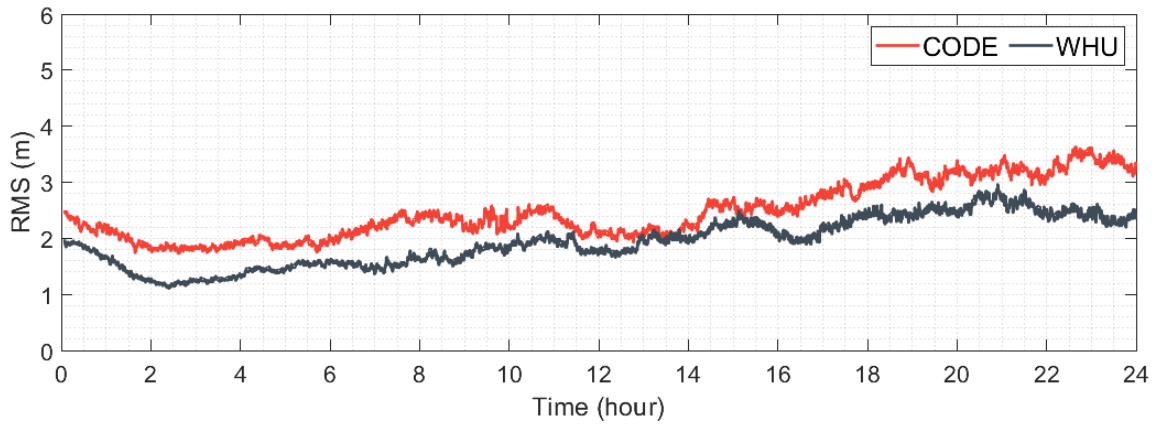

Figure 6.9: Temporal variation of 3D RMS errors for the multi-GNSS single-frequency code pseudontage positioning solutions with CODE and WHU ultra-rapid products.

To investigate the positioning performance in a general perspective, Figure 6.10 presents RMS values computed for horizontal, vertical, and 3D positioning errors obtained from all single-frequency code pseudorange solutions with ultra-rapid products for each station separately. Herein, the GPS-only solutions which employ CODE, IGS, and WHU ultra-rapid products are named CODE (G), IGS (G), and WHU (G) respectively, while CODE (M) and WHU (M) refers to the multi-GNSS solutions with CODE and WHU ultra-rapid products. For the GPS-only solution, the employment of IGS ultra-rapid products provides the best horizontal positioning performance in all stations. The multi-GNSS solution employing CODE ultra-rapid products stays behind the positioning performance of GPS-only solutions in most of the stations despite it enhances the positioning accuracy of its own GPS-only solution. The multi-GNSS solution with WHU ultra-rapid products provides the lowest positioning error horizontally in all stations except for DJIG, FFMJ, NNOR, and REUN stations where the GPS-only solution with IGS products has the best positioning performance. For the vertical component, the situation is quite similar to that of the horizontal positioning error. The multi-GNSS solution with WHU ultra-rapid products has the best positioning accuracy in all stations excluding MADR, NNOR, and REUN stations. Analyzing the 3D positioning performance, it is obvious that the multi-GNSS solution with WHU ultra-rapid products enhances the positioning performance considerably apart from a few stations, i.e. MADR, NNOR, and REUN.

Finally, Table 6.5 indicates average RMS values of horizontal, vertical, and 3D positioning errors calculated for all single-frequency code pseudorange positioning solutions with ultra-rapid products considering all epoch-wise positioning results at 15 stations during the two-week period. For the GPS-only solution, IGS ultra-rapid products present the best positioning performance where RMS values are 1.111, 2.475, and 2.713 m for the horizontal, vertical, and 3D positioning errors. Despite the horizontal positioning error, the multi-GNSS solution with CODE provides slightly better 3D positioning accuracy in comparison

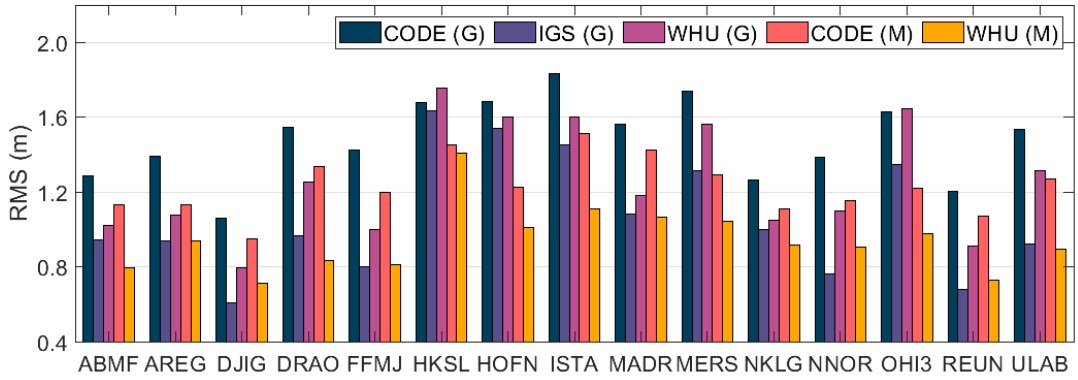

(a) Horizontal positioning errors.

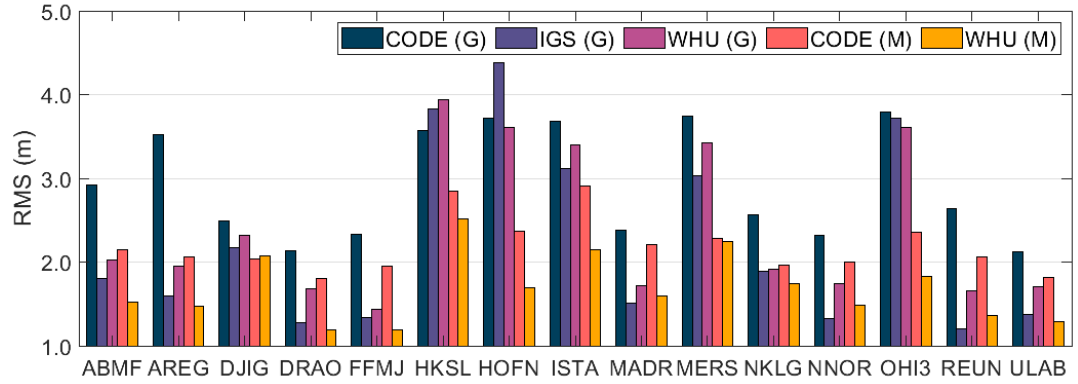

(b) Vertical positioning errors.

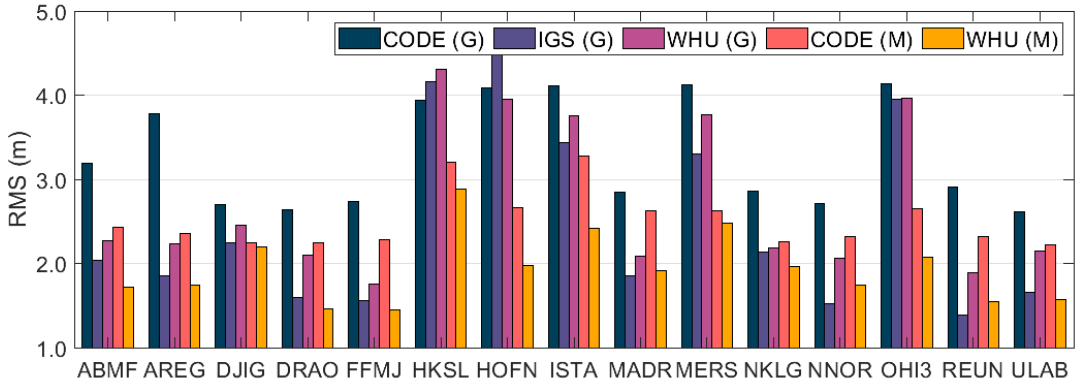

(c) 3D positioning errors.

Figure 6.10: Station-based RMS values of horizontal, vertical and 3D positioning errors for all single-frequency code pseudorange positioning solutions with ultra-rapid products.

to the GPS-only solution employing IGS ultra-rapid products. RMS values computed for the multi-GNSS solution with WHU ultra-rapid products are 0.958, 1.737, and 1.983 m for the horizontal, vertical, and 3D positioning errors. From the results, it can be stated that the integration of multi-constellation enhances the performance of real-time single-frequency code pseudorange positioning. Besides, a 3D positioning accuracy of under 2 m can be reached when WHU ultra-rapid products are utilized.

Table 6.5: Average RMS values of horizontal, vertical, and 3D positioning errors for all single-frequency code pseudorange positioning solutions with ultra-rapid products.

Product	Solution	RMS Errors (m)		
		Horizontal	Vertical	3D
CODE	GPS-only	1.496	2.995	3.348
IGS	GPS-only	1.111	2.475	2.713
WHU	GPS-only	1.293	2.564	2.871
CODE	Multi-GNSS	1.241	2.210	2.535
WHU	Multi-GNSS	0.958	1.737	1.983

6.3.2. Single-frequency Code-Phase Combination with Ultra-rapid Products

This section analyzes the performance of real-time single-frequency code-phase combination employing the ultra-rapid products. Similarly, three different ultra-rapid products, namely CODE, IGS, and WHU, are utilized for positioning processes and their solutions are called according to the applied ultra-rapid product. The positioning strategies applied for the real-time single-frequency code-phase combination are described in Table 6.6 comprehensively. To evaluate the positioning performance, the positioning errors which are described in the previous sections are adopted similarly.

Figure 6.11 shows daily variation of 3D positioning errors calculated for the GPS-only single-frequency code-phase combination with CODE, IGS, and WHU ultra-rapid products at ISTA station on April 26, 2020. From the figure, it can be observed that an initial time is required to achieve a relatively high positioning accuracy from the single-frequency code-phase combination because of unconverged phase ambiguity parameters. For this example, 3D positioning error decrease under 2 m after almost an hour on average, even maybe a longer initial period is required for the stabilization of positioning solution obtained from WHU ultra-rapid products. Therefore, convergence time is used as an additional performance measure in this thesis for the positioning solutions where carrier-phase observations are employed, i.e. single-frequency code-phase combination and dual-frequency PPP.

Figure 6.12 depicts probability distributions of epoch-wise positioning errors obtained from the GPS-only single-frequency code-phase combination solutions with CODE, IGS, and WHU ultra-rapid products. Herein, it should be mentioned that the positioning errors acquired from the first-hour period of each positioning solution were excluded from the distributions to avoid the impact of unconverged phase ambiguities.As shown in the figure, the positioning accuracy which can be obtained from single-frequency code-phase combination is considerably better than that of single-frequency code pseudorange positioning. RMS errors of the north component are 0.403, 0.439, and 0.586 m for the GPS-only solutions which

Table 6.6: Processing strategies applied for the single-frequency code-phase combination solutions with ultra-rapid products.

Item	**Processing strategy**
Observations	Code pseudorange and phase observations on L1 for GPS and GLONASS, E1 for Galileo, B1 for BDS
Satellite orbit and clock source	Ultra-rapid ephemeris
Dry part of troposphere	Corrected using Saastamoinen (Saastamoinen, 1972) model with the GPT3 and VMF3 (Landskron and Böhm, 2018)
Wet part of troposphere	Estimated
Ionosphere	Single-frequency ionosphere-free combination
TGD	Corrected with IGS MGEX products (Section 3.2)
Relativistic clock error	Corrected (Section 3.3)
Relativistic path error	Corrected (Section 3.3)
Satellite antenna PCOs and PCVs	Corrected with IGS antenna model (Section 3.6)
Receiver antenna PCOs and PCVs	Corrected with IGS antenna model (Section 3.6)
Receiver antenna reference point	Corrected (Section 3.6)
Carrier wind-up	Corrected (Section 3.7)
Cycle slip detection	Implemented (Section 3.9)
Site displacement effects	Corrected (Section 3.8)
Standard deviations of observations	0.3 m for code pseudoranges,0.003 m for phase observations
Initial ratios of multi-GNSS observations	$\sigma^2_{P_1^G} : \sigma^2_{P_1^R} : \sigma^2_{P_1^E} : \sigma^2_{P_1^C} = 1 : 2 : 2 : 2$ $\sigma^2_{L_1^G} : \sigma^2_{L_1^R} : \sigma^2_{L_1^E} : \sigma^2_{L_1^C} = 1 : 2 : 2 : 2$
Observation weights	Elevation dependent
Adjustment method	Robust Kalman filter with improved IGG III function (Section 4.3.1)

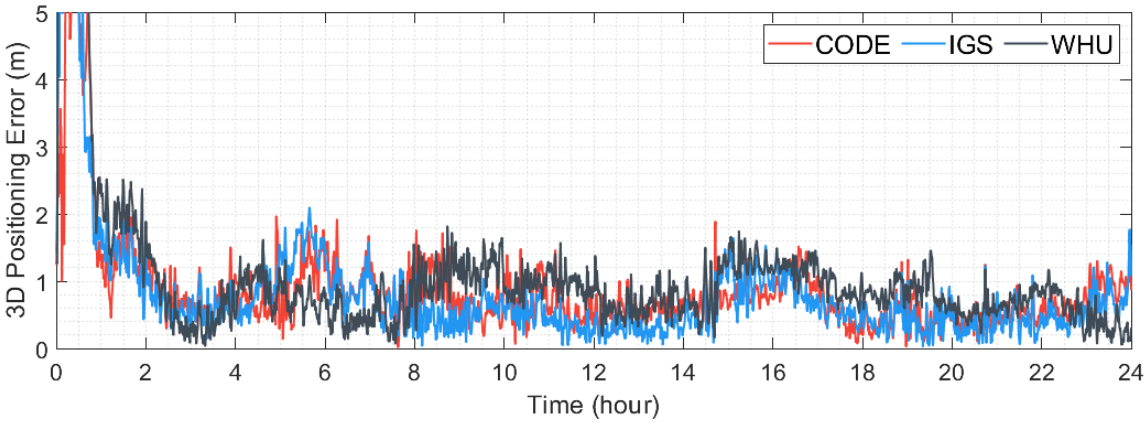

Figure 6.11: Daily variation of 3D positioning errors computed for GPS-only single-frequency code-phase combination with CODE, IGS, and WHU ultra-rapid products at ISTA station on April 26, 2020.

employ CODE, IGS, and WHU ultra-rapid products, while the corresponding RMS errors are calculated as 0.569, 0.629, and 0.798 m for the east component. RMS errors in the up direction are 0.781, 0823, and 1.080 m for the GPS-only solutions of CODE, IGS, and WHU

ultra-rapid products. The results exhibits that the GPS-only solution where CODE ultra-rapid products are utilized have the positioning accuracy better than the other solutions in all directions.

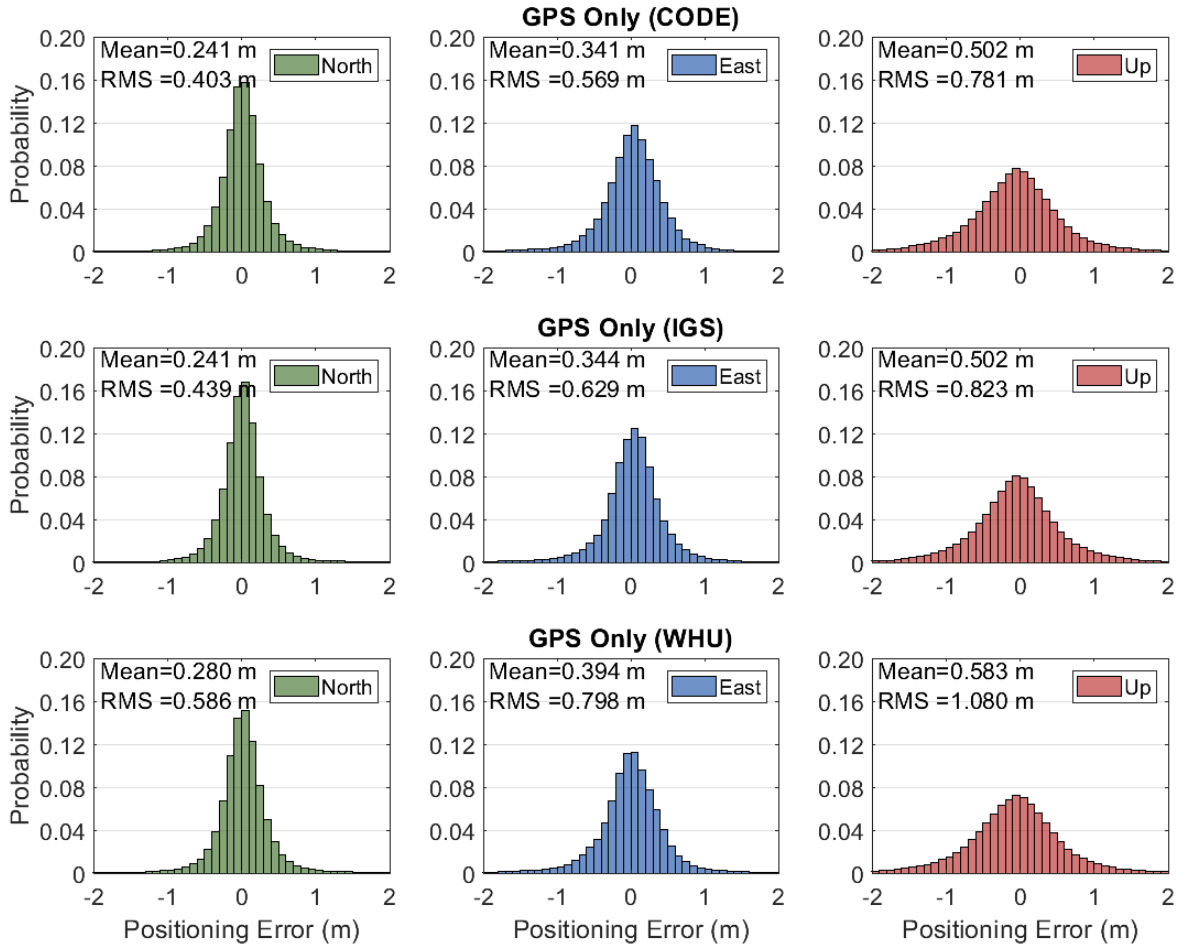

Figure 6.12: Probability distributions of positioning errors for the GPS-only single-frequency code-phase combination solutions with CODE, IGS and WHU ultra-rapid products.

Considering all positioning solutions at 15 stations over the two-week period, Figure 6.13 presents temporal variation of 3D positioning errors obtained from the GPS-only single-frequency code-phase combination solutions with CODE, IGS, and WHU ultra-rapid products. As previously described, the impact of convergence time is quite apparent in the figure. Unlike single-frequency code pseudorange positioning, the impact of time-dependent accuracy degradation in the ultra-rapid products is not remarkable for the single-frequency code-phase combination. The reason behind that is the presence of carrier phase observations. From the figure, it can be seen that the positioning performance obtained from the single-frequency code-phase combination is stable after phase ambiguities are converged. Although the positioning performance of three ultra-rapid products is compatible for the first hours after the convergence, It can be observed that the positioning accuracy of WHU ultra-

rapid products gets differentiated from the others, especially after the tenth hour. As regards the convergence performance, it can be seen from the figure that the GPS-only solution applying CODE ultra-rapid products provides the shortest convergence period compared with the other solutions, while the worst performance is coming from the solution which employs the WHU ultra-rapid products. The performance of convergence times will be evaluated subsequently in this section.

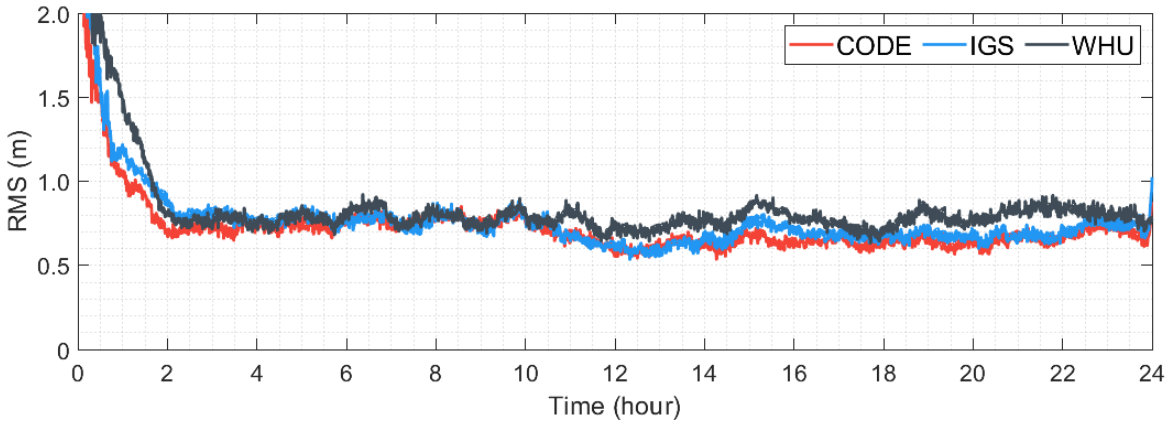

Figure 6.13: Temporal variation of 3D RMS errors for the GPS-only single-frequency code-phase combination solutions with CODE, IGS, and WHU ultra-rapid products.

On the other hand, Figure 6.14 shows probability distributions of epoch-wise positioning errors acquired from the multi-GNSS single-frequency code-phase combination solutions with CODE and WHU ultra-rapid products. RMS values are 0.282, 0.436, and 0.579 m in the north, east, and up directions for the multi-GNSS solution with CODE ultra-rapid products, while these values are computed as 0.264, 0.392, and 0.540 m for the solution employing WHU ultra-rapid products. Therefore, it can be stated that the performance of multi-GNSS solution where WHU ultra-rapid products are used is relatively better than that of CODE products. When compared with the GPS-only solution with CODE ultra-rapid products which provides the best positioning accuracy, the multi-GNSS solution of WHU ultra-rapid products improves the positioning accuracy by 34.5%, 31.1%, and 30.8% in the north, east, and up directions.

Figure 6.15 depicts temporal variations of 3D RMS values computed for multi-GNSS single-frequency code-phase combination solutions with CODE and WHU ultra-rapid products. When compared to the GPS-only solutions, it can be said that the positioning performance is augmented with the multi-GNSS integration. After a convergence period, positioning accuracy of under 1-m can be achieved by both multi-GNSS solutions. As shown in the figure, the multi-GNSS solution employing WHU ultra-rapid products has considerably better positioning performance for the first 14 hours, while the performance of two multi-GNSS solutions is quite compatible in the remaining observation period. Also, it can be said that the use of CODE ultra-rapid products presents quite better convergence period in comparison to the

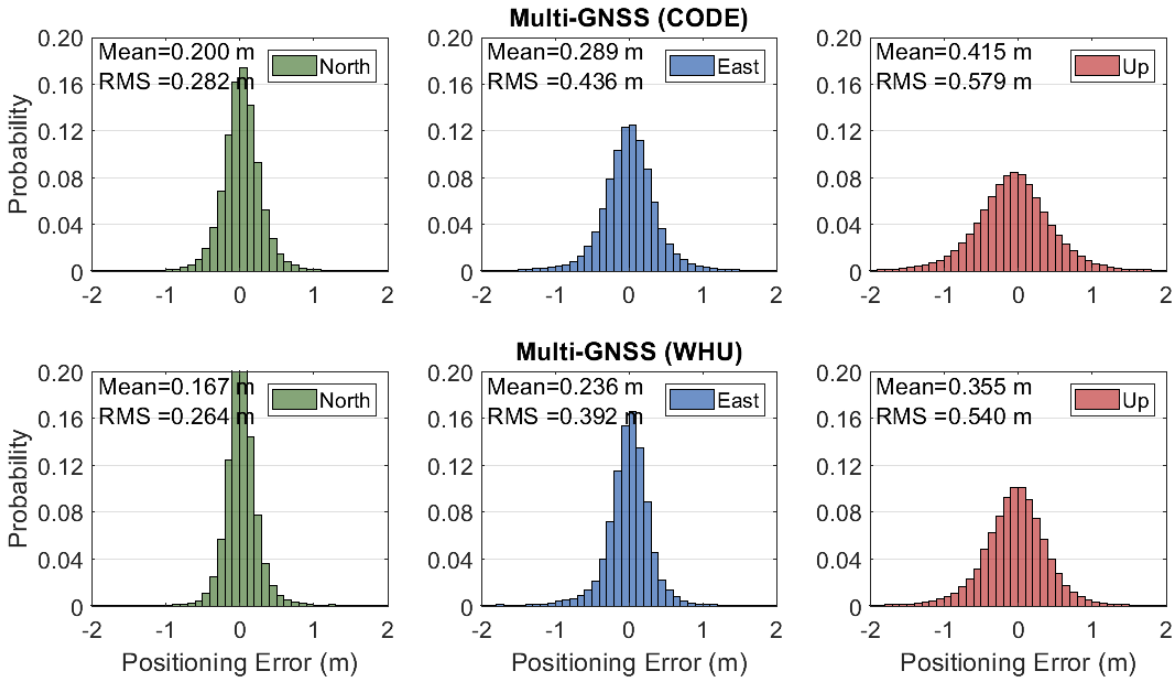

Figure 6.14: Probability distributions of positioning errors for the multi-GNSS single-frequency code-phase combination solutions with CODE, IGS and WHU ultra-rapid products.

other solutions.

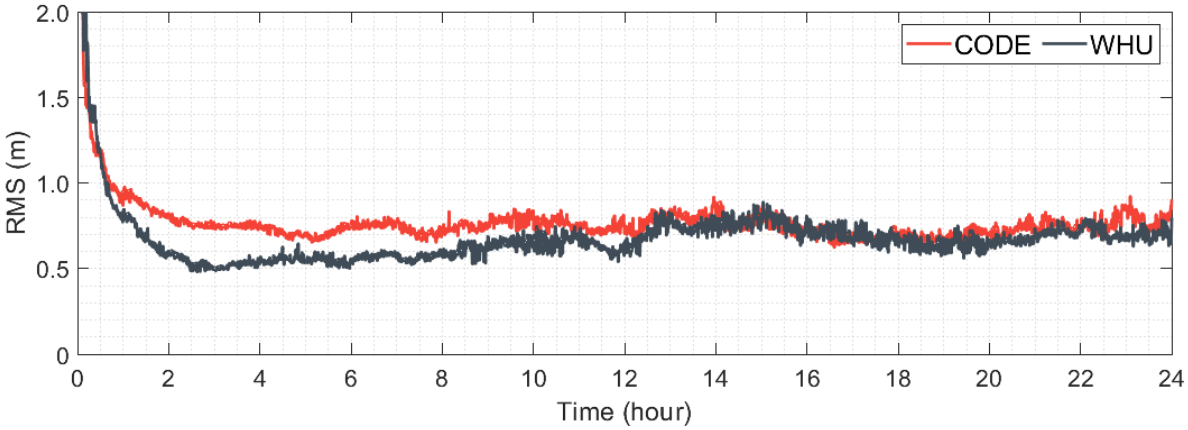

Figure 6.15: Temporal variation of 3D RMS errors for the multi-GNSS single-frequency code-phase combination solutions with CODE and WHU ultra-rapid products.

As previously stated, the convergence period is an important performance measure for the positioning solutions where carrier-phase observations are utilized. Therefore, an additional analysis was performed to assess the convergence performance of single-frequency code-phase combination solutions. Herein, convergence time was defined as the time in which 3D positioning error decrease under 1 m and also does not pass over the 1-m threshold for the following 10 minutes. In this regard, Table 6.7 indicates average convergence times

computed for all single-frequency code-phase combination solutions with ultra-rapid products. It can be observed from the table that the CODE ultra-rapid products provide the best convergence performance among the GPS-only solutions, while the multi-GNSS solution with WHU ultra-rapid products is quite better than that of the corresponding solution with CODE ultra-rapid products. For both multi-GNSS solutions, it apparent that the integration of multi-constellation improves convergence times significantly in comparison with the GPS-only solutions. When compared to the GPS-only solution with CODE ultra-rapid products, the multi-GNSS solution employing WHU ultra-rapid products lessens the convergence time by 32.1% on average.

Table 6.7: Average convergence times (in:min) for all single-frequency code-phase combination solutions with ultra-rapid products.

Product	**Solution**	
	GPS-only	**Multi-GNSS**
CODE	61.57	42.66
IGS	66.61	-
WHU	82.01	41.78

Figure 6.16 shows station-based RMS values calculated for horizontal, vertical, and 3D positioning errors obtained from all single-frequency code-phase combination solutions utilizing ultra-rapid products. Similarly, all positioning solutions of 15 stations over the two-week period, except for the first hour of the corresponding observation period, were taken into consideration for the calculation of station-based RMS values. For the horizontal component, the GPS-only solution with WHU ultra-rapid products has the largest positioning error in most stations. Also, the multi-GNSS solutions improve the positioning accuracy for almost all stations. The best positioning performance comes from the multi-GNSS solutions with WHU ultra-rapid products for all stations except for DRAO, MADR, MERS, and ULAB stations where the multi-GNSS solution with CODE ultra-rapid products has the highest positioning accuracy. The situation is also quite similar for the vertical and 3D positioning errors.

Finally, Table 6.8 presents average RMS values computed for horizontal, vertical, and 3D positioning errors for all single-frequency code-phase combination solutions with ultra-rapid products. For the GPS-only solution, the positioning accuracy ranges from 0.698 to 0.990 m horizontally, while the accuracy is between 0.781 and 1.080 m for the vertical component. For the GPS-only solution with ultra-rapid products, a positioning accuracy of around 1 m can be achieved after a convergence period. Moreover, both multi-GNSS solutions enhance the positioning accuracy of single-frequency code-phase combination solutions considerably, and it is possible to reach submeter positioning accuracy with these solutions. Still, the multi-GNSS solution with WHU ultra-rapid products provide relatively better positioning

accuracy and augments the positioning performance of GPS-only solution with CODE ultra-rapid products, which has the best positioning performance for the GPS-only solution, by 32.4%, 30.8%, and 31.5% for the horizontal, vertical and 3D positioning errors.

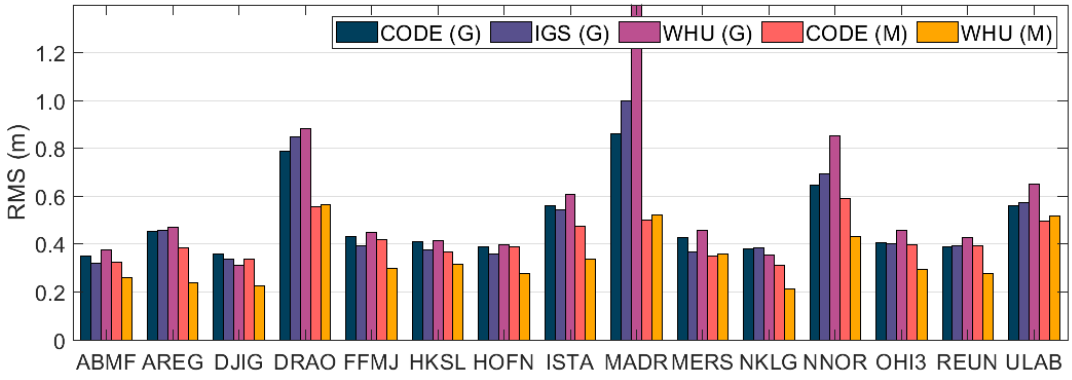

(a) Horizontal positioning errors.

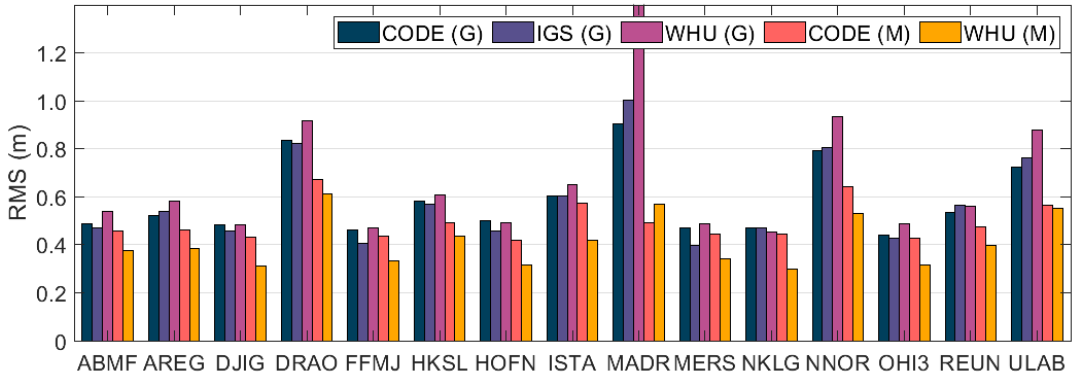

(b) Vertical positioning errors.

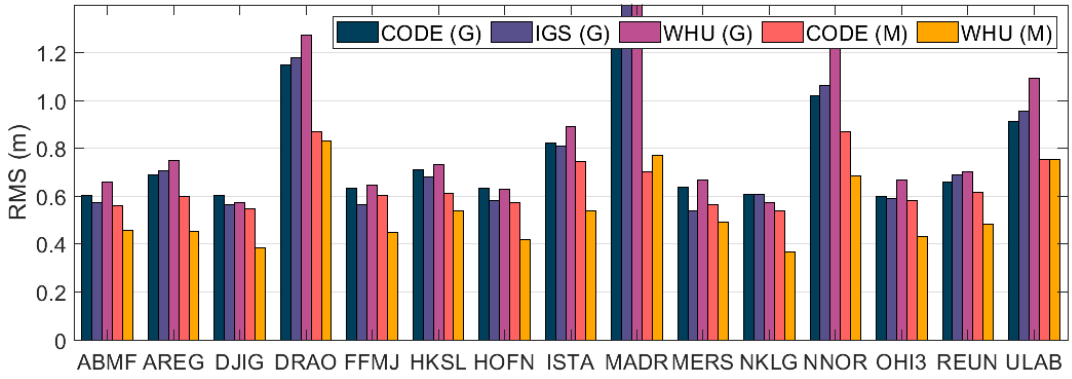

(c) 3D positioning errors.

Figure 6.16: Station-based RMS values of horizontal, vertical and 3D positioning errors for all single-frequency code-phase combination solutions with ultra-rapid products.

Table 6.8: Average RMS values of horizontal, vertical, and 3D positioning errors for all single-frequency code-phase combination solutions with ultra-rapid products.

Product	Solution	RMS Errors (m)		
		Horizontal	Vertical	3D
CODE	GPS-only	0.698	0.781	1.047
IGS	GPS-only	0.767	0.823	1.125
WHU	GPS-only	0.990	1.080	1.465
CODE	Multi-GNSS	0.518	0.579	0.777
WHU	Multi-GNSS	0.472	0.540	0.717

6.3.3. Dual-frequency PPP with Ultra-rapid Products

The positioning performance of real-time dual-frequency PPP with ultra-rapid products is evaluated in this section. Three ultra-rapid products which are CODE, IGS, and WHU are utilized to conduct dual-frequency PPP solutions in GPS-only and multi-GNSS scenarios, while a detailed description of the dual-frequency PPP technique, including the functional and stochastic models, is provided in the previous chapter. Table 6.9 presents a summary of the processing strategies applied for the dual-frequency PPP solutions. Similarly, the positioning errors and convergence time defined in the previous sections are employed to assess the positioning performance of dual-frequency PPP solutions.

When it comes to the positioning performance, Figure 6.17 first indicates probability distributions of epoch-wise positioning errors obtained from the GPS-only dual-frequency PPP solutions with CODE, IGS, and WHU ultra-rapid products. Similar to the previous section, the positioning errors obtained from the first-hour of each positioning solution were excluded in the calculations to prevent the influence of unconverged phase ambiguities. At a first glance, it can be observed that the positioning errors of dual-frequency PPP solutions with ultra-rapid products are significantly lower than those of single-frequency code pseudorange and code-phase combination solutions. For the horizontal components, the GPS-only solution with WHU ultra-rapid products has a better positioning performance, while the CODE ultra-rapid products have better positioning accuracy for the up component when compared to other solutions.

Figure 6.18 shows temporal variation of RMS values computed for 3D positioning errors of the GPS-only dual-frequency PPP solutions with CODE, IGS, and WHU ultra-rapid products respectively. RMS values were calculated considering all positioning solutions at 15 stations over the two-week period. The impact of the convergence period can be observed in the figure, however, it is considerably shorter in comparison with that of the single-frequency code-phase combinations. On the other side, the positioning accuracy which can be acquired from the dual-frequency PPP after a convergence period is not influenced by decreasing

Table 6.9: Processing strategies applied for the dual-frequency PPP solutions with ultra-rapid products.

Item	**Processing strategy**
Observations	Dual-frequency code pseudorange and phase observations on L1 and L2 for GPS and GLONASS, E1 and E5a for Galileo, B1 and B2 for BDS
Satellite orbit and clock source	Ultra-rapid ephemeris
Dry part of troposphere	Corrected using Saastamoinen (Saastamoinen, 1972) model with the GPT3 and VMF3 (Landskron and Böhm, 2018)
Wet part of troposphere	Estimated
Ionosphere	Dual-frequency ionosphere-free combination
TGD	Not corrected
Relativistic clock error	Corrected (Section 3.3)
Relativistic path error	Corrected (Section 3.3)
Satellite antenna PCOs and PCVs	Corrected with IGS antenna model (Section 3.6)
Receiver antenna PCOs and PCVs	Corrected with IGS antenna model (Section 3.6)
Receiver antenna reference point	Corrected (Section 3.6)
Carrier wind-up	Corrected (Section 3.7)
Cycle slip detection	Implemented (Section 3.9)
Site displacement effects	Corrected (Section 3.8)
Standard deviations of observations	0.3 m for code pseudoranges,0.003 m for phase observations
Initial ratios of multi-GNSS observations	$\sigma^2_{P_1^G} : \sigma^2_{P_1^R} : \sigma^2_{P_1^E} : \sigma^2_{P_1^C} = 1 : 2 : 2 : 2$ $\sigma^2_{L_1^G} : \sigma^2_{L_1^R} : \sigma^2_{L_1^E} : \sigma^2_{L_1^C} = 1 : 2 : 2 : 2$
Observation weights	Elevation dependent
Adjustment method	Robust Kalman filter with improved IGG III function (Section 4.3.1)

accuracy of ultra-rapid products which was the case for the single-frequency code positioning. As shown in the figure, the GPS-only solution with WHU ultra-rapid products provides relatively better positioning performance after the first seven hours. Still, the GPS-only solutions with CODE and IGS ultra-rapid products have lower positioning errors in the first hours, which impacts the convergence performance considerably.

Figure 6.19 depicts probability distributions of positioning errors acquired from the multi-GNSS dual-frequency PPP solutions with CODE and WHU ultra-rapid products. From the figure, it is apparent that the multi-GNSS integration enhances the positioning performance of dual-frequency PPP solutions significantly. Especially, there is a considerable improvement in the horizontal components. RMS values computed for the multi-GNSS solutions with CODE ultra-rapid products are 0.112, 0201, and 0.287 m in the north, east, and up directions, whereas the values are calculated as 0.080, 0.132, and 0.252 m for the multi-GNSS solution employing WHU ultra-rapid products. The results demonstrate that the employment of WHU ultra-rapid products provides more accurate positioning performance for dual-

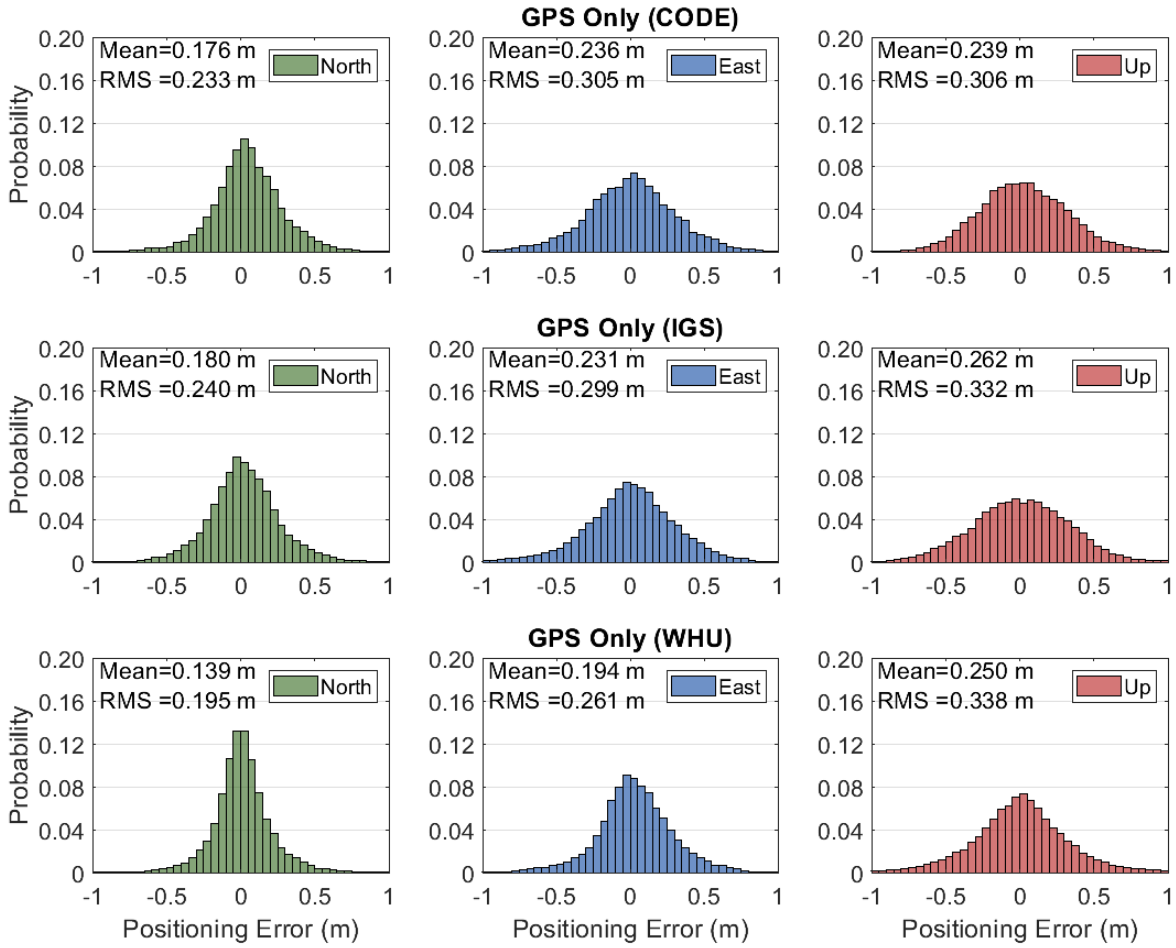

Figure 6.17: Probability distributions of positioning errors for the GPS-only dual-frequency PPP solutions with CODE, IGS and WHU ultra-rapid products.

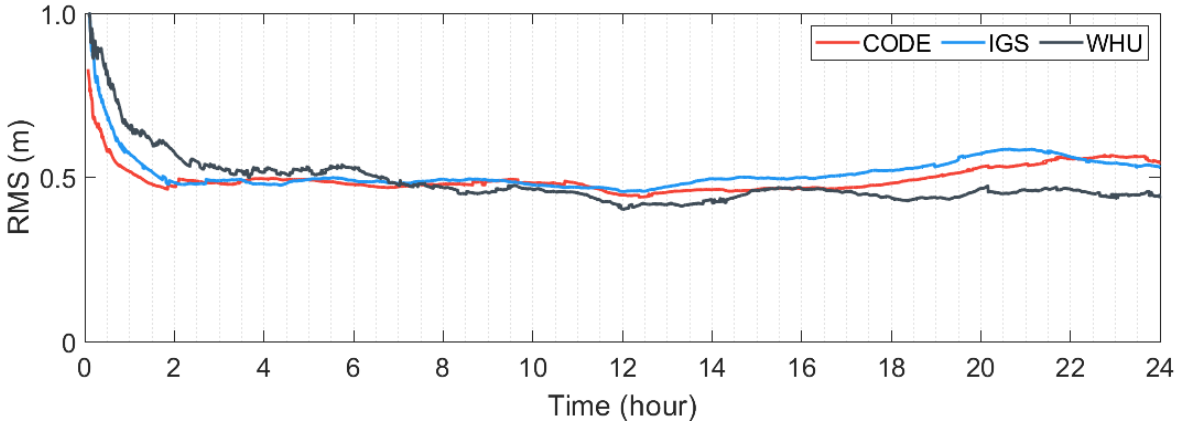

Figure 6.18: Time-dependent variations of 3D RMS errors for the GPS-only dual-frequency PPP solutions with CODE, IGS, and WHU ultra-rapid products.

frequency PPP owing to the advantage of an additional navigation system. When compared with the GPS-only solution of WHU ultra-rapid products, the multi-GNSS solution employing the same ultra-rapid products improves the positioning accuracy by 48.9%, 22.9%, and

25.4% in the north, east, and up directions.

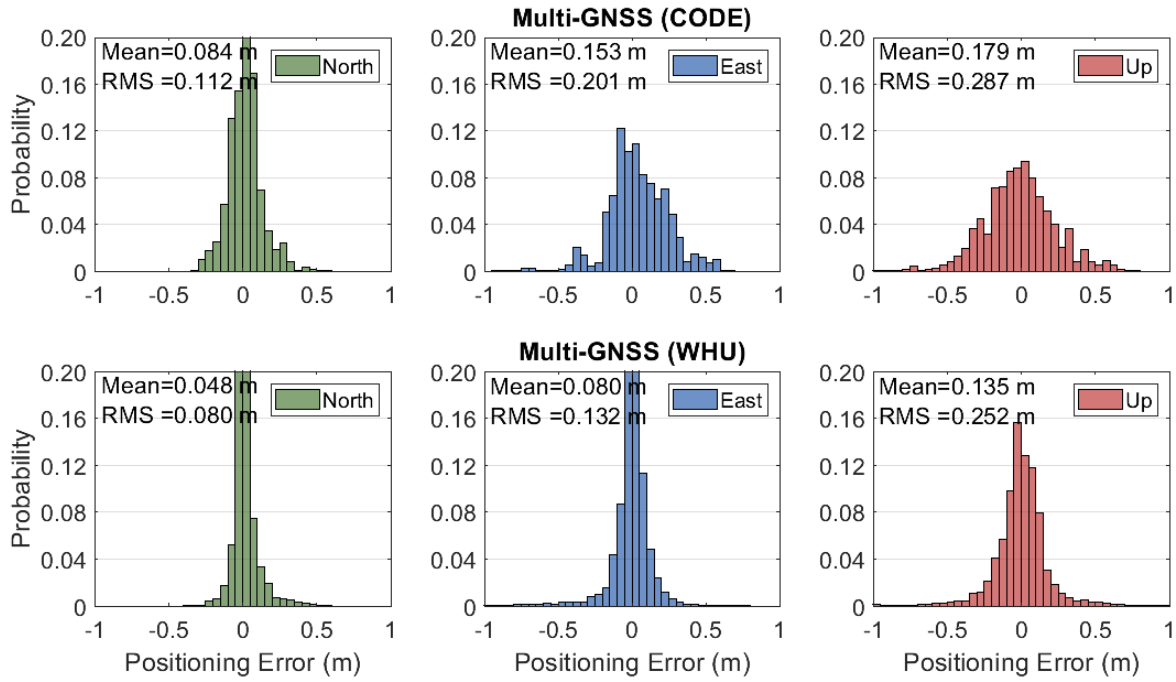

Figure 6.19: Probability distributions of positioning errors for the multi-GNSS dual-frequency PPP solutions with CODE, IGS and WHU ultra-rapid products.

Figure 6.20 shows temporal variation of RMS values computed for 3D positioning errors of the multi-GNSS dual-frequency PPP solutions with CODE and WHU ultra-rapid products respectively. As can be shown in the figure, the performance of multi-GNSS solutions is quite stable after a relatively short convergence period. From the figure, it is also apparent that the performance of multi-GNSS solution with WHU ultra-rapid products is considerably better than that of the corresponding solution with CODE ultra-rapid products throughout the 24 hours.

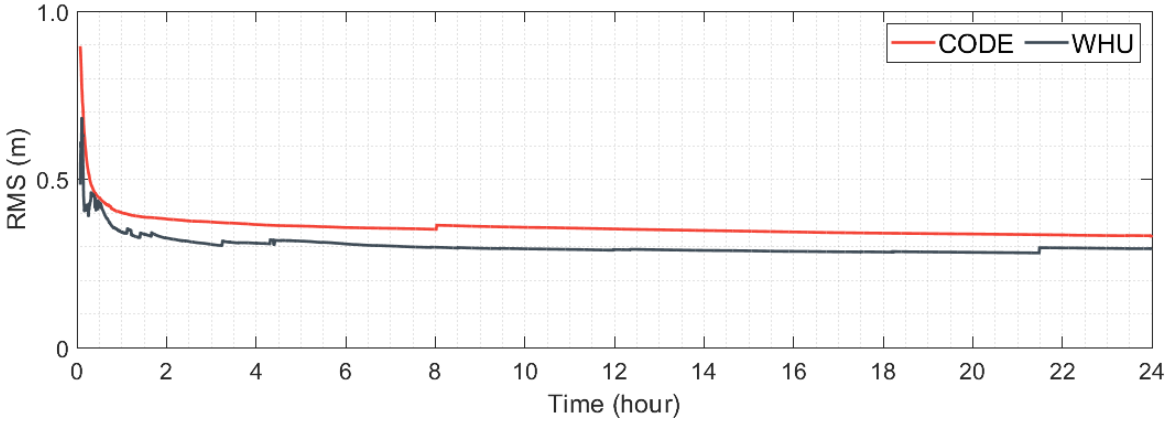

Figure 6.20: Temporal variation of 3D RMS errors for the multi-GNSS dual-frequency PPP solutions with CODE, IGS, and WHU ultra-rapid products.

Table 6.10 presents average convergence times calculated for all dual-frequency PPP solutions with ultra-rapid products. For the sake of consistency, the convergence times were determined depending on the criterion defined in the previous section. From the table, it can be observed that convergence times acquired from dual-frequency PPP solutions are substantially shorter when compared to those of single-frequency code-phase combination solutions. For the GPS-only solutions, CODE ultra-rapid products have the best convergence performance with a convergence time of 22.67 minutes on average. The multi-GNSS solution where WHU ultra-rapid products are employed provide a convergence time of 16.90 minutes on average, which means an almost 25% improvement when compared with the GPS-only solution with CODE ultra-rapid products.

Table 6.10: Average convergence times (in:min) for all dual-frequency PPP solutions with ultra-rapid products.

Product	**Solution**	
	GPS-only	**Multi-GNSS**
CODE	22.67	17.69
IGS	25.43	-
WHU	37.86	16.90

Table 6.11 presents average RMS values computed for horizontal, vertical, and 3D positioning errors for all dual-frequency PPP solutions with ultra-rapid products. For the GPS-only solutions, the employment of WHU ultra-rapid products provides the best positioning performance with a 3D positioning error of 0.469 m. On the other hand, the multi-GNSS solution with WHU ultra-rapid product augments the positioning performance in comparison with the other solutions substantially. The multi-GNSS solution with WHU ultra-rapid product has a positioning accuracy of almost 0.3 m in total.

Table 6.11: Average RMS values of horizontal, vertical, and 3D positioning errors for all dual-frequency PPP solutions with ultra-rapid products.

Product	**Solution**	**RMS Errors (m)**		
		Horizontal	**Vertical**	**3D**
CODE	GPS-only	0.384	0.306	0.490
IGS	GPS-only	0.383	0.332	0.507
WHU	GPS-only	0.325	0.338	0.469
CODE	Multi-GNSS	0.230	0.287	0.348
WHU	Multi-GNSS	0.154	0.252	0.296

Figure 6.21 illustrates station-based RMS values which are computed for horizontal, vertical, and 3D positioning errors acquired from all dual-frequency PPP solutions with ultra-rapid products. As shown in the figure, a higher positioning accuracy can be reached with the dual-frequency PPP solutions when compared with the single-frequency solutions. As can be observed from the figure, the multi-GNSS solutions augment the positioning performance

for almost all stations in terms of horizontal, vertical, and 3D positioning errors considerably. When the RMS values computed for 3D positioning errors are analyzed, the multi-GNSS solution with WHU ultra-rapid products provides the best positioning accuracy in the whole stations except for MADR station.

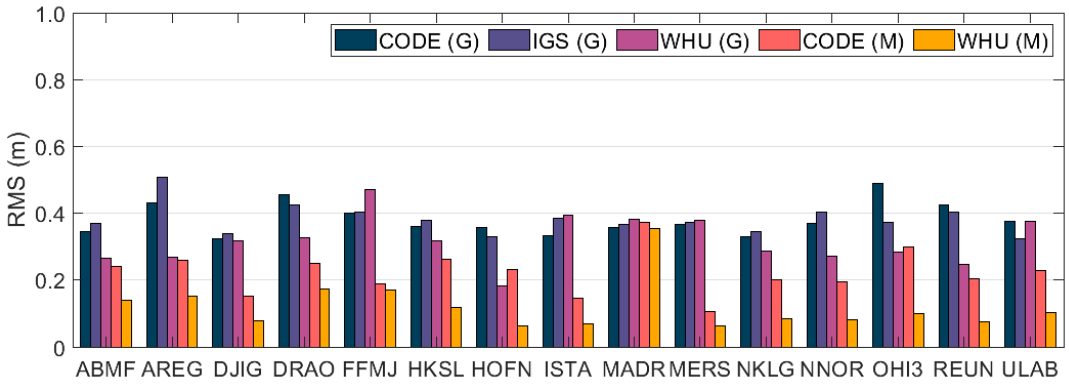

(a) Horizontal positioning errors.

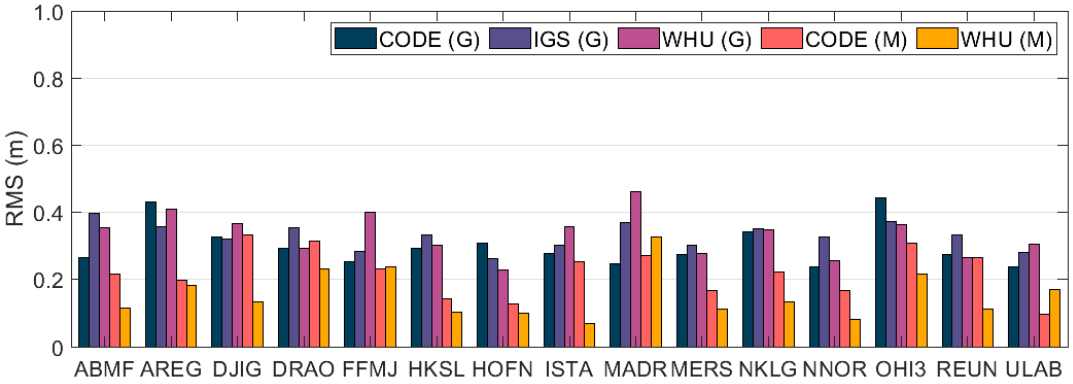

(b) Vertical positioning errors.

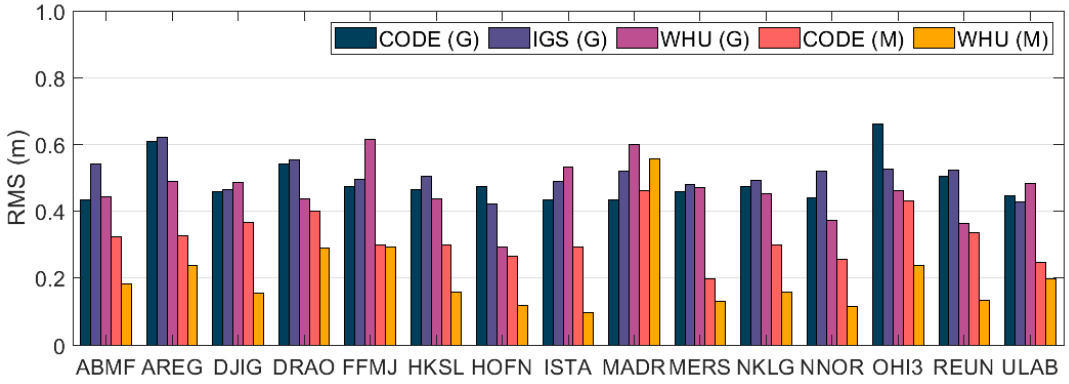

(c) 3D positioning errors.

Figure 6.21: Station-based RMS values of horizontal, vertical and 3D positioning errors for all dual-frequency PPP solutions with ultra-rapid products.

6.4. Performance Analysis of Real-time Absolute GNSS Positioning with IGS Real-time Products

The performance of real-time absolute GNSS positioning techniques which utilize the IGS-RTS products is evaluated in this section. Three absolute GNSS positioning techniques, which are single-frequency code pseudorange positioning, single-frequency code-phase combination, and dual-frequency PPP, are included in the experimental tests conducted to analyze the positioning performance similar to the previous section. The SSR message disseminated by the Centre National d'Etudes Spatiales (CNES) through IGS-RTS, which is called "SSRA00CNE0", was employed to acquire the real-time orbit and clock corrections. The CNES real-time product includes satellite orbits and clock corrections for GPS, GLONASS, Galileo, and BDS satellites together with the real-time ionospheric corrections. Similarly, the real-time positioning processes were performed with the GPS-only and multi-GNSS scenarios to investigate the contribution of multi-constellation. Basically, the same observation dataset and performance indicators employed in the previous section are utilized to evaluate positioning performance for the sake of consistency.

6.4.1. Single-frequency Code Pseudorange Positioning with IGS Real-time Products

Using the IGS-RTS product provided by the CNES analysis center, the observation dataset was processed under the GPS-only and multi-GNSS single-frequency code pseudorange positioning separately. The comprehensive processing strategy is presented in Table 6.12. To analyze the positioning accuracy, the same procedure applied in the previous section was employed to compute the positioning errors.

Figure 6.22 illustrates probability distributions of positioning errors computed for the GPS-only and multi-GNSS single-frequency code pseudorange positioning solutions with IGS-RTS products separately. In the computations, all positioning solutions at 15 stations over the two-week period were taken into consideration. As shown in the figure, RMS values are 0.684, 0.539, and 2.153 m in the north, east, and up directions for the GPS-only solution, while they are calculated as 0.476, 0.399, and 1.389 m for the multi-GNSS solution respectively. The results show that both of the single-frequency code pseudorange solutions with IGS-RTS products provide better positioning accuracy in all components when compared to their equivalent solutions with ultra-rapid products. Furthermore, the multi-GNSS solution improves the positioning accuracy of GPS-only solutions by 30.1%, 25.9%, and 35.4% for the north, east, and up directions.

On the other side, Figure 6.23 indicates temporal variation of 3D positioning errors ob-

Table 6.12: Processing strategies applied for the single-frequency code pseudorange positioning solutions with IGS-RTS products.

Item	**Processing strategy**
Observations	Code pseudorange observations on L1 for GPS and GLONASS, E1 for Galileo, B1 for BDS
Satellite orbit and clock source	Broadcast ephemeris and IGS-RTS corrections
Dry part of troposphere	Corrected using Saastamoinen (Saastamoinen, 1972) model with the GPT3 and VMF3 (Landskron and Böhm, 2018)
Wet part of troposphere	Estimated
Ionosphere	IGS-RTS corrections
TGD	Corrected with IGS MGEX products (Section 3.2)
Relativistic clock error	Corrected (Section 3.3)
Relativistic path error	Corrected (Section 3.3)
Satellite antenna PCOs and PCVs	Not corrected
Receiver antenna PCOs and PCVs	Corrected with IGS antenna model (Section 3.6)
Receiver antenna reference point	Corrected (Section 3.6)
Carrier wind-up	Not corrected
Cycle slip detection	Not implemented
Site displacement effects	Not corrected
Standard deviations of observations	0.3 m for code pseudoranges
Initial ratios of multi-GNSS observations	$\sigma^2_{P_1^G} : \sigma^2_{P_1^R} : \sigma^2_{P_1^E} : \sigma^2_{P_1^C} = 1 : 2 : 2 : 2$
Observation weights	Elevation dependent
Adjustment method	Robust Kalman filter with improved IGG III function (Section 4.3.1)

tained from the GPS-only and multi-GNSS single-frequency code pseudorange positioning solutions with IGS-RTS products. As shown in the figure, the performance of the single-frequency code pseudorange positioning with IGS-RTS products does not change with time remarkably, unlike the positioning solutions with the ultra-rapid products, which is one of the main advantages when compared with ultra-rapid products. Additionally, it is apparent from the figure that the multi-GNSS solution has a significantly better positioning performance throughout the 24-hour period.

Table 6.13 shows station-based RMS values of horizontal, vertical, and 3D positioning errors for the GPS-only and multi-GNSS single-frequency code pseudorange solutions with IGS-RTS products. Besides, the table also provides corresponding average RMS values taking all stations into consideration. For the GPS-only solution, horizontal RMS values range from 0.481 m to 1.506 m, while RMS values are between 0.749 m and 3.894 m for the vertical positioning errors. Also, 3D positioning errors vary between 0.922 m and 4.176 m considering all stations. For the multi-GNSS solution, horizontal RMS errors are under 1 m for all stations except for HKSL station, while vertical RMS values range from 0.595 m to 2.326 m. The highest RMS value is 2.527 m for the 3D positioning error, while 3D RMS values obtained from seven stations are under 1-m for the multi-GNSS solution. Consider-

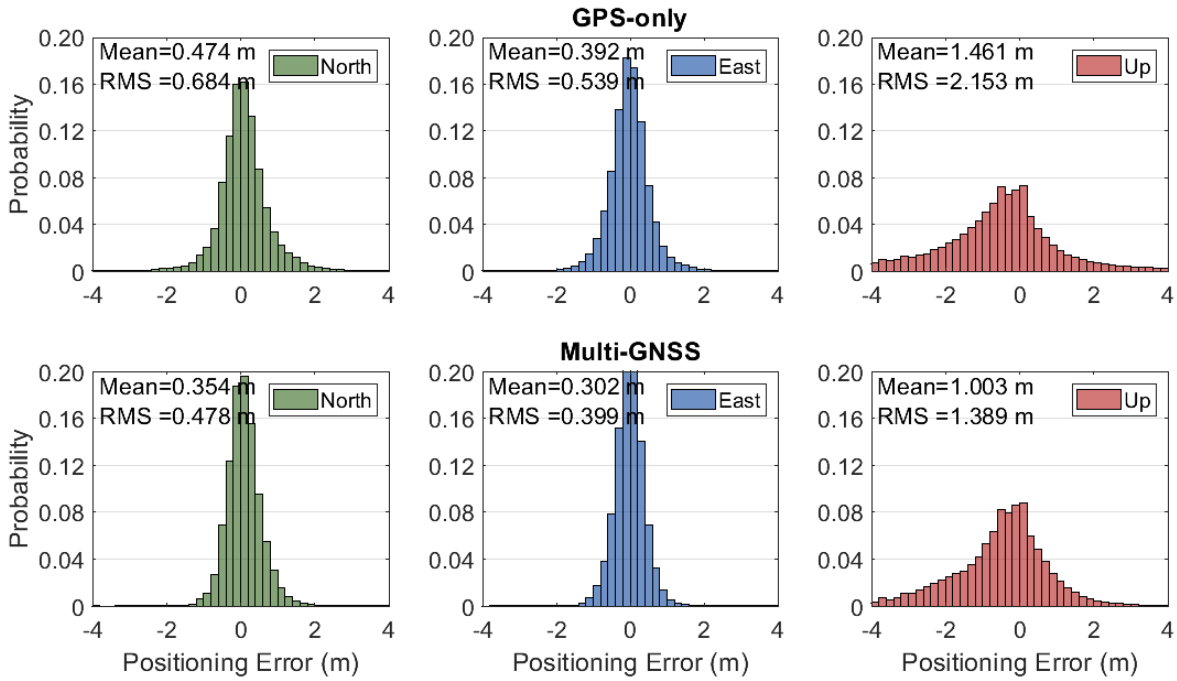

Figure 6.22: Probability distributions of positioning errors for the GPS-only and multi-GNSS single-frequency code pseudorange positioning solutions with IGS-RTS products.

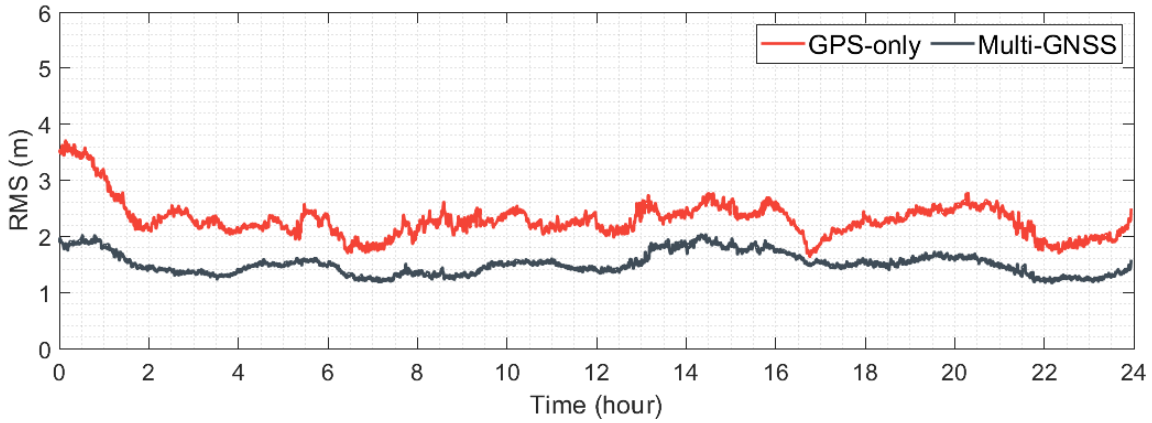

Figure 6.23: Temporal variation of 3D RMS errors for the GPS-only and multi-GNSS single-frequency code pseudorange positioning solutions with IGS-RTS products.

ing all stations, average RMS values of horizontal, vertical, and 3D positioning errors are 0.872, 2.153, and 2.323 m for the GPS-only solution, whereas RMS values were computed as 0.623, 1.389, and 1.522 m respectively for the multi-GNSS solution. The results show that the combination of multi-GNSS improves the performance of single-frequency code pseudorange positioning by 28.5%, 35.5%, 34.5% in the horizontal, vertical, and 3D positioning errors compared to the GPS-only solution.

Table 6.13: Station-based RMS values of horizontal, vertical, and 3D positioning errors (in:m) for the GPS-only and multi-GNSS single-frequency code pseudorange positioning solutions with IGS-RTS products.

Station	GPS-only			Multi-GNSS		
	Horizontal	Vertical	3D	Horizontal	Vertical	3D
ABMF	0.580	1.027	1.179	0.541	0.918	1.066
AREG	0.575	0.884	1.055	0.558	0.740	0.927
DJIG	0.504	1.999	2.062	0.466	1.879	1.936
DRAO	0.552	0.749	0.931	0.436	0.595	0.738
FFMJ	0.502	0.774	0.922	0.427	0.724	0.840
HKSL	1.506	3.894	4.176	1.168	2.241	2.527
HOFN	1.190	3.168	3.380	0.668	1.220	1.391
ISTA	1.268	3.350	3.583	0.754	2.188	2.314
MADR	0.633	0.940	1.133	0.539	0.804	0.968
MERS	1.195	3.096	3.319	0.755	2.326	2.446
NKLG	0.732	1.642	1.798	0.644	1.564	1.692
NNOR	0.584	0.962	1.126	0.511	0.834	0.978
OHI3	1.153	3.127	3.333	0.564	1.198	1.324
REUN	0.481	1.001	1.111	0.421	0.730	0.843
ULAB	0.576	1.026	1.177	0.452	0.751	0.876
ALL	0.872	2.153	2.323	0.623	1.389	1.522

6.4.2. Single-frequency Code-Phase Combination with IGS Real-time Products

The performance of the GPS-only and multi-GNSS single-frequency code-phase combination positioning with IGS-RTS products are analyzed in this subsection. The observation dataset was processed under the GPS-only and multi-GNSS scenarios respectively. Table 6.14 provides related processing strategies applied for the single-frequency code-phase combination positioning in detail. The same procedure employed in the previous chapters was similarly utilized to evaluate the positioning performance.

Figure 6.24 indicates probability distributions of positioning errors in the north, east, and north components for the GPS-only and multi-GNSS single-frequency code-phase combination solutions with IGS-RTS products. Herein, the positioning solutions in the first-hour period were excluded in the production of probability distributions to avoid the influence of unconvergenced phase ambiguity parameters similar to previous analyses applied for the carrier phase-based positioning models. As shown in the figure, RMS values are 0.205, 0.260, and 0.386 m for the GPS-only solution, while they were calculated as 0.137, 0.181, and 0.261 m for the multi-GNSS solution. The positioning accuracy of both solutions is considerably better than those of corresponding positioning solutions which employ ultra-rapid products. Moreover, the multi-GNSS solution provides better positioning accuracy by 33.2%, 30.4%, and 32.3% in the north, east and up directions respectively compared with the GPS-only

Table 6.14: Processing strategies applied for the single-frequency code-phase combination solutions with IGS-RTS products.

Item	**Processing strategy**
Observations	Code pseudorange and phase observations on L1 for GPS and GLONASS, E1 for Galileo, B1 for BDS
Satellite orbit and clock source	Broadcast ephemeris and IGS-RTS corrections
Dry part of troposphere	Corrected using Saastamoinen (Saastamoinen, 1972) model with the GPT3 and VMF3 (Landskron and Böhm, 2018)
Wet part of troposphere	Estimated
Ionosphere	Single-frequency ionosphere-free combination
TGD	Corrected with IGS MGEX products (Section 3.2)
Relativistic clock error	Corrected (Section 3.3)
Relativistic path error	Corrected (Section 3.3)
Satellite antenna PCOs and PCVs	Not corrected
Receiver antenna PCOs and PCVs	Corrected with IGS antenna model (Section 3.6)
Receiver antenna reference point	Corrected (Section 3.6)
Carrier wind-up	Corrected (Section 3.7)
Cycle slip detection	Implemented (Section 3.9)
Site displacement effects	Corrected (Section 3.8)
Standard deviations of observations	0.3 m for code pseudoranges,0.003 m for phase observations
Initial ratios of multi-GNSS observations	$\sigma^2_{P_1^G} : \sigma^2_{P_1^R} : \sigma^2_{P_1^E} : \sigma^2_{P_1^C} = 1 : 2 : 2 : 2$ $\sigma^2_{L_1^G} : \sigma^2_{L_1^R} : \sigma^2_{L_1^E} : \sigma^2_{L_1^C} = 1 : 2 : 2 : 2$
Observation weights	Elevation dependent
Adjustment method	Robust Kalman filter with improved IGG III function (Section 4.3.1)

solution.

On the other side, Figure 6.25 depicts temporal variations of 3D positioning errors obtained from the GPS-only and multi-GNSS single-frequency code-phase combination solutions with IGS-RTS products. As shown in the figure, it requires an initial time to converge the phase ambiguity parameters when the single-frequency code-phase combination is employed. From the figure, It can be seen that the multi-GNSS solution has a significantly shorter convergence period in comparison to the GPS-only solution. Furthermore, the multi-GNSS solution has the better positioning accuracy than the GPS-only solution throughout the 24-hour period. Also, it can be said that the positioning performance of both solutions is quite stable after a convergence period and does not change with time on contrary to the solutions employing ultra-rapid products. On the other side, average convergence times computed for the GPS-only and multi-GNSS solutions are 60.98 and 44.47 minutes respectively. The results exhibit that the employment of IGS-RTS products augments the convergence performance in comparison with the ultra-rapid products. Also, the multi-GNSS solution lessens the convergence time of GPS-only solution by 27.1% on average.

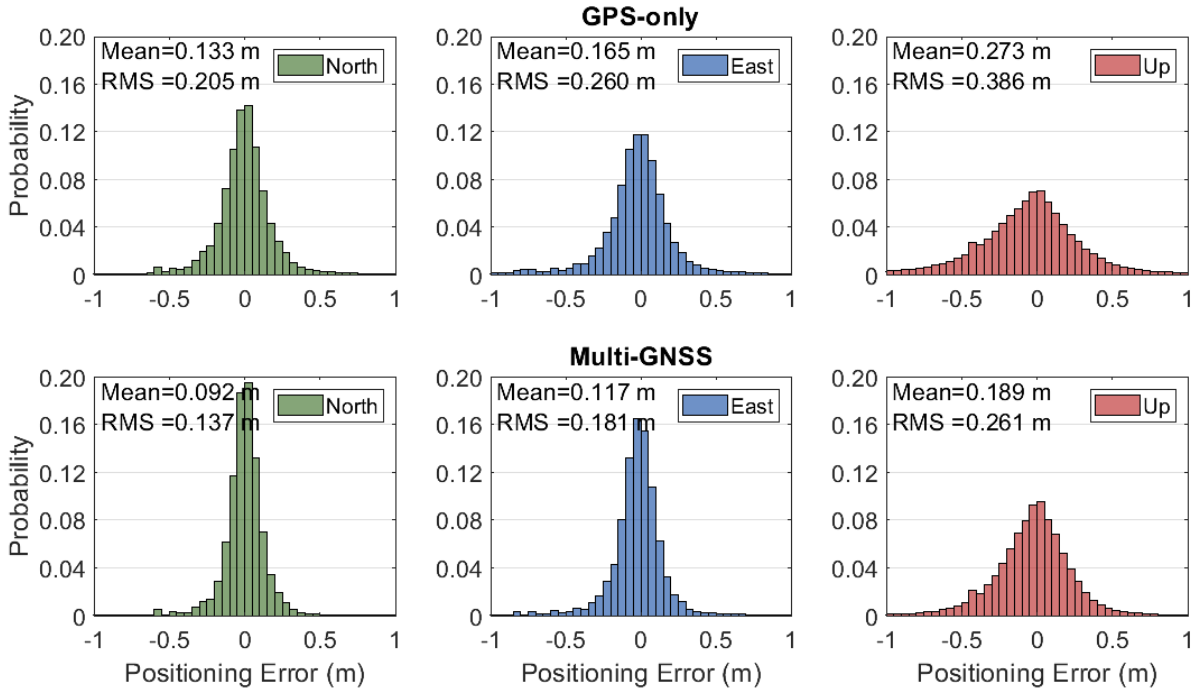

Figure 6.24: Probability distributions of positioning errors for the GPS-only and multi-GNSS single-frequency code-phase combination solutions with IGS-RTS products.

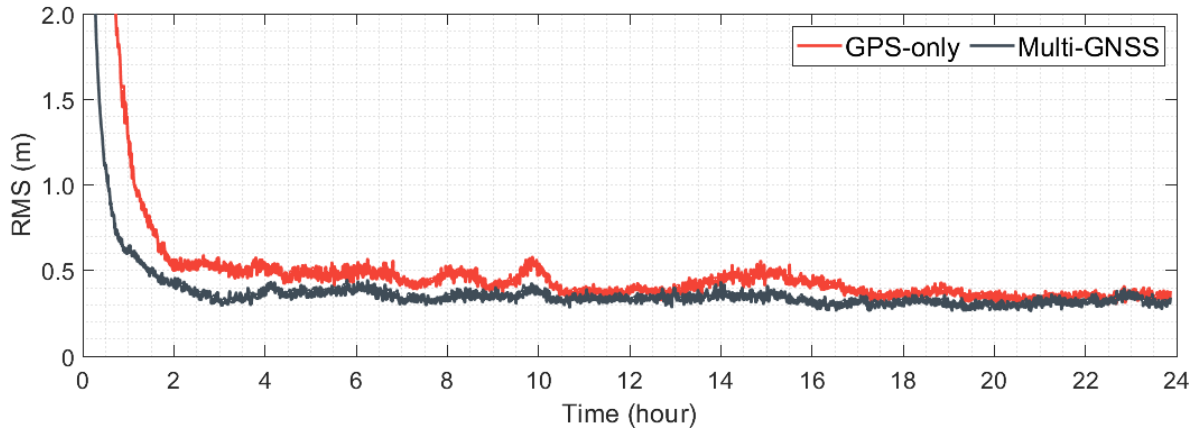

Figure 6.25: Temporal variation of 3D RMS errors for the GPS-only and multi-GNSS single-frequency code-phase combination solutions with IGS-RTS products.

Table 6.15 presents station-based RMS values of horizontal, vertical, and 3D positioning errors for the GPS-only and multi-GNSS single-frequency code-phase combination solutions with IGS-RTS products. In addition, the table shows their average RMS values computed considering all stations. It can be observed from the table that station-based horizontal RMS values of the GPS-only solution range from 0.163 to 0.765 m, while they are between 0.110 and 0.569 m for the multi-GNSS solution. For the vertical component, RMS values of the GPS-only solution change between 0.224 and 0.737 m, whereas they range from 0.166 and 0.547 m for the multi-GNSS solution. When average RMS values are analyzed, the multi-

GNSS solution increases the positioning accuracy of GPS-only solution by 31.5%, 32.2%, and 31.9% on average for the horizontal, vertical, and 3D positioning errors.

Table 6.15: Station-based RMS values of horizontal, vertical, and 3D positioning errors (in:m) for the GPS-only and multi-GNSS single-frequency code-phase combination solutions with IGS-RTS products.

Station	GPS-only			Multi-GNSS		
	Horizontal	Vertical	3D	Horizontal	Vertical	3D
ABMF	0.211	0.310	0.375	0.167	0.232	0.286
AREG	0.163	0.224	0.277	0.110	0.178	0.209
DJIG	0.175	0.293	0.341	0.123	0.195	0.231
DRAO	0.601	0.610	0.857	0.326	0.353	0.480
FFMJ	0.282	0.261	0.384	0.208	0.194	0.285
HKSL	0.270	0.336	0.431	0.208	0.223	0.305
HOFN	0.245	0.290	0.380	0.167	0.166	0.235
ISTA	0.403	0.442	0.598	0.254	0.262	0.365
MADR	0.765	0.737	1.062	0.569	0.547	0.789
MERS	0.238	0.292	0.377	0.149	0.197	0.247
NKLG	0.251	0.303	0.394	0.138	0.201	0.244
NNOR	0.430	0.477	0.642	0.223	0.303	0.376
OHI3	0.226	0.294	0.371	0.152	0.196	0.248
REUN	0.250	0.334	0.417	0.194	0.213	0.288
ULAB	0.306	0.508	0.593	0.228	0.345	0.413
ALL	0.332	0.386	0.508	0.227	0.261	0.346

6.4.3. Dual-frequency PPP with IGS Real-time Products

This section presents the performance analysis of the GPS-only and multi-GNSS dual-frequency PPP solutions with IGS-RTS products. The processing strategies employed in the dual-frequency PPP solutions are provided in Table 6.16. Also, the same procedure applied in the previous assessments was utilized to analyze the positioning performance of dual-frequency PPP solutions.

Figure 6.26 shows probability distributions of positioning errors for the GPS-only and multi-GNSS dual-frequency PPP solutions with IGS-RTS products. Similarly, the positioning solutions within the first-hour period were excluded in the analysis because of preventing the impact of unconverged phase ambiguity parameters and also providing consistency with previous assessments. As can be observed from the figure, RMS values of the GPS-only solution are 0.200, 0.250, and 0.318 m in the north, east, and up directions, while they are 0.074, 0.092, and 0.131 m respectively for the multi-GNSS solution. The positioning performance of both solutions is considerably better than corresponding solutions where ultra-rapid prod-

Table 6.16: Processing strategies applied for the dual-frequency PPP solutions with IGS-RTS products.

Item	**Processing strategy**
Observations	Dual-frequency ode pseudorange and phase observations on L1 and L2 for GPS and GLONASS, E1 and E5a for Galileo, B1 and B2 for BDS
Satellite orbit and clock source	Broadcast ephemeris and IGS-RTS corrections
Dry part of troposphere	Corrected using Saastamoinen (Saastamoinen, 1972) model with the GPT3 and VMF3 (Landskron and Böhm, 2018)
Wet part of troposphere	Estimated
Ionosphere	Dual-frequency ionosphere-free combination
TGD	Not corrected
Relativistic clock error	Corrected (Section 3.3)
Relativistic path error	Corrected (Section 3.3)
Satellite antenna PCOs and PCVs	Not corrected
Receiver antenna PCOs and PCVs	Corrected with IGS antenna model (Section 3.6)
Receiver antenna reference point	Corrected (Section 3.6)
Carrier wind-up	Corrected (Section 3.7)
Cycle slip detection	Implemented (Section 3.9)
Site displacement effects	Corrected (Section 3.8)
Standard deviations of observations	0.3 m for code pseudoranges,0.003 m for phase observations
Initial ratios of multi-GNSS observations	$\sigma^2_{P_1^G} : \sigma^2_{P_1^R} : \sigma^2_{P_1^E} : \sigma^2_{P_1^C} = 1 : 2 : 2 : 2$ $\sigma^2_{L_1^G} : \sigma^2_{L_1^R} : \sigma^2_{L_1^E} : \sigma^2_{L_1^C} = 1 : 2 : 2 : 2$
Observation weights	Elevation dependent
Adjustment method	Robust Kalman filter with improved IGG III function (Section 4.3.1)

ucts are employed. Besides, the combination of multi-constellation increases the positioning accuracy substantially and can provide sub-decimeter positioning errors in the horizontal directions.

On the other hand, Figure 6.27 shows temporal variation of 3D positioning errors obtained from the GPS-only and multi-GNSS dual-frequency PPP solutions with IGS-RTS products. As shown in the figure, the performance of dual-frequency PPP is better than the other positioning models. Also, the multi-GNSS integration enhances the positioning performance of the GPS-only solution considerably in terms of both positioning accuracy and convergence time. The multi-GNSS solution with IGS-RTS provides the best positioning performance for real-time absolute GNSS positioning techniques. Moreover, average convergence times computed for the GPS-only and multi-GNSS solutions are 20.27 and 11.43 minutes respectively, which means that the multi-GNSS solution improves the convergence performance of the GPS-only solution by 43.6%. For real-time absolute GNSS positioning techniques, the

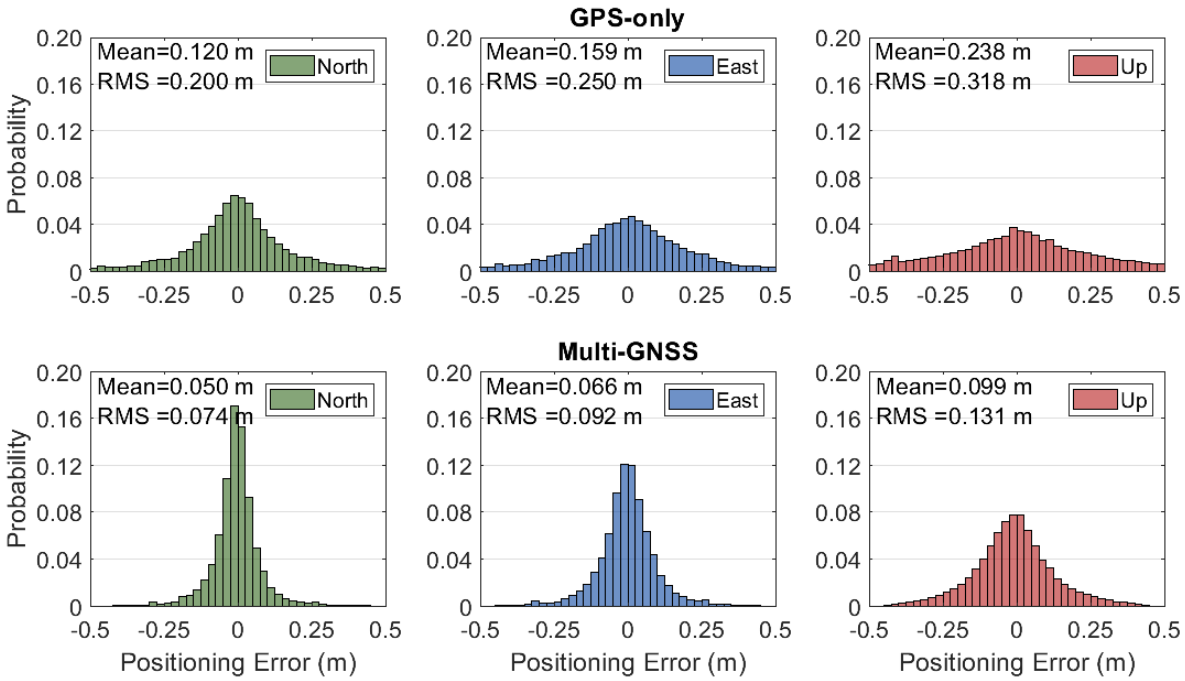

Figure 6.26: Probability distributions of positioning errors for the GPS-only and multi-GNSS dual-frequency PPP solutions with IGS-RTS products.

shortest convergence time can be acquired from the multi-GNSS dual-frequency PPP with IGS-RTS products.

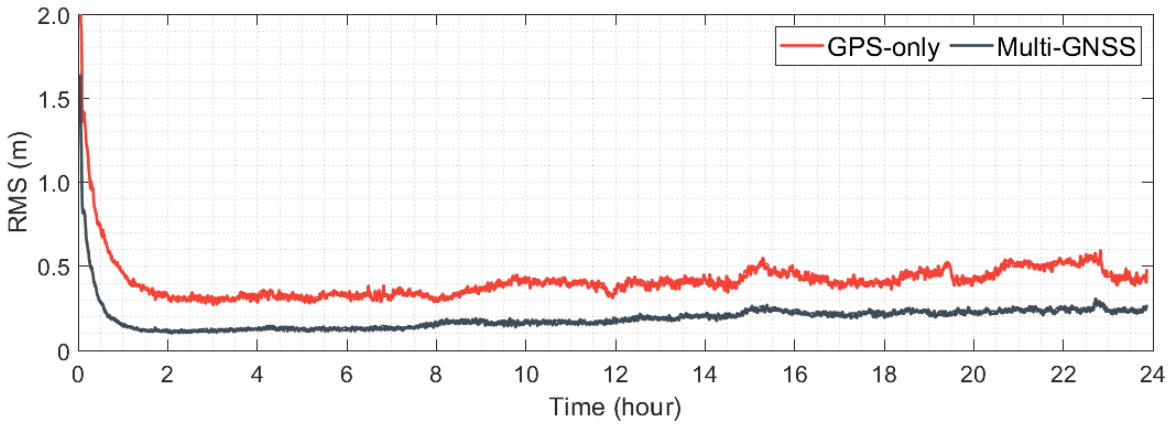

Figure 6.27: Temporal variation of 3D RMS errors for the GPS-only and multi-GNSS dual-frequency PPP solutions with IGS-RTS products.

Finally, Table 6.17 presents station-based RMS values of horizontal, vertical, and 3D positioning errors for the GPS-only and multi-GNSS dual-frequency PPP solutions with IGS-RTS products. Also, average RMS values calculated taking all stations into consideration are provided in the last row. From the table, it can be observed that the multi-GNSS solution has considerably better positioning accuracy in the whole components for all stations. Average RMS values of horizontal, vertical, and 3D positioning errors are 0.298, 0.318, and 0.468 m

for the GPS-only solution, while they are 0.119, 0.131, and 0.177 respectively for the multi-GNSS solution. The results show that the multi-GNSS solution enhances the positioning performance better than 50% for all components. Also, 3D positioning accuracy of under 20 cm can be achieved by real-time multi-GNSS dual-frequency PPP solution with IGS-RTS products.

Table 6.17: Station-based RMS values of horizontal, vertical, and 3D positioning errors (in:m) for the GPS-only and multi-GNSS dual-frequency PPP solutions with IGS-RTS products.

Station	**GPS-only**			**Multi-GNSS**		
	Horizontal	**Vertical**	**3D**	**Horizontal**	**Vertical**	**3D**
ABMF	0.261	0.337	0.426	0.093	0.115	0.148
AREG	0.254	0.300	0.393	0.093	0.129	0.159
DJIG	0.287	0.371	0.469	0.091	0.135	0.163
DRAO	0.248	0.253	0.354	0.135	0.124	0.184
FFMJ	0.424	0.348	0.548	0.138	0.142	0.198
HKSL	0.322	0.322	0.455	0.125	0.146	0.192
HOFN	0.252	0.243	0.350	0.096	0.102	0.140
ISTA	0.473	0.384	0.609	0.109	0.128	0.168
MADR	0.498	0.473	0.687	0.179	0.161	0.241
MERS	0.385	0.417	0.568	0.135	0.141	0.195
NKLG	0.296	0.370	0.474	0.105	0.146	0.180
NNOR	0.417	0.415	0.588	0.114	0.116	0.163
OHI3	0.429	0.420	0.600	0.123	0.123	0.174
REUN	0.359	0.376	0.520	0.087	0.111	0.141
ULAB	0.438	0.316	0.584	0.164	0.159	0.228
ALL	0.298	0.318	0.468	0.119	0.131	0.177

6.5. Summary of Positioning Analysis for Real-time Absolute GNSS Positioning

To evaluate the positioning results in a single chart, Table 6.18 summarizes RMS values of horizontal, vertical, and 3D positioning errors obtained from all real-time absolute GNSS positioning techniques provided in the previous sections. In this regard, it is possible to provide a general perspective on the performance of real-time absolute positioning techniques and to understand the level of positioning accuracy that can be acquired from these techniques. The table compiles average RMS values computed considering all positioning solutions which are already provided in the previous sections. The results are grouped regarding the positioning techniques, the applied products, and positioning modes. Together with the absolute positioning techniques adopted in this thesis, the performance of SPP with the GPS-only and multi-GNSS modes are also provided in the table.

Table 6.18: Positioning performance of real-time absolute GNSS positioning techniuqes adopted in the thesis.

Pos. Technique	Product	Pos. Mode	RMS (m)		
			Horizontal	Vertical	3D
SPP	Broadcast Eph.	GPS-only	4.658	6.876	7.821
		Multi-GNSS	4.376	5.184	6.255
Single-frequency code pseudorange positioning	CODE ultra-rapid	GPS-only	1.496	2.995	3.348
		Multi-GNSS	1.241	2.210	2.535
	IGS ultra-rapid	GPS-only	1.111	2.475	2.713
	WHU ultra-rapid	GPS-only	1.293	2.564	2.871
		Multi-GNSS	0.958	1.737	1.983
	IGS-RTS	GPS-only	0.872	2.153	2.323
		Multi-GNSS	0.623	1.389	1.522
Single-frequency code-phase combination	CODE ultra-rapid	GPS-only	0.698	0.781	1.047
		Multi-GNSS	0.518	0.579	0.777
	IGS ultra-rapid	GPS-only	0.767	0.823	1.125
	WHU ultra-rapid	GPS-only	0.990	1.080	1.465
		Multi-GNSS	0.472	0.540	0.717
	IGS-RTS	GPS-only	0.332	0.386	0.508
		Multi-GNSS	0.227	0.261	0.346
Dual-frequency PPP	CODE ultra-rapid	GPS-only	0.384	0.306	0.490
		Multi-GNSS	0.230	0.287	0.348
	IGS ultra-rapid	GPS-only	0.383	0.332	0.507
	WHU ultra-rapid	GPS-only	0.325	0.338	0.469
		Multi-GNSS	0.154	0.252	0.296
	IGS-RTS	GPS-only	0.298	0.318	0.468
		Multi-GNSS	0.119	0.131	0.177

For the single-frequency code pseudorange positioning, the multi-GNSS solution with WHU ultra-rapid products provides the highest positioning accuracy among the ultra-rapid products with a 3D RMS error of 1.983 m. Still, the employment of IGS-RTS products improves the positioning performance remarkably. When considering all the single-frequency code pseudorange positioning solutions, the multi-GNSS solution with IGS-RTS products presents the best positioning performance by providing a 3D positioning accuracy of nearly 1.5 m. In comparison with SPP, which is the fundamental positioning technique for real-time single-frequency positioning, there is a significant improvement in the positioning performance.

As regards the single-frequency code-phase combination, a 3D positioning accuracy of almost 0.7 m can be achieved with the multi-GNSS solutions using CODE and WHU ultra-rapid products. The results show that it is possible to reach sub-meter positioning accuracy with the multi-GNSS solutions of ultra-rapid products. Furthermore, the GPS-only and

multi-GNSS solutions with IGS-RTS products improve the positioning performance considerably when compared to the corresponding solutions with ultra-rapid products. The multi-GNSS solution with IGS-RTS products provides the best positioning performance with the 3D positioning error of 0.346 m, which is nearly two times better than the best positioning accuracy which can be acquired from ultra-rapid products.

When it comes to the dual-frequency PPP solutions, the multi-GNSS solutions with WHU ultra-rapid products have a 3D RMS error of 0.296 m, which is the best positioning performance among the ultra-rapid products. Similarly, the multi-GNSS with IGS-RTS products improves the positioning accuracy considerably with RMS values of 0.119, 0.131, and 0.177 m for the horizontal, vertical, and 3D positioning errors. The results show that the multi-GNSS dual-frequency PPP solution with IGS-RTS products has the best positioning accuracy considering all real-time absolute positioning techniques.

6.6. Impact of Different Robust Kalman Filter Methods on the Performance of Real-time Absolute GNSS Positioning

As part of this thesis, the proposed filtering method, whose details are provided in Section 5.1, combines the variance component estimation with the robust Kalman filtering. Herein, the improved version of the IGG III function is adopted as a fundamental robust estimator. Still, it is known that there are many robust Kalman filter methods employed for different applications in the literature, such as aerospace engineering, automation systems, geodetic applications, etc (Mu, Kuok and Yuen, 2017; Zhao et al., 2019; Yang, Song and Xu, 2002; Guo and Zhang, 2014). The robust Kalman filter methods which are most commonly employed in the GNSS applications are provided in Section 4.3.1. In this regard, the experimental analysis was conducted to investigate the impact of different robust Kalman filter methods on the performance of real-time absolute GNSS positioning in this section.

Up to this point, all absolute GNSS positioning processes for the thesis were performed using the robust Kalman filter method that includes improved IGG III function together with higher variance ratios. This section looks for the answer to the question of what would be the impact of using different robust Kalman filter methods on the real-time absolute positioning performance. As the influence of variance component estimation will additionally be evaluated in the following section, the employment of higher variance ratios still remains, while different robust Kalman filters are utilized in this section. In this regard, four different filtering modes are constructed to assess the impact of different robust Kalman filters, whose details are provided in Table 6.19. Moreover, only the multi-GNSS solution with IGS-RTS products, which has the best positioning performance for all real-time absolute GNSS positioning techniques,

are adopted in the experimental analysis for the sake of simplicity. In this context, the observation dataset was processed in four different filtering modes for three absolute GNSS positioning techniques adopted in this thesis, which are the single-frequency code pseudorange positioning, single-frequency code-phase combination, and dual-frequency PPP. The results obtained from the positioning processes were evaluated using the similar procedure applied in the previous sections.

Table 6.19: Filtering modes adopted for the experimental test.

Filtering Mode	**Description**
SKF	Includes the standard Kalman filter without any robust function.
CRF	Employs the robust Kalman filter with the IGG III function for each individual observation
TRF	Applies the robust Kalman filter with the t-test criterion-based classification method for each individual observation
IRF	Utilizes the robust Kalman filter with the improved procedure which employs the IGG III function only for the observation having the largest standardized residual iteratively.

As regards the single-frequency code pseudorange positioning, Figure 6.28 illustrates 3D positioning errors computed for the solutions of SKF, CRF, TRF, and IRF filtering modes at NNOR station on April 26, 2020. As shown in the figure, the positioning performance can change considerably depending on the applied filtering method. In the SKF mode, which employs directly standard Kalman filtering without any robust function, the positioning performance is influenced by the outliers and unexpected errors substantially. Moreover, the implementation of robust Kalman filters improves the positioning performance considerably as can be observed from the figure. Still, it can be seen that there are substantial differences between the positioning performance acquired from different robust Kalman filter methods. It is apparent from the figure that the TRF and IRF filtering modes provide better positioning accuracy when compared to the SKF and CRF filtering modes.

The posterior observation residuals computed after the estimation processes are important indicators for the filtering performance because they actually reflect the harmony between measurements and defined dynamic model. In other words, the higher coherence between measurements and projected stochastic and functional properties pave the way for a better positioning performance, which also means the lower observation residuals. In this regard, Figure 6.29 depicts observation residuals of GPS, GLONASS, Galileo, and BDS satellites computed for the single-frequency code pseudorange positioning solutions with the SKF, CRF, TRF, and IRF filtering modes at NNOR station on April 26, 2020. In the figure, observation residuals are aligned according to the satellite elevation angle. It can be observed from the figure that the behavior of observation residuals is very different for each navigation system. Especially, observation residuals of BDS satellites seem less dependent on the satel-

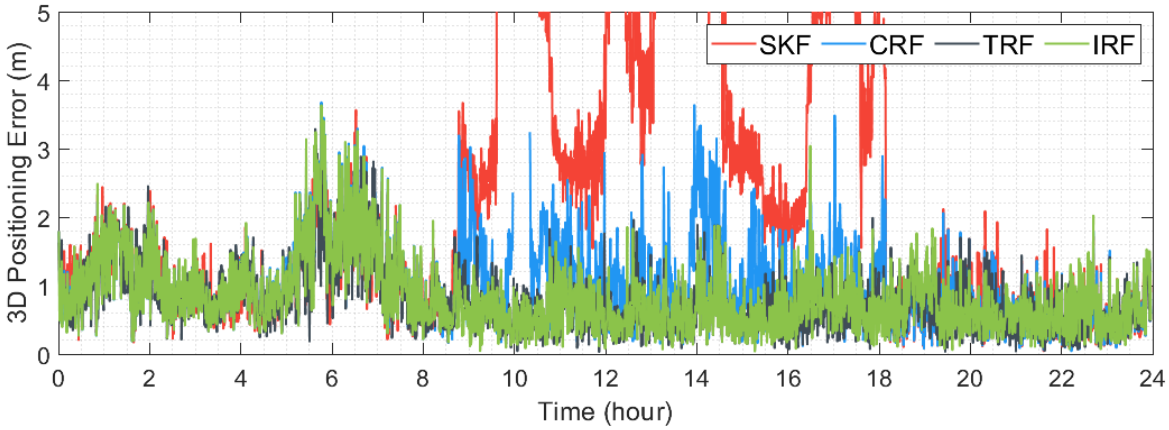

Figure 6.28: Daily 3D positioning errors acquired from the single-freequncy code pseudorange positioning solutions with the SKF, CRF, TRF and IRF filtering modes at NNOR stations on April 26, 2020.

lite elevation. The reason behind that is the presence of geostationary BDS satellites in the Asia-pacific region, in which the station is located. Additionally, relatively lower quality of real-time satellite orbit and clock products for BDS satellites can be another factor to acquire higher observation residuals. It can be said that observation residuals of other navigation systems are comparable with each other. As regards the evaluation of observation residuals for different filtering modes, it is apparent from the figure that lower observation residuals are acquired from the CRF, TRF, and TRF filtering modes, which applies the robust Kalman filters, in comparison of the SKF mode for each navigation system. Robust Kalman filters usually determine the outliers as well as the observations which have weights unnecessarily higher, and decrease their impact in the estimation process. In this way, it is possible to achieve a better filtering performance and therefore the lower observation residuals. Also, it should be mentioned that observation outliers are excluded from the filtering process, so it is possible to not see any observation residual, which is already been in other filtering modes, in some filtering mode. It means that the filtering mode interprets this observation as an outlier. Consequently, the CRF and IRF filtering modes provide considerably lower observation residuals for all navigation systems.

Figure 6.30 shows probability distributions of positioning errors for the single-frequency code pseudorange positioning solutions with the SKF, CRF, TRF and IRF filtering modes respectively. Probability distributions were constructed considering all epoch-wise positioning solutions at 15 stations over the two-week period similar to the previous sections. In the figure, RMS values in the north, east, and up directions are also provided for the corresponding positioning solutions. As shown in the figure, RMS values obtained from the SKF mode are 0.876, 0.728, and 2.404 m in the north, east, and up directions, which is quietly the worst positioning performance. The positioning performance is improved with the employment of robust Kalman filters in the CRF, TRF, and IRF filtering modes. The solution with the IRF

filtering mode has the lowest positioning errors with RMS values of 0.478, 0.399, and 1.389 m in the north, east, and up directions respectively, which refers to improvements better than 40% in all directions when compared to the SKF mode.

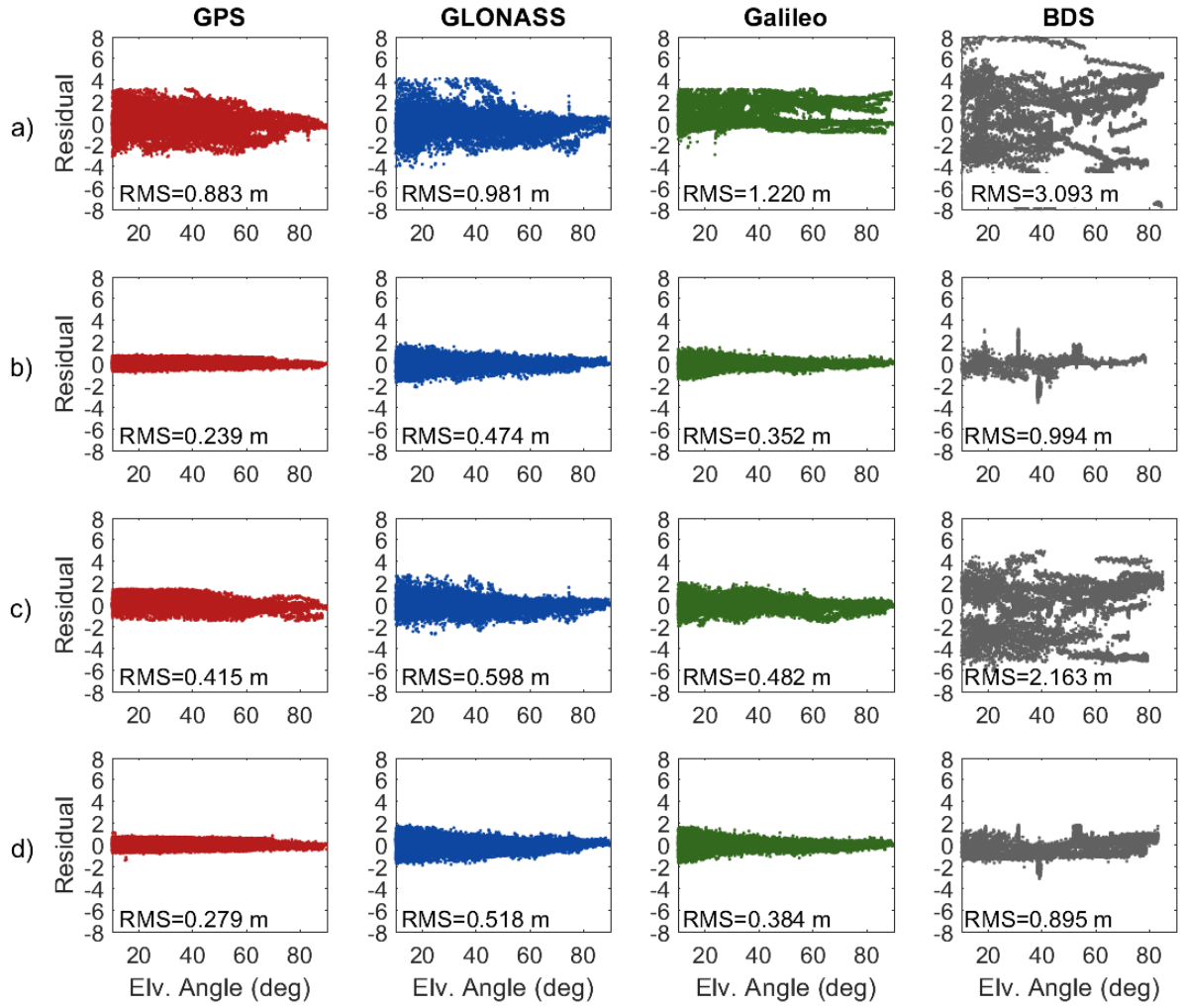

Figure 6.29: Residuals of GPS, GLONASS, Galileo and BDS satellites (in:m) obtained from the single-frequency code pseudorange positioning solutions with the SKF (a), CRF (b), TRF (c) and IRF (d) filtering modes at NNOR station on April 26, 2020.

Table 6.20 presents average RMS values of horizontal, vertical, and 3D positioning errors calculated for the single-frequency code pseudorange positioning solutions with the SKF, CRF, TRF and IRF filtering modes considering all positioning solutions. From the table, it can be observed that the filtering modes which employ robust Kalman filter methods enhance the positioning performance significantly in comparison with the SKF mode. Although the positioning performance of CRF, TRF, and IRF modes is quite compatible, the IRF filtering mode provides the best positioning accuracy in all the directions with RMS values of 0.623, 1.389, and 1.522 m of horizontal, vertical, and 3D positioning errors.

Regarding the single-frequency code-phase combination solutions, Figure 6.31 illustrates

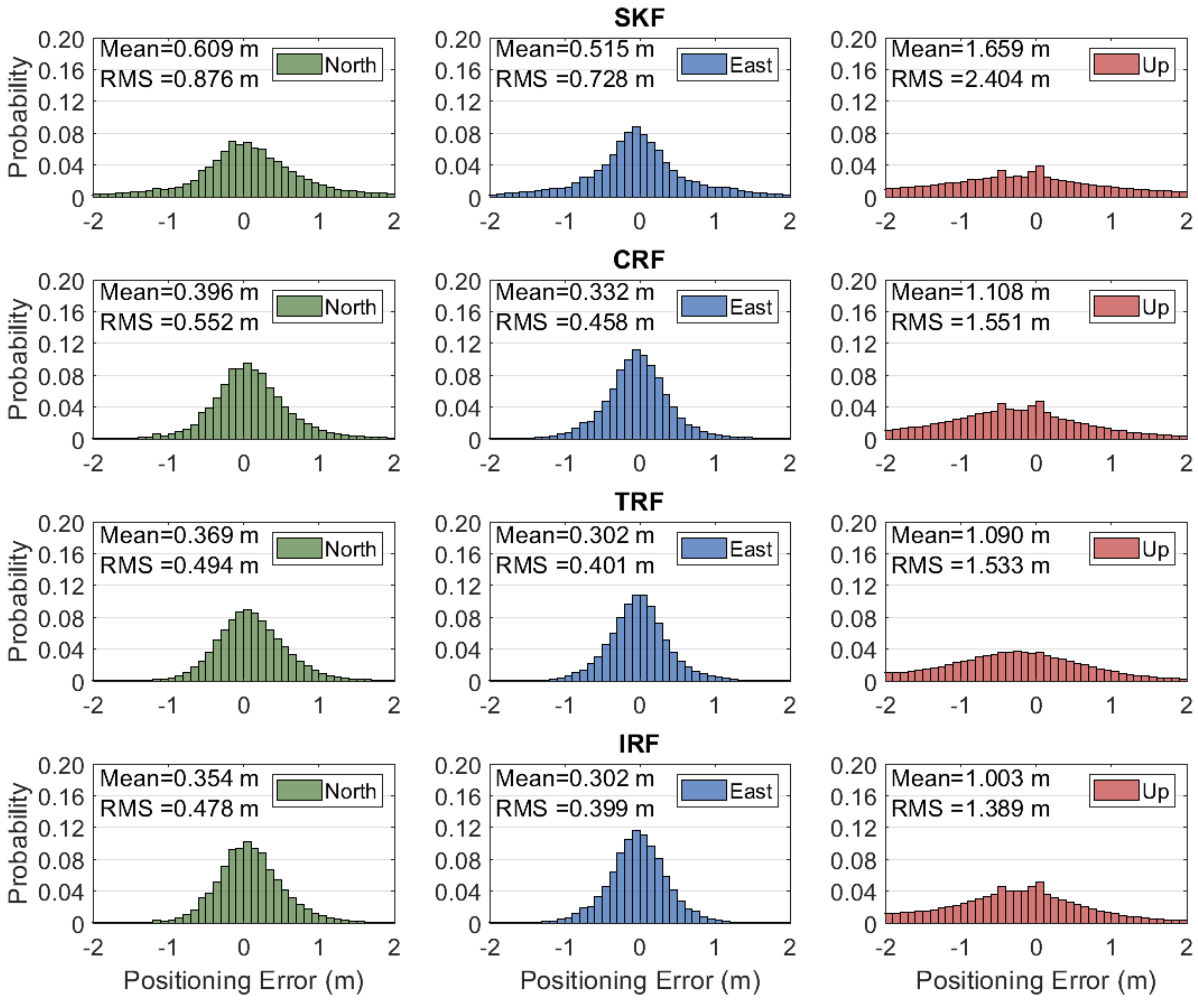

Figure 6.30: Probability distributions of positioning errors for the single-frequency code pseudorange positioning solutions with the SKF, CRF, TRF and IRF filtering modes.

Table 6.20: Average RMS values of horizontal, vertical, and 3D positioning errors for the single-frequency code pseudorange positioning solutions with the SKF, CRF, TRF and IRF filtering modes.

Filtering Mode	**RMS Errors (m)**		
	Horizontal	**Vertical**	**3D**
SKF	1.139	2.404	2.660
CRF	0.718	1.551	1.709
TRF	0.637	1.533	1.660
IRF	0.623	1.389	1.522

3D positioning errors computed for the SKF, CRF, TRF and IRF filtering modes at NNOR station on April 26, 2020. As can be seen from the figure, the applied filtering method has a considerable impact on the positioning performance which can be acquired from the single-frequency code-phase combination solutions. It is also apparent in the figure that the positioning performance with the SKF filtering mode is behind the other filtering modes.

Similar to the single-frequency code pseudorange positioning solutions, the employment of robust Kalman filter methods augments the positioning accuracy considerably compared with the SKF mode.

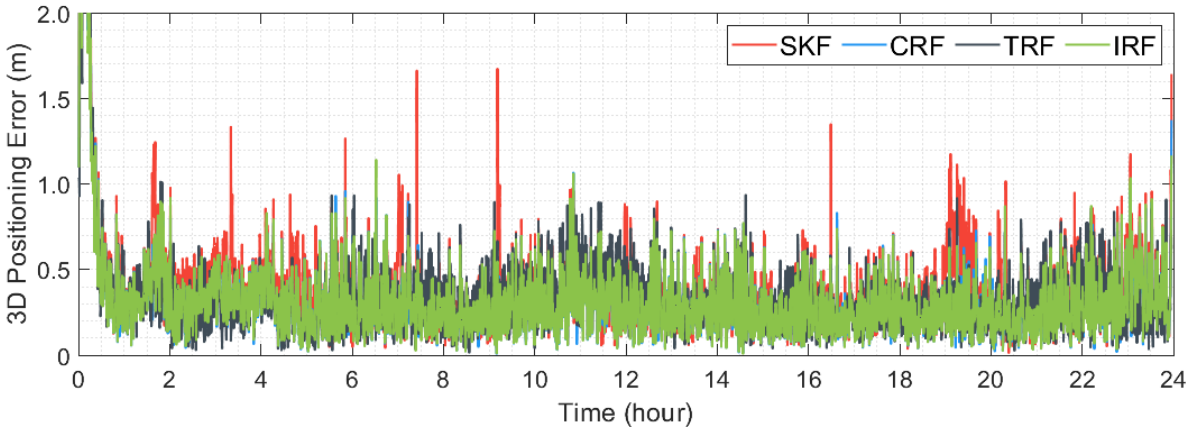

Figure 6.31: Daily 3D positioning errors acquired from the single-frequency code-phase combination solutions with the SKF, CRF, TRF and IRF filtering modes at NNOR station on April 26, 2020.

Figure 6.32 illustrates observation residuals of GPS, GLONASS, Galileo and BDS satellites calculated for the single-frequency code- phase combination solutions with the SKF, CRF, TRF and IRF filtering modes at NNOR station on April 26, 2020. The first thing standing out in the figure is that observation residuals acquired from the single-frequency code-phase combination solutions are substantially lower than those of the single-frequency code pseudorange positioning solutions owing to the presence of carrier-phase observations. Additionally, observation residuals of different navigation systems are quite compatible with each other when compared to the single-frequency code pseudorange solutions. Still, the highest observation residuals for all the navigation systems are acquired with the SKF filtering mode. With the robust Kalman filter methods, the lower observation residuals are obtained for the whole navigation system. Although the results are quite similar for the CRF, TRF, and IRF filtering modes, the TRF mode provides the lowest RMS values for observation residuals of GPS, GLONASS, Galileo, and BDS satellites.

Probability distributions of positioning errors for the single-frequency code-phase combination solutions with the SKF, CRF, TRF and IRF filtering modes are provided in Figure 6.33. As shown from the figure, RMS values computed for the single-frequency code-phase combination solutions are significantly lower than those of the single-frequency code pseudorange positioning solutions. The SKF filtering mode has RMS values of 0.188, 0.234, and 0.333 m in the north, east, and up directions, which is the worst positioning performance. The employment of robust Kalman filters increases the positioning accuracy considerably. Although RMS values of the TRF and IRF filtering modes are very close, the positioning performance of the IRF mode is quite better than those of other filtering modes with RMS

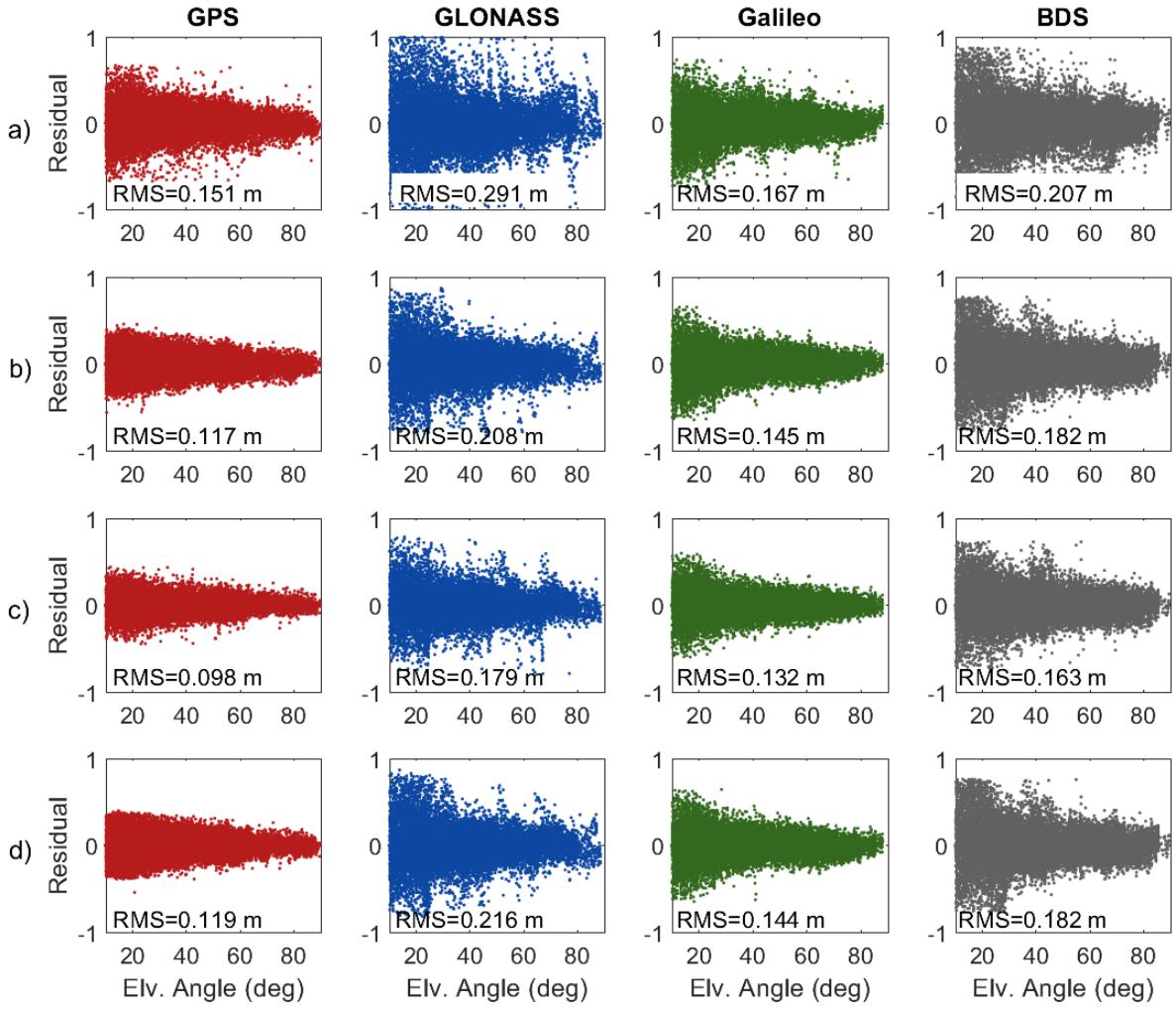

Figure 6.32: Residuals of GPS, GLONASS, Galileo and BDS satellites (in:m) obtained from the single-frequency code-phase combination solutions with the SKF (a), CRF (b), TRF (c) and IRF (d) filtering modes at NNOR station on April 26, 2020.

values of 0.137, 0.181, and 0.261 m respectively.

As previously stated, the convergence time is an important measure for the performance of positioning techniques which includes carrier-phase observations. In this context, Table 6.21 presents average convergence times calculated for the single-frequency code-phase combination solutions with the SKF, CRF, TRF, and IRF filtering modes considering all positioning solutions at 15 stations over the two-week periods. As can be shown from the figure, average convergence times are 64.74, 47.62, 46.12, and 44.47 minutes for the SKF, CRF, TRF, and IRF filtering modes, respectively. Similarly, the filtering modes including robust Kalman filter methods lessen the convergence time substantially, and the IRF filtering mode provides the best convergence performance.

Finally, average RMS values of horizontal, vertical, and 3D positioning errors acquired from the single-frequency code-phase combination solutions with the SKF, CRF, TRF and IRF

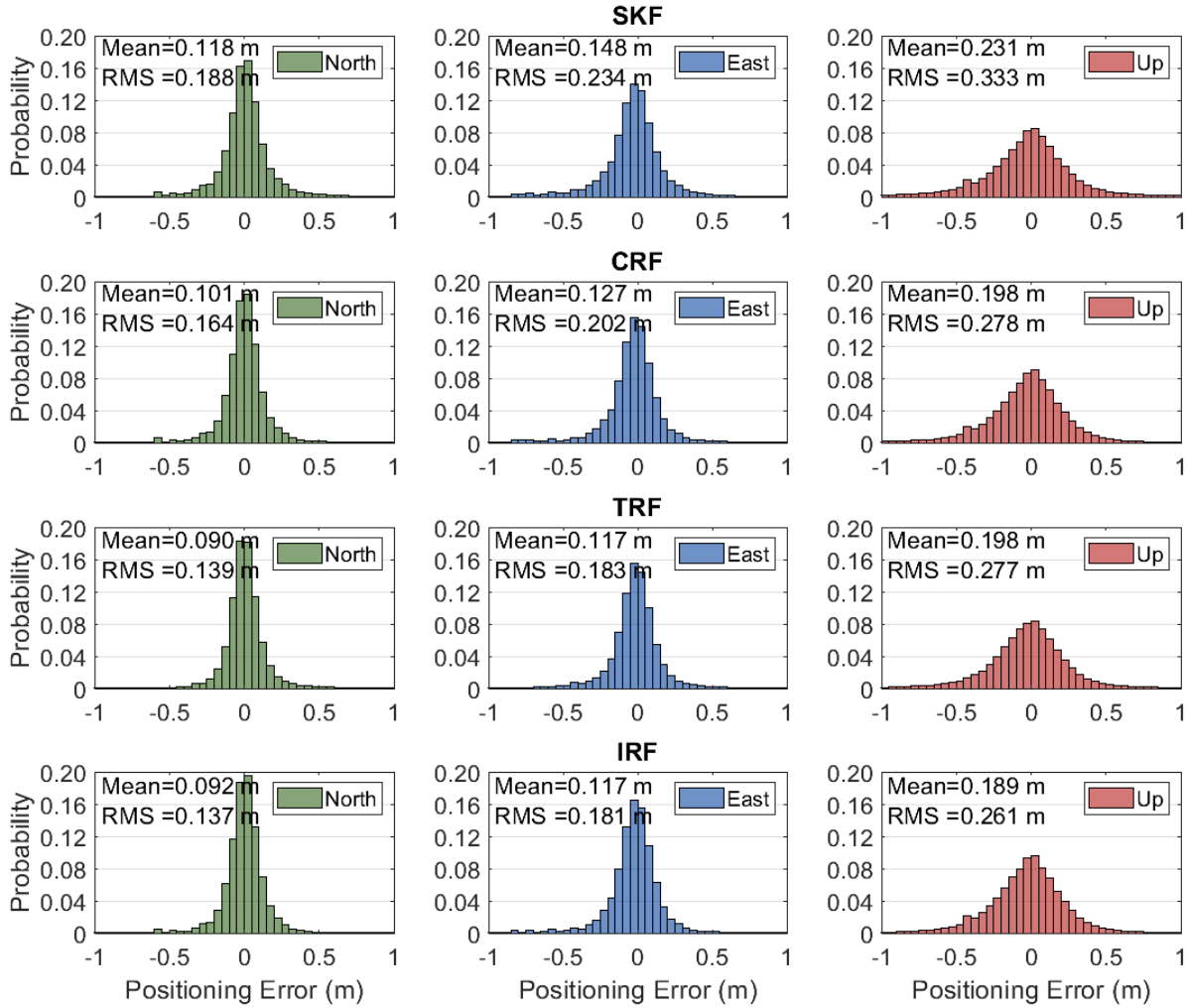

Figure 6.33: Probability distributions of positioning errors for the single-frequency-phase combination solutions with the SKF, CRF, TRF and IRF filtering modes.

Table 6.21: Average convergence times for the single-frequency code-phase combination solutions with the SKF, CRF, TRF and IRF filtering modes.

Filtering Mode	**Convergence Times (min)**
SKF	64.74
CRF	47.62
TRF	46.12
IRF	44.47

filtering modes are presented in Table 6.22 respectively. Similarly, the highest RMS values are coming from the single-frequency code-phase combination solution employing the SKF filtering mode with RMS values of 0.300, 0.332, and 0.448 m for the horizontal, vertical, and 3D positioning errors. Again, it can be stated that the positioning performance is improved with the implementation of robust Kalman filter methods. Although the results are quite similar for the whole filtering modes where robust Kalman filter methods are employed, the

IRF mode has the best positioning accuracy with RMS values of 0.227, 0.261, and 0.346 m for the horizontal, vertical and 3D positioning errors.

Table 6.22: Average RMS values of horizontal, vertical, and 3D positioning errors for the single-frequency code-phase combination solutions with the SKF, CRF, TRF and IRF filtering modes.

Filtering Mode	**RMS Errors (m)**		
	Horizontal	**Vertical**	**3D**
SKF	0.300	0.333	0.448
CRF	0.260	0.278	0.381
TRF	0.230	0.277	0.360
IRF	0.227	0.261	0.346

On the other hand, Figure 6.34 depicts 3D positioning errors computed for the dual-frequency PPP solutions with the SKF, CRF, TRF and IRF filtering modes at NNOR station on April 26, 2020. From the figure, it can be observed that the positioning performance acquired from the SKF mode is behind those of other filtering modes. Although the robust Kalman filter methods augment the positioning accuracy, the positioning performance of the CRF filtering mode is influenced by the outliers and unexpected errors more than those of TRF and IRF filtering modes. Still, the convergence performance of the CRF mode is quite better than the others. It is also apparent from the figure that the TRF and IRF provide considerably better positioning performance compared with the other filtering modes.

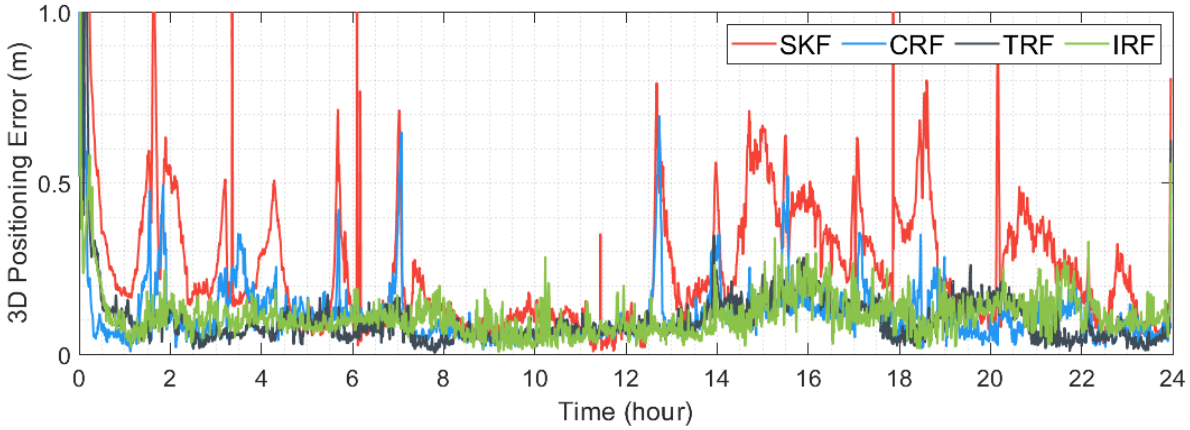

Figure 6.34: Daily 3D positioning errors acquired from the dual-frequency PPP solutions with the SKF, CRF, TRF and IRF filtering modes at NNOR station on April 26, 2020.

Similarly, Figure 6.35 shows observation residuals for dual-frequency ionosphere-free phase observations of GPS, GLONASS, Galileo and BDS satellites acquired from the dual-frequency PPP solutions with the SKF (a), CRF (b), TRF (c) and IRF (d) filtering modes at NNOR station on April 26, 2020. It is clear from the figure that, observation residuals computed for dual-frequency ionosphere-free phase observations are substantially lower than single-frequency observations provided previously for all the navigation systems. When the figure

is analyzed, it can be observed that the SKF filtering mode has the highest observation residuals for all navigation systems. Also, the use of robust Kalman filter methods decreases the phase observation residuals obtained from the dual-frequency PPP solutions. From the figure, it can also be observed that the CRF filtering mode presents the lowest observation residuals for GPS, GLONASS, Galileo, and BDS satellites, while observation residuals are quite comparable for the TRF and IRF filtering modes.

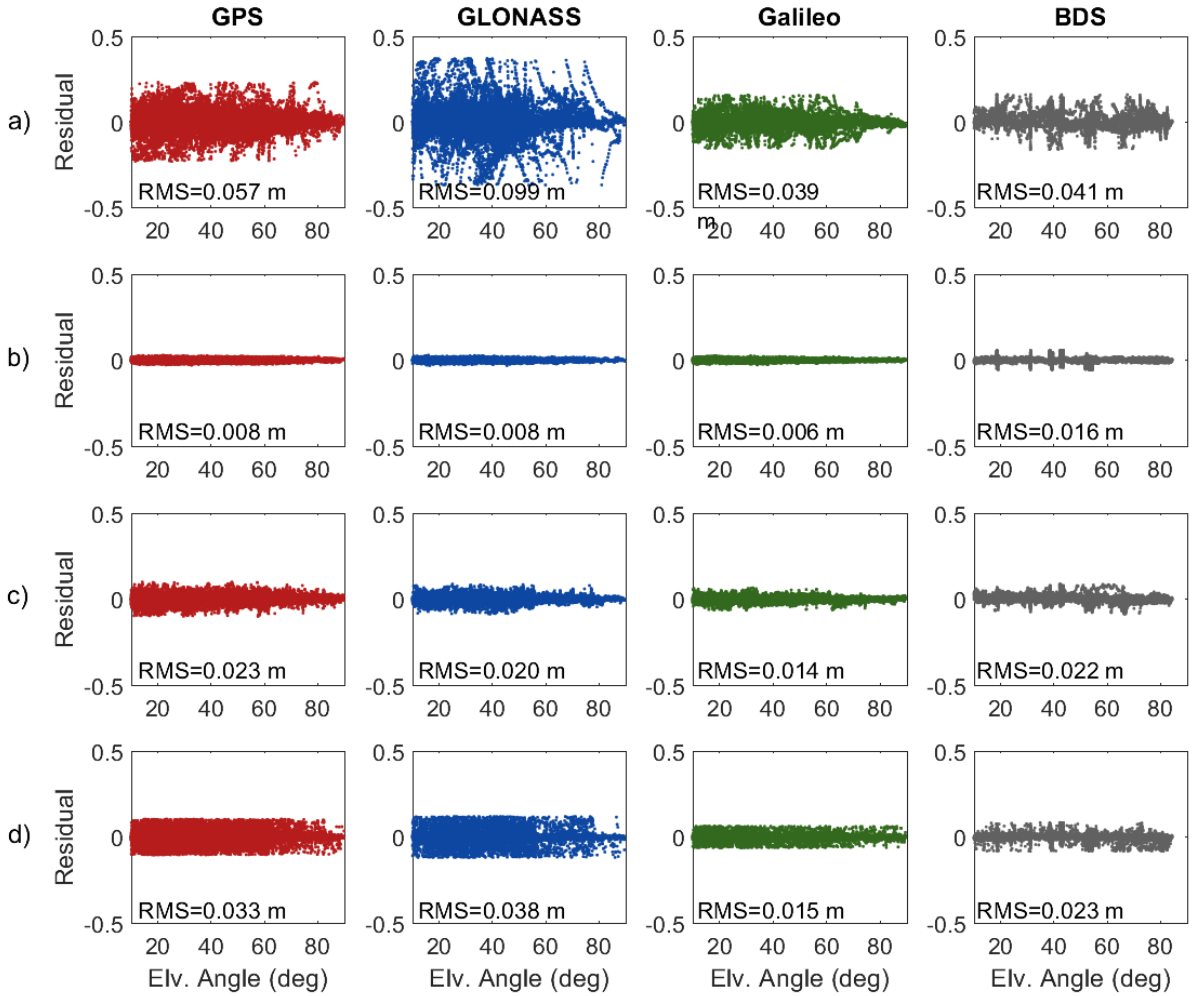

Figure 6.35: Phase observation residuals of GPS, GLONASS, Galileo and BDS satellites (in:m) obtained from the dual-frequency PPP solutions with the SKF (a), CRF (b), TRF (c) and IRF (d) filtering modes at NNOR station on April 26, 2020.

Probability distributions of positioning errors for the dual-frequency PPP solutions with the SKF, CRF, TRF and IRF filtering modes are demonstrated in Figure 6.36. As shown in the figure, the SKF filtering mode provides the worst positioning performance with RMS values of 0.108, 0.136, and 0.217 m in the north, east, and up directions respectively. When RMS values computed for the CRF, TRF, and IRF filtering modes are analyzed, it can be said that the positioning accuracy of the SKF mode is improved considerably with the use of robust Kalman filter methods. For the up direction, the TRF and IRF filtering modes have quite compatible RMS values, which are 0.130 and 0.131 m. Still, the TRF filtering mode

provides better horizontal positioning performance with RMS values of 0.054 and 0.076 m in the north and east directions respectively when compared to the other robust Kalman filter methods.

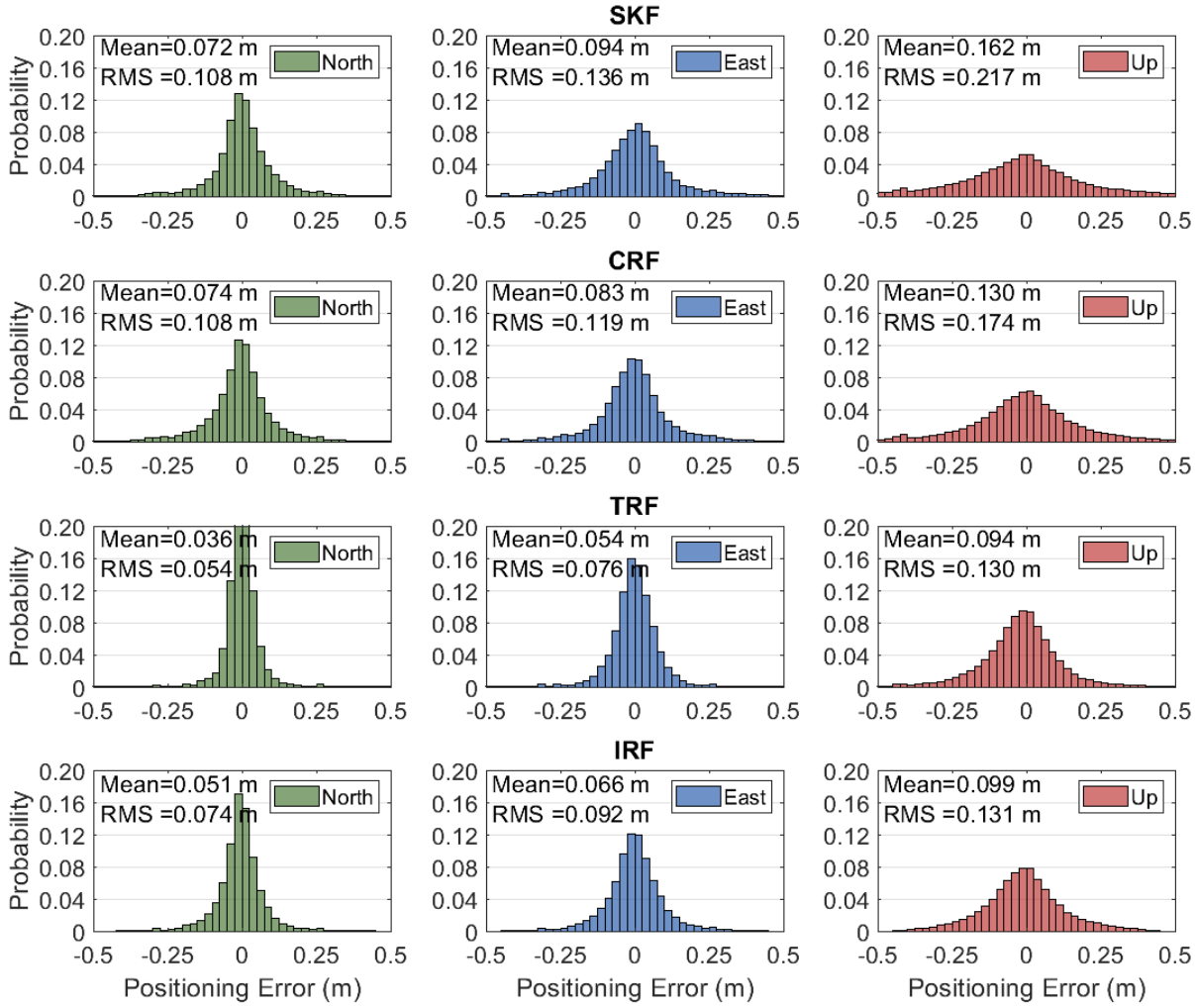

Figure 6.36: Probability distributions of positioning errors for the dual-frequency PPP solutions with the SKF, CRF, TRF and IRF filtering modes.

Considering all positioning solutions at 15 stations over the two-week periods, average convergence times computed for the dual-frequency PPP solutions with the SKF, CRF, TRF, and IRF filtering modes are presented in Table 6.23. As can be seen from the table, the SKF filtering mode provides an average convergence time of 34.42 minutes, which is quite longer than those of other filtering modes. From the table, it can be observed that the convergence performance is enhanced by the use of filtering modes where the robust Kalman filter methods are employed. The IRF filtering mode presents the bets convergence performance with an average convergence time of 11.43 minutes.

Table 6.24 presents average RMS values of horizontal, vertical, and 3D positioning errors computed for the dual-frequency PPP solutions with the SKF, CRF, TRF and IRF filtering

Table 6.23: Average convergence times for the dual-frequency PPP solutions with the SKF, CRF, TRF and IRF filtering modes.

Filtering Mode	**Convergence Times (min)**
SKF	34.42
CRF	12.75
TRF	16.18
IRF	11.43

modes taking all positioning solutions into account. From the table, it is apparent that the SKF filtering mode has the worst positioning performance with RMS values of 0.174, 0.217, and 0.278 m for the horizontal, vertical, and 3D positioning errors. It can also be seen that the positioning accuracy of the filtering modes employing the robust Kalman filter methods is substantially better than the SKF mode. While the vertical positioning performance is comparable for the TRF and IRF filtering modes, the horizontal positioning accuracy obtained from the TRF mode is slightly better than that of the IRF mode. Therefore, the TRF filtering mode has the lowest 3D positioning error with an RMS value of 0.160 m.

Table 6.24: Average RMS values of horizontal, vertical, and 3D positioning errors for the dual-frequency PPP solutions with the SKF, CRF, TRF and IRF filtering modes.

Filtering Mode	**RMS Errors (m)**		
	Horizontal	**Vertical**	**3D**
SKF	0.174	0.217	0.278
CRF	0.161	0.174	0.237
TRF	0.094	0.130	0.160
IRF	0.119	0.131	0.177

Consequently, the results show that the employment of robust Kalman filter methods improves the positioning performance of real-time absolute GNSS positioning techniques considerably. For the single-frequency code pseudorange positioning, the IRF filtering mode provides a substantially better positioning performance in comparison to the other filtering modes employing the robust Kalman filter methods, i.e. the CRF and TRF modes. Similarly, the IRF filtering mode has the best positioning performance for the single-frequency code-phase combination in terms of both positioning accuracy and convergence time. Regarding the dual-frequency PPP solution, the TRF filtering mode provides the best positioning accuracy, while the IRF filtering mode has a better convergence performance compared with the other filtering modes. As a consequence, it can be said that the IRF filtering mode presents a better positioning performance for the real-time absolute GNSS positioning techniques in a general perspective. It is actually the reason why the IRF filtering mode is adopted in the proposed filtering method in this thesis.

6.7. Contribution of Variance Component Estimation to the Performance of Real-time Absolute GNSS Positioning

As previously mentioned, traditional stochastic approaches for GNSS positioning assign constant initial variance ratios for different types of observations which are obtained from various navigation systems. Through these initial constant variance ratios, the weights of different types of observations are specified in the filtering process. Most commonly, higher variance ratios are defined for the observations of other navigation systems with respect to GPS observations assuming that the observations and orbit and clock products of other navigation have a relatively lower precision level, which assigns lower weights for these observations. Still, this type of traditional approach can be unsuccessful to reflect the actual stochastic properties of different types of observations as they are based on an assumption in specifying the observation variances, that is the observation weights. Additionally, the variance ratios are assumed to be constant for all observation processes, however, the stochastic properties of different observation types can change with time. To overcome these drawbacks and provide a more rigorous weighting approach, a novel filtering approach including variance component estimation is proposed as a part of this thesis (Section 5.1).

In the previous section, the influence of robust Kalman filter methods is analyzed in detail, and the results indicate that the IRF filtering mode including the improved version of the IGG III function provides a relatively better positioning performance for real-time absolute GNSS positioning techniques. The improved IGG III function is therefore adopted in the proposed filtering method in this thesis. Besides, the proposed filtering approach contains variance component estimation to specify the observation weights adaptively. In this regard, this section presents experimental tests conducted to assess the impact of variance component estimation on the performance of real-time absolute GNSS positioning techniques. All of the previous processes, results of which are presented in the previous sections, were performed depending on the weighting approach containing the higher variance ratios, i.e. assigning higher but constant variance ratios to GLONASS, Galileo and BDS with respect to GPS, as described in the related processing strategy tables. To understand the impact of variance component estimation, the observation dataset was processed in two additional filtering modes. The first, which is called SKF-VCE, employs the standard Kalman filter together with the variance component estimation. This filtering mode is constructed to assess the influence of robust Kalman filter and variance component estimation separately. The second integrates the robust Kalman filter containing the improved IGG III function, that is the IRF filtering mode in the previous section, with the variance component estimation. This filtering mode is the proposed filtering method as a part of this thesis and will be called IRF-VCE in the rest of this section. Moreover, the results of the two filtering modes provided in the pre-

vious section are provided here again for the sake of comparison. These two filtering modes, which are the SKF and IRF, include the standard Kalman filter and improved IGG III unction respectively together with the higher variance ratios. They will be named the SKF-HVR and IRF-HVR in the rest of this section.

The same procedure provided in the previous sections is similarly adopted herein to analyze the positioning performance of real-time absolute GNSS positioning techniques. In this context, Figure 6.37 presents 3D positioning errors obtained from the single-frequency code pseudorange positioning solutions with the SKF-HVR, SKF-VCE, IRF-HVR and IRF-VCE filtering modes at NNOR station on April 26, 2020. It can be observed from the figure that the positioning performance is improved with the use of variance component estimation. Even, the integration of the standard Kalman filter with the variance component estimation (SRF-VCE) provides significantly better positioning performance in compared to the SKF-HVR mode. Furthermore, as shown in the figure, the positioning performance of the IRF-VCE filtering mode is slightly better than that of the IRF-HVR mode.

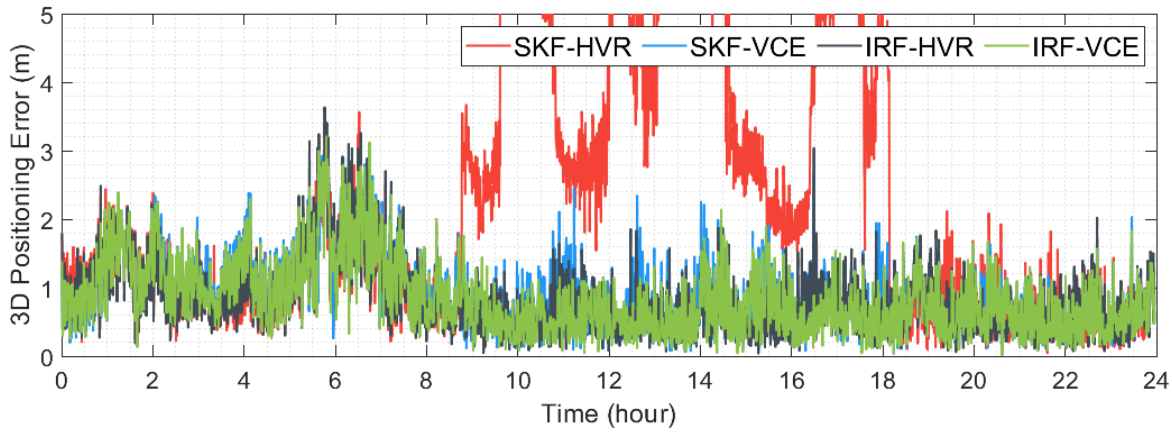

Figure 6.37: Daily 3D positioning errors acquired from the single-frequency code pseudorange positionig solutions with the SKF-HVR, SKF-VCE, IRF-HVR and IRF-VCE filtering modes at NNOR station on April 26, 2020.

Figure 6.38 illustrates observation residuals of GPS, GLONASS, Galileo and BDS satellites computed for the single-frequency code pseudorange positioning solutions with the SKF-HVR, SKF-VCE, IRF-HVR and IRF-VCE filtering modes at NNOR station on April 26, 2020. For the SKF filtering mode, the employment of variance component estimation decreases the observation residuals for all navigation systems significantly. As regards the IRF mode, observation residuals of GLONASS, Galileo, and BDS satellites are lowered with the variance component estimation, while the observation residuals of GPS satellites are slightly higher in the IRF-VCE filtering mode. From the results, it can be said that lower observation residuals can be obtained employing the variance component estimation in the filters. It actually means that the variance component estimation represents the actual stochastic characteristics of multi-GNSS observation better in comparison with the traditional approaches.

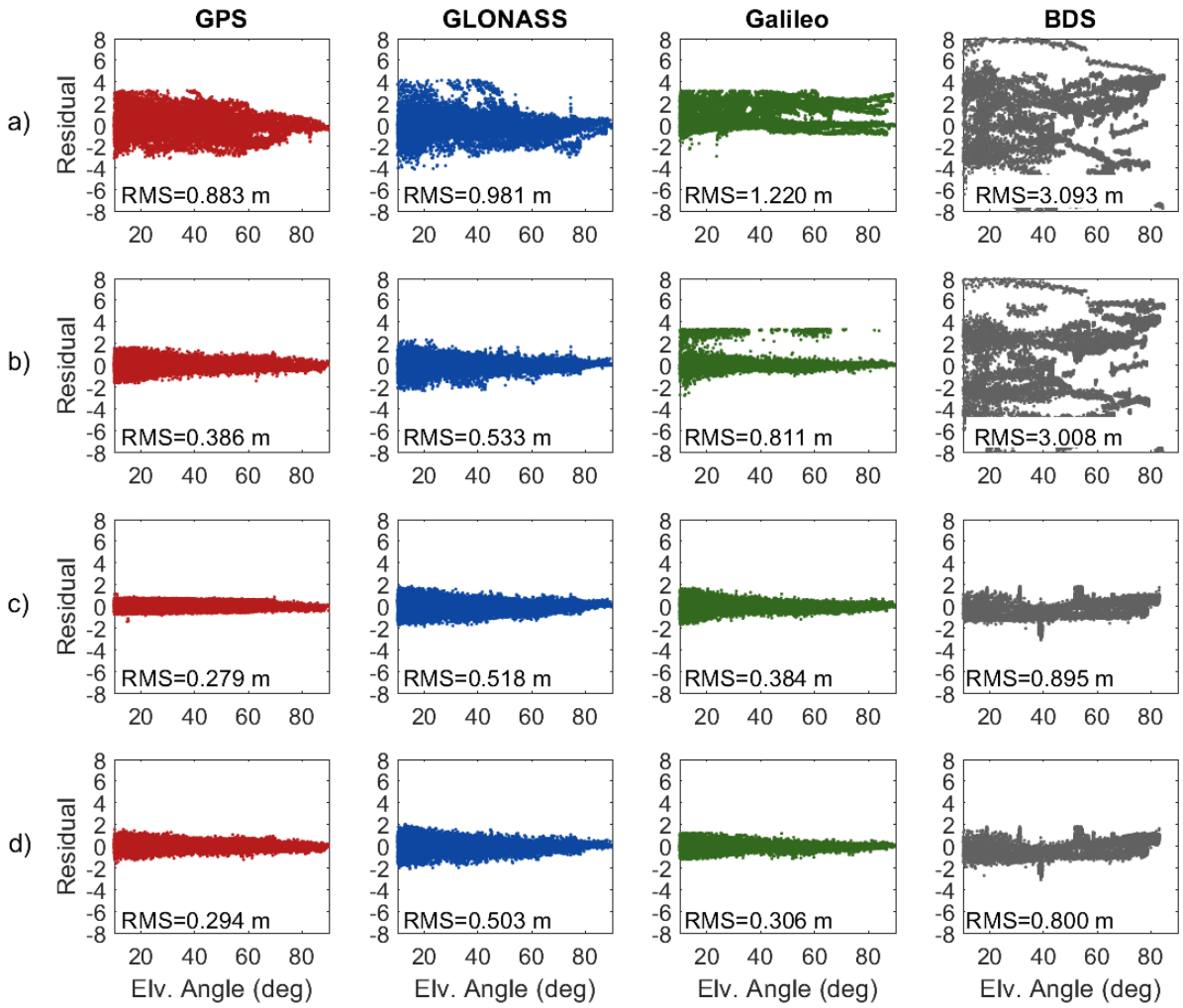

Figure 6.38: Residuals of GPS, GLONASS, Galileo and BDS satellites (in:m) obtained from the single-frequency code pseudorange positioning solutions with the SKF-HVR (a), SKF-VCE (b), IRF-HVR (c) and IRF-VCE (d) filtering modes at NNOR station on April 26, 2020.

Considering the whole positioning solutions at 15 stations over the two-week period, probability distributions of epoch-wise positioning errors in the north, east and up directions for the single-frequency code pseudorange positioning solutions with the SKF-HVR, SKF-VCE, IRF-HVR and IRF-VCE filtering modes are provided in Figure 6.39. The SKF-VCE filtering mode provides RMS values of 0.464, 0.368, and 1.172 m in the north, east, and up directions, which refers to improvements of nearly 50% for all the positioning components when compared with the SKF-HVR mode. Furthermore, the IRF-VCE filtering mode has RMS values of 0.440, 0.339, and 1.135 m in the north, east, and up directions, which means the improvements by 7.9%, 15.1%, and 18.3% in comparison to the IRF-HVR mode. Therefore, the IRF-VCE mode provides the best positioning performance in all directions, which reveals the contribution of the proposed filtering method.

Average RMS values of horizontal, vertical, and 3D positioning errors calculated for the

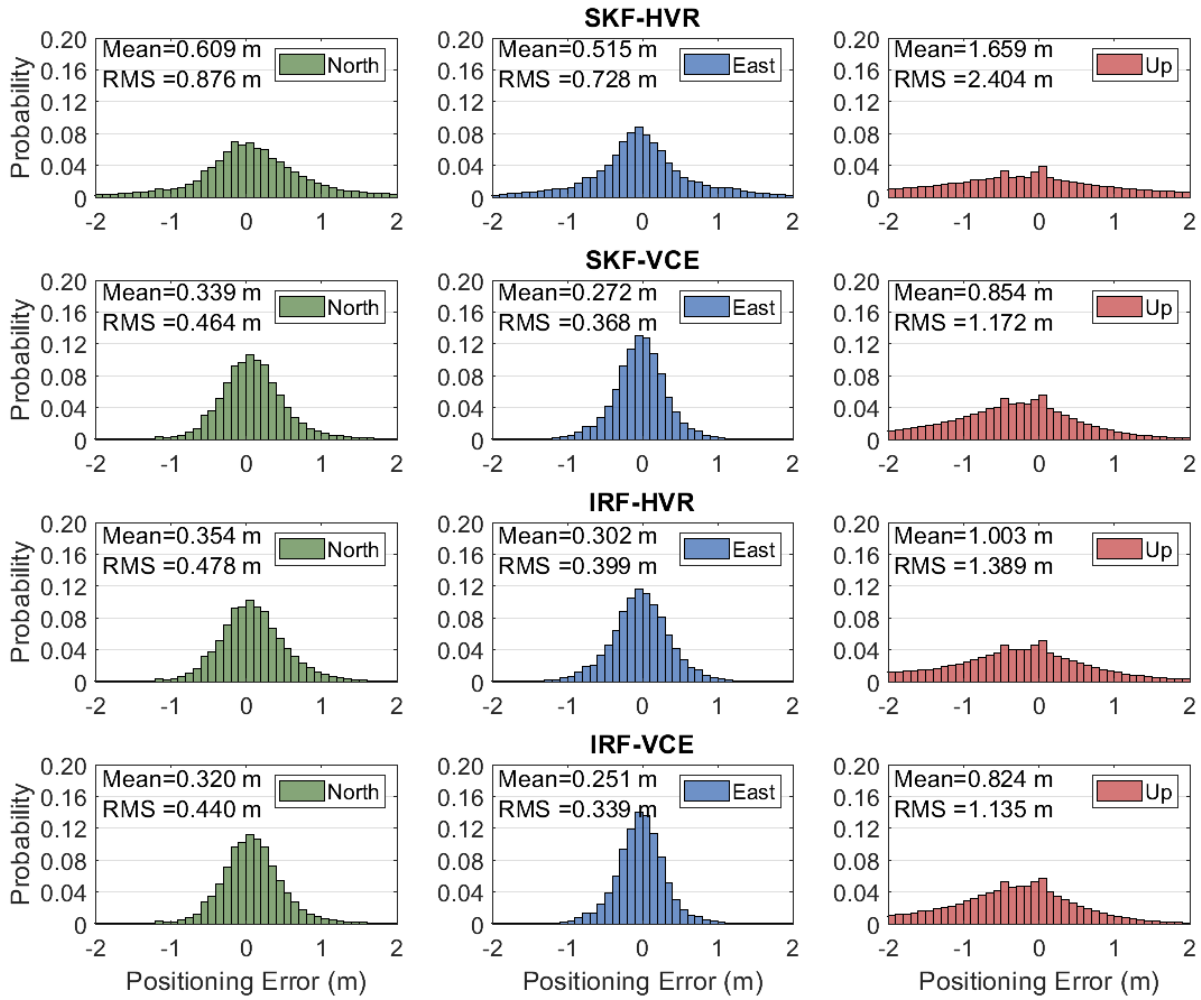

Figure 6.39: Probability distributions of positioning errors for the single-frequency code pseudorange positioning solutions with the SKF-HVR, SKF-VCE, IRF-HVR and IRF-VCE filtering modes.

single-frequency code pseudorange positioning solutions the SKF-HVR, SKF-VCE, IRF-HVR and IRF-VCE filtering modes are presented in Table 6.25. As shown in the table, the employment of variance component estimation improves the 3D positioning accuracy from 2.660 m to 1.313 m for the SKF filtering mode, which is an improvement of 50% approximately. Also, the SKF-VCE filtering mode presents relatively better positioning performance than the IRF-HVR mode for all positioning components. The IRF-VCE mode enhances the positioning performance of the IRF-HVR mode by 17% on average when 3D RMS values are considered. The improvement ratio raises to 52.5% if the comparison is made with the SKF-HVR filtering mode. Consequently, it can be stated that the proposed filtering method improves the positioning performance of real-time single-frequency code pseudorange positioning significantly.

Figure 6.40 depicts 3D positioning errors computed for the single-frequency code-phase combination solutions with the SKF-HVR, SKF-VCE, IRF-HVR and IRF-VCE filtering

Table 6.25: Average RMS values of horizontal, vertical, and 3D positioning errors for the single-frequency code pseudorange positioning solutions with the SKF-HVR, SKF-VCE, IRF-HVR and IRF-VCE filtering modes.

Filtering Mode	**RMS Errors (m)**		
	Horizontal	**Vertical**	**3D**
SKF-HVR	1.139	2.404	2.660
SKF-VCE	0.592	1.172	1.313
IRF-HVR	0.623	1.389	1.522
IRF-VCE	0.556	1.135	1.264

modes at NNOR station on April 26, 2020. As shown in the figure, the positioning performance of the SKF-HVR filtering mode is augmented by the use of variance component estimation with the SKF-VCE mode. Although the performance of the IRF-HVR mode is better in the first hours, its performance is slightly outperformed with the SKF-VCE filtering mode in the following epochs. This figure provides an initial idea about the performance of the proposed filtering method for the real-time single-frequency code and phas combination solutions.

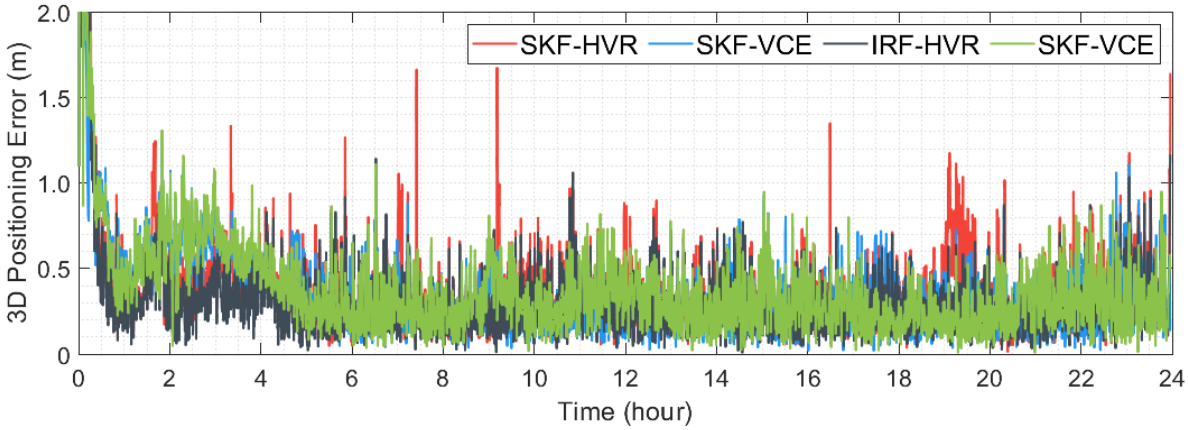

Figure 6.40: Daily 3D positioning errors acquired from the single-freequncy code-phase combination solutions with the SKF-HVR, SKF-VCE, IRF-HVR and IRF-VCE filtering modes at NNOR station on April 26, 2020.

As an indicator of the filtering performance, observation residuals of GPS, GLONASS, Galileo and BDS satellites acquired from the single-frequency code-phase combination solutions with the SKF-HVR, SKF-VCE, IRF-HVR and IRF-VCE filtering modes at NNOR station on April 26, 2020 are presented in Figure 6.41. It can be observed from the figure that the SKF-VCE mode provide lower observation residuals for all navigation systems when compared to the SKF-HVR filtering mode. Moreover, the IRF-VCE filtering mode decreases the observation residuals acquired from the IRF-HVR mode for all navigation system excluding GPS satellites. From these specific example, it can be stated that the employment of variance component estimation represents actual stochastic characteristics of multi-GNSS observations.

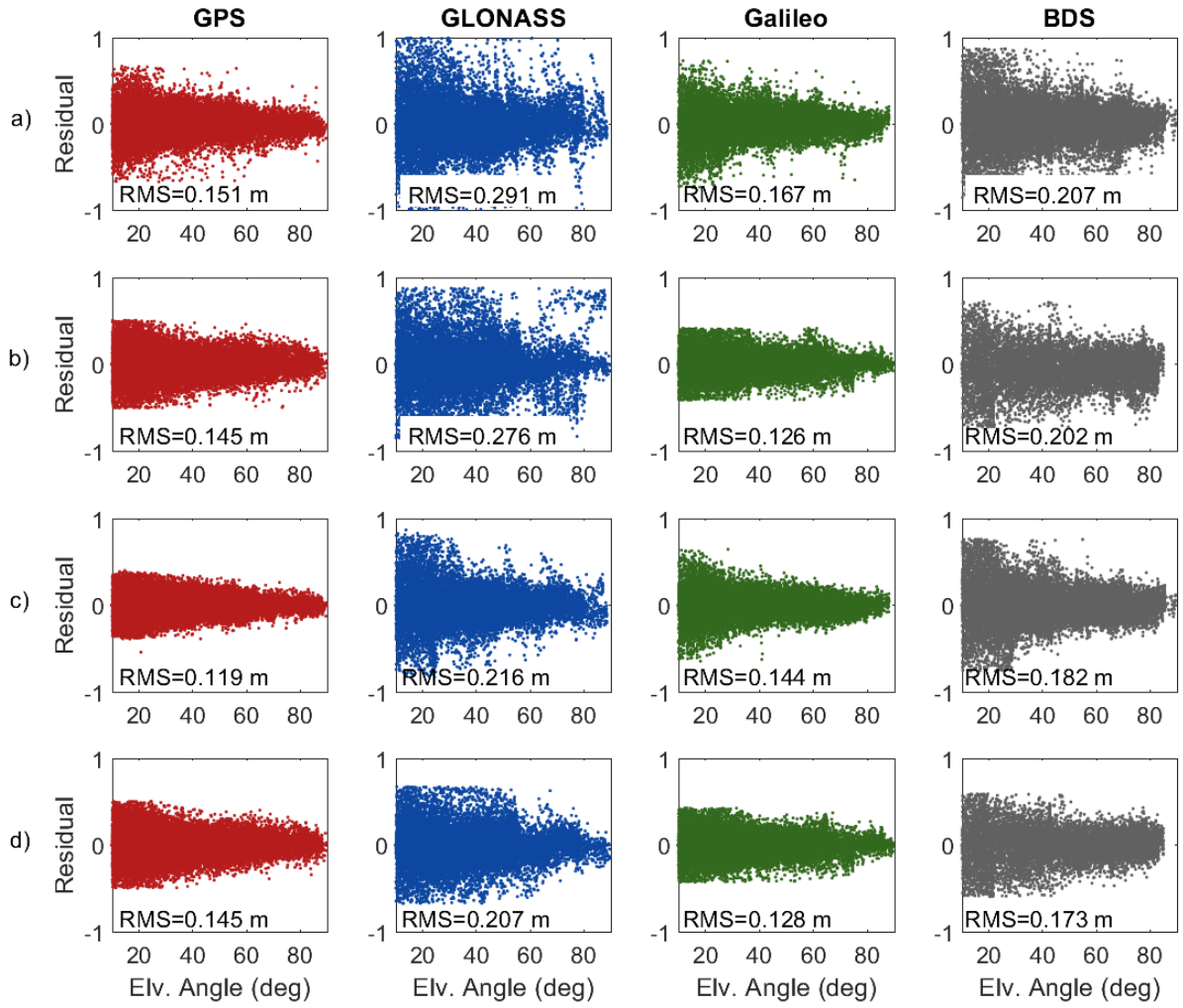

Figure 6.41: Residuals of GPS, GLONASS, Galileo and BDS satellites (in:m) obtained from the single-freequncy code-phase combination solutions with the SKF-HVR (a), SKF-VCE (b), IRF-HVR (c) and IRF-VCE (d) filtering modes at NNOR station on April 26, 2020.

Figure 6.42 illustrates probability distributions of epoch-wise positioning errors acquired from the single-frequency code-phase combination solutions with the SKF-HVR, SKF-VCE, IRF-HVR and IRF-VCE filtering modes considering all positioning solutions. The SKF-VCE filtering mode provides a better positioning performance than the SKF-HVR filtering mode with RMS values of 0.146, 0.204, and 0.277 m in the north, east, and up directions. Besides, the positioning accuracy of IRF-HVR mode is slightly improved with the proposed filtering method in all directions. With RMS values of 0.135, 0.180, and 0.250 m in the north, east, and up directions, the IRF-VCE provide the best positioning performance for the real-time single-frequency code-phase combination solution.

Regarding the convergence performance, Table 6.26 presents average convergence times for the single-frequency code-phase combination solutions with the SKF-HVR, SKF-VCE, IRF-HVR and IRF-VCE filtering modes. Average convergence times were calculated as 64.74,

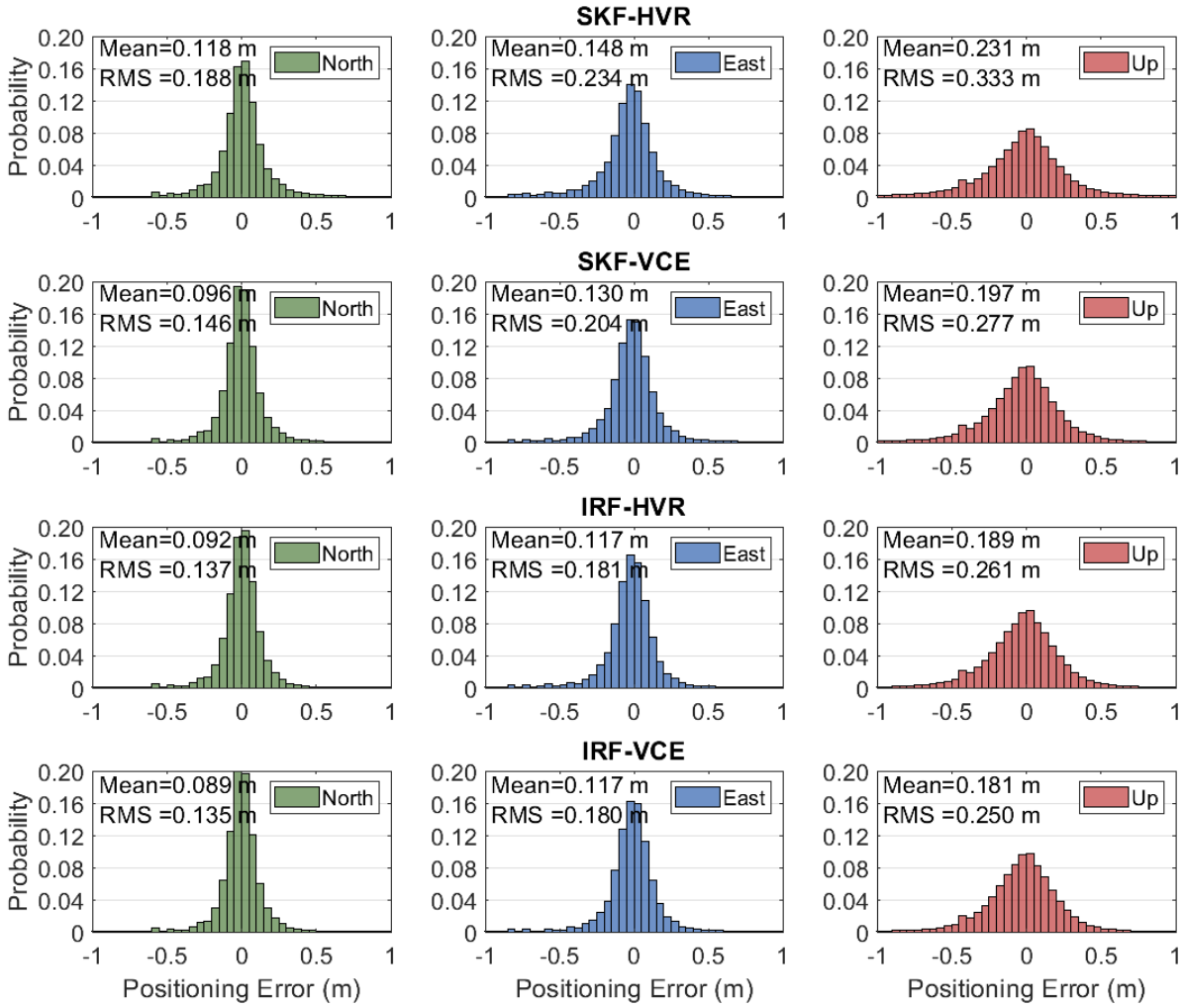

Figure 6.42: Probability distributions of positioning errors for the single-frequency code-phase combination solutions with the SKF-HVR, SKF-VCE, IRF-HVR and IRF-VCE filtering modes.

52.01, 44.47, and 43.07 minutes for the SKF-HVR, SKF-VCE, IRF-HVR, and IRF-VCE filtering modes. The IRF-VCE filtering mode, that is the proposed filtering approach, has the best convergence performance for the real-time single-frequency code-phase combination solution.

Table 6.26: Average convergence times for the single-frequency code-phase combination solutions with the SKF-HVR, SKF-VCE, IRF-HVR and IRF-VCE filtering modes.

Filtering Mode	**Convergence Times (min)**
SKF-HVR	64.74
SKF-VCE	52.01
IRF-HVR	44.47
IRF-VCE	43.07

Additionally, Table 6.27 shows average RMS values of horizontal, vertical, and 3D posi-

tioning errors calculated for the single-frequency code-phase combination solutions with the SKF-HVR, SKF-VCE, IRF-HVR and IRF-VCE filtering modes. With the SKF-VCE filtering mode, the positioining performance of SKF-HVR mode is improved by 16.7% on average when 3D RMS values are taken into consideration. Also, the IRF-VCE filtering mode provide slightly better positioning accuracy compared with the IRF-HVR mode, which has the best positioning performance. The results again confirms that the proposed filtering method presents enhanced positioning performance for the real-time single-frequency code-phase combination solution.

Table 6.27: Average RMS values of horizontal, vertical, and 3D positioning errors for the single-frequency code-phase combination solutions with the SKF-HVR, SKF-VCE, IRF-HVR and IRF-VCE filtering modes.

Filtering Mode	**RMS Errors (m)**		
	Horizontal	**Vertical**	**3D**
SKF-HVR	0.300	0.333	0.448
SKF-VCE	0.251	0.277	0.373
IRF-HVR	0.227	0.261	0.346
IRF-VCE	0.225	0.250	0.337

On the other side, the positioning performance of dual-frequency PPP solutions was evaluated similarly as regards the contribution of variance component estimation. Figure 6.43 illustrates Daily 3D positioning errors computed for the dual-frequency PPP solutions with the SKF-HVR, SKF-VCE, IRF-HVR and IRF-VCE filtering modes at NNOR station on April 26, 2020. It can be observed from the figure that the integration of variance component estimation with the standard Kalman filter decreases the positioning errors obtained from the SKF-HVR filtering method for almost all epochs. The IRF-HVR and IRF-VCE filtering modes provide better positioning accuracies when compared with the SKF filtering modes. From the figure, it can also be seen that the performance of the IRF-VCE filtering mode is slightly better than that of the IRF-HVR mode in most of the epochs.

Figure 6.44 presents observation residuals for dual-frequency ionosphere-free phase combinations of GPS, GLONASS, Galileo and BDS satellites acquired from the dual-frequency PPP solutions with the SKF-HVR, SKF-VCE, IRF-HVR and IRF-VCE filtering modes at NNOR station on April 26, 2020. It is apparent from the figure that the SKF-VCE filtering mode decreases the observation residuals of all navigation systems in comparison with the SKF-HVR mode, excluding Galileo whose residuals are computed equally for both filtering modes. Moreover, it can be observed from the figure that the observation residuals of GPS and GLONASS satellites in the IRF-HVR are decreased with the IRF-VCE mode, while there is no improvement in the observation residuals of Galileo and BDS satellites. Especially, the observation residuals of BDS satellites in the IRF-HVR mode are quite lower when compared with the other filtering modes. Still, it can be said that the employment of

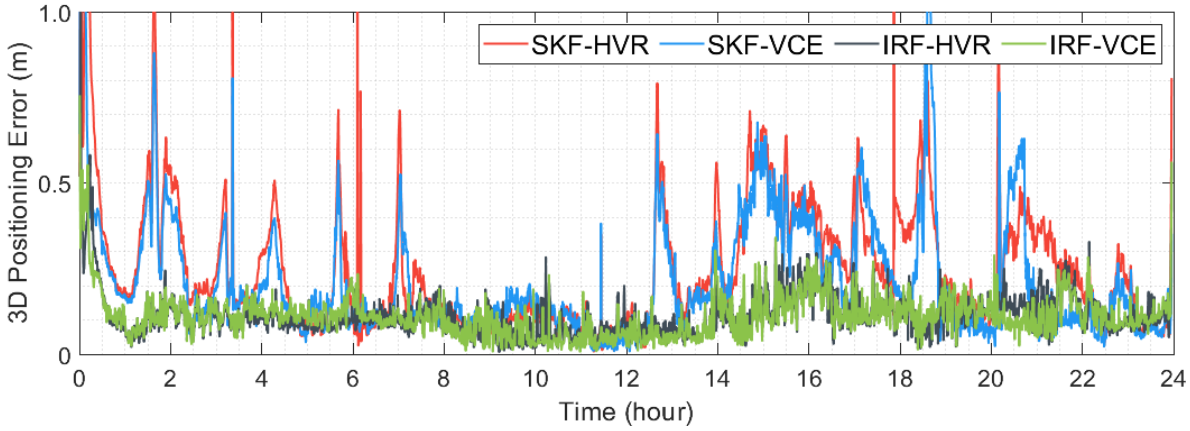

Figure 6.43: Daily 3D positioning errors acquired from the dual-frequency PPP solutions with the SKF-HVR, SKF-VCE, IRF-HVR and IRF-VCE filtering modes at NNOR station on April 26, 2020.

variance component estimation mostly provides a considerable contribution to specify actual stochastic characteristics of multi-GNSS satellites.

Taking the whole positioning solutions into account, probability distributions of epoch-wise positioning errors computed for the dual-frequency PPP solutions with the SKF-HVR, SKF-VCE, IRF-HVR and IRF-VCE filtering modes are presented in Figure 6.45. For the SKF-HVR filtering mode, RMS values are 0.108, 0.136, and 0.217 m in the north, east, and up directions, while corresponding RMS values were computed as 0.106, 0.135, and 0.213 m respectively for the SKF-VCE filtering mode. From these results, it can be said that the positioning performance of SKF-HVR mode is augmented in a small proportion with the use of variance component estimation. Moreover, RMS values obtained from the IRF-HVR mode are 0.074, 0.092, and 0.131 m in the north, east, and up directions, whereas related RMS values were calculated as 0.072, 0.089, and 0.113 m respectively for the IRF-VCE mode. So, it means that the IRF-VCE mode improves the performance of IRF-HVR mode by 2.7%, 3.3%, and 13.7% in the north, east, and up directions, respectively.

To evaluate the convergence performance, the average convergence times are computed for the dual-frequency PPP solutions with the SKF-HVR, SKF-VCE, IRF-HVR and IRF-VCE filtering modes (Table 6.28). Average convergence times are 34.42, 32.15, 11.43, and 10.95 minutes for the SKF-HVR, SKF-VCE, IRF-HVR, and IRF-VCE filtering modes. Herein, it is apparent that the IRF filtering modes improve the convergence performance significantly in comparison with the SKF filtering modes. Also, the IRF-VCE filtering mode, that is the proposed filtering method, provides the shortest convergence period when compared with the other filtering modes.

Finally, Table 6.29 presents average RMS values of horizontal, vertical, and 3D position-

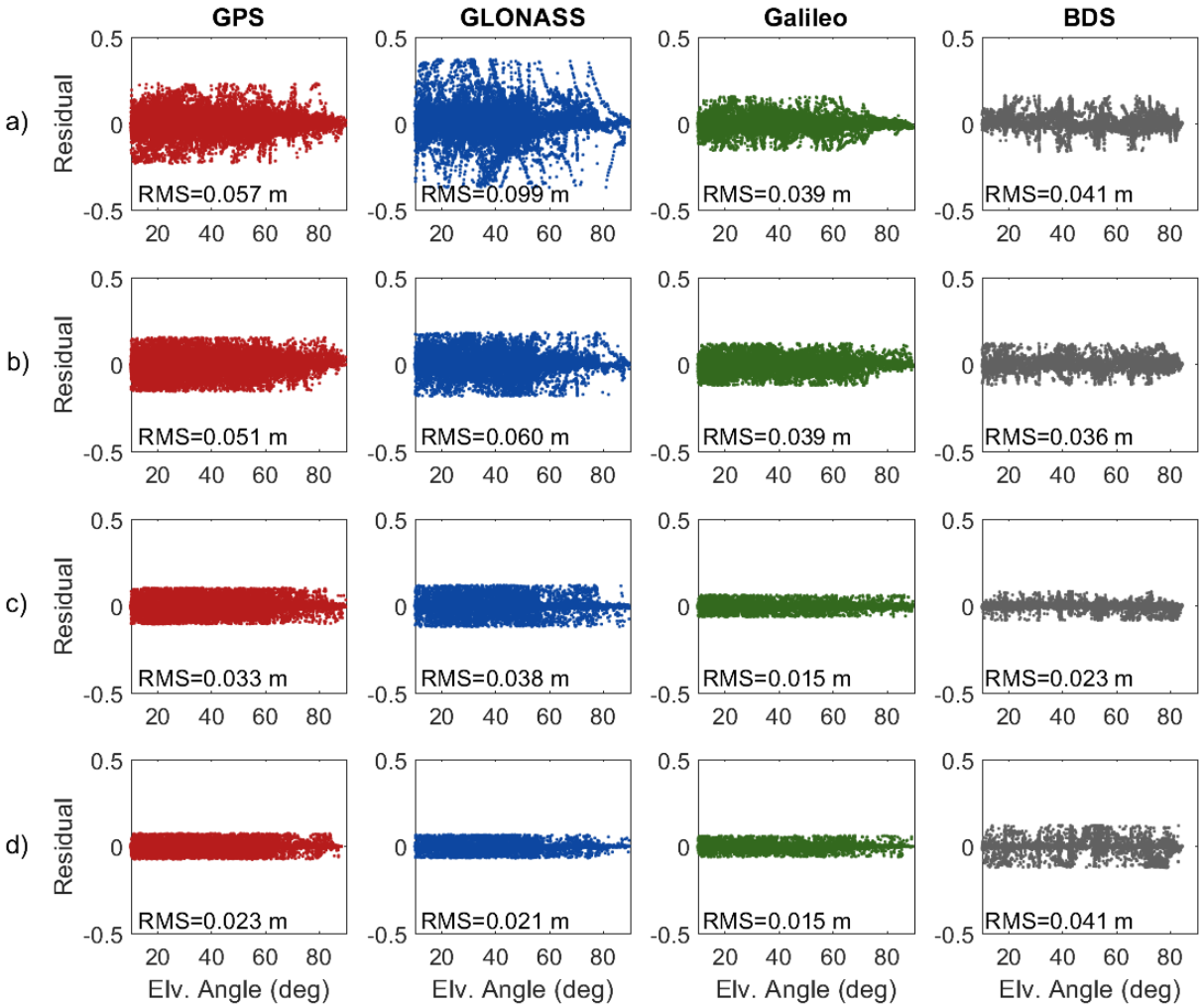

Figure 6.44: Phase observation residuals of GPS, GLONASS, Galileo and BDS satellites (in:m) obtained from the dual-frequency PPP solutions with the SKF-HVR (a), SKF-VCE (b), IRF-HVR (c) and IRF-VCE (d) filtering modes at NNOR station on April 26, 2020.

Table 6.28: Average convergence times for the dual-frequency PPP solutions with the SKF-HVR, SKF-VCE, IRF-HVR and IRF-VCE filtering modes.

Filtering Mode	**Convergence Times (min)**
SKF-HVR	34.42
SKF-VCE	32.15
IRF-HVR	11.43
IRF-VCE	10.95

ing errors computed for the dual-frequency PPP solutions with the SKF-HVR, SKF-VCE, IRF-HVR and IRF-VCE filtering modes considering all positioning solutions at 15 stations over the two-week period. The results show that the positioning accuracy of the SKF-HVR filtering mode is augmented slightly with the SKF-VCE filtering mode. When 3D RMS values are considered, the SKF-VCE mode augments the positioning accuracy of SKF-HVR

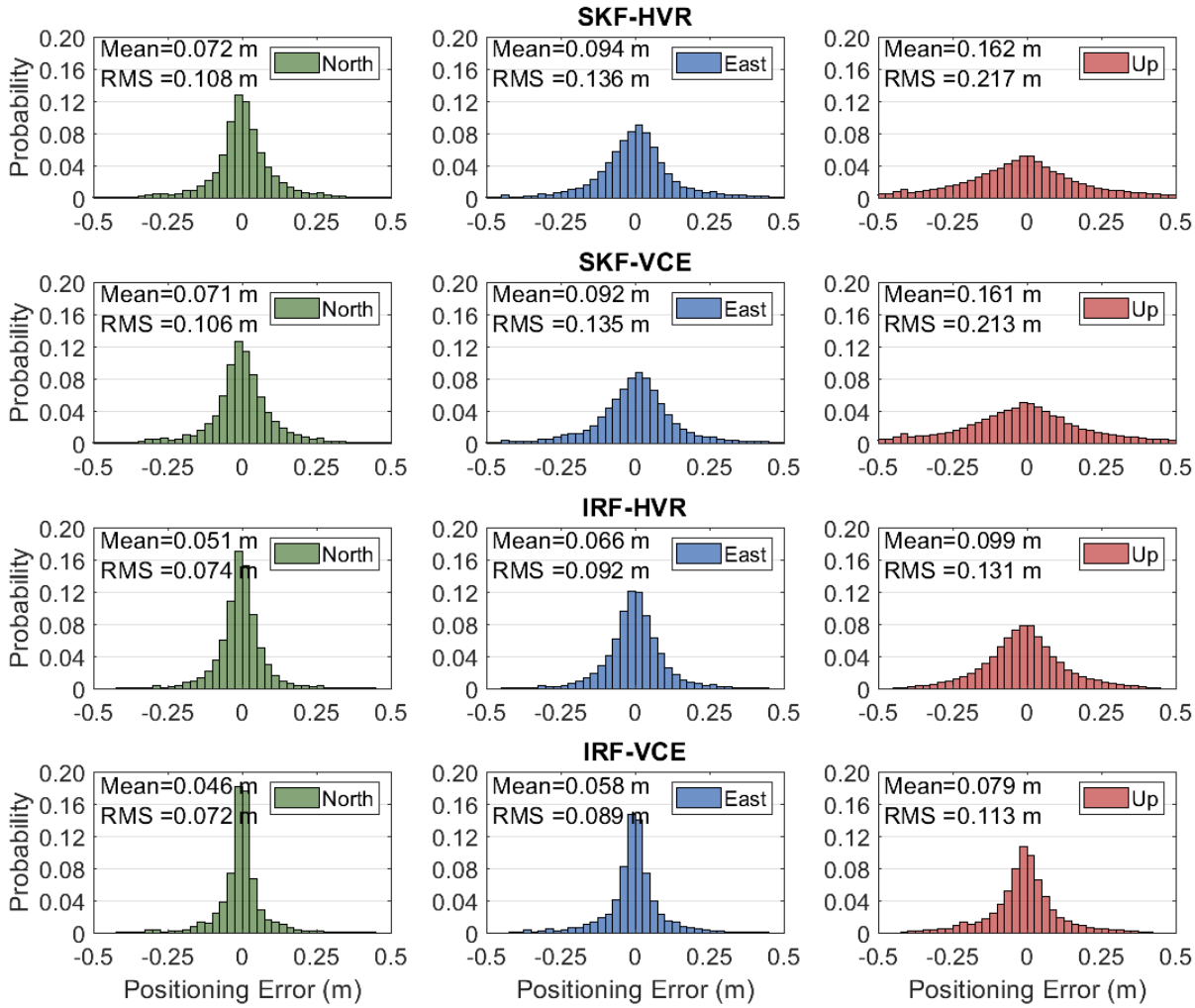

Figure 6.45: Probability distributions of positioning errors for the dual-frequency PPP solutions with the SKF-HVR, SKF-VCE, IRF-HVR and IRF-VCE filtering modes.

mode by 4.7%. On the other side, the IRF-VCE filtering mode provides better positioning accuracy for all positioning components when compared with the IRF-HVR filtering mode. Considering 3D RMS values, the positioning performance of IRF-HVR mode is improved by 11.8% with the IRF-VCE filtering mode. So, the IRF-VCE filtering mode presents the best positioning performance for the real-time dual-frequency PPP solution.

Table 6.29: Average RMS values of horizontal, vertical, and 3D positioning errors for the dual-frequency PPP solutions with the SKF-HVR, SKF-VCE, IRF-HVR and IRF-VCE filtering modes.

Filtering Mode	**RMS Errors (m)**		
	Horizontal	**Vertical**	**3D**
SKF-HVR	0.174	0.217	0.278
SKF-VCE	0.171	0.213	0.265
IRF-HVR	0.119	0.131	0.177
IRF-VCE	0.116	0.113	0.156

In a summary, the 3D positioning performance of single-frequency code pseudorange positioning is improved with the employment of variance component estimation by 17% in comparison with the IRF-HVR mode which includes higher variance ratios approach together with the improved IGG III function. Similarly, the use of variance component estimation enhances positioning performance of single-frequency code-phase combination considerably in terms of positioning accuracy and convergence times. For the dual-frequency PPP solutions, an improvement of 11.8% in 3D positioning accuracy is provided with the use of variance component estimation in addition to the robust Kalman filter, that is the IRF-VCE mode. Also, the IRF-VCE mode provides the best convergence performance for the dual-frequency PPP solutions. Consequently, the results confirm that the proposed filtering method that integrates robust Kalman filter including improved IGG III function with the variance component estimation is able to represent the actual stochastic characteristics of multi-GNSS observations as well as providing the resistance to observation outliers and unexpected dynamic system errors. Therefore, an improved positioning performance can be acquired from the proposed filtering method for the real-time absolute GNSS positioning techniques.

7. SUMMARY, CONCLUSIONS AND RECOMMENDATIONS

Global technological trends, such as digitalization, big data, artificial intelligence, unmanned aerial vehicles, autonomous cars, wearable and mobile technologies, etc., have dramatically influenced the expectations for GNSS positioning techniques. The requirement for instantaneous positioning information driven mainly by these global trends has had importance nowadays like never before. Therefore, there exists a growing demand within the GNSS community for achieving higher positioning accuracy in real-time with relatively more cost-effective solutions. As a consequence of growing attention, so many efforts have been made in recent years to improve the existing positioning models as satisfying the requirement of simultaneous positioning solutions with more cost-effective GNSS receivers. Especially, absolute positioning techniques have drawn a considerable attention from the GNSS users owing to their operational simplicity and relatively low cost, unlike the relative/differential GNSS positioning techniques. On the other hand, GNSS receivers in mobile devices dominates the low-cost GNSS market. Though most of them contain single-frequency GNSS receivers, new low-cost GNSS chipsets which can provide dual-frequency code and phase observations have been released by some manufacturer recently. Moreover, absolute positioning techniques can be employed with these GNSS receivers effectively. Still, more complicated and improved approaches are required to achieve higher positioning accuracy with the more cost-effective solutions in real-time absolute GNSS positioning techniques. In this regard, the main motivation of this thesis is to provide enhanced positioning approaches dealing with all positioning components comprehensively for real-time absolute GNSS techniques, considering both dual- and single-frequency GNSS receivers.

To achieve enhanced positioning approaches, it is required to deal with the whole positioning steps, including the selection of navigation data, preprocessing, mitigation of GNSS error sources, filtering estimation, etc., carefully and to propose appropriate solutions for these processing steps. In this context, the principal objectives of this thesis can be summarized as follows:

- The fundamental part of real-time GNSS applications is to access satellite orbits and clock corrections instantaneously. In general, two essential sources which are ultra-rapid and IGS-RTS products can be utilized to reach real-time orbits and clock corrections as an alternative to broadcast data. Although both options can be employed for real-time GNSS applications, there are considerable differences between these two products in terms of their processing characteristics and implementation strategies. At this point, one of the main objectives of this thesis is to employ these two products for

real-time absolute GNSS positioning separately by developing the proper models and algorithms and also to evaluate their performance to determine the optimal real-time positioning solution.

- For the single-frequency code pseudorange positioning, it is essential to mitigate the impact of ionospheric delay on GNSS signals since the ionosphere-free combinations are not usable. Global ionosphere models broadcasted with the navigation message are not accurate enough for precise positioning. Alternative ionosphere sources, such as the predicted version of GIMs and real-time ionospheric corrections disseminated by IGS-RTS products, can be employed for the real-time single-frequency code pseudorange positioning. This thesis also aims to propose more suitable solutions in the elimination of ionospheric delay for the single-frequency code pseudorange positioning with both IGS-RTS and ultra-rapid products.

- The GNSS community has been experiencing dramatic changes with the emergence of new global and regional satellite systems. The integration of multi-GNSS offers considerable possibilities to enhance the performance of real-time absolute positioning techniques. Still, more complex functional and stochastic models which can represent essential differences between the navigation systems are required to make use of the potential benefits of multi-constellation. Another purpose of this thesis is to ensure the interoperability of multi-GNSS by providing optimal positioning approaches and by this means to augment the performance of real-time absolute GNSS positioning techniques.

- To achieve the optimum positioning results, it is fundamental to specify appropriate functional and stochastic models in the Kalman filter estimation because its performance is influenced by observation outliers and unexpected dynamic model errors substantially. Furthermore, it is quite challenging to identify stochastic characteristics of multi-GNSS observations for the real-time absolute GNSS positioning techniques as there are different observation types coming from distinct navigation systems. In this regard, this thesis aims at proposing a novel filtering method that is able to represent stochastic characteristics of multi-GNSS observation more rigorously and to provide a better positioning performance for the real-time absolute GNSS positioning techniques.

- It is not possible to perform the extensive researches that are projected as a part of this thesis with the existing GNSS analysis software packages. Hence, this thesis also aims to develop a GNSS analysis software that enables the real-time absolute GNSS positioning solutions including the enhanced positioning approaches and algorithms proposed in this thesis.

In this thesis, three absolute GNSS positioning techniques, which are the single-frequency code pseudorange positioning, code-phase combination, and dual-frequency PPP, were adopted for real-time positioning solutions. Considering different real-time satellite orbit and clock sources, two fundamental positioning approaches were proposed in this thesis as being compatible with three absolute GNSS positioning techniques. The first approach employs IGS-RTS products as the fundamental orbit and clock source, while the second is designed to work with ultra-rapid products. All processing steps applied in both positioning approaches, e.g. data handling, preprocessing, modeling, and filtering, were adjusted in accordance with the typical characteristics of the applied real-time product. For the first approach, the ionosphere corrections disseminated within the IGS-RTS products were utilized for the mitigation of the ionospheric delay in the single-frequency code pseudorange positioning. On the other side, the 1-day predicted GIMs generated by CODE were utilized for eliminating the ionospheric delay in the second approach since ultra-rapid products do not contain any atmospheric correction parameters. Finally, two positioning approaches were also designed to perform the multi-GNSS solutions that include GPS, GLONASS, Galileo, and BDS satellites along with the GPS-only solution.

Unexpected dynamic system errors and undetected observation outliers have a negative influence on the performance of Kalman filtering. Also, the Kalman filter suffers from the inappropriate definition of stochastic properties for both the estimated parameters and observations. In this regard, it is also very tough to specify actual stochastic characteristics of multi-GNSS observations acquired from different navigation systems. In order to overcome these troubles, the thesis proposed a novel filtering method that integrates the robust Kalman filter with the variance component estimation. The robust Kalman filter which includes an improved procedure of IGG III function resists the impacts of unexpected observation residuals and dynamic system errors and also balances the contribution of observations and dynamic model epoch by epoch. Furthermore, the observation variances were determined adaptively in each epoch with the Helmert variance component estimation method. By this means, it is possible to obtain a more realistic and rigorous filtering approach for the real-time absolute GNSS positioning techniques.

Finally, a GNSS analysis software was developed as a part of this thesis to perform the real-time GNSS absolute positioning solutions compatible with the proposed positioning approaches and algorithms. The software, PPPH-RT, was developed as an extensive version of PPPH software which was prepared as a part of the author's master of science study. PPPH-RT can process GPS, GLONASS, Galileo, and BDS data for real-time absolute GNSS positioning solutions. Additionally, PPPH-RT is completely compatible with two fundamental positioning approaches proposed in this thesis, so it can perform real-time positioning solutions with IGS-RTS products and ultra-rapid products separately. PPPH-RT has a lot of func-

tionalities for the real-time absolute GNSS positioning ranging from different atmospheric models to several filtering properties, which makes it a very efficient and comprehensive software for real-time GNSS applications.

In this thesis, numerous experimental tests were made for the performance assessment of enhanced positioning approaches proposed for real-time absolute GNSS positioning techniques. An observation dataset collected at fifteen IGS stations over a period of two weeks was employed in the experimental tests. As an important factor influencing the performance of absolute positioning techniques, satellite visibility was firstly investigated at the selected stations. Considering all stations, average visible satellite numbers were calculated as 9.1, 6.2, 6.5, and 9.0 for GPS, GLONASS, Galileo, and BDS constellations. The results indicate that GPS is still the dominant navigation constellation on the global scale in terms of satellite visibility. Furthermore, the new-emerged satellite systems present significant opportunities for positioning, navigation, and timing applications thanks to their increasing number of satellites. With the advances in the BDS-3 program, the BDS constellation has recently increased its satellite number considerably, which offers substantial prospects for the positioning and navigation applications, especially in the Asia-pacific region.

On the other hand, the performance of real-time absolute GNSS positioning using ultra-rapid products was evaluated comprehensively. Three different products, namely CODE, IGS, and WHU, were employed in the positioning solutions. While IGS ultra-rapid products include only GPS satellites, two ultra-rapid products, which are CODE and WHU, provides satellite orbit and clock corrections for multi-GNSS satellites. As the essential characteristics of these ultra-rapid products are quite different, the positioning performance obtaining from real-time absolute GNSS positioning can alter considerably depending on the applied ultra-rapid products. Moreover, the positioning performance was evaluated in the GPS-only and multi-GNSS scenarios separately to analyze the contribution of multi-constellation. The results demonstrate that the multi-GNSS solution employing WHU ultra-rapid products provides the best positioning performance for the single-frequency code pseudorange positioning with a 3D positioning accuracy of 1.983 m, which is considerably better than that of multi-GNSS SPP solution that has a 3D positioning accuracy of 6.255 m. However, the results also indicate that the positioning performance which can be acquired from the single-frequency code pseudorange positioning solutions with ultra-rapid products deteriorates over time because of the potential decrease in the accuracy of ultra-rapid products moving away from the prediction epoch. Therefore, it can be concluded that the update interval of ultra-rapid products is a critical factor for the single-frequency code pseudorange positioning. Herein, WHU ultra-rapid products distinguish from other products with an update interval of 1 hour. So, it can be also said that better positioning accuracy can be reached with the single-frequency code pseudorange positioning with ultra-rapid product in closer periods to the prediction epoch.

The best positioning performance was obtained from the multi-GNSS solution with WHU ultra-rapid products with a 3D positioning accuracy of 0.717 m for the single-frequency code-phase combination. Also, the multi-GNSS solution with WHU products provides the shortest convergence period with 41.78 minutes on average. The results are quite similar for the dual-frequency PPP, the multi-GNSS solution with WHU ultra-rapid products provides the best positioning performance with a positioning accuracy of 0.296 m and an average convergence time of 16.90 minutes. Also, the results demonstrate that the performance of the absolute positioning techniques which contains carrier phase observations are not affected substantially by the potential degradation in the accuracy of ultra-rapid products owing to the convergence of phase observations. When these results are analyzed, it can be concluded that the positioning performance of real-time absolute positioning techniques can be augmented with the enhanced positioning approach with ultra-rapid products. The integration of multi-constellation also enhances the positioning accuracy of real-time absolute GNSS positioning techniques significantly. The multi-GNSS solution with WHU ultra-rapid products which is the only product group including GPS, GLONASS, Galileo, and BDS satellites offers better positioning performance for all the real-time absolute GNSS positioning techniques. Consequently, this thesis proves that ultra-rapid products with the enhanced positioning approaches proposed in this thesis are an important alternative for real-time absolute GNSS positioning solutions. Especially, the employment of ultra-rapid products without any additional connection is a substantial advantage for the GNSS applications in cases where it is not possible to access external connections.

On the other side, the observation dataset was processed additionally with IGS-RTS products for real-time absolute GNSS positioning techniques. The results show that it is possible to obtain a 3D positioning error of 1.522 from the multi-GNSS single-frequency code pseduorange positioning with IGS-RTS products, which means an improvement of 23.2% when compared with the corresponding solution of WHU ultra-rapid products. For the single-frequency code-phase combination, the multi-GNSS solution with IGS-RTS products presents a 3D positioning accuracy of 0.346 m with an improvement of 51.7% in comparison with the corresponding ultra-rapid products. Furthermore, the multi-GNSS solution with IGS-RTS products provides the best positioning performance for the dual-frequency PPP solution with a positioning accuracy of 0.177 m. The results also indicate that the convergence time of real-time absolute positioning techniques is lessened considerably with the employment of IGS-RTS products. From these results, this thesis concludes that the enhanced positioning approach with IGS-RTS products provides better positioning performance for all real-time absolute GNSS positioning techniques when compared with ultra-rapid products. In addition, the multi-GNSS integration augments considerably the positioning performance of all real-time absolute GNSS positioning techniques with IGS-RTS products. Still, the requirement of an external connection can be seen as a drawback for the IGS-RTS prod-

ucts. However, if it is accessible, the multi-GNSS solution with IGS-RTS products presents the best positioning performance for all the real-time absolute GNSS positioning solutions. Also, unlike ultra-rapid products, there is not any time-dependent deterioration in the positioning performance obtained from the IGS-RTS products, which is a significant advantage for the single-frequency GNSS users.

The observation dataset was processed in various filtering modes to analyze the performance of the proposed filtering method. Firstly, the results show that the robust Kalman filter method that includes the improved procedure of IGG III function provides better positioning performance for all the real-time absolute GNSS positioning solutions when compared to the other robust filter methods. If the traditional filtering approach which includes a standard Kalman filter with the weighting scheme depending on higher variance ratios is assumed as the typical solution, the proposed filtering method improves the 3D positioning accuracy of real-time single-frequency code pseudorange solution by 52.5%. Furthermore, the proposed filtering method augments the 3D positioning accuracy obtained from the typical solution by 24.8% and 43.9% respectively for the single-frequency code-phase combination and dual-frequency PPP solutions. When compared with the IRF-HVR filtering mode which includes the improved IGG III function with the higher variance ratios, the improvement percentages were computed as 17.0%, 2.6%, and 11.8% respectively for the single-frequency code pseudorange positioning, single-frequency code-phase combination, and dual-frequency PPP solutions. Furthermore, the proposed filtering method provides the best convergence performance for all the real-time absolute positioning techniques. Consequently, the results demonstrate that the proposed filtering method is capable of specifying stochastic properties of multi-GNSS observations better than conventional approaches. By this means, the positioning performance of real-time absolute GNSS positioning solutions was improved considerably with the proposed filtering method. Thus, a novel filtering method that can be applied in various GNSS applications including multi-GNSS observations was proposed as a part of this thesis.

Finally, considering the results and conclusions drawn from this thesis, the recommendations for future works can be ordered as follows:

- The demand for achieving higher positioning accuracy with more cost-effective solutions increases by each day, therefore more sophisticated functional and stochastic models that can satisfy this growing demand are required in the near future.

- To benefit from multi-GNSS better, the long-term stochastic characteristics of multi-GNSS observations should be analyzed and better weighting approaches that can reflect the actual stochastic properties of different observation types should be developed.

- The performance of real-time absolute GNSS positioning solutions may be augmented with the implementation of external corrections obtained from the local networks, such as satellite clock and atmospheric corrections.
- Extended studies can be made to investigate the estimation performance of tropospheric zenith delay with real-time absolute GNSS positioning solutions.
- There is an increasing demand for GNSS software packages that enable real-time GNSS applications, therefore the development of GNSS analysis software packages is going to be an important topic in the future.

REFERENCES

Abd-Rabbou, M., El-Shazly, A., Ahmed, K., Comparative analysis of multiconstellation GNSS single-frequency precise point positioning, Survey Review, Vol. 50 (**2018**) 361 373–382, doi:10.1080/00396265.2017.1296628.

Alkan, R., Ocalan, T., Usability of the GPS precise point positioning technique in marine applications, Journal of Navigation, Vol. 66 (**2013**) 579–588, doi:10.1017/S0373463313000210.

Bahadur, B., Nohutcu, M., PPPH: a MATLAB-based software for multi-GNSS precise point positioning analysis, GPS Solutions, Vol. 22 (**2018**) 113, doi:10.1007/s10291-018-0777-z.

BDS, Test and Assessment Research Center of China Satellite Navigation Office, http://www.csno-tarc.cn/en/system/constellation, **2020**, accessed: 18.12.2020.

BeiDou-ICD, BeiDou open service signal-in-space Interface Control Document (ICD), http://en.beidou.gov.cn/SYSTEMS/ICD/, **2020**, accessed: 21.12.2020.

Boehm, J., Niell, A., Tregoning, P., Schuh, H., Global Mapping Function (GMF): a new empirical mapping function based on numerical weather model data, Geophysical Research Letters, Vol. 33 (**2006**) 7 L07304, doi:10.1029/2005GL025546.

Cai, C., Gao, Y., Modeling and assessment of combined GPS/GLONASS precise point positioning, GPS Solutions, Vol. 17 (**2013**) 2 223–236, doi:10.1007/s10291-012-0273-9.

Cai, C., Gao, Y., Pan, L., Zhu, J., Precise point positioning with quad-constellations: GPS, BeiDou, GLONASS, and Galileo, Advances in Space Research, Vol. 56 (**2015**) 1 133–143, doi:10.1016/j.asr.2015.04.001.

Cai, C., Pan, L., Gao, Y., A precise weighting approach with application to combined L1/B1 GPS/BeiDou positioning, Journal of Navigation, Vol. 67 (**2014**) 5 911–925, doi:10.1017/S0373463314000320.

Choy, S., Bisnath, S., Rizos, C., Uncovering common misconceptions in GNSS Precise Point Positioning and its future prospect, GPS Solutions, Vol. 21 (**2017**) 1 13–22, doi:10.1007/s10291-016-0545-x.

Collins, P., Bisnath, S., Lahaye, F., Heroux, P., Undifferenced GPS ambiguity resolution using the decoupled clock model and ambiguity datum fixing, Navigation, Vol. 57 (**2010**) 2 123–135, doi:10.1002/j.2161-4296.2010.tb01772.x.

Davis, J.L., Herring, T.A., Shapiro, I.I., Rogers, A.E.E., Elgered, G., Geodesy by radio interferometry: Effects of atmospheric modeling errors on estimates

of baseline length, Radio Science, Vol. 20 (**1985**) 6 1593–107, doi:10.1029/RS020i006p01593.

EC, Open Service-Ionospheric correction algorithm for Galileo single frequency users, https://op.europa.eu/en/publication-detail/-/publication/bfefce99-f54a-11e9-8c1f-01aa75ed71a1/language-en, **2016**, accessed: 28.12.2020.

El-Mowafy, A., Deo, M., Cycle Slip and Clock Jump Repair with Multi-Frequency Multi-Constellation GNSS data for Precise Point Positioning, in International Global Navigation Satellite Systems Society (IGNSS) Symposium, Burleigh Heads, Qld., Australia, **2015** pp. 1–15.

El-Mowafy, A., Deo, M., Kubo, N., Maintaining real-time precise point positioning during outages of orbit and clock corrections, GPS Solutions, Vol. 21 (**2017**) 937–947, doi:10.1007/s10291-016-0583-4.

Fan, C., Guan, Q., Zhu, Z., Peng, F., Xiang, W., Fuzzy weighting approach for single point positioning with single-frequency pseudo-range observations, Advances in Space Research, Vol. 63 (**2019**) 9 2982–2994, doi:10.1016/j.asr.2018.03.027.

Galileo, European GNSS Service Center, https://www.gsc-europa.eu/system-service-status/constellation-information, **2020**, accessed: 17.12.2020.

Galileo-ICD, Galileo open service signal-in-space Interface Control Document (ICD), https://galileognss.eu/wp-content/uploads/2020/08/Galileo-OS-SIS-ICD-v1.3.pdf, **2018**, accessed: 21.12.2020.

Ge, M., Gendt, G., Rothacker, M., Shi, C., Liu, J., Resolution of GPS carrier-phase ambiguities in precise point positioning (PPP) with daily observations, Journal of Geodesy, Vol. 82 (**2008**) 7 389–399, doi:10.1007/s00190-007-0187-4.

Gelb, A., Applied optimal estimation, MIT press, Cambridge, **1974**, ISBN 9780262570480.

Geng, J., Meng, X., Dodson, A., Ge, M., Teferle, F., Rapid re-convergences to ambiguity-fixxed solutions in precise point positioning, Journal of Geodesy, Vol. 84 (**2010**) 12 705–714, doi:10.1007/s00190-010-0404-4.

GLONASS-ICD, GLONASS Interface Control Document (ICD), http://russianspacesystems.ru/wp-content/uploads/2016/08/ICD-GLONASS-CDMA-General.-Edition-1.0-2016.pdf, **2016**, accessed: 21.12.2020.

GPS, GPS Overview, https://www.gps.gov/systems/gps/space/, **2020**, accessed: 16.12.2020.

GPS-ICD, GPS Interface Control Document (ICD), https://www.gps.gov/technical/icwg/IS-GPS-800G.pdf, **2020**, accessed: 21.12.2020.

GSA, GNSS market report, https://op.europa.eu/en/publication-detail/-/publication/bfefce99-f54a-11e9-8c1f-01aa75ed71a1/language-en, **2019**, accessed: 28.12.2020.

Guo, F., Zhang, X., Adaptive robust Kalman filtering for precise point positioning, Measurement Science and Technology, Vol. 25 (**2014**) 10 105011, doi:10.1088/0957-0233/25/10/105011.

Hadas, T., Bosy, J., IGS RTS precise orbits and clocks verification and quality degradation over time, GPS Solutions, Vol. 19 (**2015**) 1 93–105, doi:10.1007/s10291-014-0369-5.

Hofmann-Wellenhof, B., Lichtenegger, H., Wasle, E., GNSS – Global Navigation Satellite Systems: GPS, GLONASS, Galileo, and more, Springer-Verlag, Wien, Austria, **2007**, ISBN 978-3-211-73017-1.

Hopfield, H.S., Two-quartic tropospheric refractivity profile for correcting satellite data, Journal of Geophysical Research, Vol. 74 (**1969**) 18 4487–4499, doi:10.1029/JC074i018p04487.

IGS-SSR, IGS State Space Representation (SSR) Format Description, https://files.igs.org/pub/data/format/igs_ssr_v1.pdf, **2020**, accessed: 21.12.2020.

Jin, S., Su, K., Co-seismic displacement and waveforms of the 2018 Alaska earthquake from high-rate GPS PPP velocity estimation, Journal of Geodesy, Vol. 93 (**2019**) 9 1559–1569, doi:10.1007/s00190-019-01269-3.

Klobuchar, J., Ionospheric time-delay algorithm for single-frequency GPS users, IEEE Transactions on Aerospace and Electronic Systems, Vol. 23 (**1987**) 3 325–331, doi:10.1109/TAES.1987.310829.

Koch, K.R., Parameter Estimation and Hypothesis Testing in Linear Models, Springer, Berlin, Heidelberg, **1999**, ISBN 978-3-642-08461-4.

Kouba, J., Measuring seismic waves induced by large earthquakes with GPS, Studia Geophysica et Geodaetica, Vol. 47 (**2003**) 4 741–755, doi:10.1023/A:1026390618355.

Kouba, J., A guide to using International GNSS Service (IGS) products, http://kb.igs.org/hc/en-us/articles/201271873-A-Guide-to-Usingthe-IGS-Products, **2015**, accessed: 26.12.2020.

Kouba, J., Héroux, P., Precise Point Positioning Using IGS Orbit and Clock Products, GPS Solutions, Vol. 5 (**2001**) 2 12–28, doi:10.1007/PL00012883.

Lagler, K., Schindelegger, M., Böhm, J., Krásná, H., Nilsson, T., GPT2: Empirical slant delay model for radio space geodetic techniques, Geophysical Research Letters, Vol. 40 (**2013**) 6 1069–1073, doi:10.1002/grl.50288.

Landskron, D., Böhm, J., VMF3/GPT3: refined discrete and empirical troposphere mapping functions, Journal of Geodesy, Vol. 92 (**2018**) 349–360, doi:10.1007/s00190-017-1066-2.

Laurichesse, D., Mercier, F., Bertias, J., Broca, P., Cerri, L., Integer ambiguity resolution on undifferenced GPS phase measurements and its applications to PPP and satellite precise orbit determination navigation, Navigation, Vol. 56 (**2009**) 2 135–149, doi:10.1002/j.2161-4296.2009.tb01750.x.

Li, G., Geng, J., Characteristics of raw multi-GNSS measurement error from Google Android smart devices, GPS Solutions, Vol. 23 (**2019**) 3 90, doi:10.1007/s10291-019-0885-4.

Li, M., Yuan, Y., Wang, N., Li, Z., Huo, X., Performance of various predicted GNSS global ionospheric maps relative to GPS and JASON TEC data, GPS Solutions, Vol. 22 (**2018**) 55, doi:10.1007/s10291-018-0721-2.

Li, X., Dick, G., Ge, M., Heise, S., Wickert, J., Bender, M., Real-time GPS sensing of atmospheric water vapor: Precise point positioning with orbit, clock, and phase delay corrections, Geophysical Research Letters, Vol. 41 (**2014**) 10 3615–3621, doi:10.1002/2013GL058721.

Li, X., Ge, M., Dai, X., Ren, X., Fritsche, M., Wickert, J., Schuh, H., Accuracy and reliability of multi-GNSS real-time precise positioning: GPS, GLONASS, BeiDou, and Galileo, Journal of Geodesy, Vol. 89 (**2015**) 6 607–635, doi:10.1007/s00190-015-0802-8.

Li, Z., Wang, N., Wang, L., Liu, A., H, H.Y., Zhang, K., Regional ionospheric TEC modeling based on a two-layer spherical harmonic approximation for real-time single-frequency PPP, Journal of Geodesy, Vol. 93 (**2019**) 9 1659–1671, doi:10.1007/s00190-019-01275-5.

Liu, W., Li, J., Zeng, Q., Guo, F., Wu, R., Zhang, X., An improved robust Kalman filtering strategy for GNSS kinematic positioning considering small cycle slips, Advances in Space Resarch, Vol. 63 (**2019**) 9 2724–2734, doi:10.1016/j.asr.2017.11.041.

Lu, C., Li, X., Ge, M., Heinkelmann, R., Nilsson, T., Soja, B., Dick, G., Schuh, H., Estimation and evaluation of real-time precipitable water vapor from GLONASS and GPS, GPS Solutions, Vol. 20 (**2016**) 4 703–713, doi:10.1007/s10291-015-0479-8.

Montenbruck, O., Schmid, R., Mercier, F., Steinberger, P., Noll, C., adn S. Kogure, R.F., Ganeshan, A.S., GNSS satellite geometry and attitude models, Advances in Space Research, Vol. 56 (**2015**) 6 1015–1029, doi:10.1016/j.asr.2015.06.019.

Montenbruck, O., Steigenberger, P., Prange, L., Deng, Z., Zhao, Q., Perosanz, F., I.Romero, Noll, C., Stürze, A., Weber, G., Schmid, R., MacLeod, K., Schaer, S., The Multi-GNSS Experiment (MGEX) of the International GNSS Service (IGS) – Achievements, prospects and challenges, Advances in Space Research, Vol. 59 (**2017**) 7 1671–1697, doi:10.1016/j.asr.2017.01.011.

Mu, H.Q., Kuok, S.C., Yuen, K.V., Stable robust extended Kalman filter, Journal of Aerospace Engineering, Vol. 30 (**2017**) 2 B4016010, doi:/10.1061/(ASCE)AS.1943-5525.0000665.

Nie, Z., Liu, F., Gao, Y., Real-time precise point positioning with a low-cost dual-frequency GNSS device, GPS Solutions, Vol. 24 (**2020**) 1 9, doi:10.1007/s10291-019-0922-3.

Nilsson, T., Böhm, J., Wijaya, D.D., Tresch, A., Nafisi, V., Schuh, H., Path delays in the neutral atmosphere. In Atmospheric Effects in Space Geodesy, Springer, Springer, Berlin, Heidelberg, **2013**, ISBN 978-3-642-36932-2.

Ning, Y., Han, H., Zhang, L., Single-frequency precise point positioning enhanced with multi-GNSS observations and global ionosphere maps, Measurement Science and Technology, Vol. 30 (**2018**) 1 015013, doi:10.1088/1361-6501/aaf0f6.

Pan, L., Zhang, X., Li, X., Li, X., Lu, C., Liu, J., Wang, Q., Satellite availability and point positioning accuracy evaluation on a global scale for integration of GPS, GLONASS, BeiDou and Galileo, Advances in Space Research, Vol. 63 (**2019**) 9 2696–2710, doi:10.1016/j.asr.2017.07.029.

Pan, L., Zhang, X., Liu, J., Li, X., Li, X., Performance evaluation of single-frequency precise point positioning with GPS, GLONASS, BeiDou and Galileo, Journal of Navigation, Vol. 70 (**2017**) 3 465–482, doi:10.1017/S0373463316000771.

Pan, Z., Chai, H., Kong, Y., Integrating multi-GNSS to improve the performance of precise point positioning, Advances in Space Research, Vol. 60 (**2017**) 12 2596–2606, doi:10.1016/j.asr.2017.01.014.

Paziewski, J., Sieradzki, R., Baryla, R., Multi-GNSS high-rate RTK, PPP and novel direct phase observation processing method: application to precise dynamic displacement detection, Measurement Science and Technology, Vol. 29 (**2018**) 035002 893–904, doi:10.1088/1361-6501/aa9ec2.

Petit, G., Luzum, B. (Eds.), IERS Conventions 2010, IERS Techn. Note 36, Verlag des Bundesamts für Kartographie und Geodäsie, Frankfurt am Main, Germany, **2010**, ISBN 3-89888-989-6.

Prange, L., Villiger, A., Sidorov, D., Schaer, S., Beutler, G., Dach, R., Jäggi, A., Overview of CODE's MGEX solution with the focus on Galileo, Advances in Space Research, Vol. 66 (**2020**) 12 2786–2798, doi:10.1016/j.asr.2020.04.038.

Rao, C.R., Estimation of variance and covariance components—MINQUE theory, Journal of Multivariate Analysis, Vol. 1 (**1971**) 3 257–275, doi:10.1016/0047-259X(71)90001-7.

Rebischung, P., Schmid, R., IGS14/igs14.atx: a new framework for the IGS products, in 2016 AGU Fall Meeting, San Francisco, CA, USA, **2016** .

Saastamoinen, J., Contributions to the theory of atmospheric refraction, Bulletin Geodesique, Vol. 105 (**1972**) 279–298, doi:10.1007/BF02521844.

Schüler, T., Diessongo, H., Poku-Gyamfi, Y., Precise ionosphere-free single-frequency GNSS positioning, GPS Solutions, Vol. 15 (**2011**) 2 139–147, doi:10.1007/s10291-010-0177-5.

Shi, J., Yuan, X., Y.Cai, Wang, G., GPS real-time precise point positioning for aerial triangulation, GPS Solutions, Vol. 21 (**2017**) 2 405–414, doi:10.1007/s10291-016-0532-2.

Steigenberger, P., Hugentobler, U., Loyer, S., Perosanz, F., Prange, L., Dach, R., Uhlemann, M., Gendt, G., Montenbruck, O., Galileo orbit and clock quality of the IGS multi-GNSS experiment, Advances in Space Research, Vol. 55 (**2015**) 1 269–281, doi:10.1016/j.asr.2014.06.030.

Sterle, O., Stopar, B., Prešeren, P.P., Single-frequency precise point positioning: an analytical approach, Journal of Geodesy, Vol. 89 (**2015**) 8 793–810, doi:10.1007/s00190-015-0816-2.

Subirana, J.S., Zornoza, J., Hernández-Pajares, M., GNSS Data Processing, Vol. I: Fundamentals and Algorithms, ESA Communications, ESA, **2013**, ISBN 978-92-9221-886-7.

Teunissen, P., Montenbruck, O., Springer handbook of global navigation satellite systems, Springer, Springer, **2017**, ISBN 978-3-319-42926-7.

Teunissen, P.J.G., Amiri-Simkooei, A.R., Least-squares variance component estimation, Journal of Geodesy, Vol. 82 (**2008**) 2 65–82, doi:10.1007/s00190-007-0157-x.

Wang, A., Chen, J., Zhang, Y., Meng, L., Wang, J., Performance of selected ionospheric models in multi-global navigation satellite system single-frequency positioning over China, Remote Sensing, Vol. 11 (**2019**a) 17 2070, doi:10.3390/rs11172070.

Wang, M., Wang, J., Dong, D., Meng, L., Chen, J., Wang, A., Cui, H., Performance of BDS-3: satellite visibility and dilution of precision, GPS Solutions, Vol. 23 (**2019**b) 56, doi:10.1007/s10291-019-0847-x.

Wang, N., Yuan, Y., Li, Z., Montenbruck, O., Tan, B., Determination of differential code biases with multi-GNSS observations, Journal of Geodesy, Vol. 90 (**2016**) 3 209–228, doi:10.1007/s00190-015-0867-4.

Welch, G., Bishop, G. (Eds.), An introduction to the Kalman Filter, University of North Carolina at Chapel Hill, Chapel Hill, NC 27599-3175, **1995**, ISBN TR 95-401.

Wu, J., Wu, S., Hajj, G., Bertiger, W., Liehten, S., Effects of antenna orientation on GPS carrier phase, Manuscripta Geodaetica, Vol. 18 (**1993**) 2 91–98.

Xu, P., Shi, C., Fang, R., Liu, J., Niu, X., Zhang, Q., Yanagidani, T., High-rate Precise Point Positioning (PPP) to measure seismic wave motions: an experimental comparison of GPS PPP with inertial measurement units, Journal of Geodesy, Vol. 87 (**2013**) 4 741–755, doi:10.1007/s00190-012-0606-z.

Xu, P., Shu, Y., Liu, J., Nishimura, T., Shi, Y., Freymueller, J.T., A large scale of apparent sudden movements in Japan detected by high-rate GPS after the 2011 Tohoku Mw9. 0 earthquake: Physical signals or unidentified artifacts?, Earth Planets and Space, Vol. 71 (**2019**) 1 43, doi:10.1186/s40623-019-1023-9.

Yang, Y., He, H., Xu, G., Adaptively robust filtering for kinematic geodetic positioning, Journal of Geodesy, Vol. 75 (**2001**) 2 109–116, doi:10.1007/s001900000157.

Yang, Y., Song, L., Xu, T., Robust estimator for correlated observations based on bifactor equivalent weights, Journal of Geodesy, Vol. 76 (**2002**) 6 353–358, doi: 10.1007/s00190-002-0256-7.

Yigit, C.O., Gurlek, E., Experimental testing of high-rate GNSS precise point positioning (PPP) method for detecting dynamic vertical displacement response of engineering structures, Geomatics Natural Hazards and Risk, Vol. 8 (**2017**) 2 893–904, doi:10.1080/19475705.2017.1284160.

Yuan, Y., Wang, N., Li, Z., Huo, X., The BeiDou global broadcast ionospheric delay correction model (BDGIM) and its preliminary performance evaluation results, Navigation, Vol. 66 (**2019**) 1 55–69, doi:10.1002/navi.292.

Yunck, T.P., Coping with the atmosphere and ionosphere in precise satellite and ground positioning, In: Valance-Jones A (ed) Environmental efects on spacecraft trajectories and positioning; AGU Monograph Series, Vol. 73 (**1993**) 1–16, doi: 10.1029/GM073p0001.

Zhang, B., Teunissen, P.J.G., Yuan, Y., Zhang, H., Li, M., Joint estimation of vertical total electron content (VTEC) and satellite differential code biases (SDCBs) using low-cost receivers, Journal of Geodesy, Vol. 92 (**2018**a) 4 401–413, doi: 10.1007/s00190-017-1071-5.

Zhang, Q., Zhao, L., Zhao, L., Zhou, J., An Improved Robust Adaptive Kalman Filter for GNSS Precise Point Positioning, IEEE Sensors Journal, Vol. 18 (**2018**b) 10 4176–4186, doi:10.1109/JSEN.2018.2820097.

Zhao, D., Ding, S.X., Karimi, H.R., Li, Y., Wang, Y., On robust Kalman filter for two-dimensional uncertain linear discrete time-varying systems: A least squares method, Automatica, Vol. 99 (**2019**) 203–212, doi:10.1016/j.automatica.2018.10.029.

Zhao, Q., Yao, Y., Yao, W., GPS-based PWV for precipitation forecasting and its application to a typhoon event, Journal of Atmospheric and Solar-Terrestrial Physics, Vol. 167 (**2018**) 124–133, doi:10.1016/j.jastp.2017.11.013.

Zheng, F., Gu, S., Gong, X., Lou, Y., Fan, L., Shi, C., Real-time single-frequency pseudorange positioning in China based on regional satellite clock and ionospheric models, GPS Solutions, Vol. 24 (**2020**) 1 6, doi:10.1007/s10291-019-0923-2.

Zhou, F., Dong, D., Li, W., Jiang, X., Wickert, J., Schuh, H., GAMP: An open-source software of multi-GNSS precise point positioning using undifferenced and uncombined observations, GPS Solutions, Vol. 22 (**2018**) 2 33, doi:10.1007/s10291-018-0699-9.

Zumberge, J., Heflin, M., Jefferson, D., Watkins, M., Webb, F., Precise point positioning for the efficient and robust analysis of GPS data from large networks, Journal of Geophysical Research: Solid Earth, Vol. 102 (**1997**) B3 5005–5017, doi:10.1029/96JB03860.

Publications

Bahadur, B., Nohutcu, M., (**2021**) Integration of variance component estimation with robust Kalman filter for single-frequency multi-GNSS positioning, *Measurement*, 173:108596.

Bahadur, B., Nohutcu, M., (**2021**) Real-time single-frequency multi-GNSS positioning with ultra-rapid products, *Measurement Science and Technology*, 32:014003.

Bahadur, B., Nohutcu, M., (**2021**) Impact of observation sampling rate on multi-GNSS static PPP performance, *Survey Review*, 53:378, 206-215.

Bahadur, B., Nohutcu, M., (**2020**) Galileo-based precise point positioning with different MGEX products, *Measurement Science and Technology*, 31:094009.

Bahadur, B., Nohutcu, M., (**2020**) Hassas Nokta Konumlama için robust Kalman filtresi yöntemlerinin analizi, *Harita Dergisi*, 86:164, 29-42.

Bahadur, B., Nohutcu, M., (**2020**) Multi-GNSS PPP: An alternative positioning technique for establishing ground control points, *International Journal of Environment and Geoinformatics*, 7:1, 88-92.

Bahadur, B., Nohutcu, M., (**2019**) Comparative analysis of MGEX products for post-processing multi-GNSS PPP, *Measurement*, 145, 361-369.

Bahadur, B., Nohutcu, M., (**2019**) GNSS alıcılarındaki saat sıçramalarının hassas nokta konumlama (PPP) performansına etkisinin araştırılması, *Jeodezi ve Jeoinformasyon Dergisi*, 6:2, 87-95.

Bahadur, B., Nohutcu, M., (**2019**) Galileo temelli Hassas Nokta Konumlama yönteminin performans değerlendirmesi: Türkiye örneği, *Harita Dergisi*, 85:162, 1-11.

Bahadur, B., Nohutcu, M., (**2018**) PPPH: a MATLAB-based software for multi-GNSS precise point positioning analysis, *GPS Solutions*, 22:113.

Bahadur, B., Nohutcu, M., (**2018**) Türkiye ve yakın çevresi için çoklu-GNSS kombinasyonlarının PPP performansına etkisi, *Harita Dergisi*, 84:160, 1-11.

Bahadur, B., Üstün, A., (**2014**) İnternet tabanlı GNSS veri değerlendirme servisleri, *Harita Dergisi*, 80:152, 40-50.

Oral and Poster Presentations

Bahadur, B., Nohutcu, M., (**2019**) Multi-GNSS contribution to single-frequency Precise Point Positioning, *XXIX. International Symposium on Modern Technologies, Education and Professional Practice in Geodesy and Related Fields*, 5-6 November 2019, Istanbul, Turkey

Gökçe, B., Dülger, D., **Bahadur, B.,** Nohutcu, M., Teke, K., (**2019**) Assessment of PPP positioning accuracy with different meteorological data sources, *XXIX. International Symposium on Modern Technologies, Education and Professional Practice in Geodesy and Related Fields*, 5-6 November 2019, Istanbul, Turkey

Bahadur, B., Nohutcu, M., (**2019**) GNSS alıcılarındaki saat sıçramalarının tespiti ve konum belirleme performansına etkisi, *17. Türkiye Harita Bilimsel ve Teknik Kurultayı*, 25-27 April 2019, Ankara, Turkey

Bahadur, B., Nohutcu, M., (**2019**) Multi-GNSS PPP: An alternative positioning technique for establishing ground control points, *10th Technical Symposium of the Turkish National Photogrammetry and Remote Sensing Association*, 25-27 April 2019, Aksaray, Turkey

Bahadur, B., Nohutcu, M., (**2019**) Recent Precise Point Positioning performance of Galileo, *EGU 2019 General Assembly*, 6-12 April 2019, Vienna, Austria

Bahadur, B., Nohutcu, M., (**2019**) Çoklu-GNSS Hassas Nokta Konumlamada (PPP) uyarlı robust Kalman filtresi kullanımı, *72. Türkiye Jeoloji Kurultayı*, 28 January 2019, Ankara, Turkey

Bahadur, B., Nohutcu, M., (**2018**) MGEX ürünlerinin çoklu-GNSS PPP performansına olan etkisi, *Türkiye Ulusal Jeodezi Jeofizik Birliği Bilimsel Kongresi*, 30 May-2 June 2018, Izmir, Turkey

Bahadur, B., Nohutcu, M., (**2017**) Türkiye için çoklu-GNSS PPP performansının değerlendirilmesi, *Türkiye Ulusal Jeodezi Komisyonu (TUJK) 2017 Yılı Bilimsel Toplantısı*, 2-3 November 2017, Istanbul, Turkey